Integrated Energy Management and Autonomous Driving System: A Driving Simulation Study

INTEGRATED ENERGY MANAGEMENT AND AUTONOMOUS DRIVING SYSTEM: A DRIVING SIMULATION STUDY

BY

LUCAS RIBEIRO BRUCK, B.E.

A THESIS

SUBMITTED TO THE DEPARTMENT OF MECHANICAL ENGINEERING

AND THE SCHOOL OF GRADUATE STUDIES

OF McMASTER UNIVERSITY

IN PARTIAL FULFILMENT OF THE REQUIREMENTS

FOR THE DEGREE OF

DOCTOR OF PHILOSOPHY

Doctor of Philosophy (2022) McMaster University

(Mechanical Engineering) Hamilton, Ontario, Canada

TITLE:	Integrated Energy Management and Autonomous Driving System: A Driving Simulation Study
AUTHOR:	Lucas Ribeiro Bruck B.E.(Mechanical Engineering)
SUPERVISOR:	Dr. Ali Emadi IEEE Fellow Canada Excellence Research Chair Laureate
NUMBER OF PAGES:	xxiv, 250

This thesis is dedicated to the women in my life;

The one who taught me how to walk,

The one who walks with me,

And the one I taught.

Abstract

In searching for more efficient vehicles with lower carbon emissions, researchers have invested enormous time and resources in designing new materials, components, systems, and control methods. The result is not only an immense volume of publications and patents but also a true electrification revolution in the transportation sector. Although the advancements are remarkable, much is still to be developed. Energy management systems are often designed to fulfil drive cycles that represent just a fraction of the actual use of the vehicles, disregarding essential factors such as driving conditions that may vary in real life. Furthermore, control algorithms should not ignore one of the most relevant driving aspects, comfort. Driving should be a pleasant activity since we spend much time of our lives performing this task.

This research proposes a novel algorithm for managing energy consumption in electrified vehicles, the regen-based equivalent consumption minimization strategy (R-ECMS). Its suitability for solving the power-split problem is evaluated. Experiments emulating labelling schedules are conducted considering an example application. Robustness to different drive cycles and flexibility of the algorithm to various modes of operation are assessed. Furthermore, the method is integrated into an autonomous longitudinal control. The function leverages vehicle dynamics and journey mapping to assure energy efficiency and adequate drivability.

Finally, the tests are conducted using human-driven cycles leveraging driving simulation technology. That allows for including driver subjective feelings in the design and assessing the algorithm's performance in realistic driving conditions.

Acknowledgements

I want to thank my supervisor, Dr. Ali Emadi, for the opportunity to work with the most outstanding researchers on electrified transportation technology. Thank you for your guidance, support, and patience over those years. I also would like to thank McMaster University and the Department of Mechanical Engineering for the support and infrastructure provided throughout those years.

I also thank Daniel Goretti for his mentorship and genuine friendship. Without his support and insights, this work would not have been possible.

I would also like to thank the professors that shared their time and knowledge with me: Dr. Saeid Habibi, Dr. Jennifer Bauman, Dr. Fengjun Yan, Dr. Ryan Ahmed, Dr. Stephen Veldhuis, and Dr. Mark Lawford.

This thesis would not have been possible without Atriya Biswas, Yi Huo, Pier Anselma, Bruce Haycock, Sara Rahimifard, Saeed Amirfarhangi Bonab, Giuseppe Buccoliero, Jeremy Lempert, Adam Lempert, Yue Wang, Aashit Rathore, and Joel Roeleveld whose active support was essential.

I am also grateful to my lab colleagues for their friendship: Carin Yeghiazarian, Sumedh Dhale, Diego Valencia, Peter Azer, Parisa M.Shamsabadi, Rasul Tarvirdilu Asl, Maryam Alizadeh, Jianbin Liang, Helia Jamali, Seyed Sobhan Kashfi, Mina Naguib, Joshua Taylor, and especially Mehdi Eshahian and Iman Aghabali.

Thank you also to the Brazilian community at MARC. Carlos Vidal, Silvio Rotilli Filho, Alan Callegaro, Eduardo Louback and specially Fabricio Machado and Josimar Duque, whose friendship I am the most grateful.

My recognition and thank you to all staff, especially Teresa Janes, Andy Stone, and Paul Nguyen. Your hard work makes possible all of MARC's achievements.

Finally, my eternal gratitude to all my family who cheered for me after each step. My mother, Valeria, always lifted me and pushed me forward, expecting the best of me and nothing less. My father Sayder for sharing with me his passion for vehicles, science, and technology. My beloved wife Ludimila for her never-ending support, patience, care, altruism, and love. My daughter Cecilia for being the first-light motivation each and every day.

Abbreviations

ACC	Adaptive cruise control
ABS	Anti-lock brake system
ACC	Adaptive cruise control
ACS	Active control systems
ADAS	Advanced driver assistance systems
AEB	Autonomous emergency braking
A-ECMS	Adptive-equivalent consumption minimization strategy
APU	Auxiliary power unit
BEV	Battery electric vehicle
BEVx	Range-extended battery electric vehicle
BSFC	Brake-specific fuel consumption
CAN	Control area network
CAS	Collision avoidance system

CD	Charge depleting
CO	Convex optimization
CS	Charge sustaining
DiM	Driver in motion
DOF	Degrees-of-freedom
DP	Dynamic programming
ECMS	Equivalent consumption minimization strategy
ECVT	Electronic continuously varible transmission
EMS	Energy management strategy
ESC	Electronic stability control
ESS	Energy storage system
FCW	Forward collision warning
FL	Fuzzy-logic
FoV	Field of view
GA	Genetic algorithm
GMM	Gaussian mixture model
GPS	Global positioning system
HAS	Hill start assist

HDC	Hill decendant control
HEV	Hybrid electric vehicle
HIL	Hardware-in-the-loop
HMD	Head-mounted devices
HMI	Human-machine interfaces
HMM	Hidden Markov models
HWFET	Highway fuel economy test schedule
ICE	Internal combustion engine
JM	Journey mapping
KWS	Kinematic wheel suspension
LDW	Lane departure warning
LKS	Lane keeping system
LMS	Least mean square
LSTM	Long short-term memory
MC	Markov chain
MDT	Mean dwell time
ML	Machine learning
MPC	Model predictive control

MPG	Miles per gallon
MSCA	Multi-sensory cueing algorithm
NARX	Auto regressive neural network
NMPC	Non-linear model predictive control
NN	Neural network
NSGA-II	Sorting genetic algorithm II
NVH	Noise, vibration and harshness
OCV	Open circuit voltage
OCV-R	Open circuit voltage-resistance
pHEV	Plug-in hybrid electric vehicle
PHEV	Parallel hybrid electric vehicle
PID	Proportional-integral-derivative
PMP	Pontryagin's minimum principle
PSO	Particle swarm optimization
RB	Rule-based
RC	Resistance-capacitance
R-ECMS	Regen-based equivalent consumption minimization strategy
RL	Reinforcement learning

RLS	Recursive least square
RNN	Recurrent neural network
SDP	Stochastic dynamic programming
SHEV	Series hybrid electric vehicle
SOC	State of charge
SOH	State of health
STPA	System-theoretic process analysis
TMS	Track monitoring systems
TPM	Tire pressure monitoring system
TTM	Twin-track model
UDDS	Urban dynamometer driving schedule
V2X	Vehicle to road/database
wot	Wide open throttle
ZEV	Zero emision vehicle

Contents

List of Tables

List of Figures

Chapter 1

Introduction

1.1 Background and Motivation

The prospects of climate change are not optimistic. Warmer oceans, higher sea levels, and aggressive precipitation patters originated by the accumulation of greenhouse gases in the atmosphere have been increasing temperatures catastrophically Masson-Delmotte *et al.* (2021). The industrial and transportation sectors together have been contributing the most to accelerate that deterioration Lamb *et al.* (2021). That has driven government and environmental agencies around the world, with support of the general public, to urge vehicle manufacturers to change the historical energy matrix used for the automobile, oil.

That paradigm shift created an electrification trend in the automotive sector that has allowed industry to comply with tight governmental regulations for emissions and crescent demand on the market for fuel-efficient vehicles. Besides, it has shaken the research and development centres around the world, pushing component design, control, and optimization technologies forward, increasing the investment in research,

employing thousands of people, and creating a sector of its own. As a consequence, powertrain systems of various forms and configurations emerged which made vehicles cleaner, more powerful, and efficient.

Traditional approach to powertrain design consists in virtual development followed by physical development. The former includes defining performance requirements, topology selection, initial sizing of components, and off-line optimization of controls. The latter includes consumption, dynamic, durability, and reliability assessments under diverse conditions. The two processes are often ill-connected which results in physical development overwriting some benefits planned in the virtual development.

In addition, although extensive research has investigated different optimization methods, feasibility and applicability are often limited. That is tight also to the limitations in the testing methods. Most research is conducted in the simulation environment only, never making to prototyping and deployment. That restricts most of the literature to simplified energy consumption analysis, disregarding the fact that driver feeling in the form of drivability and comfort are key aspects of automotive design.

At the epicentre of powertrain development stands the design and calibration of energy management strategies (EMS). Numerous EMS were developed in recent years making it an interesting object of research and debate.

That scenario motivates this research to developing a new control algorithm that addresses vehicle energy consumption and efficiency. Furthermore, a test platform is created to bridge the gap between virtual and physical developments.

1.2 Contributions

In summary the contributions of this research include:

1. A literature review on the relevance of driving conditions in the assessment of energy management strategies.
2. A literature review on driving simulation technology and a framework for using it to powertrain development.
3. A methodology for modelling the driveline kinematics of electrified powertrain and example models.
4. A real-time method for estimating vehicle road-load coefficients
5. A novel EMS that leverages vehicle dynamics and driving condition mapping.

1.3 Thesis Outline

This research creates and investigates the performance of a new EMS in different conditions and environments. In addition, it provides a driver-in-the-loop test platform to assess it. That helps blending virtual simulation with experimental testing and foments the creation of new real-time algorithms.

Chapter 2 reviews driving simulation state-of-the-art technology and applications. It also presents the set-up used in this thesis and validates a baseline vehicle model that is loaded in the driving simulator.

Chapter 3 presents a literature review on EMS listing and classifying relevant algorithms. It also provides an overview of the current consumption assessment methods and techniques to include driving conditions to improve fuel performance.

Chapter 4 reviews modelling methods both for vehicle and powertrain. A methodology for the creation of electrified models is detailed and applied.

In Chapter 5, the regen-based equivalent consumption minimization strategy (R-ECMS) is described in detail and then applied to an example topology. The proposed vehicle model and algorithm are assessed in regards to consumption, drivability, and performance. Its functionalities and robustness are also tested.

In Chapter 6, the R-ECMS is integrated to an autonomous feature. The longitudinal controller has its layers outlined and the integration detailed. It is then calibrated leveraging driver perception of vehicle dynamics and journey mapping. Driver comfort and energy consumption are assessed.

Finally, Chapter 7 provides a conclusion and prospects for future work. It also presents a summary of publications and contributions of the present research.

Chapter 2

Driving Simulation Technology and Applications

2.1 Introduction

The concept of simulation can be defined as the emulation of a specific behavior through a generic imitating system Slob (2008). In the automotive field, simulation is used both in academia for research and in industry for design purposes. The reason is that by using virtual simulation, new systems can be developed and evaluated within lower time and with lower financial investment. In the automotive industry for instance, virtual simulation can be used throughout all phases of development of a new vehicle. During virtual design, model-in-the-loop analysis enables the comparison of different system architectures, e.g. comparison of powertrain topologies to evaluate the fuel consumption and emissions.

Virtual simulation also speeds the testing phase. Structural, fluid dynamics, and

multibody simulation not only optimize the characteristics and geometry of the components, but also work as filters for component selection, e.g. definition of spring pre-load and shock absorber dynamic curve in suspension tuning. Without virtual simulation, not only would the development cost increase, but also the timeframe needed to accomplish each step of development would be longer. During calibration of on-board software parameters or performance components, virtual simulation reduces the number of prototypes that will eventually be manufactured for testing. In this way, the design process as we know it today, with rapid release of new products, is only possible due to simulation. Within the various types of vehicle simulation, the ability to imitate a ground vehicle's response in real time given real driver inputs is called driving simulation and it relies on virtual cues to "trick" human perception and create the illusion of immersion and motion in a controlled environment.

In the early 1910s the first motion simulators begin to appear in England and France as a means to safely provide flight training Valverde (1973). Motion simulation technology would not be restricted to flight training for long, however. It is not clear though which driving simulator was the first to appear, some researchers acknowledge the system designed in Miles and Vincent (1934), published in 1934 but given the simple architecture of this traffic simulator some authors prefer to point out later works as the real beginning of relevant developments of driving simulators. During the 1970s several 3 degree-of-freedom (DOF) driving simulators were developed by auto makers and research institutes as depicted in Slob (2008), such as the well-known device designed by Volkswagen and another at the Swedish Road and Traffic Research Institute. In addition, the pioneer work to develop the "Computer Generated Display Simulator" by General Motors together with the Virginia Polytechnic Institute and

State University from 1973 to 1975 is acknowledged in Wierwille and Fung (1975).

All previous attempts made significant contributions, but it was in 1985 that Daimler-Benz came up with a 6-DOF hexapod motion system integrated to a vehicle dome Gruening *et al.* (1998) that would be later accepted as the most common configuration of high level driving simulators around the globe. Rapid development of new graphic sources happened between the late 1990s and early 2000s Blana (1996). Digital three-dimensional (3D) graphics, new display resolution, and real-time graphic processing opened a new world of possibilities for driving simulators. The combination of various electronics improvements over the years made the increasing fidelity of driving simulators possible.

Recent studies use driving simulation technology to assess EMS, human machine interfaces (HMIs), active control systems (ACS), advanced driver assistance systems (ADAS) and road planning. The purpose of this chapter is to break down the mechanisms behind the driving simulation technology, describing the main components of a driving simulator, as a guide for resource centers that want to implement this technology. This contributes to providing a comprehensive review of the past and current state-of-the-art technologies, driving simulator examples, and applications. Former reviews of this kind can be found in Blana (1996), where a thorough survey of relevant simulators at that time was conducted. In that review, the simulators are clustered by their level of cost, a very common form of classification. Additional reviews were presented in Fisher *et al.* (2011), with example applications in medicine and engineering, in Jamson (2010), that details motion system design, and in Mohajer *et al.* (2015), where the focus is on the classification.

The chapter is organized as follows. Section 2.2 introduces the human perceptual

system. Section 2.3 explains the architecture of driving simulators. It discusses each component separately, exposing current technologies and giving examples. Section 2.4 discusses various applications throughout automotive industry and research. Section 2.5 introduces the driving simulator at the MARCdrive lab. It also details the virtual environemnts and the baseline vehicle model used in this work. Section 2.6 summarizes the review and states the prospects for driving simulation.

2.2 Human perceptual system

Since the role of a driving simulator is to imitate driving in the real world in order to deceive perception, it is important to understand how the human body perceives the driving experience. In driving simulators, multiple systems are combined to form the self-motion perception as further detailed. Because driving is primarily a visual task, one of the most important human sensors to be accounted for in driving simulation is the visual system. In fact, the visual system accounts for the majority of motion perception in a three-dimensional environment Zaal *et al.* (2006). The optical flow together with visual direction and extra-retinal direction form the visual information to be interpreted by the brain in order to define heading Wilkie and Wann (2003). Although less important than the visual system, the auditory system can also be classified as a self-motion perceptual system. It is proven in Keshavarz *et al.* (2017) that through audio means only, separate from other sensory systems, individuals are able to identify, with certain precision, the time-to-collision of sources of noise. Interesting research is conducted in Keshavarz *et al.* (2014) where the authors concluded that adding auditory cues to visual cues increases the illusion of motion.

While in static simulators the visual and auditory systems are responsible for all

motion perception, in motion simulators other body sensors are also engaged to build the driving experience. The somatosensory system is responsible for all tactile perceptions and proprioceptive sensors Wilkie and Wann (2003), the former accounting for force changes due to motion and the last accounting for position perception and accelerations. As proposed by Lackner and DiZio (2005), it is possible to create an illusion of motion by vibrating postural muscles. Therefore, the better the cabin mimics the actual environment of a vehicle cockpit (e.g. by representing with fidelity the internal components, dashboard, seats, texture, commands, and pedals) as well as faithfully representing the vibration and the friction resistance for moving each component, the more realistic the driving experience.

The vestibular system is an inner ear complex comprising semi-circular canals and otolith organs, to recognize linear as well as angular motion Mohajer *et al.* (2015). As detailed in Widmaier *et al.* (2008), the semi-circular canals consist in three circular cavities filled with a fluid (endolymph) that deflect hair lining the canals when an angular acceleration is experienced, such as when the individual is nodding or tilting their head left to right, with an output proportional to angular velocity. The otolith organs, on the other hand are made by the combination of small sacs of sensitive hairs. The role of the sensitive hairs is to sense linear acceleration as well as gravitational forces and transmit it to the central nervous systems. The utricle detects the motion in the horizontal plane, while the saccule detects it in the vertical plane. A representation of the inner ear organs is depicted in Fig.2.1. An example of modelling the visual-vestibular system was presented in Markkula *et al.* (2019), showing how drivers make use of the vestibular system to determine steering angle. Furthermore, this work provides evidence that drivers adapt depending on how those cues are given.

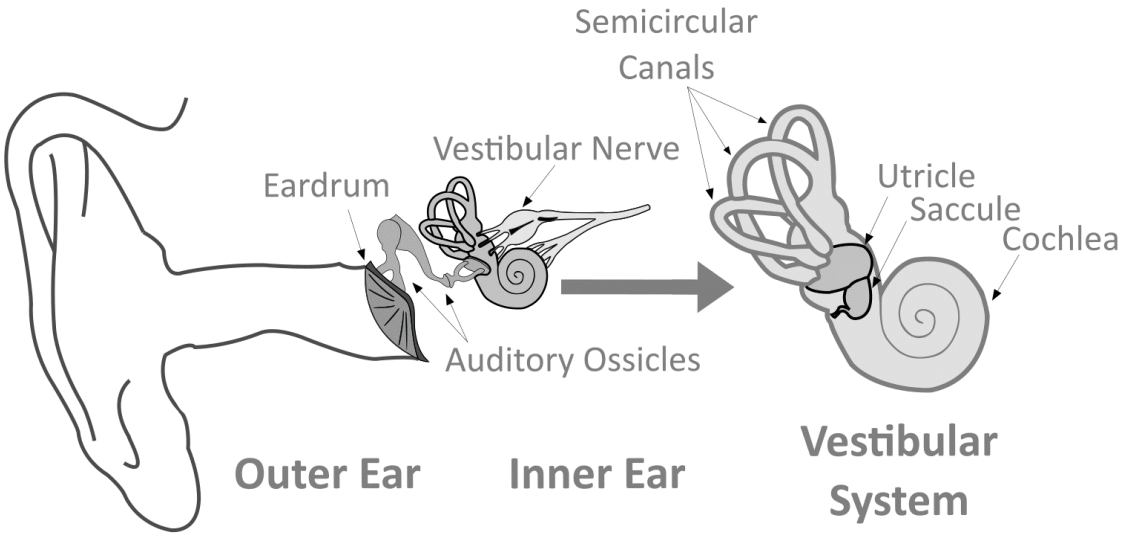

Figure 2.1: Human vestibular system

2.3 Architecture

As mentioned before, the goal of a driving simulator is to create an illusion of the driving experience. To accomplish that, different systems are combined. The diagram depicted in Fig. 2.2 shows not only the interdependence between each subsystem but also how driver and vehicle model are in the center of the process. Driver input is used to calculate the vehicle dynamics by the vehicle model, which will be used by the feedback systems to give the driver the necessary cues. The scenario control uses the definitions of environment (terrain), and the vehicle dynamics to output visual and sound cues. In simulators where multiple projectors are used to create a seamless image typically projected onto curved screens, the warping and blending of the image must be done before projection. Haptic feedback such as steering torque, active seats and belts is also used to provide cues from the vehicle dynamics.

The bold path in Fig. 2.2 shows optional systems in the sequence for providing

motion in driving simulators. This can improve the immersion considerably, and better allow for experiments examining the dynamics of the vehicles such as for the development of active systems. In motion simulators, the motion cueing algorithm will take the vehicle response and determine how to move the motion system accounting for the kinematics of that system, be transformed into actuator commands by the kinematics of the machine, and then produced by the motion system providing cueing to the human driver.

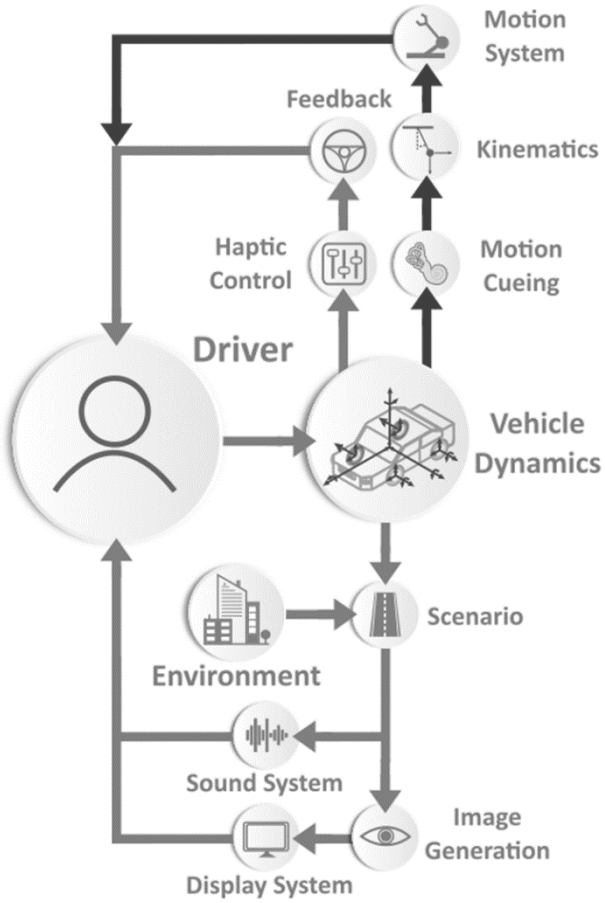

Figure 2.2: Diagram of a driving simulator

2.3.1 Vehicle dynamics model

The definition of "model" is presented in Balci (2003) as a simplified system that reproduces the characteristics of a more complex structure or organism. In vehicle simulation, often third-party software is dedicated to the vehicle dynamics model. This model must contain a mathematical representation of the vehicle subsystems (i.e. body frame, suspension, tires, brakes, steering and powertrain) Jazar (2017) and it must be able to compute the dynamic behavior relative to a fixed global orientation system, calculating component forces and non-linearities Schramm *et al.* (2014). Furthermore, driver-in-the-loop simulation applications require the vehicle models to be calculated within the available time step, without losing accuracy Blana (1996).

A simple way to represent vehicle motion is through the quarter car model detailed in Gillespie (1992) that isolates the analysis by focusing on the motion and forces of a single wheel. Although this model is helpful to understand wheel dynamics, it does not represent all motion available in a vehicle. The single-track model and the linear roll model add lateral dynamics and roll dynamics respectively Schramm *et al.* (2014), still those models do not account for the minimum necessary motion to fully reproduce driving experience. The twin-track model (TTM) is the simplest model that can support the needs of a full motion driving simulator Schramm *et al.* (2014). The TTM without the Kinematic Wheel Suspension (KWS) model has 14-DOF, i.e. it models the translational and rotational motion around the longitudinal, lateral and vertical axes (x, y, and z), the rotation of the wheels, and the vertical motion of each wheel individually. Considering the full motion of the wheel suspension and steering components the twin-track model can describe the vehicle motion accounting

for 30-DOF. Since multibody system approach is based on the relationship between rigid bodies and joints as subsystems, it is considered ideal for mechanical systems simulation. Therefore, the most common vehicle dynamics software are multibody solutions. In addition, an important characteristic these days is co-simulation with a third-party software, which enables the assessment of several advanced control systems such as electric power steering, electronic stability control, and powertrain control systems Balci (2003). Furthermore, by being able to interact with other vehicle system's modules the driving simulator becomes a platform for hardware-in-the-loop simulation and validation of those systems.

2.3.2 Scenario design

Another key feature of driving simulator is the possibility of creating specific scenarios. In driving simulation, a scenario can be described as an event that happens in a virtual environment. The event can be a predefined situation, e.g. a pedestrian crossing in front of the ego vehicle, or a situation created by the driver, e.g. a sine with dwell maneuver. In these examples, the environment is the terrain, road, signs, buildings, and other objects surrounding the ego vehicle. The scenarios are created by varying the traffic, weather, and events in that environment. As described in Matowicki *et al.* (2016), there are different methods to generate driving scenarios and pre-defined trajectory of virtual vehicles in order to simulate traffic. The trajectory of those vehicles can be developed simply based on road geometry, imported data from other simulations, or through an interface that interacts with the driving simulator engine. The work developed in Sun *et al.* (2015) instead builds a platform to co-simulate multiple driving simulators, which increases the realism of the traffic scenario. The

study in Yang *et al.* (2018) uses a traffic scenario to evaluate how traffic density affects overtaking and lane change maneuvers.

In Sharples *et al.* (2016) the scenario construction was focused on signs and road-side information warnings, instead of other vehicles. The idea was to measure how the driver's journey decision is affected by the information available. Repeatability is very important in early phase of development because engineers can easily visualize the problems a certain system presents in specific condition. Although possible to forecast, weather is usually a limitation in vehicle testing, depending on which region the manufacturer testing center is located. In the case provided by Xiao *et al.* (2017) and Chang *et al.* (2019), the low visibility in foggy situations and the risk brought by this condition is evaluated.

2.3.3 Visual cues

Over the years, visual cues evolved from analog video presentations and film to digital graphics. These digital graphics rapidly improved from a low number of polygons to high count textured and shaded polygons that provide a highly realistic environment for use in driving simulation. In addition, the improvement of projector technology with increasingly higher pixel resolution, brightness, and contrast ratio, made the accurate projection of such graphics possible Blana (1996). On the contrary, these projectors have been used with similar front projection curved screens as presented in Kemmerer Jr *et al.* (1975) since the 1970s, which has only now begin to change in limited applications with the use of head-mounted devices (HMD). Even with the advent of HMD, projection screens are still preferable in most cases, as the limited field of view, image lag, and the obscuring of the vehicle interior limit the usefulness

of this type of device. Nevertheless, a few authors explored the suitability of these systems in driving simulators in Blissing and Bruzelius (2018) and Zöller *et al.* (2019). Although they foresee an increase in the use of head-mounted devices, they agree that screen-based projection systems still are preferable among tested subjects since they give a better perception of velocity and surroundings.

In an attempt to enhance the visual cues, several authors present different add-on solutions to the conventional rounded screens presented in the most advanced driving simulators. In Colombet *et al.* (2011) a visual scale factor is used in an attempt to enhance the speed perception by changing the geometric field of view. In Schmieder *et al.* (2017), the authors replaced a monoscopic projection system with a 3D-stereoscopic system for improved depth perception, to investigate the use of 3D projector for enhancing velocity as well as distance judgement in a driving simulator. The passive stereoscopic 3D was achieved by using 10 projectors, one projector per eye for each one of the 5 channels for the forward view. The masking is done through a wavelength multiplex process which requires filtering of the projector signals and filtering glasses for the driver. The main drawbacks of such system are the cost associated with the added complexity, the packaging of the projectors in the display structure, and the potential for increased eyestrain and resulting simulator sickness. By exposing subjects with attested regular stereopsis to a simple car following scenario, the authors were not able to provide strong evidence of the improvements. Lastly in Haycock *et al.* (2019), a headlight glare system is created to help understanding how driver performance with different populations is affected by the glare of oncoming vehicles during night driving in rural highway scenarios.

Improvements in PC hardware for rendering virtual worlds has enabled the use

of gaming engines in place of the previously used custom rendering hardware. One widely used software package for rendering virtual environments in simulators is OpenSceneGraph. Other products that have gained momentum recently given their realistic rendering are Unity and Unreal Engine. Realistic animation and vast object databases can highly improve immersion. The work in Merenda *et al.* (2019) assesses how different the driver behavior given different fidelity of visual systems. In that work, a low graphic fidelity simulator was compared to a high fidelity one built with the Unreal engine. The results show that visual attention and situation awareness are highly impacted depending on the fidelity of the visual system. Given its ability to reproduce realistically external objects, Unreal can also be used as a platform to train and test autonomous systems, as developed in Leudet *et al.* (2019).

2.3.4 Auditory cues

As defined in Heitbrink and Cable (2007), the importance of the audio cues is justified by how it affects speed judgement, driver awareness, and fatigue. In fact, the audio impact on speed perception is depicted in Ramkhalawansingh *et al.* (2016). In this work, an experiment is conducted with subjects of different age ranges (young and older adults) that are exposed to driving tasks where visual cues to self-motion are provided while the respective presence/absence of auditory cues is manipulated. The conducted experiment proves the assumption that auditory cues affect longitudinal motion perception (speed and acceleration), with older adults more susceptible. Therefore, it is also important to have a well-designed audio library in order to provide quality congruent cues to the driver and maintain the immersion created by the visual system.

Three-dimensional sound is the most suitable choice in driving simulation application Blana (1996) since the noise inside the cabin is a combination of noises from different sources, i.e. aerodynamics, tire interaction with the surface, and driveline Mohajer *et al.* (2015). As explained in detail in Suikat (2005), the majority of simulators use the wave table method which consists of lookup tables that receives input values from the sources in the simulation engine (e.g. road, powertrain, and wind sounds) and outputs interpolated cues. In addition, the importance of low frequency speakers is also explained since interior cabin noises are in this frequency range.

2.3.5 Haptic cues

The control components (i.e. steering wheel and pedals) act as a bridge between human input and vehicle behavior, making them essential tools in vehicle dynamics feedback. For that reason, the human-vehicle interaction must be mimicked in order to provide a high-fidelity driving experience. Most driving simulators include components that provide force feedback through the steering wheel and braking system as exemplified in Slob (2008), Blana (1996), Bruschetta *et al.* (2017a), Nehaoua *et al.* (2008), Heitbrink and Cable (2007). The vast majority use a torque motor for the steering wheel force feedback, commanded by the vehicle dynamics model. As stated in Mohajer *et al.* (2015) the accurate vibration on the steering wheel, mimicking tire-road interaction, provides cues for speed and trajectory, enhancing driver perception.

2.3.6 Motion cueing algorithm

The presence of a motion system requires the inclusion of a motion cueing algorithm. This algorithm is responsible for creating the displacements of the motion system accounting for human perception and the available workspace Bruschetta *et al.* (2017a), therefore its role is to govern the motion of the simulator to provide the driver realistic driving sensations Fang *et al.* (2017). There are several approaches for motion cueing algorithms as described in the following sections. The work in Reid and Nahon (1985) details the development process of the classical, the optimal, and the adaptive motion cueing for flight simulators, being an essential read for motion cueing developers although it does not include newer approaches such as model predictive control.

Classical Filter

The classical filter (or washout filter) is the most simple and fast method for motion cueing design Fang and Kemeny (2012). As depicted in Fig. 2.3 the washout algorithm relies on the interaction of high- and low-pass filters that are responsible for the platform's translational and rotational cues Mohajer *et al.* (2015). In the picture, S represents the displacement cues and Ω represents the angular. The tilt coordination is a tool used to replicate low frequency sustained accelerations, it performs a tilt of the cabin in order to create a component of the gravitational force in a desired direction Bruschetta *et al.* (2017a). Although the design and implementation of the classical filter is not very complex compared to other methods, its tuning might be time consuming given the fact that it relies extensively on trial and error.

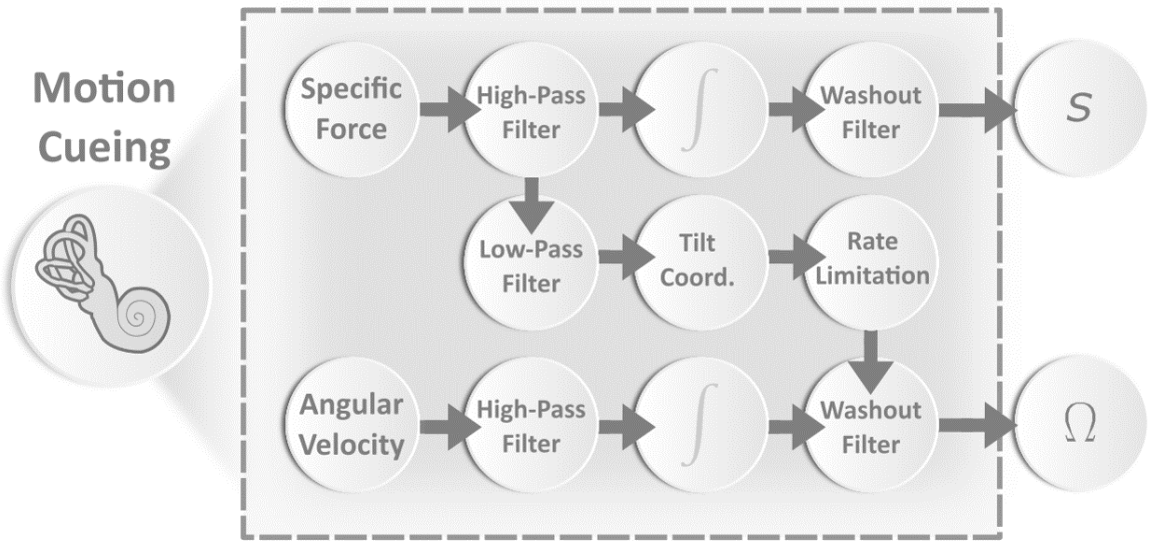

Figure 2.3: Diagram of a classical filter motion cueing algorithm

Adaptive Filter

In the adaptive filter algorithm, the parameters that make up the washout algorithm can self-tune. The work in Asadi *et al.* (2019) presents a fuzzy logic-based motion cuing classical filter that accounts for both physical boundaries of the platform and error between reference motion and actual motion when outputting the filter gains. This work develops an algorithm that not only provides a better use of space but also reduces the human perception of motion error, having a performance similar to the algorithms that use model predictive control, later explained. As detailed in Nehaoua *et al.* (2008) the parameters of the motion algorithm can also be calculated through the minimization of a cost function, based on the error between vehicle model and platform acceleration and on the motion system limits. In this case, the sensitivity equations are solved through an extension of Laplace's method (Method of Steepest Descent) which makes the filter to be non-linear. In another work in Miunske *et al.*

(2019), the authors develop an adaptive tilt-coordination that maximizes the use of the longitudinal and lateral environment instead of relying solely on tilt to sustain the acceleration imposed by the driver. The authors accomplish their objective by labeling the acceleration state and regulating the error between the perceived and actual acceleration using linear quadratic regulation. One challenge faced by the authors in this case was the difficulty in finding representative range for the adaptable parameters. The most noticeable issue with using adaptive filters though, is that filter tuning is replaced by cost function tuning. If the parameters are allowed to be updated rapidly, motion distortion resulting in false cues occur.

Optimal Filter

Another approach is the optimal filter algorithm. This method either adds the human perception model (vestibular model) or uses a reference vehicle motion previously recorded to set a comparison between the real and the virtual experience calculated by this new model Chen and Fu (2010). The comparison is built and optimized through a transfer function that links the simulator motion inputs to the actual vehicle motion. The objective is to minimize the error in human perception. The major difference between the classical and the optimal approach is the way the filters are calculated, in this case beforehand, through an optimization process that can be done as in Mohajer *et al.* (2015) through the use of different optimization techiques.

The performance of optimal filter methods is linked to the quality of the reference signal whether it comes from a model or empirical measurement. Therefore, model and test limitations can negatively impact the results. Also, the optimization might output different parameters for different set of maneuvers. The impacts of

rapidly switching between parameters should be observed as previously mentioned for adaptive filters.

Model Predictive Control Algorithm

Derived from the optimization methods, the model predictive control strategy (MPC) consists of predicting the evolution of dependent variables caused by changes in the independent variables. In essence, the MPC selects an optimal control input at the current time based on prediction of the future behaviour over a given time window. With this future prediction feature the MPC strategy can optimize the motion input, making a better use of the available workspace and motion structure when compared to simple methods such as the classical washout filter Aulia *et al.* (2019).

As shown in Bruschetta *et al.* (2017b), the inputs given by the real driver are received by the vehicle dynamics model which passes forward the vehicle's acceleration and angular velocities. This information must then be pre-processed to build a predicted sequence of reference variables. Often, the next step is to assess the vestibular model to build the perceived values of acceleration and velocity. Other methods might simply use the angular velocity and specific force. As a final step, the system displacement is calculated in order to track the perceived values before being handled to the motion control system. The importance of the reference over the MPC prediction horizon is highlighted in Lamprecht *et al.* (2019) where the future behavior of the driver is modelled as an optimal controller to have its behavior predicted and in Bukal *et al.* (2019) where the motion scale is treated as an optimization variable and a model of the kinematics of a 7-DOF motion system is used for motion prediction. In this work it is shown that the separation of the penalty on the motion gain from the

overall target perception benefits the motion reproduction since excessive high-pass filtering and tilt-coordination becomes not required when reproducing long-period forces.

Although the process is simple, the computational burden is complex given the presence of so many complex models. In Mohammadi *et al.* (2018), both the human vestibular system and dynamic platform are modelled. For the vestibular system, linear transfer functions for the otoliths (translational motion) and for the semicircular canals (angular motion) are considered. A multi-objective problem is solved using the sorting genetic algorithm-II (NSGA-II) method, where the outputs are the gains for the translational and angular displacements and velocities of the platform. The proposed nonlinear MPC in Bruschetta *et al.* (2018) uses a multi-sensory cueing algorithm (MSCA) that accounts for the coordinates of the 9-DOF motion platform together with the coordinates for the active seat and active seatbelt. In addition, a model of a seated driver is added to the vestibular model to predict the effects of the forces generated by the seat and seatbelts. It is shown that this approach has a great impact in compact simulator since the use of space is optimized.

Although the MPC method has the potential to optimize the use of space and the driver experience, its often-understated limitation resides in how far ahead it can foresee without compromising the real time requirement. It is important to highlight how imprecise prediction can undermine the fidelity of motion. Some works focused on different methods aiming to reduce the optimization time. In Rengifo *et al.* (2018), a continuous-time recurrent neural network (RNN) is used. In this work the authors model the dynamic platform kinematics and use a RNN to compute and apply the optimal trajectory of the platform online.

It is possible to conclude that the MPC method allows better use of the available hardware and automated tuning of the cues when compared to the previous methods, although its implementation requires complex modelling of different systems and massive computation power. Nevertheless, the MPC approach is considered promising for enabling state-of-the-art simulators to deliver best possible motion cueing.

2.3.7 Kinematics

The kinematics algorithm plays an important role connecting the motion cueing commands with the motion system's structure and hardware. The output of the motion cueing algorithm is trajectory of the cabin in Cartesian space, and this trajectory must be achieved by varying the length of the actuators. Therefore, actuator's action is a function of desired cabin motion. As explained in Chiew *et al.* (2008) and Zeng *et al.* (2014), the concept of kinematics in driving simulation can be classified either as forward kinematics or inverse kinematics. The authors agree that forward kinematics is the process of determining the position of the motion platform once the actuators lengths are known (or predefined). Inverse kinematics is the process of acquiring the actuators length given the desired position of the motion platform. Likewise, in Jin *et al.* (2015), inverse kinematics is defined in a more generic way as the process of calculating the joint coordinates from the end-effector coordinates. In driving simulation, the end-effector is the mock-up cabin, and the joints are the couplings of each actuator to the motion platform. Since actuator length is a function of the desired motion of the cabin as previously mentioned, authors often specify the kinematics process in driving simulators as inverse kinematics.

The Stewart platform mechanism powered by electric/hydraulic actuators is very

common among the state-of-the-art driving simulators. In Jia *et al.* (2019), the authors describe a virtual modeling process of defining the kinematics of a Stewart platform and its boundaries, accounting for the type of the actuators, joints, and hinges. Stability is key to achieve real driving experience. Therefore, other studies focus on control methods to assure stability of those platforms. In Kumar and Bandyopadhyay (2012), the requested position of the motion platform is performed using high order sliding mode control. In Tamir *et al.* (2019), a virtual PD+ controller on the basis of the passivity properties of the system was design to assure that the mechanism is asymptotically stable.

2.3.8 Motion System

The better the motion system is matched with the vehicle dynamics model, likely the higher the fidelity of the motion will be. There are several mechanisms to reproduce vehicle motion, from low fidelity systems with 2-DOF Zhang and Zhang (2013) and 3-DOF Suh *et al.* (2016), to high fidelity systems with up to 13-DOF Wilkinson *et al.* (2012). These mechanisms can be comprised of serial and/or parallel actuators. The parallel manipulators mechanism is a synergistic machine, where multiple actuators work together to support a single platform. The most common arrangement of parallel actuators applied in driving and flight simulators is the hexapod configuration, also called a Stewart platform, which is a compact design allowing for 6-DOF. The hexapod provides translational movement along, and rotational movement about, the three axes, x, y, and z Blana (1996). The hexapod consists of a lower platform and an upper platform coupled together with six identical linear actuators. Another example of parallel actuators is the tripod, with one actuator at each corner of the moving

platform it allows 3-DOF; roll, pitch and heave Suh *et al.* (2016). One advantage of these type of systems over robotic manipulators is that an entire vehicle or a vehicle cabin can be mounted on them as seen in several cases. That represents a level of immersion difficult to achieve with a robotic arm manipulator for example.

In a serial mechanism, actuators are stacked and work independently, the most common example in industrial automation being a series of links connected by actuated joints from the base to one end-effector. An example of using this arrangement for simulator motion is depicted in Katliar *et al.* (2019) where a jointed robot arm moves around a motion envelope in order to create the motion cues. In the cited work, the motion trajectory was optimized for the 8-DOF motion system, combining the six-axis serial manipulator with a linear track and translational-actuated cabin. Although this has some advantages over the hexapod system, such as a larger motion envelope typically, it has some drawbacks. These include the limitations of speed and acceleration imposed by the joints, the lack of immersion given its form, a high degree of motion noise created by the high friction system, and the most notorious, the need for a very specific inverse kinematics algorithm.

Although many state-of-the-art simulators use a hexapod as the primary source of translational and rotational motion, the most advanced motion systems employ additional mechanisms creating redundant degrees of freedom for increased range of motion in a hybrid combination of parallel and serial actuation. Adding a turntable below the vehicle cabin or on top of the upper platform may help reduce simulator sickness as well as minimizing frame drops in the visual system by removing the need for the visuals to render a high yaw velocity, such investigation is conducted in Mourant and Yin (2010). Another hybrid system employed is coupling a linear

longitudinal-lateral motion structure to the lower platform, for a much larger longitudinal and lateral displacement. The large motion area set-up will provide most of the midrange frequency longitudinal and lateral motion, filling the large transfer function dip between the high-passed filtered specific forces and the low-pass filtered tilt coordination inherent with a hexapod alone. A sizing method for this type of configuration is presented in Sadraei *et al.* (2018).

Some advanced driving simulators have this longitudinal-lateral motion in the form of a rail system like in the University of Leeds Driving Simulator Wei *et al.* (2019), the Stuttgart Driving Simulator located in Stuttgart University Pitz *et al.* (2014), others in the form of a steel belt drive on oil and bearings like the National Advanced Driving Simulator (NADS-1) Wilkinson *et al.* (2012) located in Iowa, United States. As explained in Wilkinson *et al.* (2012) the motion system of the NADS-1 presents 13-DOF achieved by the combination of a turntable (able to turn ± 330 degrees) mounted on top of a hexapod (6-DOF) that is attached to a longitudinal-lateral platform with a large displacement area (close to 400 m^2). A dome is assembled on the upper part of the turntable to house the vehicle cabin that is mounted above high-frequency electric actuators. the longitudinal-lateral rail track featured in the VTI IV simulator of the Swedish National Road Transport Research Institute Kharrazi *et al.* (2020). In this work, the competence of this set-up (hexapod + rail track) in providing a motion that delivers realistic cues is proven. Experienced drivers were capable of noticing detailed handling differences caused by variations of the vehicle parameters.

Although the system presented in Wilkinson *et al.* (2012) is considered to be one of the most capable of providing an accurate reproduction of real-world motion in a driving simulator, building systems such as this is not feasible for most testing

centers, research institutes, or even vehicle manufactures due to the very high cost and physical space required. Using the concept of a hexapod and linear motion mechanisms, the Driver in Motion (DiM) 9-DOF platform was designed. As detailed in Bruschetta *et al.* (2016), this type of motion system (DiM 150 and DiM 250) relies on the hexapod to provide rotational motion as well as small linear displacements. In addition, the hexapod is coupled to a planar tripod frame that slides on a flat surface through air pads, which allows lateral, longitudinal and yaw motion. This redundant DOF design provides larger workspace use and system bandwidth when compared to the classical hexapods Bruschetta *et al.* (2017b), but at a lower cost than larger linear motion systems. Other configuration of the DiM simulator is presented in Rengifo *et al.* (2018), DiM 700 uses a central pulley (called discframe) driven by four cables. With this configuration, the DiM motion system achieves an even larger motion envelope, which makes it a more suitable choice for applications that require the reproduction of longer sustained accelerations.

The DiM solution is objective of study of several papers regarding MPC motion cueing algorithms such as Bruschetta *et al.* (2019), and figures as one product of higher motion fidelity. When building a simulator, the definition of the motion system is key, and should be done based on the intended application. The work in Bruck *et al.* (2019b) develops an objective approach to be used when selecting between a 2-DOF, 3-DOF, or 6-DOF motion systems. The work also proposes a method to optimize the motion system geometry based on the future application of the driving simulator. Likewise, the work in Sadraei *et al.* (2018) proposes an approach to lower the cost of the set-up by optimizing the size of the motion system accounting for the available workspace and a high-fidelity motion response. Both works can be used together as

relevant guides for institutes looking for designing their own driving simulators. When designing a motion system, the actuators are equally as important as the architecture. Most recent simulator hexapods use electric actuators in place of hydraulics due to their lower cost and maintenance. They also allow for a higher motion bandwidth, but at a cost of higher friction and motion noise.

2.4 Applications

Driving simulation is broadly applied in research and industry. As discussed in Bruck *et al.* (2019a), the use of driving simulators expands with the increasing necessity of developing fast, cost-effective, and safe means of testing interactivity between vehicle, passengers, and environment. The following section showcases some applications for different types of driving simulators.

2.4.1 Driver-centered Studies

For all driver-in-the-loop simulators in the context of this review, the driver is an integral component of the total system being tested. However, one key branch of research is driver assessment, examining specifically the driver's behavior or performance rather than the vehicle systems. The most common use of driving simulation focused on the driver specifically are studies about driver training. Driving simulators can help drivers to enhance their ability and mitigate occurrence of accidents in the real world by presenting risky scenarios as in Ou *et al.* (2018) and Urlings *et al.* (2019), typical common situations as in Ali *et al.* (2016) and Imamura *et al.* (2013), or using both as shown in van Leeuwen *et al.* (2015).

An example of testing driver performance is examining how substances such as alcohol and cannabis impair the ability to drive. To perform these experiments on real roads with real vehicles would be not only unethical but also irresponsible, while this kind of experiment can be safely performed in virtual environments. Examples using driving simulation with alcohol consumption is presented in Irwin *et al.* (2017) and Mohajer *et al.* (2015). In those studies, subjects were evaluated in low and high quantities of alcohol while others were provided with placebo. The authors agree that the ingestion of alcohol raises the risk-taking behavior of the drivers. They also agreed that lowering the legal limits of blood alcohol concentration (BAC) would lower the likelihood of accidents. Newest studies were similarly performed for cannabis in Mohajer *et al.* (2015) and Mohajer *et al.* (2015).

Simulation can also be used to assess sources of distractions. In Mohajer *et al.* (2015) the influence surrounding vegetation has on driver's attention is evaluated through the use of an eye tracker. The results show that the vegetation plays a minor influence in longitudinal speed and lateral deviation although the roadside clear zone width can impact driving safety. Another use of an eye tracker system is presented in Mohajer *et al.* (2015), where the system monitors driver's gaze to understand the effects of fatigue on eye tracking measures. It is shown that there is a significant change in the pupil when the driver is alert compared to a fatigued driver, demonstrating the effectiveness of the device on assessing fatigue. A similar device is introduced and tested in Mohajer *et al.* (2015), using not only eye tracking but also heart rate and skin conductance measurements. Fatigue is also analyzed in Mohajer *et al.* (2015), and how it leads to driver sleepiness during automated drives. In this paper a dedicated camera monitored head movement in addition to driver's gaze

and the results showed that common features used for detecting drowsiness during manual driving might not be sufficient for performing the same detection during automated driving. Other driver assessments that would represent potential harm if performed in real environment but are easily done using simulators include testing mobile distractions Mohajer *et al.* (2015), performance decay in older drivers Mohajer *et al.* (2015), and the effects of daylight on sleepiness Mohajer *et al.* (2015).

Driving simulators can also be used to test HMI. Some studies focus on how to design an interface that will be better for the driver to interact with, where simulators can be of great help. That is the case in Large *et al.* (2019), where the authors evaluate how drivers interact with a secondary device. The participants interacted with a touchscreen, rotary-controller, steering-wheel-controls, and a touchpad. This type of analysis can rate the ease of use of a device during the driving task and show what to employ depending on the purpose of the device. Again, performing these tests in real life could compromise the safety of the people involved. In addition, the ease of integration and testing of such systems in a driving simulator can be beneficial compared to implementing them in a real vehicle.

Most recently, the interaction between automated driving systems and drivers is being a subject of intense debate. In Yun *et al.* (2019), the authors develop an approach to design and verify an HMI system to facilitate the transition from automated driving to manual driving. Other studies even propose interfaces that aim to build trust between passengers and machine in fully automated scenarios, such as in Morra *et al.* (2019). In this work the authors use VR system to provide the passenger a collection of cues that shares information from the sensors and the route planning.

2.4.2 Autonomous Systems

Driving simulation can also be used to test ADAS. A very common driving assistant system is the adaptive cruise control (ACC). This feature allows the driver to specify its maximum speed and minimum distance to the preceding vehicle. Examples of this work can be seen in Benedito and Dòria-Cerezo (2018) where driving simulation is used to explore the use of an ACC system in traffic situations, and in Bianchi Piccinini *et al.* (2019) where system failure is explored in different traffic scenarios.

One of the most important scenarios involving human interaction with ADAS is explored in Blommer *et al.* (2017), where the take-over maneuver is evaluated in different conditions. The volunteers had to face a forward collision situation with three different systems: autonomous vehicle with and without collision avoidance assistant, and manual drive mode. The results showed a lack of reaction by subjects when driving in the autonomous modes. In fact, the take-over maneuver is object of study of several papers regarding ADAS. In Cohen-Lazry *et al.* (2019) take-over request is studied and an investigation of the orientation of the tactical alert given to the driver (whether towards to the hazard or away from it) is conducted. The transition is assessed in a lane change maneuver where the current lane presents a hazard four seconds ahead. In Petermeijer *et al.* (2017), tactile, visual, and auditory requests are given to the driver in order to understand the differences those modalities have in gaining driver's attention. The work in Ogitsu and Mizoguchi (2015) highlights the importance of instruction and driver training on using ADAS.

Other works assessing take-over maneuvers can be found in Favarò *et al.* (2019) where different drivers are evaluated during a failure of the autonomous system, and in Lotz *et al.* (2019) where truck drivers face time critical take-over situations while

performing a non-driving tasks. In Wu *et al.* (2019), the authors evaluate how scheduled manual driving affects drowsiness and contribute to better take-over maneuvers when needed. In Koglbauer *et al.* (2018), an autonomous emergency braking system (AEB) that adapts to road friction is evaluated in comparison to a non-adaptable system. This scenario illustrates the highest level of assistance a driving simulator can provide during vehicle design because it allies the validation of a new safety feature in a driving condition very difficult to reproduce consistently (i.e. low-friction snowy road). It also highlights the importance of the ability to adapt to a changing situation or condition. Another example of AEB assessment is presented in Duan *et al.* (2017), where several vehicle-bicycle imminent collision events are proposed with the objective of redesigning validation tests in order to cover a larger number of scenarios. A very well-known system is the lane keeping assistant. As described in Wang *et al.* (2017), the lane keeping system helps the driver to keep the vehicle on a lane by applying torque (also called haptic feedback) to the steering wheel. In this work, the impact this system has on driver's fatigue during monotonous driving is investigated by monitoring the standard deviation of lateral position. The benefit of haptic feedback is also evaluated in Pakdamanian *et al.* (2018), where the authors found that whole-body feedback during curves can be effective in avoiding hazardous situations when take-over is needed. Furthermore, in Benloucif *et al.* (2019), a real-time adaptable haptic feedback is proposed based on the level of distraction of the driver.

Finally, driving simulation can be used to test the interaction between fully autonomous vehicles and passengers. In Ulahannan *et al.* (2020), the authors investigate

the preference of passengers regarding the level of information the autonomous system exchanges, such as sensor information, directions, and status. This study points out that different users will require different levels of information, which should be accounted for when designing autonomous systems. Smoothness of the autonomous driving is assessed in Wei *et al.* (2019), where a non-linear model predictive control (NMPC) is developed to govern the vehicle trajectory, accounting for safety and comfort, intended to develop a system with a human-like behavior. Another assessment of an autonomous driving system from the perspective of the passengers is depicted in Strauch *et al.* (2019). Here, passengers' eye movement is tracked using eye tracking systems to rate the trust in the system. In this work, the results show that driving styles appeared to affect the trust. This shows a relevant paradigm in the use of driving simulators for autonomous systems testing. Not only should safety and efficiency be pursued, but also interaction and compliance with passengers' expectations of motion, to achieve mainstream acceptability and a comfortable driving experience.

2.4.3 Chassis Systems

In industry, one of the mainstream uses of driving simulators is for subjective dynamic evaluation and pre-design of chassis components. Although this is one of the larger use cases, due to the confidential nature of industry work, publications are not common. The work performed in Kharrazi *et al.* (2020) proves that experienced drivers are able to identify handling differences given parameter modifications using a driving simulator. The authors used different vehicle parameters such as roll stiffness and tire compliance to reproduced well-known maneuvers, e.g. single lane change. The driver subjective feeling was compared, as well as a comparison between

the actual measurements and virtual values of yaw rate, roll, and steering torque. The results motivate works tuning lateral dynamics through suspension, steering, and active control systems. A similar test is conducted in Di Loreto *et al.* (2019), where acceleration of the driver's head was measured during a braking maneuver in a real vehicle and in a 6-DOF simulator. The study was to investigate if the whiplash motion of the neck could be reproduced in the simulator, validating its use for longitudinal dynamics assessments. In Rodriguez *et al.* (2016), different configurations of the steering system are tested by several subjects in three different scenarios, to evaluate how the environment and the system influence the driver's perception of controllability, ease of use and fun while driving. The work developed in Shida *et al.* (2016) goes even deeper into an active steering system and proposed a new model that incorporates driver's gaze, justified by the fact that the steering behavior of drivers change with sightline distances. The results show that this concept can be further used in autonomous systems, since it was shown to achieve more precision than current proportional-integral-derivative (PID) controllers.

As mentioned before, suspension systems are also an object of study in driving simulation, due to the ease of changing components, configurations, geometry, and dynamics without prototyping parts. For active systems, different tunings can be assessed without the need for software compilation. Active control systems such as electronic stability control (ESC) can also be tuned through driving simulation. The work detailed in Papelis *et al.* (2010) uses the driving simulator to prove the loss of control reduction provided by the ESC system. In that work, 120 subjects drove into typical crash situations with and without the assistance system. The results show the benefit of having ESC in all scenarios. Another work featuring an ESC

system is depicted in Yoon *et al.* (2010), where vehicle behavior during anti-rollover interventions is investigated. This kind of test is important as it shows how safety systems behave in standard validation maneuvers compared to how well they perform in real world experiments.

More recent work described in Romano *et al.* (2019) assesses the validity of a driving simulator in mimicking the dynamics of a low-friction test track, showing that although driving simulation can be used for dynamic assessment, there are still limitations in reproducing certain maneuvers and environments.

2.4.4 Powertrain Systems

In powertrain design, the HMI analysis is also important. An investigation on how augmented reality displays can guide the driver during the driving task is proposed in Wang and Söffker (2016), where the electrified vehicle is emulated using a co-simulation between a hardware in the loop (HIL) test rig and a driving simulator. This study showed that fuel efficiency can be increased using simple display systems that guide the driver during the journey. The same concept is explored in Rommerskirchen *et al.* (2014) and Jones *et al.* (2016), where the ability to foresee events using a V2X (vehicle to road/vehicle/database communication) is used in order to display instructions to the driver.

Using the same concept of driver guidance, several eco-driving studies were performed in Pampel *et al.* (2015) and Wu *et al.* (2017) to evaluate fuel consumption improvement by instructing drivers on eco-friendly driving behavior. The work in Jamson *et al.* (2013) investigates the role gas pedal feedback can play in making drivers achieve a higher fuel efficiency. In this work two different pedal systems were

tested by twenty drivers. The results show that the most fuel-efficient behavior is achieved when drivers are provided guiding force feedback (such as a step change in the pedal force) compared to a system that provided increased firmness.

In another study examining fuel consumption, Kok *et al.* (2012) integrates a static simulator with a dynamometer. This integration makes it possible to evaluate the performance of electric vehicle systems in tests performed by real human in several driving conditions. In Phuc *et al.* (2018), ten different drivers were placed in a car following scenario that replicates a realistic driver model for fuel economy assessment. The different driver behaviors were analyzed and categorized. This data is used to develop a car following driver model for evaluating fuel consumption, and to create a reference virtual driver that can provide real time feedback to human drivers.

Subjective longitudinal acceleration can also be validated using driving simulation. The authors in Baumgartner *et al.* (2019) used a 6-DOF driving simulator to present different engine configurations to drivers in a tip-in maneuver defined by a sudden step on the accelerator pedal from a constant engine speed (1500 rpm in second gear) without gearshift. The results showed that drivers have the sensibility to perceive changes in the acceleration profile for different engine configurations. That indicates that driving simulators can be used for subjective drivability assessment of powertrains prior to prototyping. In addition, the authors in Wang *et al.* (2019) have shown that it is possible to categorize acceleration levels. That is an important insight to HEV developers since drivability and driver's perception has very tight requirements.

2.4.5 Road Design

In addition to the aforementioned vehicle design, road design can also be studied and improved through driving simulation. In Filtness *et al.* (2017), driving performance is evaluated for different configurations of road signs. A similar work is presented in Kang and Momtaz (2018), where audio warnings through differing pavement surfaces (rumble strips) in addition to visual warnings were examined, something that would be costly to create in a physical environment.

2.5 MARCdrive Lab

Static simulators are the most common structure applied in research centres, both for the lower cost and simple implementation. Among this type of simulators is the driving simulator of the MARCdrive lab installed at the McMaster Automotive Resource Centre (MARC) in Hamilton, Canada, Fig. 2.4.

Although a static simulator, its high immersion is achieved by using a complete real vehicle facing a cylindrical screen with 210 degrees of field of view (FoV). The screen is powered by three projectors at 120 Hz. Dedicated software applies the warping and blending needed due to this configuration. Five speakers distributed by the vehicle cabin and a sub-woofer at the backseat provide a three-dimensional surround system

Low fidelity motion cues are provided by active seat and seat-belts. The first, built from six air bladders distributed inside the driver's seat, provides soft handling lateral cues (less than 10 Hz). The second, pulls the driver's five-point contact belt to provide longitudinal cues. Active steering and brakes also add realistic haptic cues.

Figure 2.4: Static driving simulator at the MARCdrive lab.

Various vehicle dynamics models such as CarSim and VI-CarRealTime can be used in the modular structure. VI-WorldSIM provides MARCdrive's graphic engine. It allows for easy control of start/stop operations, run-time control of lighting, time of day and creation of scenarios the driver needs to react to. Including features like traffic, pedestrians, lighting, weather, and sensor emulation enables the user to create anything from simple to complex scenarios. Using a high-quality graphics environment, built on an Unreal graphics engine, allows a significantly improved immersive subjective feel and drive.

This driving simulator architecture provides the means for studies involving driver impairment, autonomous features, the analysis of hybrid powertrains, and energy management systems. Some vehicle dynamics assessments with low feedback to the driver can also be performed.

In this research, the vehicle model in the driving simulator is treated as the vehicle

object for implementation of the energy management and the autonomous systems. It also serves as a platform to create virtual testing environments. Furthermore, using the driving simulator allows adding the human component to the design.

2.5.1 Driving Simulator Environments

The driving simulator allows for the creation of virtual environments that emulate real-world conditions. In this thesis, the term environment is used to describe the surroundings in which the subject driver is inserted. Environment is classified in four categories: highway, commercial area, residential area, and proving ground. Driving conditions are time-related incidental events or states such as traffic, weather, visibility, road quality, etc. The term scenario is used to indicate a combination of environment and a set of driving conditions.

The term highway is used for express express roads that connect towns or cities. The velocity range of highways is the highest among the regulated driving environments, showing speeds from 60 km/h to 120 km/h. However, given its continuous characteristic, low levels of acceleration are expected. Commuting using highways is part of the day of many drivers, hence the importance of testing in this environment.

Commercial areas include areas where the commercial activity takes place. Speed limits may vary between 30 km/h to 50 km/h, although the most significant characteristic of commercial areas is the high volume of traffic agents (vehicles and pedestrians). That contributes to high traffic and aggressive driver behavior shown in a wide range of acceleration values.

Residential areas are neighbourhood roads such as suburbs. The speed limits, traffic of vehicles and pedestrians are usually in the lower end of commercial areas.

Nevertheless, lack of signage can contribute to accidents.

Finally, proving grounds include race tracks and test facilities. They can be closed circuits, tracks that imitate real roads, large, paved areas for free testing, or areas marked with specific geometry such as circles, ovals, and straight lanes. Proving grounds are broadly used in industry since they provide a relatively repeatable and controlled environment for testing. For that reason, they are adopted specially for the testing of safety-related systems.

Throughout this thesis, four set of virtual environments are used: a simple two-lane straight road for consumption assessment, a virtual proving ground for drivability and performance testing, a neighbourhood area, and a express way environments. The last two are used for emulation of real-world scenarios with traffic conditions. The environments are created using Mathworks RoadRunner and imported to the simulator environment through Unreal Engine.

Straight Road

A virtual straight road is created for the emulation of consumption and performance tests. To this environment no traffic condition is added, its pupose is to solely provide a simple straight path for driver to follow during the emulation of consumption tests.

Proving Ground

A virtual proving ground is created to provide an environment for testing performance and drivability. Figure 2.5 shows an aerial image of that environment.

The proving ground provides a standard circle with outer diameter of 100 m and markings every 10 m. This circle is used for lateral assessment and characterization.

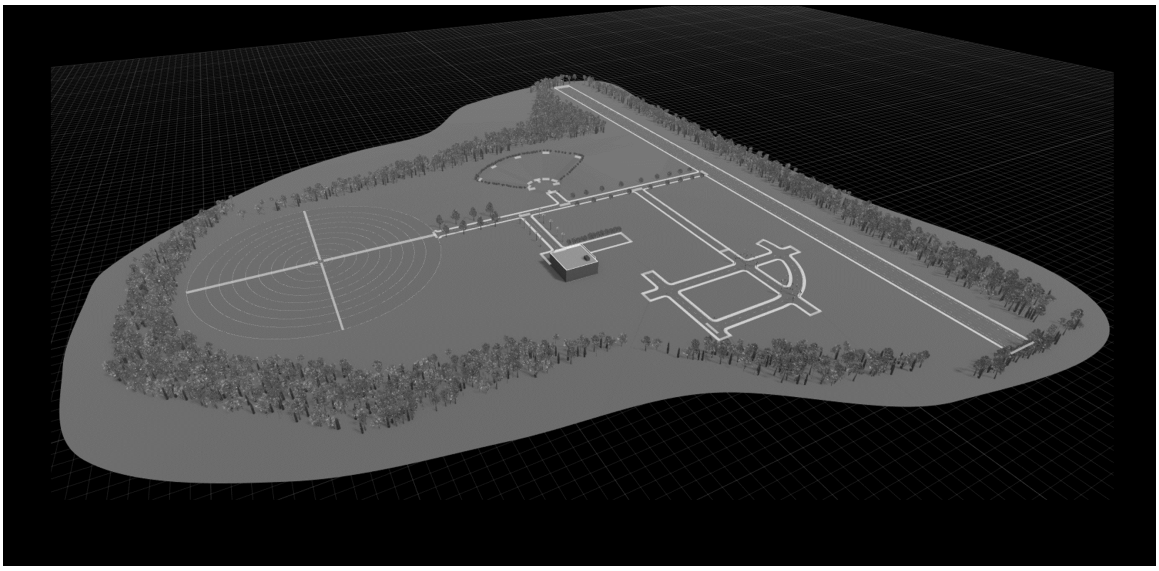

Figure 2.5: Aerial image of the virtual proving ground environment.

In the centre, five straight hills are placed with slopes of 5 %, 10 %, 15 %, 20 %, and 25 %. The hills are created to test gradeability. On the far right and bottom, a straight path and a mock-up traffic area are also added, respectively. The former is used for performance assessment and the latter for rapid testing under stop and go traffic conditions.

Neighbourhood

The neighbourhood area available in the simulator database is used for testing under realistic urban conditions, with traffic and pedestrians. The behaviour of the computer-controlled pedestrians and surrounding vehicles is set to "wander" and "swarm", respectively. That means that the pedestrians will walk around the map and their interaction with the human-driven vehicle is incidental. As for the vehicles, the "swarm" function means that they will be constantly spawned around the

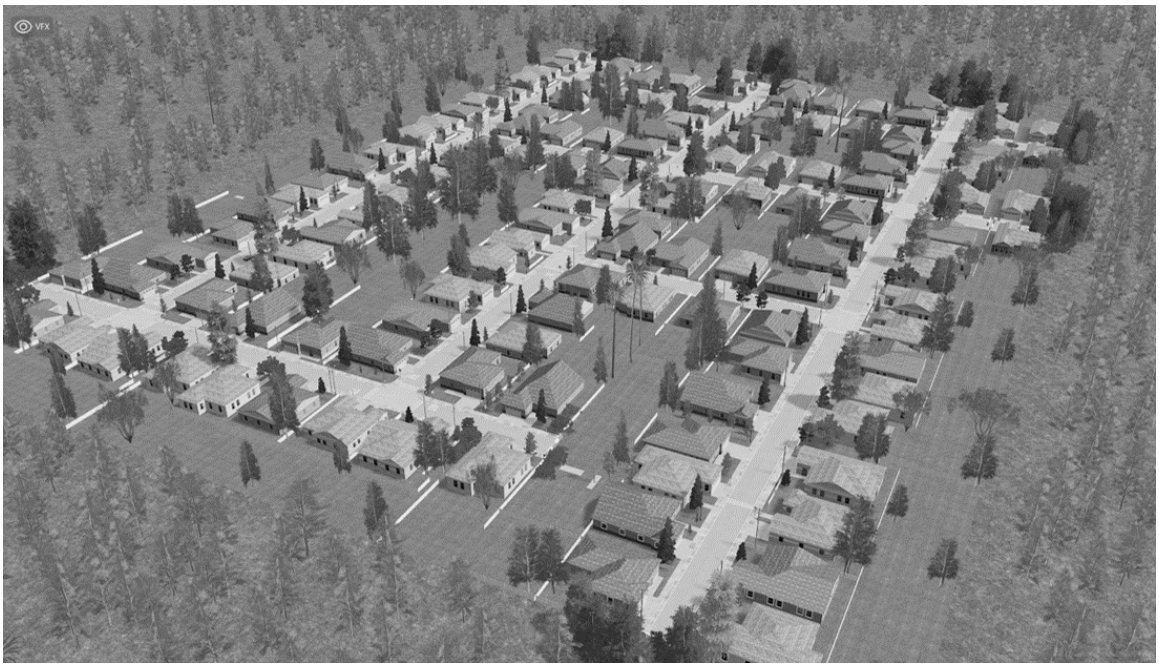

Figure 2.6: Aerial image of the neighbourhood environment.

human-driven vehicle in order to create the perception of traffic. Weather and visibility may vary depending on the testing purpose. Figure 2.6 shows an aerial image of the neighbourhood environment.

Express way

The express way available in the software database is used for testing under realistic highway conditions. The behaviour of the computer-controlled surrounding vehicles is set to "swarm" in the same fashion as in the neighbourhood scenario. Weather and visibility conditions are also variables that can be changed depending on the purpose of the test. Figure 2.7 shows an aerial image of the express way environment.

Figure 2.7: Aerial image of the express way environment.

2.5.2 Driving Simulator Model

In this thesis, a real-time model for a small-sized passenger vehicle is built and validated using the driving simulator in the MARC drive lab. That is important so it defines a benchmark vehicle for comparison. Once this model is validated, it is used for assessing the control algorithms developed. The baseline, is created using VI-CarRealTime, and Matlab/Simulink. Both software function together and with the simulator's hardware in the loop thanks to the co-simulation environment enabled by SIMulation Workbench.

The VI-CarRealTime provides a platform for modelling simplified four-wheel vehicles. Its interface allows for the editing of vehicle subsystems such as body, brakes, wheels, suspension, and powertrain. The vehicle model is then the assembly of fundamental subsystems. The model is exportable using C and C++ code generation

for usage in driving simulator. The library of vehicle models include a vast number of types and segments, from smal-sized city cars to pick-up trucks.

The model is a reduced degree-of-freedom version of an actual vehicle, including 14 degrees-of-freedom (DOF) of the assembly of 5 rigid parts. The rigid parts are body and wheels, and the 14-DOF are the linear and rotational displacement of the body in three axes (longitudinal, lateral, and vertical) with respect to vehicle body, plus the linear and rotational motion of each wheel in the vertical axis and rotational motion around its own centre.

Each subsystem is modelled using a quasi-static approach, where the components and systems are modelled with the use of look-up tables. The purpose of the model is to provide accurate vehicle response for driver input and road conditions during braking, acceleration, and cornering manoeuvrer.

The batery electric vehicle (BEV) used in this work as the baseline vehicle is based on the Chevrolet Spark model year 2015. The vehicle is front-wheel drive, electric powered, with a single final drive ratio. Each subsystem is briefly decribed. Their parameters are compiled in Appedix A.

Body

The body system provides information of mass, inertia, and overall vehicle dimensions.

Suspensions

The front and rear suspension system is modelled through look-up tables of geometric kinematics and compliances.

Wheels and Tires

The front and rear wheels are modelled using the Pacejka model Pacejka (2005). It computes forces and momentum in all three directions plus it adds relaxation.

Steering

The steering subsystem defines the kinematics of the system given its geometry. The steering is considered to be rigid. It outputs wheel steer angle given steering wheel input and tire forces.

Friction Brakes

The friction brakes subsystem is defined by constant parameters. It is important to note that in an electrified vehicle, friction brakes and regenerative braking work together to provide the braking effort.

Battery

The battery is principal power source of an electric vehicle, thus it key in the present analysis. In the baseline vehicle, the battery type is Lithium-ion and consists of 192 cells distributed in 6 modules. Each module contains 2 cells in parallel and 16 cells in series.

A simple battery model is used with look-up tables for charge and discharge resistances as function of the SOC. Coulomb counting is the chosen method for computing the SOC at every time-step given the power requirement from the motor and auxiliary loads. The battery open circuit voltage (OCV) as a function of the state of charge (SOC) is extracted from the experimental data by filtering regions of low current

($I \leq 2$ A). The experiment is conducted by the Idaho National Laboratory (INL) at a C-rate of 1/3 C (0-100 % in three hours). The final OCV-SOC curve is depicted in Fig. 2.8. The charge and discharge resistances are extracted from the report of the Idaho National Laboratory on battery pack testing of the same model year vehicle.

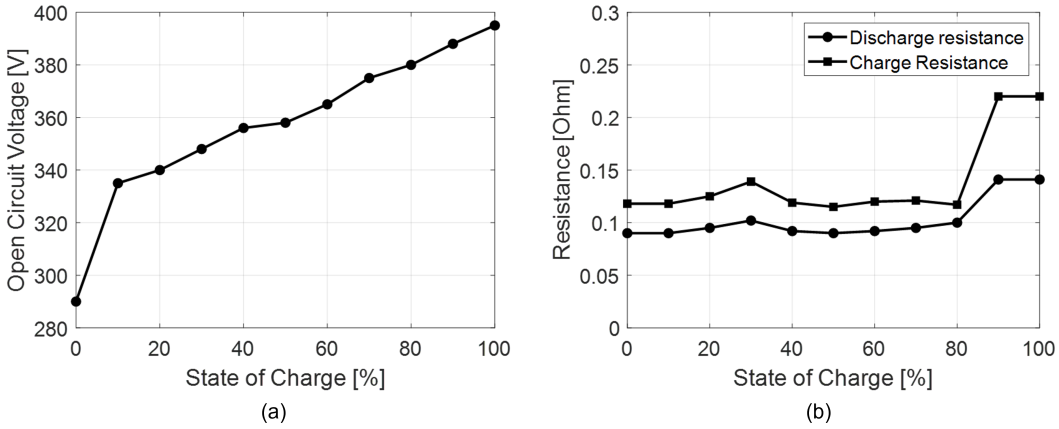

Figure 2.8: Battery OCV-SOC curve and charge/discharge resistances

Powertrain

The powertrain model is composed by assembling components such as internal combustion engine (ICE), motors, generators, clutches, transmisison, drive shaft, and propeller shaft. The first step to model the desired powertrain is to select the appropriate components that configure the desired topology. For the baseline model, the configuration of the powertrain is a clutch-less front-wheel drive propelled by a single motor with a single final drive ratio.

The motor is a permanent magnet synchronous and maximum power and torque of 105 kW and 444 Nm, respectively. Top speed is 5000 rpm. Figure 2.9 shows the motor torque and speed curve with an estimated efficiency map. Also, it depict the

pedal map that receives the inputs of throttle and brake pedal positions and outputs demanded torque at the traction motor. Regenerative braking pedal map follows the same approach. The difference is that the magnitude of the torque request is negative and the blending factor between friction and regenerative braking.

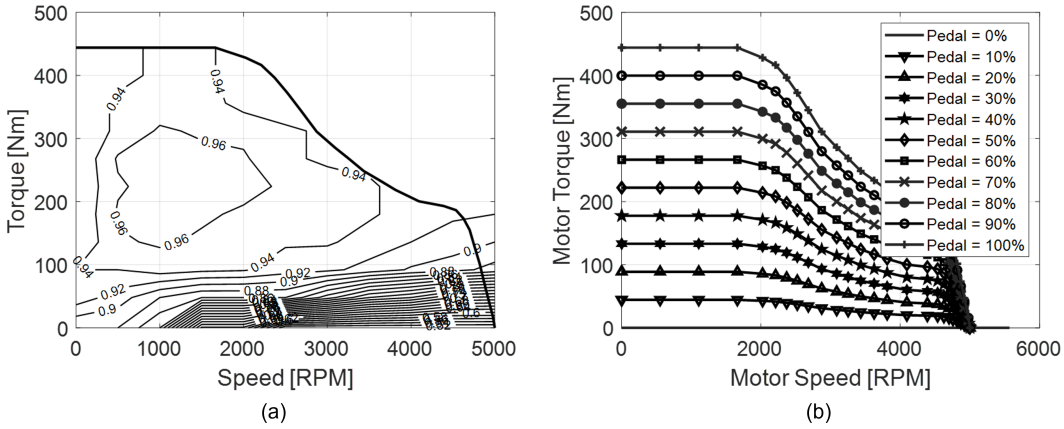

Figure 2.9: Permanent magnet synchronous motor map and pedal map.

Regenerative Braking

Besides being of key importance in vehicle design to assure safety by providing the means of deceleration Gillespie (1992), the brake system is also intrinsically connected to the powertrain system of electrified vehicles through regenerative braking.

In electrified powertrains, the electric motors mechanically connected to the wheels can not only deliver energy in propelling events but also capture energy in braking events. When drivers press the brake pedal negative torque request signal is sent out. Then, the momentum of the moving vehicle drives the engaged electric motor, generating current that can be used to charge the battery Emadi (2014). That is a clever use of the traction motor and it motivates all sorts of control strategies

including the one proposed in this thesis.

The blending factor is the ratio between friction and regenerative braking in electrified powertrains. It is necessary since the regenerative braking alone is not enough to provide all the required braking efforts Chandak and Bhole (2017). The blending factor is often defined as a function of the braking event (captured by the rate of deceleration), and vehicle.

Figure 2.10 shows the calibrated blending factor as a function of the vehicle speed. The factor is calibrated so the SOC profile of the mentioned cycles is accurate with measurements.

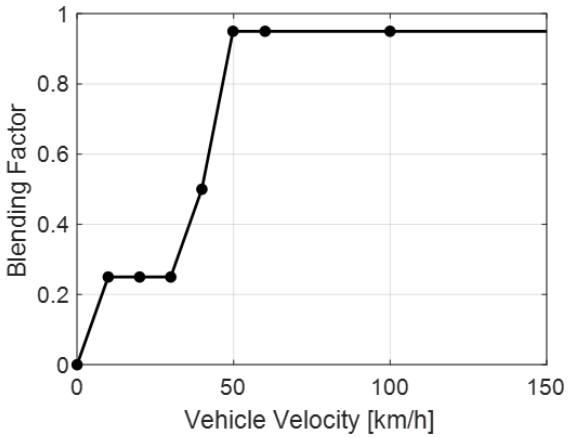

Figure 2.10: Blending factor as a function of vehicle velocity.

Road Loads

The road loads are included using the models devised in Chapter 4. The coefficients are deduced using the reference road load coefficients provided by ANL and EPA experimental tests. The reference values are showed in Appendix A.

Communication

Lastly, the communication subsystem is responsible for building the bridge between powertrain and vehicle model. All signals created in the powertrain model (torques, speeds, battery information, and road-loads) are sent to the real-time environment through the real-time data base tool provided by the Simulation WorkBench toolkit. The inputs needed by the powertrain are the driver commands, vehicle and components speed, acceleration, and actual torque. They are imported in the same manner as the outputs of the vehicle model. Once edited to the desired configuration, the powertrain model is compiled and sent to the real-time machine for implementation with the driving simulator.

The simulation structure is created in the real-time machine using the Simulation Workbech software. In that structure, each process is performed by a single core of the real-time machine. The co-simulation structure is then the result of the compilation of the vehicle subsystems built with VI-CarRealTime and the powertrain-battery models created with Simulink.

The frame rate of the simulation is of 1000 Hz. The average run time of the powertrain model (3.41 μs) is far lower than the vehicle model (302.17 μs). The objective is to keep the total run time under the execution frame of 1000 μs.

2.5.3 Model Validation

The validation study uses experimental testing data on the baseline vehicle provided by the Argonne National Laboratory (ANL) and by the Idaho National Laboratory (INL).

Consumption

The validation of the model is performed in four steps. First, current and voltage data logged from a charge depleting test is used to validate the rated battery capacity. Although battery specification states 52 Ah, it was verified that an efficiency of 0.95 is needed to match the SOC profile using Coulomb counting method. Figure 2.11 shows the result of this first step.

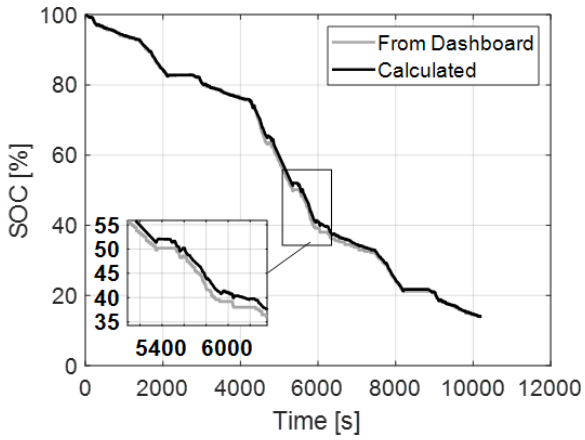

Figure 2.11: SOC from measurements of current and voltage in charge depleting test.

The second step is to validate the battery model. From the simple model previously devised, terminal voltage and SOC profiles are calculated using the inputs of power request. Figure 2.12 shows the result.

Then, the battery model is attached to the other models to validate vehicle energy economy. The UDDS and HWFET are used and simulated using the backward approach. The resultant SOC profiles are depicted in Fig. 2.13. The comparison between the energy economy calculated and the reported by the INL can be found on Tab. 2.1.

A comparison of the battery model performance is provided in Tab. 2.2

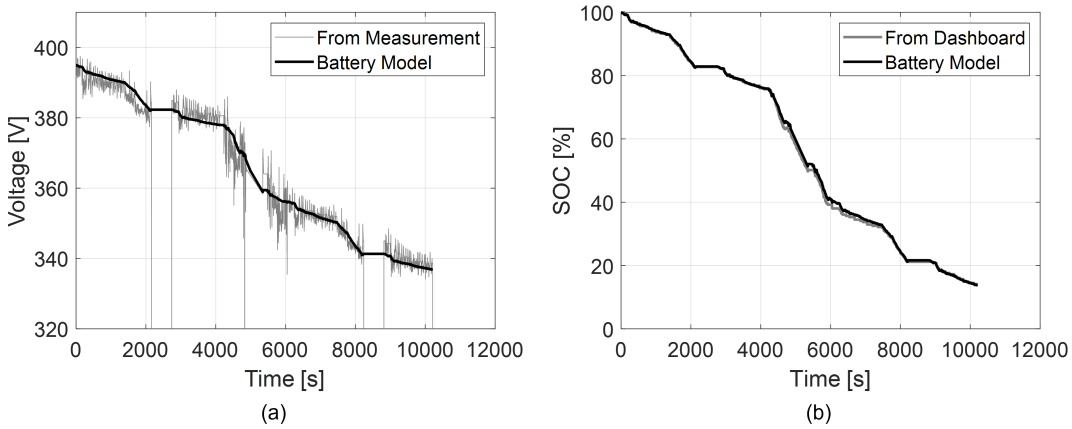

Figure 2.12: Battery voltage (a) and SOC (b), from simple battery model.

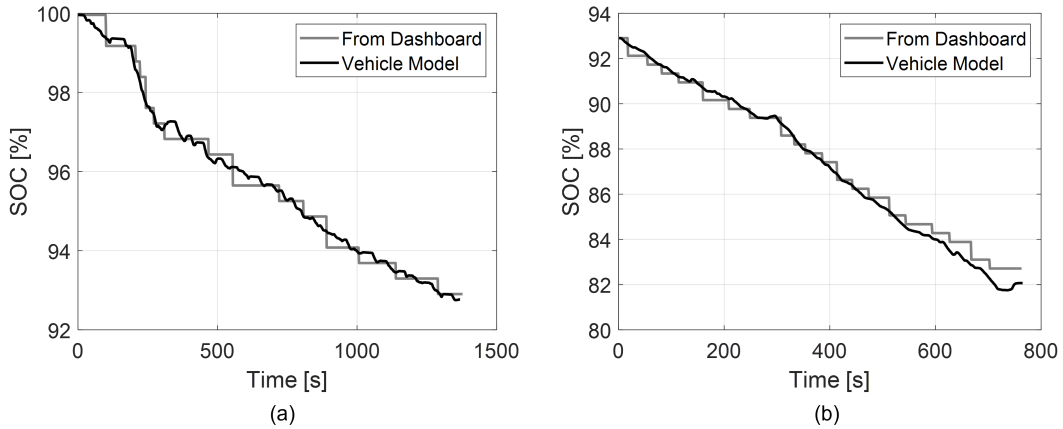

Figure 2.13: Resulting SOC profiles for the UDDS (a) and HWFET (b) cycles.

Table 2.1: Consumption comparison between model and experimental results.

	Experiment	Model	Accuracy
UDDS	198.1 Wh/mi	201.5 Wh/mi	98.3 %
HWFET	212.4 Wh/mi	225.8 Wh/m	94.1 %

Table 2.2: Battery comparison between model and experimental results

	Final SOC Diff.	SOC RMSE	SOC Max Error
UDDS	0.14 %	2.011e-04 %	0.62 %
HWFET	0.64 %	0.14 %	1.02 %

Finally, both cycles (UDDS and HWFET) are performed iteratively until SOC reaches a lower level of 5.0 % emulating the labelling procedure conducted by EPA. This step functions as a referencing for the adjusted energy consumption and range. Table 2.3 shows the comparison between model and label. The vehicle mass and rolling resistance coefficients are adjusted to the reported by the EPA test procedure. For this final simulation, the battery capacity is also adjusted to the rated value of 60 Ah reported by EPA.

Table 2.3: Comparison between model and reported results.

	MPGe Adjusted (UDDS / HWFET / Combined)	Miles Adjusted
Model	120.9 / 110.4 / 116.2	79.7
Label	128 / 109 / 119	82
Accuracy	94.4 % / 98.7 % / 97.6 %	97.2 %

Performance

The performance of the vehicle is also object of interest. Top speed assessment is conducted on the simulator to quantify the powertrain acceleration performance. Vehicle is accelerated from halt with wide open throttle (wot) until its velocity is saturated and cannot increase.

From the top speed test three metrics are extracted, the final top speed itself, the time for the vehicle accelerate from 0 to 60 mph (96 kph), and 0 to 30 mph (48 kph). The results are compared with values reported by the manufacturer. Table 2.4 depicts the results. Figure 2.14 shows the time-series results for the top speed experiment.

Table 2.4: Acceleration performance results.

Metric	BEV Model	Experimental	Accuracy
Top-speed [kph]	143.12 kph	145.0 kph	98.07 %
Acceleration 0-48 kph	3.38 s	3.0 s	88.75 %
Acceleration 0-96 kph	7.72 s	7.20 s	93.26 %

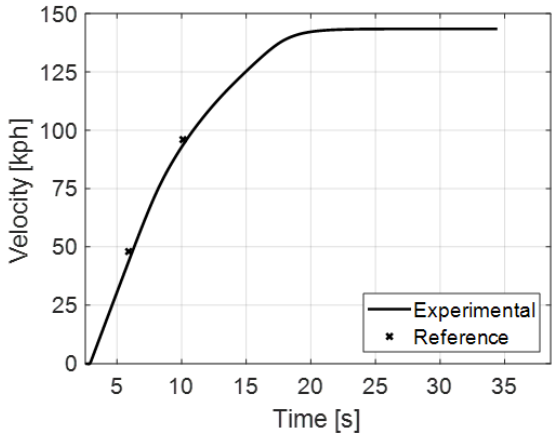

Figure 2.14: Acceleration profile from experiment compared with reference values.

The BEV model is found to reproduce well the published performance of the baseline vehicle.

2.6 Summary

This chapter has explained the mechanisms of driving simulation technology by describing each system in its architecture.

State-of-the-art systems aim for the highest level of fidelity by providing highly immersive set-ups with full vehicle mock-ups, a large field of view, and accurate vehicle dynamics models. The ability to create and control driving conditions and scenarios such as weather and traffic are also key. When using motion, these simulators also include well-developed motion cueing algorithms that account not only for the limitations of the human perceptual system but also for the boundaries of the motion system. Static simulators can often be used in studies where the focus is not primarily closed loop control of the vehicle by a human driver, while motion simulators offer an increased scope of use, including analysis of chassis control and autonomous features.

Although some studies were already performed assessing powertrain systems, these analysis will become more common and precise as the need to virtually validate those systems increases. Moreover, driving simulation allows the validation of the interaction between different systems, both at the component and system level. It enables engineers to test the integration between autonomous systems with energy management for example, as well as analyzing it from the driver's perspective. This integrated interactive approach is key to develop systems that work as one. In summary, although not fully explored for powertrain design and test, driving simulators can be a powerful tool specially in regards to testing integrated systems.

Finally, the simulator at the MARCdrive lab is presented and its suitability for this research is detailed. An electric vehicle is modelled and validated with experimental data to serve as the baseline in the following studies.

Chapter 3

Journey Mapping Applied to Energy Management

3.1 Introduction to Energy Management Strategies

Governmental concern about environment and scarce fuel resources has forced vehicle manufacturers to develop all sorts of strategies to improve overall vehicle's efficiency. In this scenario, engineers have been struggling to deliver the state-of-the-art technologies that will enhance efficiency but not at the cost of low performance.

Even with the appearance of new energy sources and fuel, the electrification trend is proved to be the most interesting path to follow and the ultimate solution Emadi (2011). The governments also play their role by developing more accurate forms of evaluation for emission and consumption. The so called roller bench tests are developed to emulate real world scenarios in order to label the vehicles in a scale of efficiency Barlow *et al.* (2009), thus the importance of the driving cycle. Nonetheless, driving cycles are also used in vehicle design, and not only in final assessment. It is

important that, in development phase, the manufacturer is able to simulate different driving scenarios and estimate not only standard cycle behaviour but also daily usage. It is essential to note though, that the gap between real and standard scenarios is usually larger than desired.

Energy Management Strategies (EMS) are developed to assure the best balance between performance and energy consumption, therefore they are the object of interest of several recent works about hybrid technology. As it will be further portrayed, there are numerous strategies oriented for that purpose and comparative methods has been developed to guide further designs Jiang *et al.* (2017) and Serrao *et al.* (2011). The design will appoint to the most beneficial strategy for a specific vehicle, based on the available information, the computational effort, and expected efficiency. The EMS will also depend on the chosen architecture, e.g. if the vehicle is a hybrid electric vehicle (HEV) or a battery electric vehicle (BEV) and how the power is delivered to the wheels.

Even though this chapter will not describe deeply the different architectures and components of electrified vehicles, some of them such as series, parallel and power-split are acknowledged. Comprehensive survey on that topic is available in Barroso *et al.* (2022).

The level of information available can enhance the performance of the EMS. Currently, the world is living an increase of connectivity and system integration. Nowadays, Global Positioning Systems (GPS) are connected directly to the vehicle itself via multimedia interfaces or indirectly via smart phones. Traffic information, distance, and travel duration are also available in the global network. Beyond that, not only self-information is available but the whole cloud of connected information from

different sources known as big data produces new ways of energy management that are yet to come Lee and Wu (2015).

This chapter reviews and connect all of these technologies in order to appoint a reasonable use of them together. The following sub-ections present different EMSs. They can be categorized in two major groups of control strategies, off-line, and on-line methods. The former meaning its control actions are feasible with real-time implementation while the latter being unfeasible due to the nature of the algorithm or high computational power. The following section gives exemples of each type of strategy. Next, consumption assessment methods are presented followed by a review of driving condition mapping. Finally, prospects of condition mapping applied to energy management and autonomous driving are listed.

3.1.1 Off-line Methods

This sub-section will detail the three most used off-line methods, convex optimization (CO), dynamic programming (DP), Pontryagin's minimum principle (PMP), and genetic algorithm (GA). Although those methods are unfeasible for vehicle application, they are often used to define optimum torque split profile between the sources of torque in a HEV. They can also be used to define penalties and weights of the modes to achieve a desired behaviour of fuel and battery consumption. In summary, off-line optimization methods must be used in circumstances where the whole driving cycle is known, with the purpose to achieve the mode shift profile that provides the lowest fuel consumption. For that reason, the off-line methods are usually applied to build the reference profile, to be used as a target for the real-time application methods.

Dynamic Programming

Global optimization strategies are based on the knowledge of the complete driving cycle a priori Serrao *et al.* (2011) with the objective to find the optimal control strategy. One of the most extended used methods is DP. DP is a decision making algorithm usually used to split power between two or more sources in simplified architectures Asus *et al.* (2014). As described in Serrao *et al.* (2011), it is necessary to write the system behaviour in a discrete-time form, including the states and control domain. Therefore, a large finite number of possible solutions are found. For a defined conjunct π of control rules $u_{N(t)}$ where n is the number of time steps in which the optimization is divided, and t is the time instant. Considering the instantaneous cost $L(x_k, u_k, t_k)$, the cost of the control policy can be described as in 3.1 and the optimal policy in Eq. 3.2.

$$J_0(\pi) = \Phi(x_N) + \sum_{0}^{N-1} L(x_k, u_k, t_k) \tag{3.1}$$

$$\pi = \arg\max_{x} J_0(\pi) \tag{3.2}$$

The cost $J_k(\pi)$ is the cost to move from a certain time step to the optimization horizon, for the known policy π. This cost is computed using Bellman's principle and it starts from the last time step toward the first (going backwards), hence the necessity of having the whole cycle in advance, in addition the computational load would imply an unfeasible effort for the eventual on-board controllers Serrao *et al.* (2011). In Asus *et al.* (2014), DP strategy was used to split power between the battery and an ICE range extender where battery SOC is defined as the state variable. It is

important to note that every system is subjected to physical constrains, in this case the power that the engine can deliver and battery power recuperation limit. Other approaches considering the same deterministic decision could be to assume engine rotational speed as the state variable Chrenko *et al.* (2015). The use of DP described in Zhao *et al.* (2017) aims to recognize an optimum number of gears as a matter to achieve a larger fuel economy area. This contribution shows a rational use of DP in vehicle design. Since it is not real-time implementable, it can be used for component choice.

Convex Optimization

The CO method follows DP as a numerical optimization method. In this strategy the energy minimization problem is depicted as a convex function with the following standard form according to Egardt *et al.* (2014).

$$\text{minimize } f(x) \text{ subject to } g_i(x) \leq 0, i = 1, ..., m \tag{3.3}$$

Where x is the group of optimization parameters, f is the objective function, g_i represents the constraint functions (that can be inequality or equality constraints). In the EMS application of an electric/hybrid vehicle, the objective function must be the equation that represents the cost of fuel and electric power. Using the work in Gao and Du (2016) as an example that cost is defined in Eq. 3.4

$$J_c = \int_0^t C_f H_f m_f dt + C_{el}(SOC_f - SOC_0) \cdot Q_n \cdot V_{oc} \tag{3.4}$$

Where C_f is the fuel price and C_{el} is the electrical price per joule, H_f is the fuel heating value, m_f is the mass flow rate in grams per second, SOC_f and SOC_0 are

the final and the initial state of charge, respectively, Q_n is the nominal capacity of the battery, and V_{OC} is the open circuit voltage of the battery.The constraints define the boundaries for the engine and the electric motor, SOC, and current. In addition, it defines the mass flow rate and the motor loss as polynomials to make sure that the optimization problem becomes convex. Another broader use of the convex method is for component sizing as proposed in Pourabdollah *et al.* (2017).

Pontryagin's Minimum Principle

The PMP is an analytical optimization method and it states that if the control law $u(t)$ is optimal, then it will exist a vector that gathers the co-states $\lambda(t)$ and is able to satisfy the constrains of the system Geering (2007). The optimal co-states variables are calculated by a binary search algorithm. Therefore, the role of the control law $u(t)$ is to minimize at each instant the Hamiltonian of the optimal problem, which is defined in Eq. 3.5.

$$H(x(t), u(t), \lambda(t), t) = \lambda^T(t) \cdot f(x(t), u(t)) + L(x(t), u(t), t) \tag{3.5}$$

Where $f(x(t), u(t))$ is the dynamic equation of the system, and $L(x(t), u(t), t)$ is the instantaneous cost. The study presented in Jiang *et al.* (2017) evaluates PMP as a benchmark strategy to compare the performance obtained from real-time strategies for the energy management of a HEV vehicle. It highlights application issues of PMP such as local discontinuities. For the HEV energy minimization problem as described in Serrao *et al.* (2011), the instantaneous cost is the fuel mass flow, as a function of battery power and required power, and the system dynamics can be modelled as a function of the SOC.

An issue is that PMP might not always output a single solution, in that case, the possible solutions must be compared prior to appoint the optimal one, in terms of lowest fuel consumption Serrao *et al.* (2011). An example of this phenomena is given in Jiang *et al.* (2017) where the presence of two local minimal where the Hamiltonian assume two values very close to each other. This results in a small discontinuity of the state variable SOC. The phenomena can be explained by the fact that the Hamiltonian function is not convex in this particular time step.

Genetic Algorithm

The GA strategy is a well-known numerical search method-based Darwin's evolution theory where the vector of individual solutions is called population, best solutions are then gathered by different mathematical methods to form a new population, which classifies a new generation, this is repeated until predefined conditions are met Chrenko *et al.* (2015). The use of GA has numerous applications regarding EMS and it is commonly used to optimize the performance of rule-based controllers as in Arani *et al.* (2016) and Herrera *et al.* (2015).

As illustrated in Arani *et al.* (2016), the GA is used to optimize the fuzzy controller of an EV that includes two power sources, a super-capacitor and a battery. In this work, a mixed integer GA was applied, which proposes several modifications in the Laplace crossover function. Given the construction of the fuzzy controller, a membership function for each controlled state (battery SOC, super-capacitor SOC and power) can be defined by choosing the function parameters. The GA is applied to optimally define the fuzzy rules and fuzzy membership parameters. A similar application is brought in Herrera *et al.* (2015), where the objective is to develop an

optimization of the control levels of a RB EMS. In this case cost factors were defined as battery and super-capacitor cycling cost, recharging from grid cost, and fuel consumption cost.

3.1.2 On-line Methods

The on-line methods can be described as instantaneous optimization methods (or local optimization methods) Chrenko *et al.* (2015). Once again, the effect achieved is the minimization of fuel consumption through the optimization of torque split between the sources, but the optimization here is done considering just the current time step (with its current conditions and characteristics), since future information is not available or is limited. That makes the online methods greedy methods, optimizing the use of fuel at each instant but not looking at the big picture (whole driving cycle). Since it does not require previous knowledge of the whole driving cycle, online methods are the ones used in real-time vehicle application, where the speed profile is unknown. Another limitation in real-time application is the available computational capability. Therefore, the computational effort in online methods must be lower when compared to the previous strategies so they can be implementable. One common methodology is to use an off-line strategy to build the torque split reference for a given powertrain in a given drive cycle, and then develop and tune an implementable online strategy aiming the fuel consumption achieved in the reference. The next sub-sections will describe in detail the most adopted online optimization tools.

Rule-based

Rule-based (RB) control strategies rely on human experience or intuition when building the mathematical models that will govern the system and divide it into different states Chrenko *et al.* (2015). The action of the controller usually depends only on the current state, justifying the importance of the human knowledge about the system behaviour for its design.

Rule-based EMS is the most recurrent choice of manufacturers since its level of complexity and computational effort are low. The rules can be implemented in the form of calibration tables that can be optimized Bruck *et al.* (2020). This also allow intuitive calibration of drivability. A special case of the RB approach is the fuzzy-logic (FL) method.

Fuzzy-logic

The FL strategy can be understood as an advanced version of the deterministic RB approach since it proposes a blending between states through membership functions, which has the objective to achieve smooth state.

This is achieved by using membership functions that show how much an input belongs to each set of rules. A membership function is stablished in 3.6, where u_A is the membership value of the fuzzy set A and X is the input/state. If the membership value is 1, the element X belongs to the fuzzy set A completely. If it is zero it does not belong at all.

$$u_A : X \rightarrow \{0\,1\} \tag{3.6}$$

The fuzzy membership functions are usually optimized through GA which is a

step forward toward optimization Fatehi *et al.* (1998). The benefit of choosing a FL as a controller strategy is augmented when the knowledge of plant behaviour is high. This makes fuzzy controllers fit better for straight forward applications such as regenerative braking strategy Tao *et al.* (2017), but considering the possibility of membership optimization and the simplicity of implementation, there are also many applications where this type of control is used, e.g., in Arani *et al.* (2016) and Herrera *et al.* (2015) that will be detailed in the following section. In the optimization-based strategies, the optimal operational mode is defined by minimizing a cost function that usually describes vehicle's energy consumption.

Stochastic Dynamic Programming

In the stochastic dynamic programming (SDP) even though the vehicle model is deterministic the power demand that comes from the driver is stochastic which means that the optimization is not specific for a driving cycle but for general driving conditions given power demand probabilities Liu and Peng (2008). It is important to note that the relevance of the results relies on the quality of the data acquired in order to build the stochastic chain Jiang *et al.* (2017), hence the importance of the input driving cycle in the probability matrix.

Model Predictive Control

The model predictive control (MPC) strategy is considered an on-line method although the optimization is performed for a finite interval instead of at each time step and it is considered to have a fair trade-off relationship between computational effort and non-causality Ma *et al.* (2017). Usually the optimization problem goes through a

linearization process when using MPC method. The generic equation is given in Eq. 3.7, subject to Eq. 3.8.

$$\Delta U^* = \arg\min_{\Delta U} \Delta U^T H \Delta U^T f \tag{3.7}$$

$$A\Delta U \leq b \tag{3.8}$$

Where H and f are constant matrices, A is a constrain coefficient matrix, b is the column vector, and ΔU^* is the optimal sequence defined in Eq. 3.9

$$u(k) = u(k-1) + \Delta u(k) \tag{3.9}$$

The MPC strategy is adopted in Ma *et al.* (2017) in order to decrease the hydrogen consumption and extend life time of the fuel cell hybrid powertrain system. To achieve that, the quadratic cost function considering hydrogen consumption and battery charge-sustainability is built.

An adaptive algorithm based on the MPC model is used to dynamically change the weights of each target. Another use of MPC strategy is presented in Zhang *et al.* (2017) where an EMS with the objective of extending travel distance of an EV is build based on the information of a preceding vehicle and road terrain profile. This article highlights the importance of driving conditions in defining system behaviour.

The MPC method can be also applied in other systems such as torque vectoring control. In Vasiljevic and Bogdan (2016) it was applied with the objective to distribute the torque to individual wheels during a path assuring passengers safety.

Optimal Control Law

As proposed in Sampathnarayanan *et al.* (2014), it is possible to perform the power-split optimization of a HEV by a nonlinear regulator and disturbance rejecter method where analytical equations of the power components are used to establish a state feedback control law aiming asymptotic stability. The authors in both Jiang *et al.* (2017) and Ma *et al.* (2017) approximate the ICE consumption using the Williams line model, which says that for a given speed the input power is an affine function of the engine power. The electric motor and battery are then modelled using each component average efficiency. Although the time response of this method is one of the fastest, the average consumption obtained with this method tends to be much higher than others such as the following ECMS.

Equivalent Consumption Minimization Strategy

The equivalent consumption minimization strategy (ECMS) is an instantaneous minimization method used in HEV architectures that uses fuel consumption as cost function. For that, ECMS method proposes a way to translate battery energy effort in fuel usage, since the engine has the obligation of charge-sustain the battery Chrenko *et al.* (2015). That way the battery is seen as a fuel reservoir, to be refilled only by the ICE. In other words, all energy can be translated in fuel consumption as described by Eq. 5.12.

$$\dot{m}_{eq}(t) = \dot{m}_f(t) + \dot{m}_{batt}(t) = \dot{m}_f(t) + \frac{s}{Q_{LHV}} \cdot P_{Batt}(t) \cdot p(x) \tag{3.10}$$

Where $\dot{m}_f(t)$ represents instantaneous engine fuel consumption, Q_{LHV} is the fuel lower heating coefficient, $\dot{m}_{batt}(t)$ is the virtual fuel consumption of the battery,

$P_{Batt}(t)$ is the battery power and $p(x)$ is an optional correction function that accounts for SOC variation Sciarretta *et al.* (2004). With the same purpose of charge-sustainability through a cycle, an ECMS strategy was applied in Gurkaynak *et al.* (2010). Here, the PMP method was used to minimize the cost function at each time step and output the power split between both torque sources. For the correction coefficient an adaptation is proposed using driving cycle recognition. The patterns recognition is made by analyzing speed and acceleration profiles through neural network (NN) process. This adaptive version of the correction factor introduces an alternative version of the ECMS method, the A-ECMS, where the 'A' stands for the ability to adapt given the condition.

The articles cited previously show that the performance of the ECMS is comparable to off-line methods such as DP Gurkaynak *et al.* (2010), citesciarretta2004, and citer125. Furthermore, Hu *et al.* (2015), Jiang *et al.* (2017), and Kural and Güvenç (2015) show that A-ECMS deliver results with proximity to global optimal results. Given that, and its balance with low computational effort, the ECMS and its variations figure as the most prominent on-line optimization method.

Machine Learning

Another methodology applied to EMS that has been gaining momentum in recent years is the use of machine learning (ML). A detail framework for for developing ML algorithms that solve the energy consumption problem of HEVs is outlined in available in Murphey *et al.* (2012). As reviewed in detail in Biswas and Emadi (2019) the ML algorithms tend to have a low computational cost to run in real-time and when trained appropriately can output near-optimal global solutions. Nevertheless,

training process requires extensive collection of diverse data to make sure algorithm is bounded to every condition. For that reason, it is also usual the application of ML together with other methods so the neural network (NN) is responsible for only part of the control.

That is the case of Han *et al.* (2020), where an A-ECMS algorithm is built with the support of a RNN that provides the optimal trajectory of the SOC over a cycle also accounting for battery aging. In Jamali *et al.* (2021), another RNN is used the long short-term memory (LSTM). It is applied as a control variable prediction model for solving the power-split problem in a split-hybrid configuration. Other uses of the LSTM RNN in electrification control are battery state of charge prediction Vidal *et al.* (2020) and drive cycle classification Haußmann *et al.* (2019).

The work in Biswas *et al.* (2019) goes a step further in the ML approach and uses a reinforcement learning (RL) algorithm to solve the same problem in a similar configuration. Finally, in Biswas *et al.* (2020), two real-time methods are compared to the RL approach, a RB algorithm and a ECMS. The results showed that not only the fulfilment of the primary energy consumption criteria should be accounted for, but also the applicability and the peripheral functionalities of the EMS.

3.2 Consumption Assessment Methods

To better understand the benefits of journey mapping for EMS control, first it is important to outline how agencies currently assess the energy consumption of the vehicles for the purpose of labelling.

3.2.1 Drive Cycles

Standard driving cycles are created by regulators, their purpose is to level energy consumption and emission evaluation across different models and makes. A driving cycle consists in a predefined speed profile over a certain period of time that emulates a specific use or location Barlow *et al.* (2009). There are cycles that simulate urban scenarios with lower peak speeds and frequent stops, such as the Urban Dynamometer Driving Schedule (UDDS), and there are cycles that simulate highway scenarios, with higher speed and less transients, such as the Highway Fuel Economy Test Schedule (HWFET). To establish a fair comparison between different vehicles, dynamometer testing on standard driving cycles are performed. By using dynamometers, we mitigate those random variations, by controlling the environment at which we are testing. Nevertheless, this usually results in a difference between the label and the actual fuel consumption exhibited by the vehicle.

Dynamometer testing on driving cycles are used to assess energy performance, but depending on the powertrain topology different procedures take place.

Single-cycle Testing

For BEV with low autonomy (less than 100km), single-cycle range is applied. The battery is fully depleted over a repeated cycle, UDDS to evaluate city range, and HWFET to evaluate highway range. "Soak" times are added between cycles, where all systems are shut off for a short period of time before resuming the test. The end-of-test is called when the vehicle cannot maintain the scheduled speed due to power limitations (low state of change).

Multi-cycle Testing

If the BEV is able to provide a long range, the previously procedure could take more than twenty hours to be completed, being costly and impracticable. For that reason, another procedure takes place for BEVs with range greater than 100km. The multi-cycle range procedure combines city and highway cycles to assess both conditions at once. In addition, it places a constant-speed driving cycle between the schedules to deplete the battery more rapidly. This constant-speed cycle should be placed so the second intercalation of UDDS-HWFET-UDDS runs in a substantially lower state of charge, speeding the test.

5-Cycle Testing

Note that the previous processes are built to assess BEV range and energy consumption. In a hybrid vehicle the same process and end-of-test criterion would not work since the vehicle will always be able to maintain the desired speed. Therefore, other ways of testing HEVs and plug-in HEVs (pHEV) are devised. Since 2011, a 5-cycle test has been adopted for labelling vehicles in the U.S. and Canada. The 5-cycle testing procedure adds to the previously mentioned cycles (UDDS and HWFET) a more aggressive driving cycle, the US06, a hot weather testing with air conditioning with the SC03, and it adds a cold run of the UDDS in addition to the hot run.

For testing fuel economy of HEVs, the 5-cycle testing is used but a constraint is added. The net battery energy change tolerance must be below 1%. This tolerance is calculated by dividing the net battery energy change by the total consumed fuel energy. That allows a fair comparison to the combustion engine vehicles that run in the same test. Plug-in hybrid vehicles usually run in two different modes. First,

charge depleting (CD) mode, where the battery used is maximized. Second, charge sustaining (CS) mode, when the lower region of state of charge is reached and the ICE is turned on to assist propelling and/or to assist maintain the charge level. To measure the fuel economy in CS mode, the same criterion used for HEVs can be applied. For this test, the starting state of charge is the CS level. As for the CD mode assessment, the 2-cycle test using UDDS and HWFET cycles can be performed as if the vehicle was an EV. For this procedure, the battery is depleted to its CS level then recharged to full state of charge. The AC energy used to charge the battery is measured. The vehicle is then taken to a dynamometer by a tow or pushed. The end-of-test criterion will differ from the criterion for EVs. That is because in PHEVs the CS mode is activated once the vehicle reaches its lower level of charge. To define the end of the CD test, the NEC tolerance can be once again used, plus a rule where the state of charge variation is lower than 2% of the total depleted.

Although very representative and useful, standard driving cycles can only represent certain aspects of driving. Since they are fixed cycles, one can visualize that most of the time, manufacturers will prioritize vehicle performance in those cycles over the performance in real-world condition. Therefore the conclusion is that is not always that the standard cycles represent the real vehicle behaviour. As mentioned before, the final energy consumption and range is affected by several (often random) events. For that reason, labelled consumption and actual consumption will always differ. An aggressive driver might think the label overestimated the energy efficiency of the vehicle while a smooth driver might think it shows a realistic value. In the end the biggest accomplishment of the labelling process is to establish a fair comparison between the vehicles, providing the customer with the relevant energy consumption

information of vehicles under the same conditions.

3.2.2 Driving Conditions

Driving conditions include vehicle velocity and acceleration like in the drive cycles but also driver style, traffic, weather-related conditions such as adherence and temperature, road geometry, and every other aspect of the mission that has an energy impact. Being able to decompose the driving conditions of a mission enables more accurate consumption assessment of a vehicle under that mission.

There are several sources for acquiring information on driving conditions. Among the most common are the signals from the vehicle's control area network (CAN) that leverages in-vehicle sensors that measures pedal position, slope, accelerations, vehicle speed, among others. Global Positioning System (GPS) apps enable vehicle geolocation. V2X communication allows exchange of circumstantial information about the path, weather, and traffic.

In addition to assess consumption better, driving condition prediction allows the EMS to manage better instantaneous optimizations. Therefore, techniques for journey mapping and driving condition prediction are developed.

Track monitoring systems

The simplest systems regarding path mapping and vehicle's real-time monitoring can be called track monitoring systems (TMS). The TMS are responsible for keeping track of vehicle's position and fuel consumption. They were first developed aiming the improvement of user experience for vehicles of repeatedly use, as depicted in Yosif *et al.* (2017) in a public transportation application. Although they represent simple

systems, their concept can reach larger applications.

Two applications of TMS for EMS are proposed in Bender *et al.* (2013) and Chen *et al.* (2016). Both articles propose driving prediction for vehicles of repeatedly use. The first presents an iterative learning EMS for a hybrid hydraulic garbage truck. Here, the prediction of the driving cycle is based on speed measurement from CAN, distance and position of the vehicles. Although the integration of driver behaviour was not done, differences in speed profiles for the same path were noted because of this variable. Since the stopping positions for several measurements tend to be very similar, a learning path profile was implemented. In this case, the central database compares the real time measurements with the previously mapped scenarios and outputs system strategy in order to lower vehicle consumption.

Cycle clustering

Cycle clustering consists in classify and clustering missions that share similar driving conditions. A simple application of that concept is proposed in Haußmann *et al.* (2019) for creating an A-ECMS. K-means clustering is used to cluster standard driving cycles into two groups, low and high-powered demand cycles. The A-ECMS then switches the calibrated parameters in the cost function depending on the environment.

In Chen *et al.* (2016) that approach is employed for a pHEV. In this case, not only grade profile is added but a novel methodology of driving cycle classification is proposed using the clustering method. Machine learning technique is used to predict current cycle. A generic approach is used in Valera *et al.* (2013) where the objective is to develop an on-board prediction for the energy management optimization. In this paper, traffic information, track speed limit, and road grades from digital maps

help to adapt a reference speed profile for a specific mission. The reference speed cannot be a function of track speed limit only; otherwise the result strategy might come from a non-realistic speed profile. Therefore, driver behaviour is added by using the vehicle's speed signal. Non-linear Auto Regressive Neural Network (NARX) is used to solve the speed deviation between reference and actual speed.

Stochastic extrapolation

Not all of driving conditions are steadily predictable as road grades and weather. Some of the most important variations have random behaviour, e.g. driver pedal action and traffic. Therefore, it is reasonable to implement a tool that accounts for the random when it comes to re-create a real-world mission for consumption assessment. The Markov Chain (MC) is a discrete-time statistic tool. It defines the Markov property that states that next state depends only on the current state Souffran *et al.* (2011).

The whole process is very well-described in Lin and Niemeier (2003) where the MC is applied, accounting for traffic conditions. They are later compared to the standard driving cycles that first originate them. The complete process consists in partitioning the original driving cycle in micro-trips, and classifies them in state conditions, i.e. cruising, accelerating, decelerating, and idle.

Other approaches consist in simply choosing driving style and traffic as state conditions as in Liessner *et al.* (2016) .The MC is better explored in Souffran *et al.* (2012) where the statistical process was used to generate numerous stochastic mission profiles from measured acceleration, elevation, speed and torque data. This approach is seen as a valid method to consider various driving conditions since the probabilistic characteristic of the Markov matrix generates a large number of driving scenarios.

Then an EMS strategy is settled to adapt in between the driving scenarios.

Leveraging autonomous systems

Another way of performing cycle and condition prediction is leveraging autonomous driving features. Using autonomous features to isolate and/ predict driving action is a clever resource because most of the randomicity in the driving conditions are associated with driver behaviour.

In Kural and Güvenç (2015) the authors use the concept of ACC, which is a feature that allows the user of the host vehicle to specify the desired maximum speed and the minimum distance between the host and the target vehicle. The algorithm will then decide on the most conservative approach with the objective to prevent a front-end collision. In this way, the speed profile for the next short time window can be estimated, and the correction factor is chosen based on this information.

3.3 Journey mapping

From the previous section it is possible to conclude that the newest optimization methods are going toward integration between driving prediction and condition mapping, i.e., translating conditions such as terrain and traffic into speed and torque profiles to be used by the EMS. The adaptability of the EMS is improved when the conditions are known or at least foreseen in a reasonable time range. In that context, redefining the drive cycle by adding its driving conditions for consumption assessment and EMS design is in need.

Journey mapping (JM) is an approach that redefines the driving cycles as the journey from an origin to a destination and all the driving conditions that surround

and affect vehicle behaviour and performance Divakarla *et al.* (2016).

A straight forward application of journey mapping to driving prediction in EMS is presented in Palcu and Bauman (2017). To perform a whole-day driving control strategy the proposed controller uses mainly drivers destiny information (typed by the driver) in order to define if the engine should be turned on in the beginning of the mission. Additional information from traffic speeds and external temperature are also used.

The influence of different driving conditions on vehicle performance for a fixed path is studied in Divakarla *et al.* (2016) by performing the same known path under different conditions. The energy consumption estimated through the JM was compared to the measured data from CAN and labelled information. The results show that driver behaviour, grade variation, and auxiliary power play a relevant role in energy expenditure. In Divakarla *et al.* (2015), a driving cycle was built from a journey mapping process to characterize the battery of an BEV and perform SOC prediction. Once more, the inclusion of realistic path characteristics was proved effective and beneficial to the evaluation of electrified systems such as the battery management.

3.4 Summary

This chapter reviewed the current research on EMS, highlighting differences between off-line and on-line method. From the reviewed methods, the DP and the ECMS algorithms stand out. The former as a benchmark tool, able to provide a global optimal solution for a known drive cycle and the latter as an on-line implementable near-optimal approach. Also important to note the current bias in industry toward variations of the RB method and the increase in reasarch on NN methods.

The chapter also provided an overview on the current state of consumption testing methodology. Standard drive cycles and condition mapping techniques are presented, and their importance during vehicle design and assessment is highlighted.

Considering that mapping technologies, road-vehicle communication, and autonomous features are constantly being improved, it is possible to foresee that energy management will benefit greatly as connected and autonomous vehicles take over.

Such prospects motivate this research. Here, an EMS that captures the changes in driving conditons is designed, tested and latter integrated with an autonomous system that is enabled through journey mapping.

Chapter 4

Vehicle Dynamics

4.1 Introduction

As defined in Balci (2003), the purpose of a model is to reproduce the behaviour of a more complex real-life system.

Several modelling methods have been used in automotive engineering to reproduce the behaviour of a ground vehicle and its components. The models can be categorized into three types: empirical models, physics-based models, and gray-box models. Empirical models are formulated through measurements and observations. The model reproduces the system for a specific domain of inputs and may have no physical meaning. Quasi-static models are an example of empirical models commonly used for propulsion systems such as ICEs, and electric machines Tran *et al.* (2020). This type of model relies on look-up tables built from experimental tests. Although very simple to implement, the empirical models might not provide the engineers with enough dynamics of the system. Besides, they are constrained by the input domain

of the experimental tests performed to build them. Physics-based modelling is preferable when the transient responses are object of interest. This type of modelling uses the physical laws that govern the component or the system to model its behaviour. This method is commonly used for modelling energy storage systems Ahmed *et al.* (2014a) and vehicle dynamics Schramm *et al.* (2014). Lastly, gray-box models are a combination of the previous two.

The electrification trend has transformed the automotive industry, representing a paradigm shift for the transportation sector Emadi (2011). Electrified propulsion systems allow vehicle manufacturers to offer their customers with increasing fuel-efficient products and at the same time lower the emissions of their fleet Bilgin *et al.* (2015). Nevertheless, the drivability requirements remain. Ride smoothness and acceleration performance are key factors for a vehicle to sell well. Therefore, as manufacturers increase the market share of hybrid vehicles, it is pivotal to develop vehicle models that account for the newest technologies.

4.2 Modelling Approach

The EMS, defined in the previous chapter, is the strategy in a control system developed in order to enhance fuel efficiency Serrao *et al.* (2011). But let us not disregard the modelling methods, in fact the effect of the EMS is a function of the components, therefore the importance of reviewing this process as well. The closed-loop diagram in Fig. 4.1 shows the interdependence between driver's demand and the powertrain plant, where V_{ref} and V_{veh} are the cycle's input speed and simulated speed respectively, P_{req} is the requested power, P_{batt} is the battery power, P_{ice} is the combustion engine power, SOC is the battery's state of charge, and t is the cycle time.

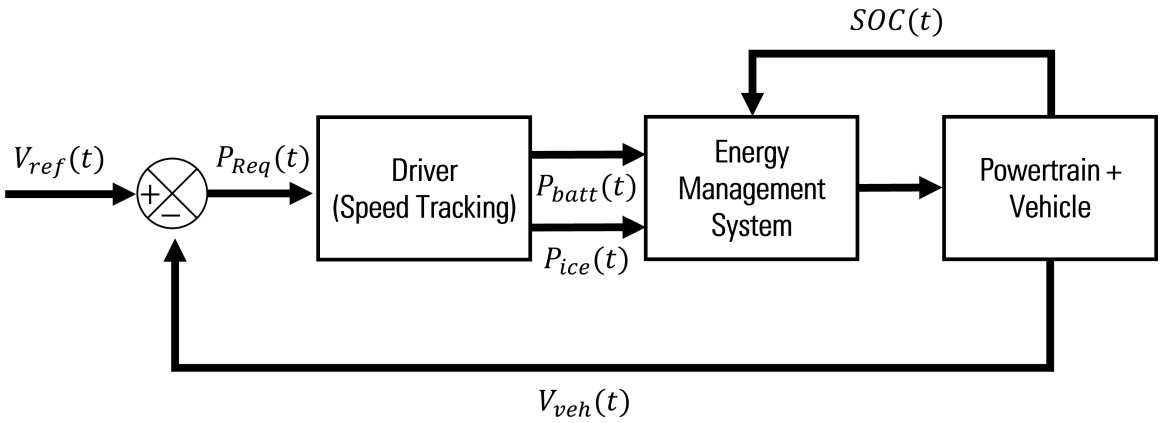

Figure 4.1: Energy management simulation diagram for a hybrid vehicle

When devising a simulation study, it is important to select the appropriate approach for modelling the system behaviour as well as each component in it.

4.2.1 System Modelling

Here, the two most used system modelling methods are detailed, the forward and the backward model. The first method considers the flow of torque from the torque source and it passes forward the torque to the following components (i.e., drive shafts, gearbox, and final drive) that will generate an output speed. Although very realistic, this method requires high amount of computational effort plus a driver model that can perform the speed controller.

The backward model in the other hand is front-to-rear model that takes the required speed at the wheels and goes back all the way through the components checking the desired speed and torque in the torque sources to meet that requirement Bender *et al.* (2013). Although not as realistic as the previous one, it is good for model validation (when vehicle test data is available). Combined backward and forward approaches are also feasible.

Other examples of model types are the functional models (that aim to represent the system through mathematical equations), and structural models (that relies on component libraries) where the user can just connect components as they are connected in the physical system. This type of modelling is getting momentum nowadays since a lot of third-party simulation software is providing this option as a toolbox.

4.2.2 Component Modelling

Component design is pivotal for a coherent analysis of the results. A vehicle is a cluster of many components, some more complex than others, thus it is understandable that the modelling method vary depending on the component. ICEs for instance are very complex systems, for that reason quasi-static models are preferable. They are a combination of look-up tables (from experimental data) that create the steady state behaviour, and a first-order system that adds the dynamic component.

For other components, quasi-static approaches might not work since the transients are the object of interest. For those components, physics-based strategies might be the solution. The idea is to model a simplified system accounting for the physical laws that govern this system with its state variables. In this way, the performance of the system will be a function of the component parameters Gao *et al.* (2007). Some examples of application of physics-based modelling inside powertrain models are the modelling of DC machines, converters, and even wheel slip.

Regarding HEV simulation, one of the most studied components is the battery pack, hence the importance on defining a robust modelling method for this system that translates the behaviour of this component. The primary importance of modelling the battery pack is to proper estimate and predicts the changes in the SOC.

The work performed by Jinhao *et al.* (2017) reviews several different categories for SOC estimation, such as coulomb counting, impedance spectroscopy method, and strategies using NN. Coulomb counting presents itself as one of the most computational effective and easy to apply methods, although its accuracy is limited due to the reliance on initial SOC measurements and recurrent current sensor error accumulation. In addition, it does not account neither for temperature change or ageing. The former two mentioned methods can foresee very sensible variations on the SOC, being very accurate, but unfortunately the high computational effort makes it difficult to perform estimations in real-time applications.

Overall, model-based methods combine different approaches in order to mimic battery behaviour in accordance to reality but also enabling online estimations. The simple battery model also called open circuit voltage – resistance (OCV-R) is a vastly used method where the focus of the research is not in the battery itself, but in the overall efficiency of the electrified vehicle as presented in Palcu and Bauman (2017). This method models the battery using internal resistances (usually one for charge and other for discharge to account for the charge-discharge hysteresis of the system) and uses the input current to calculate the terminal voltage. Coulomb counting is used to assess the OCV-SOC table, as mentioned before, this method accumulates error over time, and it is not the recommended when aging and temperature change must be accounted. Another simple approach is called the combined model Plett (2004) and it calculates terminal voltage as function of internal resistance using the combination of three different equations; Shepherd method, Unnewehr universal model, and Nernst model. Although the final equation does not represent any physical meaning

of the system, the method is very simple to apply and relatively effective in estimating terminal voltage. By using this method, the engineers must also set an off-line optimization method since the four parameters of the equation must be found using experimental data. Although more accurate than its predecessor since it can capture transients at a limited level, the combined model shows similar limitations in ageing and temperature sensitivity.

Considering full-vehicle models, simplified equivalent circuit approaches are very popular when modelling electrical components, being the resistance-capacitance (RC) model the most used method since the ability of capturing dynamic behaviour and account for ageing is valued in detailed analysis. The RC model consists in the previous OCV-R structure with the addition of a resistor-capacitor structure (Thevenin-based model). The order of the model increases with the addition of more sets of RC structures. As mentioned before, this structure allows to predict transients in the voltage estimation adding the dynamic behaviour and relaxation behaviour as depicted by Enache *et al.* (2013). Different orders for the RC model are proposed in several papers. In Li and Cheng (2014) for example, a first and a second order RC models are compared for a lithium-ion battery using the Gauss-Newton method to identify the model parameters. This comparison of different order systems performed by Li and Cheng (2014) is also present in Ahmed *et al.* (2015). The results agree that the higher the order, more robust the model is, and better in providing dynamic behaviour throughout the ageing process. Again, the choice of an efficient optimization method is extremely important in order to find the added parameters, Sangwan *et al.* (2016) presents a comparison between three different techniques; GA, particle swarm optimization PSO, and ageist spider monkey optimization. Detailed battery testing

to measure internal resistance and capture the dynamic behaviour of the terminal voltage during current pulses is also necessary.

The last battery modelling method here described is the method that tries to replicate the real physic behaviour of the molecules at the cell level, and it is called the electrochemical model. As the name suggests the chemical reactions are modelled in this method, aiming to achieve the most accurate behaviour of the cell. Although this type of modelling is very accurate, it requires deep knowledge about electrochemical behaviour, and about the values of the state variables. Therefore, it is used more often for component design instead of vehicle level analysis. An application of this approach is the modelling of a lithium-ion battery performed by Weatherhog and Sharma (2013) where a simplified electrochemical model of an isolated battery cell is proposed, and the battery model is built from the connection of those cell's models. Although accurate, the computational load makes it almost unfeasible for real-time implementation. A reduced-order model is presented by Ahmed *et al.* (2014a) as a simplification of the Doyle-Fuller-Newman method for defining all the electrochemical parameters from a battery cell during charge and discharge reactions, for several C-rates, at several points during the cell life time. A novel SOC parametrization is also proposed together with a model validation using real-world driving cycles. Furthermore, the extension of this work Ahmed *et al.* (2014b) introduces a battery ageing model able to capture battery degradation. The state-of-the-art reduced model achieves its objective, which is to reduce the main issue regarding electrochemical models, the high computation load required.

In summary, equivalent circuit-based models have the benefit of easy implementation and estimation of parameters besides being very efficient for real-time estimation. The turn down is that the lack of physical significance of some parameters makes those models limited, not being able to account for temperature change neither defining other battery properties such as state-of-health (SOH). The electrochemical models in the other hand aim to describe the ion diffusion inside the cells, which gives them high physical connection with the actual system and makes this model able to fully analyze battery states. The issue is when real-time is required since such high detailed analysis comes with a high computational cost.

4.3 Driveline Kinematics

Vehicle dynamics and driveline dynamics are highly connected. Both are present in literature either separately or combined. Works focused on driveline dynamics include, Eriksson and Nielsen (2014), and Kiencke and Nielsen (2000). Those two provide not only the modelling of powertrain components, but also discuss in detail key aspects of vehicle longitudinal dynamics such as road resistances and driveline control. Models developed in those works such as the Basic Driveline Model, the Non-linear Clutch, and the Driveshaft Model represent well the dynamics of ICE-only vehicles. Nevertheless, there is a still a lack of hybrid-propelled driveline models in literature.

In driveline control, the dynamics of the states are of high importance. For that reason, engineers often choose physics-based modelling. Those models increase in complexity as the need of adding components' inertia, friction, and flexibility increases.

This section shows a method for the modelling of the most common electrified driveline topologies: the series hybrid, the parallel hybrid and the split hybrid. The method is intuitive and can be applied to any other powertrain topology. The objective is to provide a controllable and observable model for drivability control and state estimation.

4.3.1 Modelling Methodology

Drivelines are systems made from the assembly of different components that link a propelling source (or mover) to the wheels of the vehicle Eriksson and Nielsen (2014). To analyze a topology, engineers often recur to block diagram representations where each major component is represented by a block. Here a methodology is introduced for component representation using a specific block structure. The driveline diagram is then built by connecting the blocks as the components connect in the real mechanical system. Fig. 4.2 depicts the block representation for the powertrain components.

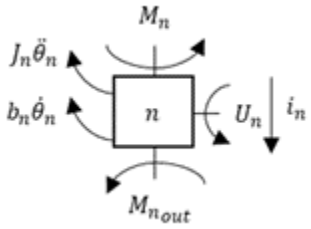

Figure 4.2: Block representation of a generic powertrain component.

The symbol n is substituted by an abbreviation of the name of the component, e.g. *ice* for engines and *cl* for clutches. Using the representation in Fig. 4.2, we are able to depict the torque transferred M_n from the previous to the current component as well as the torque output $M_{n_{out}}$ of the component n. Note that both torques have

same direction. If the component is a mover, the input torque U_n is also added on one of the sides of the block, in the same direction. On the other side, the torque losses in the component are represented, in opposite direction. The losses here are the inertia effect, where J_n is the inertia of the component, and the friction effect, where b_n is the component's internal friction. Other losses might be added as well depending on the component that is being represented. The representation of losses can be suppressed if they are disregarded. The straight arrow facing downwards represents the ratio i_n that the component may apply in the torque path. For final drives, this value is often fixed. For gearboxes, this ratio is a function of the gear engaged and varies between discrete values. For clutches, i_n works as a switch instead of a ratio. Its value is either 0 (decoupled) or 1 (coupled). If i_n is constant and equals to 1 (e.g. for shafts and movers), its graphical representation can be suppressed. The symbol Ω_n represents the angular position of the component n. Thus, its first and second derivative represent the rotational speed and rotational acceleration, respectively.

Newton's second law is applied to perform the torque balance of the block. The torque output $M_{n_{out}}$ will be a function of the torque transferred M_n, the torque input U_n, the ratio i_n, and the torque losses (inertia, friction, etc.). Equation 4.1 shows the torque balance.

$$M_{n_{out}} = (M_n + U_n)i_n - J_n\ddot{\Omega}_n - b_n\dot{\Omega}_n \tag{4.1}$$

The rotational speed of the component $\dot{\Omega}_n$ will be a function of the previous component speed $\dot{\Omega}_{n-1}$ and the current ratio i_n.

$$\dot{\Omega}_n = \dot{\Omega}_{n-1}/i_n \tag{4.2}$$

Note that for disengaged clutches ($i_{cl} = 0$), Eq. 4.2 will return an undefined value (due to the division by zero). For that reason, we assume clutch engaged in the speed analysis and suppress i_{cl}, since it is equal to one. The i_{cl} switch is still added in the torque analysis.

Before introducing the modelling method in steps, it is important to understand the goals of modelling the driveline. The intention is to provide a model that represents the plant dynamic behaviour.

The powertrain control module keeps track of the system's states, defines the best inputs at each time-step, and assures smooth longitudinal dynamics. One issue is that not all states are easy to measure with precision. In addition, electrified topologies present a high number of components. To assign a sensor to each component would represent a significant addition of cost. Therefore, driveline models are built. They enable state estimation as well as providing the means for longitudinal dynamic control.

Step 01: Diagram

The first step of modelling is to draw a diagram of the topology. Each component in the driveline should be represented by a block defined in the previous section. We start the diagram with the propelling system and then add the other blocks vertically, following the order the components appear in the powertrain topology. In the diagram, the torque output term of one block becomes the torque transferred term of the next block. If two components are in parallel in the topology, the respective blocks will also be in parallel in the diagram, horizontally. This is especially necessary for parallel hybrids and planetary gears, as further detailed. The last component

added is the block representing the wheels. Figure 4.3 shows a generic driveline propelled by a single mover. This generic driveline will be also used in the following steps.

In Fig. 4.3, the generic mover gm can be coupled and decoupled from the driveline through the clutch cl. The clutch couples the mover to a transmission tr. The transmission ratio i_{tr} is a function of the gear engaged. The transmission connects to a propelling shaft ps that is linked to the final drive fd. The final drive has a fixed ratio i_{fd} and transfers torque to the driveshaft ds that spins the wheels wh. Note from Fig. 4.3 that not all the components are modelled with internal inertia and friction. The decision of including those terms should be part of the modelling strategy.

Also note that road resistance torque M_{ROAD} is added to the wheels block as one of its losses. The road resistance torque is resultant of the road loads acting on the vehicle, F_{ROAD}. They are the sum of drag, rolling resistance, and gravity effect. Those can be modelled using different techniques. The road resistance torque is equal to the road load times the wheel rolling radius r_{wh}.

$$M_{ROAD} = F_{ROAD} \cdot r_{wh} \tag{4.3}$$

The bottom of the diagram shows the final resultant torque to the ground ($M_{ground} = m \cdot \ddot{\Omega}_{wh} r_{wh}^2$). To achieve that expression, we use Newton's second law once again. If there is no slip, the torque to the ground is equal to the output torque of the wheels $M_{wh_{out}}$. If the vehicle is moving, $M_{wh_{out}}$ is the torque responsible for the vehicle's acceleration as showed in Eq. 4.4.

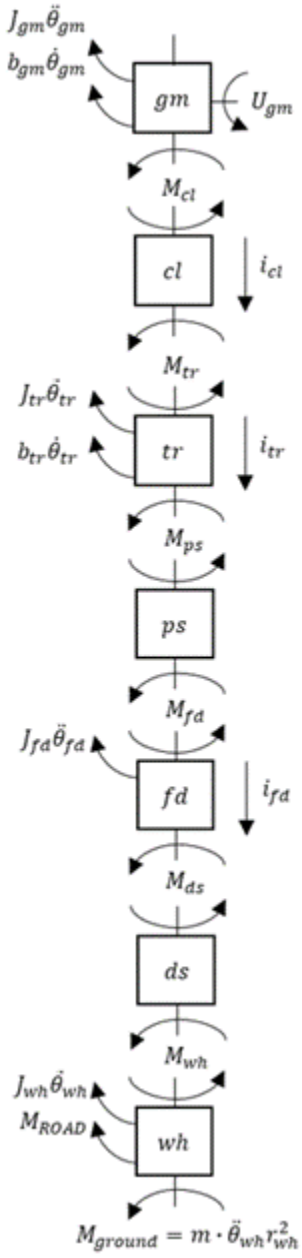

Figure 4.3: Generic driveline represented by the block diagram method.

$$M_{ground} = M_{wh_{out}} = F_{acc} \cdot r_{wh} = m\vec{a} \cdot r_{wh} \tag{4.4}$$

Where F_{acc} is the resultant acceleration force, m is the vehicle's mass, and $\vec{a}$ is the vehicle's longitudinal acceleration.

Assuming no slip, the conversion of vehicle linear acceleration to wheel rotational acceleration is:

$$\vec{a} = \ddot{\Omega}_{wh} \cdot r_{wh} \tag{4.5}$$

Substituting 4.5 in 4.4, we arrive at the equation for the torque to the ground as depicted in Fig. 4.3.

$$M_{ground} = m \cdot \ddot{\Omega}_{wh} r_{wh}^2 \tag{4.6}$$

Step 02: Block Connections

The next step is to write the torque and speed equations of each link (block connections) on the diagram. Equation 4.7 shows the structure that should be built for every block connection.

$$Block_{n-1} \rightarrow Block_n : \begin{cases} M_n = M_{n-1_{out}} = [...] \\ \dot{\Omega}_n = \dot{\Omega}_{n-1}/i_n = [...] \end{cases} \tag{4.7}$$

Once this structure is set-up, we fill the blank spaces [. . .] with expressions derived from Eq. 4.1 and Eq. 4.2 for torque and speed of each component, respectively. If a propelling source has no block on top of it, its torque transferred term (M_n) is equal

to zero. If two blocks are in parallel in the diagram, the torque transferred forward should be the sum of each output torques from the blocks in parallel.

As we move downwards the diagram, writing the equations for the connections, we achieve expressions of torque and speed that relate to the input torques and speeds from the top of the diagram. This step is performed for the present example in the following structure of Eq. 4.8.

$$
gm \rightarrow cl: \begin{cases} M_{cl} = M_{gm_{out}} = U_{gm} - J_{gm}\ddot{\Omega}_{gm} - b_{gm}\dot{\Omega}_{gm} \\ \dot{\Omega}_{cl} = \dot{\Omega}_{gm} \end{cases}
$$

$$
cl \rightarrow tr: \begin{cases} M_{tr} = M_{cl_{out}} = M_{cl} i_{cl} = U_{gm} i_{cl} - J_{gm}\ddot{\Omega}_{gm} i_{cl} - b_{gm}\dot{\Omega}_{gm} i_{cl} \\ \dot{\Omega}_{tr} = \dot{\Omega}_{cl}/i_{tr} = \dot{\Omega}_{gm}/i_{tr} \end{cases}
$$

$$
tr \rightarrow ps: \begin{cases} M_{ps} = M_{tr_{out}} = M_{tr} i_{tr} - J_{tr}\ddot{\Omega}_{tr} - b_{tr}\dot{\Omega}_{tr} \\ \dot{\Omega}_{ps} = \dot{\Omega}_{tr}/1 = \dot{\Omega}_{gm}/i_{tr} \end{cases}
$$

$$
ps \rightarrow fd: \begin{cases} M_{fd} = M_{ps_{out}} = M_{tr} i_{tr} - J_{tr}\ddot{\Omega}_{tr} - b_{tr}\dot{\Omega}_{tr} \\ \dot{\Omega}_{fd} = \dot{\Omega}_{ps}/i_f = \dot{\Omega}_{gm}/i_{tr} i_{fd} \end{cases}
$$

$$
fd \rightarrow ds: \begin{cases} M_{ds} = M_{fd_{out}} = M_{fd} i_{fd} - J_{fd}\ddot{\Omega}_{fd} \\ \dot{\Omega}_{ds} = \dot{\Omega}_{fd}/1 = \dot{\Omega}_{gm}/i_{tr} i_{fd} \end{cases}
$$

$$
ds \rightarrow wh: \begin{cases} M_{wh} = M_{ds_{out}} = U_{gm} i_{cl} i_{tr} i_{fd} - J_{gm}\ddot{\Omega}_{gm} i_{cl} i_{tr} i_{fd} - b_{gm}\dot{\Omega}_{gm} i_{cl} i_{tr} i_{fd} ... \\ -J_{tr}\ddot{\Omega}_{tr} i_{fd} - b_{tr}\dot{\Omega}_{tr} i_{fd} - J_{fd}\ddot{\Omega}_{fd} \\ \dot{\Omega}_{wh} = \dot{\Omega}_{ds}/1 = \dot{\Omega}_{gm}/i_{tr} i_{fd} \end{cases}
$$

$$
wh \rightarrow gd: \begin{cases} M_{ground} = M_{wh_{out}} = M_{wh} - J_{wh}\ddot{\Omega}_{wh} - F_{ROAD} r_{wh} \\ m\ddot{\Omega}_{wh} r_{wh}^2 = U_{gm} i_{cl} i_{tr} i_{fd} - J_{gm}\ddot{\Omega}_{gm} i_{cl} i_{tr} i_{fd} - b_{gm}\dot{\Omega}_{gm} i_{cl} i_{tr} i_{fd} - J_{tr}\ddot{\Omega}_{tr} i_{fd} ... \\ -b_{tr}\dot{\Omega}_{tr} i_{fd} - J_{fd}\ddot{\Omega}_{fd} - J_{wh}\ddot{\Omega}_{wh} - F_{ROAD} r_{wh} \\ V_{veh} = \dot{\Omega}_{wh} r_{wh} \end{cases} \tag{4.8}
$$

By the end of the process ($wh \rightarrow gd$) we use Eq. 4.6 for M_{ground} and the expression

found for M_{wh} to produce a final torque equation. As for the speed, the conversion of rotational to linear speed is used to have an expression that is function of vehicle speed.

Step 03: States and Inputs

The state variables are the variables that describe the conditions of the system, while the inputs are the variables that have the ability to change the value of the states Nise (2020). For powertrain control, component's rotational speeds are a good example of state variables, and the torque provided from the movers is an example of inputs. This section shows important considerations when choosing both. Let us start with the inputs.

In a driveline, the torque applied by the movers is considered the input. Since the present method aims to include hybrid powertrains, more than one propelling system may be present. In this step, we gather all the propelling inputs in the topology and add it to a matrix U, called the propelling matrix. From the previous step, if a block generates torque (U_n), then this torque is added to the matrix U. In the current example, the torque in the generic mover (U_{gm}) is the only propelling input. Eq. 4.9 depicts the propelling matrix U for the example.

$$U = \begin{bmatrix} U_{gm} \end{bmatrix} \tag{4.9}$$

Regarding the states, the following two rules aim to help state selection for a driveline model.

- If the model is rigid, all rotational speeds are linear functions of each other, therefore a single component's rotational speed is selected as state variable.

Preferably wheel speed.

- If the model contains a flexible component, the first state will be the speed variable from a block that is above the flexible component in the diagram. the second state will be the speed variable from a block that is below the flexible component in the diagram. The third state will be the angle position difference created in the flexible component.

If there are more than one flexible components, the same process is applied. There should always be a state from above a flexible component, another from below, and another as the angle position difference created in the component. Equation 4.10 shows the state vector x for the generic driveline example. Since it is a rigid driveline, we use the first rule and select wheel speed as state variable.

$$x = \left[\dot{\Omega}_{wh}\right] \tag{4.10}$$

Step 04: State Dynamics

The next step is to find the state dynamics from the torque and the speed equations derived in Step 02. For a rigid model, the last torque equation derived in Step 02 describes the impacts of the input torques and the losses in the acceleration performance. Equation 4.11 is a transcription of that final torque equation.

$$\begin{aligned} m\ddot{\Omega}_{wh}r_{wh}^2 = U_{gm}i_{cl}i_{tr}i_{fd} - J_{gm}\ddot{\Omega}_{gm}i_{cl}i_{tr}i_{fd} - b_{gm}\dot{\Omega}_{gm}i_{cl}i_{tr}i_{fd} - J_{tr}\ddot{\Omega}_{tr}i_{fd}... \\ -b_{tr}\dot{\Omega}_{tr}i_{fd} - J_{fd}\ddot{\Omega}_{fd} - J_{wh}\ddot{\Omega}_{wh} - F_{ROAD}r_{wh} \end{aligned} \tag{4.11}$$

Using the speed equations found in Step 02 to put Eq. 4.11 in terms of our chosen state, $\ddot{\Omega}_{wh}$:

$$\begin{aligned} m\ddot{\Omega}_{wh}r_{wh}^2 = U_{gm}i_{cl}i_{tr}i_{fd} - J_{gm}\ddot{\Omega}_{wh}i_{cl}i_{tr}^2i_{fd}^2 - b_{gm}\dot{\Omega}_{wh}i_{cl}i_{tr}^2i_{fd}^2 - J_{tr}\ddot{\Omega}_{wh}i_{fd}^2... \\ -b_{tr}\dot{\Omega}_{wh}i_{fd}^2 - J_{fd}\ddot{\Omega}_{wh} - J_{wh}\ddot{\Omega}_{wh} - F_{ROAD}r_{wh} \end{aligned} \tag{4.12}$$

Isolating for $\ddot{\Omega}_{wh}$, we find the equation for the state dynamics.

$$\ddot{\Omega}_{wh} = \dot{\Omega}_{wh}\left[-\frac{1}{J_T}\cdot(b_{gm}i_{cl}i_{tr}^2i_{fd}^2 + b_{tr}i_{fd}^2)\right] + \left[\frac{i_{cl}i_{tr}i_{fd}}{J_T}\cdot U_{gm}\right] - \frac{1}{J_T}\cdot(F_{ROAD}r_{wh}) \tag{4.13}$$

Where J_T is the total inertia effect

$$J_T = J_{wh} + mr_{wh}^2 + J_{gm}i_{cl}i_{tr}^2i_{fd}^2 + J_{tr}i_{fd}^2 + J_{fd} \tag{4.14}$$

It is important to note that in the example, wheel speed was chosen as state variable and Eq. 4.13 is the equation for the derivative of that state. The same process could be used to put Eq. 4.13 in terms of another state variable of choice.

If a component in our driveline model is considered to be flexible, we can split the dynamic analysis in three parts: the dynamics prior to the flexible component, the dynamics post the flexible component, and the dynamics of the flexible component. Here we use the same generic driveline example but considering the driveshaft as being flexible. Following the second rule of state selection in Step 03 we arrive with a new state vector x'.

$$x' = \begin{bmatrix} \dot{\Omega}_{tr} \\ \dot{\Omega}_{wh} \\ \Delta\Omega_{ds} \end{bmatrix} \tag{4.15}$$

Where the states selected are the rotational speed of the transmission block $\dot{\Omega}_{tr}$, wheel speed $\dot{\Omega}_{wh}$, and the difference in the angle position at the driveshaft $\Delta\Omega_{ds}$. The latter can be easily calculated using Eq. 4.16.

$$\Delta\Omega_{ds} = \Omega_{fd} - \Omega_{wh} = \Omega_{tr}/i_{fd} - \Omega_{wh} \tag{4.16}$$

If the driveshaft is a flexible component, the flexibility has effect in the torque transferred from the driveshaft $M_{ds_{out}}$ to the wheels M_{wh}:

$$M_{wh} = M_{ds_{out}} = k_{ds}\Delta\Omega_{ds} + c_{ds}\Delta\dot{\Omega}_{ds} \tag{4.17}$$

Therefore, we use Eq. 4.17 in the link $ds \rightarrow wh$, and solve it for $\dot{\Omega}_{tr}$. Likewise, we use 4.17 in the link $wh \rightarrow groundgd$, and solve it for $\dot{\Omega}_{wh}$. Equations 4.18 and 4.19 describe the outcome of that process for $\dot{\Omega}_{tr}$ and $\dot{\Omega}_{wh}$, respectively.

$$\ddot{\Omega}_{tr} = \dot{\Omega}_{tr}\left[\frac{1}{J_1}\cdot(-b_{gm}i_{cl}i_{tr}^2 i_{fd} - b_{tr}i_{fd} - \frac{c_{ds}}{i_{fd}})\right] + \dot{\Omega}_{wh}\left[\frac{1}{J_1}\cdot c_{ds}\right] + \Delta\Omega_{ds}\left[\frac{1}{J_1}\cdot(-k_{ds})\right]... + \left[\frac{1}{J_1}\cdot(U_{gm}i_{cl}i_{tr}i_{fd})\right] \tag{4.18}$$

$$\ddot{\Omega}_{tr} = \dot{\Omega}_{tr}\left[\frac{1}{J_2}\cdot\left(\frac{c_{ds}}{i_{fd}}\right)\right] + \dot{\Omega}_{wh}\left[\frac{1}{J_2}\cdot(-c_{ds})\right] + \Delta\Omega_{ds}\left[\frac{1}{J_2}\cdot(k_{ds})\right]... + \left[\frac{-1}{J_2}\cdot(F_{ROAD}r_{eh})\right] \tag{4.19}$$

Where J_1 and J_2 are:

$$J_1 = J_{gm}i_{cl}i_{tr}^2 i_{fd} + J_{tr}i_{fd} + J_{fd}/i_{fd} \tag{4.20}$$

$$J_2 = J_{wh} + mr_{wh}^2 \tag{4.21}$$

The third and last state dynamics equation is shown in Eq. 4.22 and can be deduce from 4.22.

$$\Delta\dot{\Omega}_{ds} = \dot{\Omega}_{tr}/i_{fd} - \dot{\Omega}_{wh} \tag{4.22}$$

The modelling of flexible shafts such as the driveshaft is of key significance in the modelling of high accurate driveline models.

Step 05: State-space representation

Once we have the dynamic equations for our states, we can write the system in the state-space format. Figure 4.4 depicts the block diagram representation of that format.

Where $\dot{x}$ is the derivative of the states, A is the state matrix, x is the state vector, B is the input matrix, u is the input vector, H is the inertia effect matrix, and l is

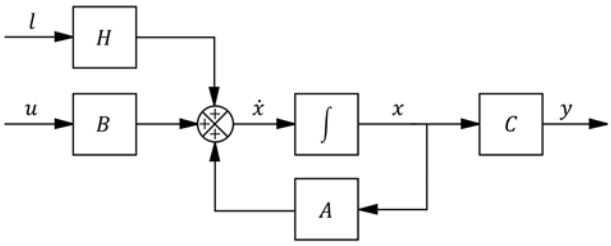

Figure 4.4: Block diagram of the state-space representation.

the road resistance vector.

For the generic driveline example, we take 4.13, and we search for propelling torques U_n. We then combine those torques into one single input u. We can also use the propelling vector U, defined in Step 03, to assist finding the propelling torques in the system.

$$\ddot{\Omega}_{wh} = \dot{\Omega}_{wh}\left[-\frac{1}{J_T}\cdot(b_{gm}i_{cl}i_{tr}^2 i_{fd}^2 + b_{tr}i_{fd}^2)\right] + \left[\frac{i_{cl}i_{tr}i_{fd}}{J_T}\cdot(u)\right] - \frac{1}{J_T}\cdot(F_{ROAD}r_{wh}) \tag{4.23}$$

Where $u = U_{gm}$.

The state vector was defined in Step 03. The state matrix contains the terms linked to the state vector. The input matrix contains the terms linked to the input vector. The matrix H computes the inertia effect $-r_w h/J_T$. By leaving the road load as an external vector (l), the modelling process becomes more flexible to the use of different road resistance models. The generic state-space equation is presented in Eq. 4.24.

$$\dot{x} = Ax + Bu + Hl \tag{4.24}$$

Therefore, we can inspect 4.23 and rearrange it to achieve the state-space format of our driveline example.

$$[\ddot{\Omega}_{wh}] = [-a_r/J_T]\dot{\Omega}_{wh} + [(i_{cl}i_{tr}i_{fd})/J_T]u + [-r_w h/J_T]l \tag{4.25}$$

Where the value of F_{ROAD} varies with the model chosen to represent the road resistances and a_r:

$$a_r = b_{gm}i_{cl}i_{tr}^2 i_{fd}^2 + b_{tr}i_{fd}^2 \tag{4.26}$$

Similarly, in the example considering the driveshaft as a flexible component, we use Eq. 4.18 and 4.22 to find the state-space format shown in 4.27.

$$\begin{bmatrix} \ddot{\Omega}_{tr} \\ \ddot{\Omega}_{wh} \\ \Delta\dot{\Omega}_{ds} \end{bmatrix} = \begin{bmatrix} -a_f/J_1 & c_{ds}/J_1 & k_{ds}/J_1 \\ c_{ds}/(J_2 i_{fd}) & -c_{ds}/J_2 & k_{ds}/J_2 \\ 1/i_{fd} & -1 & 0 \end{bmatrix} \cdot \begin{bmatrix} \dot{\Omega}_{tr} \\ \dot{\Omega}_{wh} \\ \Delta\Omega_{ds} \end{bmatrix} + \begin{bmatrix} (i_{cl}i_{tr}i_{fd})/J_1 \\ 0 \\ 0 \end{bmatrix} u + \begin{bmatrix} 0 \\ -r_w h/J_2 \\ 0 \end{bmatrix} l \tag{4.27}$$

Where the vectors u and l are the same of the rigid model and a_f is defined by:

$$a_f = b_{gm}i_{cl}i_{tr}^2 i_{fd} + b_{tr}i_{fd} + c_{ds}/i_{fd} \tag{4.28}$$

As for the output equation $y = Cx$, it will depend on the necessity. Any of the component's speeds can be found from the chosen state variable. The output matrix C will show the term needed to convert the state into a desired output. Those factors were found in Step 02, in the equations of speed of each component. Assuming the desired output of the model is the vehicle longitudinal speed V_{veh}, the C matrix is

shown in Eq. 4.29 and Eq. 4.30 for the rigid and the flexible generic driveline models, respectively.

$$y = v_{veh} = [r_{wh}] \cdot \dot{\Omega}_{wh} \tag{4.29}$$

$$y = v_{veh} = [r_{wh}] \times \begin{bmatrix} \dot{\Omega}_{tr} \\ \dot{\Omega}_{wh} \\ \Delta\Omega_{ds} \end{bmatrix} \tag{4.30}$$

Once the state space formulation is done, a controllability check is performed. A system is called controllable when the input is able to shift every state variable from an initial to a desired value Nise (2020). The first step to achieve satisfactory drivability is to assure that the driveline model is controllable. In other words, the torque inputs can drive the speed states to desired values. As explained in detail in Nise (2020), the system is controllable if the controllability matrix C_M is of rank k, where k is the order of the system. The matrix C_M is calculated using the formula in Eq. 4.31.

$$C_M = \begin{bmatrix} B & AB & A^2B & ... & A^{k-1}B \end{bmatrix} \tag{4.31}$$

Both previous examples are controllable systems as showed in Eq. 4.32 and Eq. 4.33. The rigid model being a system of first order ($k = 1$), and the flexible model being a system of third order ($k = 3$).

$$C_{Rigid} = \begin{bmatrix} B \end{bmatrix} = \begin{bmatrix} \frac{i_{cl} i_{itr} i_{fd}}{J_T} \end{bmatrix} \rightarrow rank(C_{Rigid}) = k = 1 \tag{4.32}$$

$$C_{Flex} = \begin{bmatrix} B & AB & A^2B \end{bmatrix} = \begin{bmatrix} \frac{i_{cl}i_{itr}i_{fd}}{J_1} & \frac{-a_f i_{cl}i_{itr}i_{fd}}{J_1^2} & \frac{i_{cl}i_{itr}i_{fd}(\frac{a_f^2}{J_1^2} - \frac{k_{ds}}{J_1 i_{fd}} + \frac{c_{ds}^2}{J_1 J_2 i_{fd}})}{J_1} \\ 0 & \frac{c_{ds}i_{cl}i_{tr}}{J_1 J_2} & \frac{-i_{cl}i_{itr}i_{fd}(\frac{a_f c_{ds}}{J_1 J_2 i_{fd}} + \frac{c_{ds}^2}{J_2^2 i_{fd}} - \frac{k_{ds}}{j_2 i_{fd}})}{J_1} \\ 0 & \frac{i_{cl}i_{tr}}{J_1} & \frac{-i_{cl}i_{itr}i_{fd}(\frac{a_f}{J_1 i_{fd}} + \frac{c_{ds}}{J_2 i_{fd}})}{J_1} \end{bmatrix}$$

$$\rightarrow rank(C_{Flex}) = k = 3 \tag{4.33}$$

Another use for a driveline model is for the design of observers. Observers (or estimators) are used to give the controllers access to state variables that cannot be easily measured by sensors. A system is called observable if every state in the state vector can be found from the knowledge of the input and a measurement of the output Nise (2020). Like in controllability, a matrix can be calculated to define if the system is observable. That matrix is called observability matrix O_M.

$$O_M = \begin{bmatrix} C & CA & CA^2 & ... & CA^{k-1} \end{bmatrix}^T \tag{4.34}$$

Let us assume we need to estimate the difference in the angular position $\Delta\Omega_{ds}$ caused by the flexible driveshaft in the flexible driveline example. Adding a sensor on the driveshaft to measure $\Delta\Omega_{ds}$ would be extremely difficult and costly. Nevertheless, if our model is observable, this state variable can be inferred from the measurement of another signal, defined as an output in the model.

In Eq. 4.30, vehicle speed was chosen as output since wheel speed sensors are usually present in vehicles, making it easier to measure vehicle longitudinal speed. The observability matrix check performed in Eq. 4.35 and 4.36 proves that every

state can be extracted from the measurement of the output and knowledge of the input for both rigid and flexible model, respectively.

$$O_{Rigid} = \begin{bmatrix} C \end{bmatrix} = \begin{bmatrix} r_{wh} \end{bmatrix}^T \rightarrow rank(O_{Rigid}) = k = 1 \tag{4.35}$$

$$O_M = \begin{bmatrix} C & CA & CA^2 \end{bmatrix}^T = \begin{bmatrix} 0 & r_w h & 0 \\ \frac{c_{ds} r_{wh}}{J_2 i_{fd}} & \frac{-c_{ds} r_{wh}}{J_2} & \frac{k_{ds} r_{wh}}{J_2} \\ -r_{wh}(\frac{c_{ds}^2}{J_2^2 i_{fd}} + \frac{a_f c_{ds}}{J_1 J_2 i_{fd}} - \frac{k_{ds}}{J_2 i_{fd}}) & -r_{wh}(\frac{c_{ds}^2}{J_2^2} - \frac{k_{ds}}{J_2} + \frac{c_{ds}^2}{J_1 J_2 i_{fd}}) & -r_{wh}(\frac{c_{ds} k_{ds}}{J_2^2} + \frac{c_{ds} k_{ds}}{J_1 J_2 i_{fd}}) \end{bmatrix}$$
$$\rightarrow rank(O_{Flex}) = k = 3 \tag{4.36}$$

Note that if the chosen output (sensor) is changed to transmission speed, generic mover speed, clutch speed, or propelling shaft speed, the result is the same and the system remains observable.

4.3.2 Electrified Driveline Models

Modelling hybrid powertrains shows a higher level of complexity, given the number of components and the presence of more than one propelling system. The next subsections present three models. The models are the most common topologies for hybrid powertrain applications: series hybrid, parallel hybrid, and split hybrid. The intention is to provide the reader with models that can be promptly used as well as exemplifying the results of the devised modelling method. State-of-the-art description

and classification of hybrid vehicles and topologies can be verified in Emadi (2014) and Liu (2017). For simplicity, the output of all models is considered to be vehicle's longitudinal speed as in the previous example. The consideration of each component's inertia and friction is arbitrary and should meet the desired level of accuracy of the component. Here, the inertia and friction of movers and transmission are included. Also included the inertia of the final drive and wheels. Finally, in all cases the vector l represents the same road load vector explained before.

The Electric Driveline Model

A BEV is a vehicle which all traction effort is provided by a motor and all of its power comes from an electric energy storage system (ESS). From the perspective of driveline modelling complexity, this topology is much similar to a conventional powertrain.

Here, the model shows a transmission system coupled to the motor, and then a final drive. Such configuration is not necessary given motor characteristic of high torque at low speeds but some studies have found a multi-gearshift transmission to contribute to better efficiency Machado *et al.* (2021). The step-by-step process to develop this model is depicted in the Appendix B. Equation 4.37 shows the final model in the state-space.

$$\ddot{\Omega}_{wh} = \left[-a_{BEV}/J_{BEV}\right] \times \left[\dot{\Omega}_{wh}\right] + \left[(i_{tr}i_{fd})/J_{BEV}\right] u + \left[-r_{wh}/J_{BEV}\right] l \qquad (4.37)$$

The expressions of J_{BEV}, a_{BEV}, and the vector u are also presented in the Appendix B.

The Range Extended Driveline Model

In simple terms, the range extended battery electric vehicle, often referred to as BEVx, or REx is an electric vehicle that counts on an auxiliary power unit (APU) to support it for a limited range once its SOC is fully depleted. The APU consists of a ICE coupled to a generator that has the sole function of charging battery (no propelling).

The BEVx category was created with the objective to leverage the zero emission vehicle (ZEV) credits of BEVs while creating momentum for fully electrified vehicles. The idea of an APU to sustain a minimum SOC level addresses known user complains against BEVs such as range anxiety and charging time.

The ICE is connected to a generator that charges the battery upon engine operation. The energy in the battery is used by a traction motor to propel the vehicle. Although optional, a transmission system can be added after the traction motor, and a final drive after that. The torque is then delivered to the wheels via driveshaft. The step-by-step process to develop this model is depicted in the Appendix B. Equation 4.38 shows the final model in the state-space.

$$\ddot{\Omega}_{wh} = \left[-a_{BEVx}/J_{BEVx}\right] \times \left[\dot{\Omega}_{wh}\right] + \left[(i_{tr}i_{fd})/J_{BEVx}\right] u + \left[-r_{wh}/J_{BEVx}\right] l \quad (4.38)$$

The expressions of J_{BEVx}, a_{BEVx}, and the vector u are also presented in the Appendix B. Note that the generator (gen) and the traction motor (mot) are not mechanically connected. Therefore, the BEVx does not differ much from a BEV regarding its propelling ability. It differs from a standard BEV only by its APU

($ice \rightarrow gen$). Since the objective is to model the dynamics of the vehicle given its propelling torque input, the presented model does not include the dynamic analysis of the APU. Nevertheless, the same method could be used to generate such model. Therefore, the range extended driveline model is very similar to the previous example.

The Comprehensive Hybrid Driveline Model

In a HEV, the position where the electric motor sits in the driveline defines the powertrain topology. Regarding parallel hybrid electric vehicles (PHEV), the following classification is used Liu (2017): P0 when the electric motor is attached directly to the engine as a starter, P1 when attached to the crank-shaft, P2 when connected between engine and gearbox, P3 when between gearbox and final drive, and finally P4 when linked directly to the wheels. The comprehensive hybrid driveline model accounts all possible parallel hybrid topologies (P0P1P2P3P4).

In addition, it allows the modeling of series hybrid electric vehicles (SHEVs) with a minor change in the diagram structure. In the SHEVs the power sources are in electrochemical series Emadi (2014). The SHEVs include some benefits of the PHEV such as the ability to split the torque request between ICE and traction motor, and also some benefits of the BEVx such as the charging of the battery via ICE and generator. To achieve a SHEV topology from the comprehensive hybrid driveline model, the user should place the em_2 block right after the clutch bock, without a juntion. The equation of the torque path from clutch to traction motor and then to transmission remains.

By including all possible configurations, it is easier to visualize how each motor addition affects the powertrain. Furthermore, this complete model is a great asset

since simpler topologies will be simplifications of the complete one. Equation 4.39 shows the final model achieved.

$$\ddot{\Omega}_{wh} = \left[-a_{HEV}/J_{HEV}\right] \times \left[\dot{\Omega}_{wh}\right] + \left[1/J_{HEV}\right] u + \left[-r_{wh}/J_{HEV}\right] l \tag{4.39}$$

The expressions of J_{HEV}, a_{HEV}, and the vector u are presented in the Appendix B together with the complete process of finding the model. The abbreviation em denotes each electric motor from positions 0 to 4. The term bl indicates the belt connecting em_0 to the ice. Belts can be modelled as final drives, with fixed conversion factors i_{bl}. The cs stands for the crankshaft, to which em_1 connects to the ice. Note that the model achieved is comprehensive. In practice, fewer electric machines might be applied. Common configurations are the P0P2, P1P2, and P1P4. Therefore, when modelling such topologies, the reader can simply edit the complete parallel hybrid driveline model, removing the propelling systems there are absent.

Finally, it is important to highlight the role of the clutch. By looking at the model, specially at the input vector u, we can see how the term i_{cl} functions. It switches between 0 and 1, respectively decoupling and coupling the engine and in consequence the other components above it.

The Split Hybrid Driveline Model

The third most common hybrid topology is the split-hybrid configuration, also called series-hybrid. In this configuration a combination of the two previous concepts is applied. The driveline has the means of running either in series or parallel-hybrid modes Emadi (2014). That is done to minimize the short-comings and maximize the

benefits of each type. A device commonly used to enable that split characteristic is the planetary gearbox, also called electronic continuously variable transmission (ECVT) when applied to electrified powertrains Liu (2017). The modelling process for the split-hybrid driveline model is depicted in the Appendix B. In Step 01 the diagram was built using separate blocks for each of the three gears in the ECVT – ring (r), sun (s), and carrier (c). The three blocks are connected in parallel in the diagram. Each of the gears is able to receive individual inputs and provide individual outputs. The torque balance in each gear, according to Newton's second law is:

$$M_{gear} = M_{gear_{in}} - M_{gear_{out}} - J_{gear}\ddot{\Omega}_{gear} - b_{gear}\dot{\Omega}_{gear} \tag{4.40}$$

The term M_{gear} is the torque transferred from a gear to the one it is connected in the planetary, i.e. $s \rightarrow$, $r \rightarrow c$, $c \rightarrow s$, and $c \rightarrow r$. The term $M_{gear_{in}}$ is the individual torque input from outside the planetary, $M_{gear_{out}}$ is the individual torque output, J_{gear} is the inertia, b_{gear} is the friction. The term Ω_{gear} is the angular position of that gear. If not needed, losses can be suppressed. Besides Eq. 4.40, the torques transferred in the ECVT should respect the following three relationships as detailed in Dagci (2018) so the planetary is balanced:

$$M_c + M_r + M_s = 0 \tag{4.41}$$

$$M_s = -\frac{1}{\gamma + 1} M_c = -i_{cs} M_c \tag{4.42}$$

$$M_r = -\frac{\gamma}{\gamma + 1} M_c = -i_{cs} M_c \tag{4.43}$$

Where γ is the number of teeth in the ring gear divided by the number of teeth of the sun gear. The ratio i_{cs} is the equivalent ratio from carrier to sun gear, and i_{cr} is the equivalent ratio from carrier to ring gear. The speed constraint is given by Eq. 4.44.

$$\dot{\Omega}_c = i_{cr}\dot{\Omega}_r + i_{cs}\dot{\Omega}_s \tag{4.44}$$

Equations 4.40 to 4.44 are used in the modelling of the split hybrid driveline as depicted in the Appendix B. For the diagram of the split hybrid model, the drive systems traction motor (mot), engine (ice), and generator are connected to the input ports of the ring, carrier, and sun gears, respectively. The propelling shaft is connected to the output of the ring gear. These connections are somewhat arbitrary. Some vehicles even present more than one planetary gear-set. The number of such gearboxes and their connections are engineering decisions that may account for packaging limitations, sizing optimization, fleet standardization, among others. In the example, two propelling modes are enabled: electric drive and parallel drive. Other modes such as alternator mode (engine provides power to the generator when the vehicle is stopped), and reverse drive are disregarded here. Since we have two propelling modes, we will need two dynamic models to represent that behaviour.

In electric drive, the engine is decoupled from the planetary via clutch and turned off. In this case the traction motor is responsible for propelling. The vehicle behaves as an EV and the model will be very similar to the generic driveline formulated in previous sections. The difference here will be the absence of the clutch and the multi gear transmission. Therefore, Eq. 4.45 – for the electric drive mode – is a simplification of the generic driveline model. Where the inertia factor is the sum:

$J_1 = J_w + mr_{wh}^2 + J_{mot}i_{fd}^2$ and $u = U_{mot}$.

$$\ddot{\Omega}_{wh} = \left[-b_{mot}i_{fd}^2/J_1\right] \times \left[\dot{\Omega}_{wh}\right] + \left[i_{fd}/J_1\right] u + \left[-r_{wh}/J_1\right] l \tag{4.45}$$

In parallel drive, the engine is turned on and connected to the planetary gear set, assisting it in the propelling effort. Therefore, we need to add the engine dynamics in the model. The vehicle behaves as a parallel hybrid with both propelling systems contributing to the torque at wheels. Surplus engine torque is used by the generator to charge the battery. The generator dynamics are not shown here but can easily be achieved by performing the same steps.

Note that for the current example, engine speed and traction motor speed are independent of each other. For that reason, it is possible to run the engine in higher or lower speeds compared to the speed of the traction motor. Nevertheless, there will always be a value β that converts engine speed into traction motor speed $\dot{\Omega}_{ice} = \beta\dot{\Omega}_{mot}$. This relationship is used to achieve the final model for this mode in terms of wheel speed. Equation 4.46 shows the result model.

$$\ddot{\Omega}_{wh} = \left[-a_{SH}/J_{SH}\right] \times \left[\dot{\Omega}_{wh}\right] + \left[i_{fd}/J_{SH}\right] u + \left[-r_{wh}/J_{SH}\right] l \tag{4.46}$$

4.4 Vehicle Dynamics

Vehicle dynamics is the channel in which driver and passengers perceive controllability, comfort, safety, and quality of ground vehicles. Besides, it also impacts vehicle performance and efficiency. Therefore, understanding and planning for appropriate vehicle dynamics is key when developing any vehicle system.

4.4.1 Coordinate System and Terminology

The vehicle coordinate system used here to describe vehicle dynamics follows the definitions of SAE Recommended Practice (2008), where the vehicle body is considered to have six degrees of freedom, three linear and three rotational as depicted in Fig. 4.5.

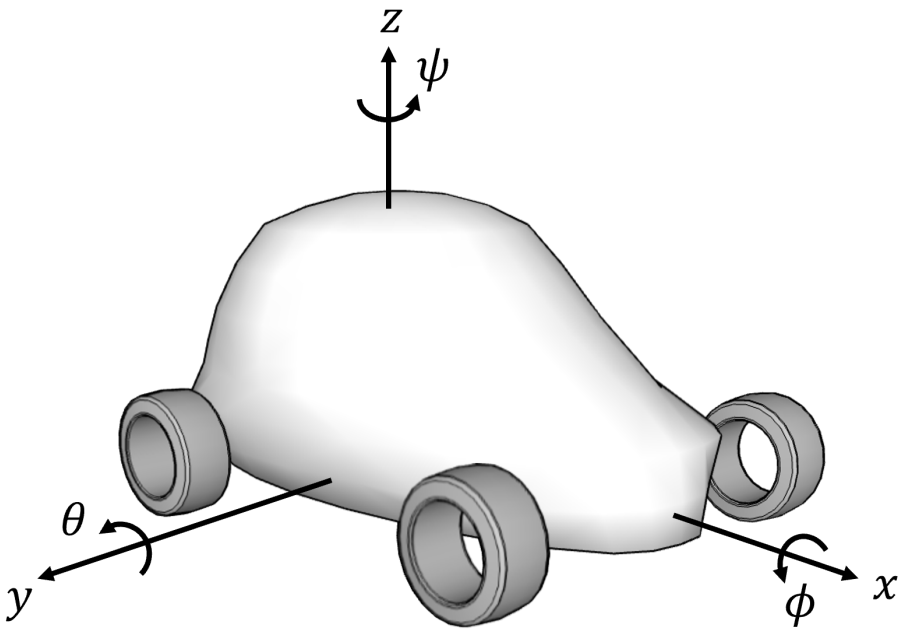

Figure 4.5: Vehicle dynamics coordinate system according to SAE Recommended Practice (2008).

Where:

- x defines the longitudinal axis with origin in the front axis
- y defines the lateral axis with origin in the mid-point of the front axis
- z defines the vertical axis with origin at in the front axis
- Φ defines the rotational motion on the x-axis, termed roll

- Θ defines the rotational motion on the y-axis, termed pitch
- Ψ defines the rotational motion on the z-axis, termed yaw

Other relevant terminology is explained as follows:

- Cues: Motion feedback from vehicle to driver
- Sprung mass: Body mass above the line of the suspension system
- Unsprung masses: Wheel house masses in each wheel below the line of the suspension system
- Wheelbase: Distance between the two axles
- Wheel track: Distance between two wheels in the same axle
- Wheel house: Inner space enclosed by the wheel

4.4.2 Vehicle Equations of Motion

Vehicle movements can be summarized in: acceleration, braking, cornering, and cruising. The dynamics of each movement are determined by the following factors: gravity, tire forces, driver action, resistances, geometry and compliances Gillespie (1992). Since gravity has effect on the equilibrium equations and the tire forces are a function of driver action, resistances, geometry and compliances Jazar (2017), one can assume that the vehicle dynamics model will be simply a function of the equilibrium and the tire equations.

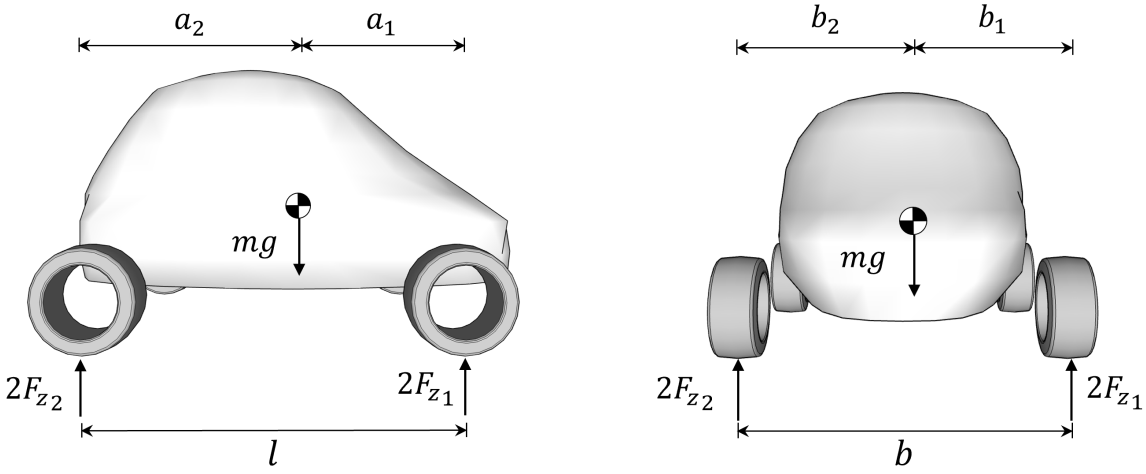

Figure 4.6: Forces acting on a four-wheel static vehicle on a flat surface.

Equilibrium Equations

Figure 4.6 exemplifies the forces acting on a static four-wheel vehicle on a flat surface,

Using Newton's second law to write the forces F on the z-axis (Eq. 4.47) and the momentum M on the x-axis (4.48), it is possible to define the longitudinal position a_1 of the centre of mass (4.49) given the wheelbase l.

$$\sum F_z = 0 \rightarrow 2F_{z_1} + 2F_{z_2} - mg = 0 \tag{4.47}$$

$$\sum M_y = 0 \rightarrow -2F_{z_1}a_1 + 2F_{z_2}a_2 = 0 \tag{4.48}$$

$$a_1 = \frac{2l}{mg}F_{z_2} = \frac{l}{mg}(mg - 2F_{z_1}) = l\left(1 - \frac{2F_{z_1}}{mg}\right) \tag{4.49}$$

Where m is vehicle mass and g is the acceleration of gravity.

Retrieving 4.48, and using Newton's second law to write the the momentum on

the y-axis (4.50, it is possible to define the lateral position b_1 of the centre of mass (4.51) given wheel track b.

$$\sum M_x = 0 \rightarrow -2F_{z_1}b_1 + 2F_{z_2}b_2 = 0 \tag{4.50}$$

$$b_1 = \frac{2b}{mg}F_{z_2} = \frac{b}{mg}(mg - 2F_{z_1}) = b\left(1 - \frac{2F_{z_1}}{mg}\right) \tag{4.51}$$

To determine the vertical position of the centre of mass h, it is necessary to analyze the mass distribution of the vehicle in a inclined surface as defined in Gillespie (1992) and depicted in Fig. 4.7.

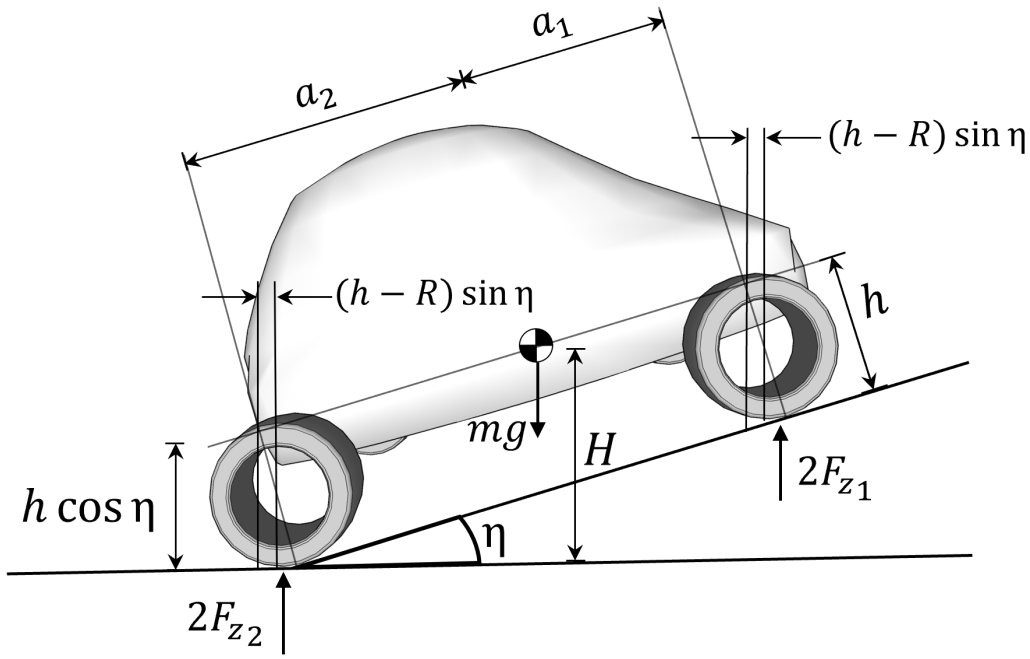

Figure 4.7: Forces acting on a four-wheel static vehicle on an inclined surface.

Where η is the inclination of the surface in degrees, H is the height of the centre of mass with reference to the flat ground, and R is the wheel radius.

The new force and momentum balance on z and x-axis are detailed in Eq. 4.54 and Eq. 4.53, respectively.

$$\sum F_z = 0 \rightarrow 2F_{z_1} + 2F_{z_2} - mg = 0 \tag{4.52}$$

$$\sum M_y = 0 \rightarrow -2F_{z_1}(a_1 \cos\eta + (h-R)\sin\eta) + 2F_{z_2}(a_2 \cos\eta + (h-R)\sin\eta = 0 \tag{4.53}$$

$$\sum h = R + \left(a_2 - \frac{2F_{z_1}}{mg} l\right) \cot\eta \tag{4.54}$$

Tire Equations

In essence, the reaction of the tires on the driving surface given driver inputs is what defines vehicle motion Gillespie (1992). Therefore, the vehicle dynamics model is directly linked to the tires dynamics. The following tire equations are written with the assistance of Jazar (2017) and Guiggiani (2014).

The tire coordinate system follows the same pattern of the vehicle's but with the origin set in the centre of each the tire. Figure 4.8 depict the forces acting on a front tire during cornering.

Tire longitudinal force $F_{x_{w_i}}$ is a function of the powertrain system as revised in Section 4.2, the brakes applied by the driver when braking, the normal force, and the road loads. The tire lateral force $F_{y_{w_i}}$ is a function of the sideslip coefficient C_α and the sideslip angle α and it has opposite signal to the vehicle lateral force (centrifugal force). The angle δ_i is the total steer angle, β_i is called the wheel sideslip angle, and

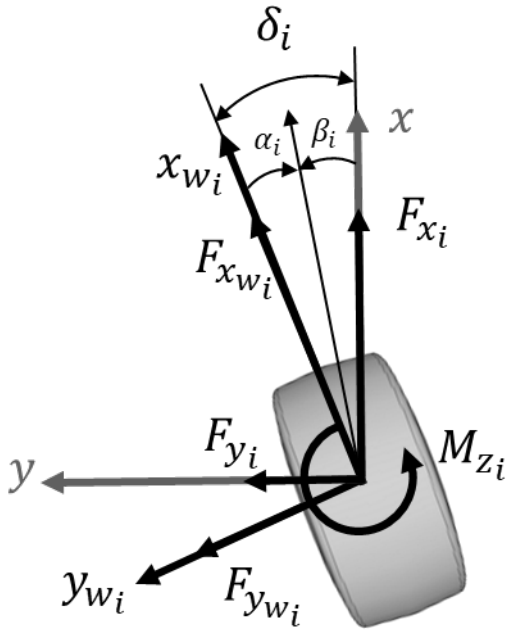

Figure 4.8: Forces acting on a front tire during cornering.

α_i is the tire sideslip angle. The steer moment M_{z_i} is about the tire z axis. The index i denotes which tire is being analyzed, it varies from 1 to 4 to denote front left, front right, rear left, and rear right, in that order.

Equations 4.55 to 4.60 denote the tire equations of motion from the tire coordinate system to the vehicle coordinate system.

$$F_{x_i} = F_{x_{w_i}} \cos\delta_i - F_{y_{w_i}} \sin\delta_i \tag{4.55}$$

$$F_{y_i} = F_{y_{w_i}} \cos\delta_i + F_{x_{w_i}} \sin\delta_i \tag{4.56}$$

$$F_{z_i} = m_{w_i} g \tag{4.57}$$

$$M_{x_i} = M_{x_{w_i}} \tag{4.58}$$

$$M_{y_i} = M_{y_{w_i}} \tag{4.59}$$

$$M_{z_i} = M_{z_{w_i}} \tag{4.60}$$

Weight Transfer

When the vehicle accelerates, weight is transfered from the front axle to the rear axle. Likewise, when the vehicle brakes weight is transfered from rear to front. That changes the normal forces on each axle (F_{z_1} and F_{z_2}) as showed in Eq. 4.61, given the cases of Eq. 4.62.

$$\begin{cases} F_{z_1} = \frac{1}{2}mg\frac{a_2}{l} - \frac{1}{2}m\ddot{x}\frac{h}{l} \\ F_{z_2} = \frac{1}{2}mg\frac{a_2}{l} + \frac{1}{2}m\ddot{x}\frac{h}{l} \end{cases} \tag{4.61}$$

Where:

$$\begin{cases} \ddot{x} \leq 0 \Rightarrow F_{z_1} \uparrow \text{and} F_{z_2} \downarrow \text{(braking)} \\ \ddot{x} \geq 0 \Rightarrow F_{z_1} \downarrow \text{and} F_{z_2} \uparrow \text{(propelling)} \\ \ddot{x} = 0 \Rightarrow F_{z_1} - \text{and} F_{z_2} - \text{(constant speed)} \end{cases} \tag{4.62}$$

Equations of Motion

The forces and momenta on a rigid vehicle will be the sum of forces and momenta at the tires on the vehicle coordinate system. Equations 4.63 to 4.68 denote the respective rigid vehicle body motion, assuming small steering angles. The left superscript on a vector denotes the coordinate frame in which the vector is expressed, the left subscript on a vector denotes the coordinate frame in which it is measured, and he right subscript indicates the coordinate frame that the vector is referred to. Here B is used for for body, G for ground coordinate frame.

$$ {}^{B}F_x = \sum F_{x_i} = \sum F_{x_{w_i}} \cos\delta_i - \sum F_{y_{w_i}} \sin\delta_i \tag{4.63} $$

$$ {}^{B}F_y = \sum F_{y_i} = \sum F_{y_{w_i}} \cos\delta_i + \sum F_{x_{w_i}} \sin\delta_i \tag{4.64} $$

$$ {}^{B}F_z = \sum F_{z_i} = \sum m_{w_i} g \tag{4.65} $$

$$ {}^{B}M_x = \sum M_{x_i} + \sum y_i F_{z_i} - \sum z_i F_{y_i} \tag{4.66} $$

$$ {}^{B}M_y = \sum M_{y_i} + \sum z_i F_{x_i} - \sum x_i F_{z_i} \tag{4.67} $$

$$ {}^{B}M_z = \sum M_{z_i} + \sum x_i F_{y_i} - \sum y_i F_{x_i} \tag{4.68} $$

The equations of motion of the vehicle in the body coordinate system are written

using Newton-Euler approach as depicted by Eq. 4.69.

$$\begin{cases} {}^{B}F = m \cdot {}^{B}\dot{\nu}_B + m \cdot {}^{B}_{G}\omega_B \times {}^{B}\nu_B \\ {}^{B}M = {}^{B}I \cdot {}^{B}_{G}\dot{\omega}_B + {}^{B}_{G}\omega_B \times ({}^{B}I \cdot {}^{B}_{G}\omega_B) \end{cases} \tag{4.69}$$

Where:

$${}^{B}F = \begin{bmatrix} F_x & F_y & F_z \end{bmatrix}^T \tag{4.70}$$

$${}^{B}M = \begin{bmatrix} M_x & M_y & M_z \end{bmatrix}^T \tag{4.71}$$

$${}^{B}\nu = \begin{bmatrix} \dot{x} & \dot{y} & \dot{z} \end{bmatrix}^T \tag{4.72}$$

$${}^{B}_{G}\omega_B = \begin{bmatrix} \dot{\phi} & \dot{\theta} & \dot{\psi} \end{bmatrix}^T \tag{4.73}$$

Therefore, the system in Eq. 4.69 can be rewritten as the two following generic equations of motion for a ground vehicle:

$${}^{B}F = m \cdot \begin{bmatrix} \ddot{x} \\ \ddot{y} \\ \ddot{z} \end{bmatrix} + m \cdot \begin{bmatrix} \dot{\phi} \\ \dot{\theta} \\ \dot{\psi} \end{bmatrix} \times \begin{bmatrix} \dot{x} \\ \dot{y} \\ \dot{z} \end{bmatrix} = \begin{bmatrix} m\ddot{x} - m(\dot{\psi}\dot{y} - \dot{\theta}\dot{z}) \\ m\ddot{y} + m(\dot{\psi}\dot{x} - \dot{\phi}\dot{z}) \\ m\ddot{z} + m(\dot{\phi}\dot{y} - \dot{\theta}\dot{x}) \end{bmatrix} \tag{4.74}$$

$$
{}^{B}M = \begin{bmatrix} I_{xx} & 0 & 0 \\ 0 & I_{yy} & 0 \\ 0 & 0 & I_{zz} \end{bmatrix} \cdot \begin{bmatrix} \ddot{\phi} \\ \ddot{\theta} \\ \ddot{\psi} \end{bmatrix} + \begin{bmatrix} \dot{\phi} \\ \dot{\theta} \\ \dot{\psi} \end{bmatrix} \times \begin{bmatrix} I_{xx} & 0 & 0 \\ 0 & I_{yy} & 0 \\ 0 & 0 & I_{zz} \end{bmatrix} \cdot \begin{bmatrix} \ddot{\phi} \\ \ddot{\theta} \\ \ddot{\psi} \end{bmatrix} = \begin{bmatrix} I_{xx}\ddot{\phi} - (I_{yy} - I_{zz})\dot{\theta}\dot{\psi} \\ I_{yy}\ddot{\theta} - (I_{zz} - I_{xx})\dot{\psi}\dot{\phi} \\ I_{zz}\ddot{\psi} - (I_{xx} - I_{yy})\dot{\phi}\dot{\theta} \end{bmatrix} \tag{4.75}
$$

Equations 4.74 and 4.75 are used in the following sections as a template for creating the appropriate models that will capture and predict vehicle motion for the autonomous driving system.

4.4.3 Longitudinal Model

A linear model is a one-dimensional vehicle dynamics model that aims to reproduce the motion of the vehicle on a single axis. This type of modelling is especially useful for describing the longitudinal dynamics and capturing part of vehicle's drivability. Given that the objective of this work is to develop a framework for integrating energy management and autonomous driving systems, it is of key importance to create a model that emulates vehicle reaction during propelling and braking.

In summary, the model accounts for the linear motion on the x-axis. That results in the following assumptions:

- Vehicle is rigid.
- Vehicle moves longitudinally: $\ddot{x} \neq 0$
- Vehicle **does not** move laterally: $\ddot{y} = 0$ and $\ddot{p}si = 0$
- Vehicle **does not** move vertically: $\ddot{z} = 0$

- Vehicle **does not** roll: $\ddot{\psi} = 0$
- Vehicle **does not** pitch/dive: $\ddot{\theta} = 0$

Applying the previous assumptions to the vehicle equations of motion, Eq.s 4.74 and 4.75:

$$ {}^{B}F = m \cdot \begin{bmatrix} \ddot{x} \\ 0 \\ 0 \end{bmatrix} + m \cdot \begin{bmatrix} 0 \\ 0 \\ 0 \end{bmatrix} \times \begin{bmatrix} \dot{x} \\ 0 \\ 0 \end{bmatrix} = \begin{bmatrix} m\ddot{x} \\ 0 \\ 0 \end{bmatrix} \tag{4.76} $$

$$ {}^{B}M = \begin{bmatrix} I_{xx} & 0 & 0 \\ 0 & I_{yy} & 0 \\ 0 & 0 & I_{zz} \end{bmatrix} \cdot \begin{bmatrix} 0 \\ 0 \\ 0 \end{bmatrix} + \begin{bmatrix} 0 \\ 0 \\ 0 \end{bmatrix} \times \begin{bmatrix} I_{xx} & 0 & 0 \\ 0 & I_{yy} & 0 \\ 0 & 0 & I_{zz} \end{bmatrix} \cdot \begin{bmatrix} 0 \\ 0 \\ 0 \end{bmatrix} = \begin{bmatrix} 0 \\ 0 \\ 0 \end{bmatrix} \tag{4.77} $$

Figure 4.9 shows the relevant forces acting on a rigid propelling vehicle.

The total longitudinal force F_x in the model is the sum of the longitudinal forces on the front F_{x_1} and rear axle F_{x_2} minus the road loads. The road loads are the rolling resistance F_{roll}, drag resistance F_{drag}, and the resistance due to road inclination (grade) F_{grade}.

$$ \sum F_x = m\ddot{x} = 2F_{x_1} + 2F_{x_2} - F_{roll} - F_{drag} - F_{grade} \tag{4.78} $$

Using Eq. 4.78 in 4.76, and isolating for $\ddot{x}$, the longitudinal model becomes:

$$ \ddot{x} = \frac{1}{m}(F_x - F_{roll} - F_{drag} - F_{grade}) \tag{4.79} $$

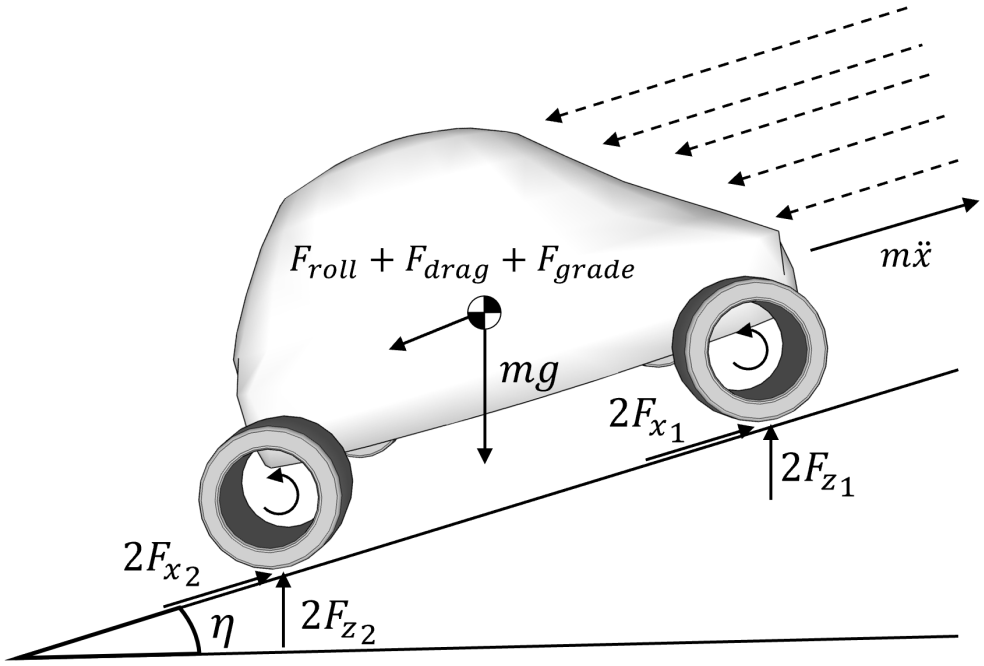

Figure 4.9: Forces acting on a propelling vehicle.

Where F_x is a function of the powertrain system (pwt) if the vehicle is propelling ($\ddot{x} > 0$), or a function of the braking system (brk) if the vehicle is braking $\ddot{x} \leq 0$:

$$\begin{aligned} F_x &= f(pwt), \ddot{x} \geq 0 \\ F_x &= f(brk), \ddot{x} < 0 \end{aligned} \tag{4.80}$$

The final equation of motion 4.80 highlights the 1-DOF characteristic of the longitudinal model.

The Eq. 4.79 is used in this work for calculating the longitudinal impact of the powertrain outputs provided by the energy management systems studied.

Rolling Resistance

Rolling resistance is caused by tire deformation when loaded. It is a function of tractive effort, temperature, wear, construction, pressure, velocity, and surface Gillespie (1992). Here, the standard model Eriksson and Nielsen (2014) is used.

$$F_{roll} = (f_0 + \dot{x} f_s) \cdot mg\cos(\eta) \tag{4.81}$$

Where f_0 and f_s are the velocity-independent and velocity-dependent rolling resistance coefficients, respectively.

Drag Resistance

Drag resistance is a function of frontal area, air density, and wind speed Eriksson and Nielsen (2014). Equation 4.82 shows this relationship.

$$F_{drag} = \frac{1}{2} \cdot C_d (v_{veh} - v_{env})^2 \tag{4.82}$$

Where C_d is the lumped drag resistance coefficient.

Grade Resistance

The grade resistance is the component of the weight in an inclined surface. Equation 4.83 shows its calculation.

$$F_{grade} = mg\sin\eta \tag{4.83}$$

Where η is the inclination of the road.

4.4.4 Planar Model

A planar model is a two-dimensional vehicle dynamics model that aims to reproduce the motion of the vehicle on the longitudinal and lateral axles. This type of modelling is especially useful for describing the cornering dynamics and capturing part of vehicle's handling.

In summary, the model accounts for the planar motion on the x and y-axis. That results in the following assumptions:

- Vehicle is rigid.
- Vehicle moves longitudinally: $\ddot{x} \neq 0$
- Vehicle moves laterally: $\ddot{y} \neq 0$ and $\ddot{psi} \neq 0$
- Vehicle **does not** move vertically: $\ddot{z} = 0$
- Vehicle **does not** roll: $\ddot{\psi} = 0$
- Vehicle **does not** pitch/dive: $\ddot{\theta} = 0$

Applying the previous assumptions to the vehicle equations of motion, Eq.s 4.74 and 4.75:

$$
{}^{B}F = m \cdot \begin{bmatrix} \ddot{x} \\ \ddot{y} \\ 0 \end{bmatrix} + m \cdot \begin{bmatrix} 0 \\ 0 \\ \dot{psi} \end{bmatrix} \times \begin{bmatrix} \dot{x} \\ \dot{y} \\ 0 \end{bmatrix} = \begin{bmatrix} m\ddot{x} - m\dot{\psi}\dot{y} \\ m\ddot{x} + m\dot{\psi}\dot{x} \\ 0 \end{bmatrix} \tag{4.84}
$$

$$
{}^{B}M = \begin{bmatrix} I_{xx} & 0 & 0 \\ 0 & I_{yy} & 0 \\ 0 & 0 & I_{zz} \end{bmatrix} \cdot \begin{bmatrix} 0 \\ 0 \\ \ddot{p}si \end{bmatrix} + \begin{bmatrix} 0 \\ 0 \\ \ddot{p}si \end{bmatrix} \times \begin{bmatrix} I_{xx} & 0 & 0 \\ 0 & I_{yy} & 0 \\ 0 & 0 & I_{zz} \end{bmatrix} \cdot \begin{bmatrix} 0 \\ 0 \\ \ddot{p}si \end{bmatrix} = \begin{bmatrix} 0 \\ 0 \\ I_{zz}\ddot{p}si \end{bmatrix} \tag{4.85}
$$

Figure 4.10 shows the relevant forces acting on a rigid vehicle during cornering.

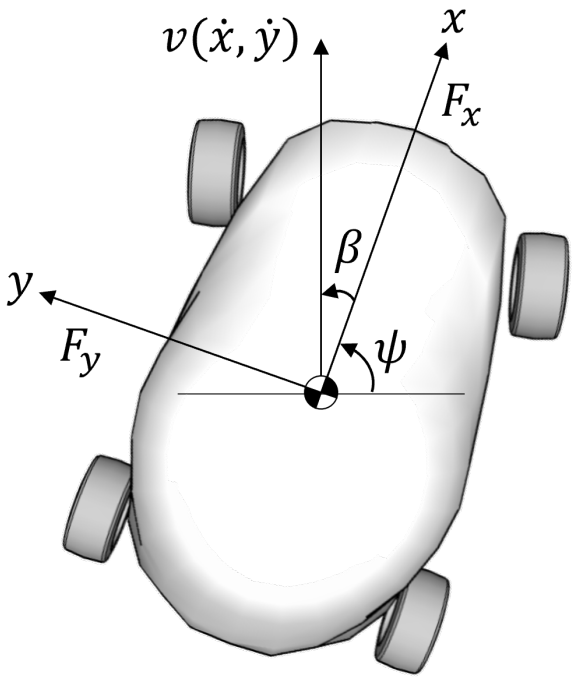

Figure 4.10: Forces acting on a vehicle during cornering.

From Eq. 4.84 and Eq. 4.85 it is possible to derive the combined forces and momentum of the vehicle during cornering:

$$
\sum F_x = m\ddot{x} = F_x + m\dot{\psi}\dot{y} \tag{4.86}
$$

$$\sum F_y = m\ddot{y} = F_y + m\dot{\psi}\dot{x} \tag{4.87}$$

$$\sum M_z = I_z\ddot{\psi} \tag{4.88}$$

Isolating for $\ddot{x}$, $\ddot{y}$, and $\ddot{\psi}$:

$$\ddot{x} = \frac{1}{m}F_x + \dot{\psi}\dot{y} \tag{4.89}$$

$$\ddot{y} = \frac{1}{m}F_y + \dot{\psi}\dot{x} \tag{4.90}$$

$$\ddot{\psi} = \frac{1}{I_{zz}}M_z \tag{4.91}$$

In this form, the equations of motion are not much useful as they depend on the knowledge of the F_x, F_y, and M_z. Longitudinal force F_x is a function of the powertrain/braking system as reviewed previously. Lateral force F_y and yaw momentum M_z are a function of steer angle, vehicle velocity and cornering coefficients. Ideally, the model should be built assuming steer angle δ as input. In that way, it is possible to predict vehicle reaction given driver action.

To deduce the equations of motion as mentioned it is necessary to make a few geometric assumptions about the vehicle during cornering. First, assuming steady-state cornering, the vehicle is simplified as a "bicycle" model as detailed in Gillespie (1992). Figure 4.11 illustrates the model simplification and shows the geometric angles during cornering.

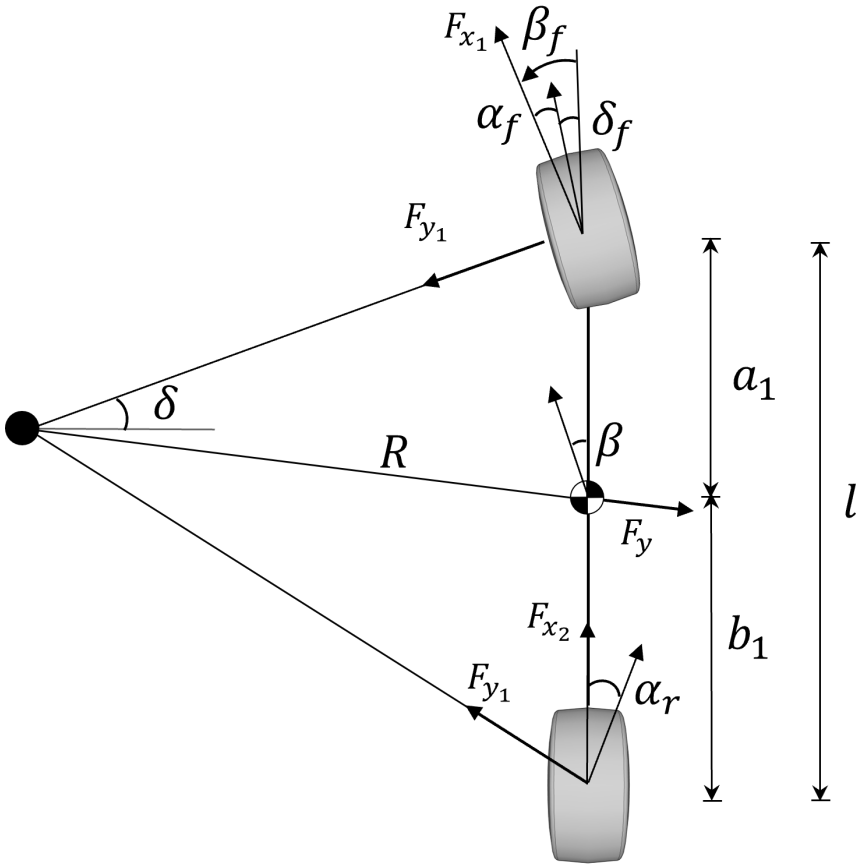

Figure 4.11: Vehicle model simplification into the "bicycle" model.

Where α is the sideslip angle, β is the steer angle, and R is the radius of the turn. Following the model simplification, the assumptions:

- Two-wheel model.
- Front-wheel steering.
- No aligning moments.
- Small steering angles.

Then, the following set of equations can be written:

$$F_x = F_{x_1} + F_{x_2} \tag{4.92}$$

$$F_y = F_{y_1} + F_{y_2} \tag{4.93}$$

$$M_z = a_1 F_{y_1} - a_2 F_{y_2} \tag{4.94}$$

Figure 4.12 is adapted from Jazar (2017). It shows that the lateral force at each wheel can be described as a function of the sideslip angles α and the cornering stiffness C_α at that wheel. The cornering stiffness is a function of the tire size, material, pressure, width, and load. The cornering stiffness is further investigated in section 4.4.2

Using the new assumptions in Eqs. 4.93 and 4.94:

$$F_y = -C_{\alpha_1}\left(\beta + \frac{a_1\dot{\psi}}{\dot{x}} - \delta\right) - C_{\alpha_2}\left(\beta + \frac{a_2\dot{\psi}}{\dot{x}} - \delta\right) \tag{4.95}$$

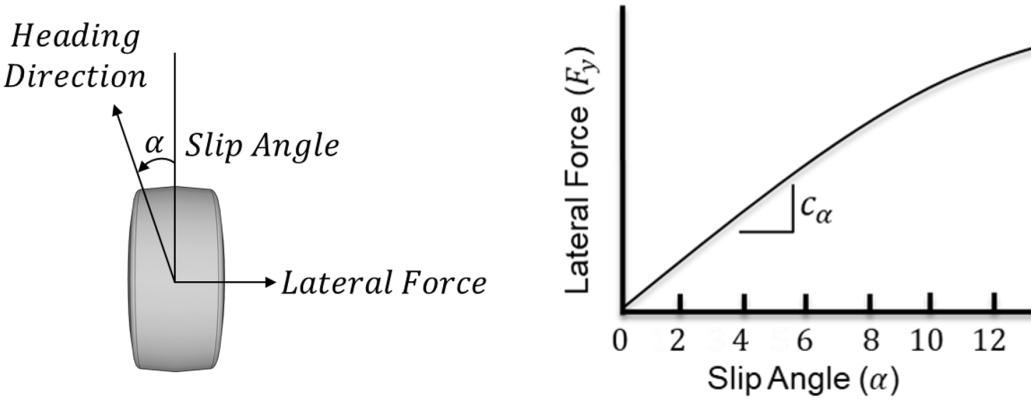

Figure 4.12: Illustrative cornering stiffness in a tire

$$M_z = a_1 C_{\alpha_1}\left(\beta + \frac{a_1\dot{\psi}}{\dot{x}} - \delta\right) - a_2 C_{\alpha_2}\left(\beta + \frac{a_2\dot{\psi}}{\dot{x}} - \delta\right) \tag{4.96}$$

Using Eq. 4.95 and 4.96 in 4.90 and 4.91, respectivelly, and retrieving Eq. 4.79 for the longitudinal dynamics, the planar model is completed:

$$\ddot{x} = \frac{1}{m}(F_x - F_{roll} - F_{drag} - F_{grade}) \tag{4.97}$$

$$\begin{bmatrix} \ddot{y} \\ \ddot{\psi} \end{bmatrix} = \begin{bmatrix} -\dfrac{C_{\alpha_1} + C_{\alpha_2}}{m\dot{x}} & \dfrac{-a_1 C_{\alpha_1} + a_2 C_{\alpha_2}}{m\dot{x}} \\ -\dfrac{a_1 C_{\alpha_1} - a_2 C_{\alpha_2}}{I_{zz}\dot{x}} & -\dfrac{a_1^2 C_{\alpha_1} + a_2^2 C_{\alpha_2}}{I_{zz}\dot{x}} \end{bmatrix} \cdot \begin{bmatrix} \dot{y} \\ \dot{\psi} \end{bmatrix} + \begin{bmatrix} \dfrac{C_{\alpha_1}}{m} \\ \dfrac{a_1 C_{\alpha_1}}{I_{zz}} \end{bmatrix} \delta \tag{4.98}$$

Where F_x is denoted by Eq. 4.80 as in the longitudinal model.

The expressions of J_{SH}, a_{SH}, and the vector u are presented in the Appendix B. The value of β can be constant or vary given vehicles conditions. It is usually defined by external optimization controllers that regulate the torque required in the engine to manage the desired battery's state of charge. For the special case where engine

and traction motor speeds are equal ($\beta = 1$), the parallel drive mode is also called direct drive and ring, sun, and carrier rotate with the same speed.

4.5 Summary

This chapter presented various modelling techniques that will be used in this thesis.

Regarding system modelling, a forward approach is used for running real-time experiments of drivability and performance while a backward approach is chosen for running the powertrain in the loop when assessing consumption.

Within the powertrain system, the components are modelled using quasi-static approach. It is chosen for its simplicity and real-time capability.

This chapter also presented a method for modelling the kinematics of drivelines. The method aids the creation of diagrams and torque flow equations that give insightful information about the topologies, especially electrified ones. Different driveline model templates are presented using the method. The examples fill the lack there is in literature for modelling of electrified drivelines.

Vehicle dynamics modelling is also discussed. It is observed as a product of the analysis of the tire forces during propelling, braking, and cornering. Depending on application, a longitudinal model or a planar model can be applied. The former being preferred for performance and drivability while the latter for handling and stability. In this thesis, the longitudinal model is used in several occasions, examples are in the estimation of road-load coefficients and in the calculation of the energy recuperation during regenerative braking which is performed in the EMS.

Chapter 5

Energy Management System

5.1 Introduction

As detailed in Bilgin *et al.* (2015), electrification stands as the ultimate solution for the attenuation of pollutants emissions associated with transportation. Furthermore, by combining different movers, engineers can take advantage of the different benefits each one of the systems provide and mitigate their short comings Emadi (2014), hence the increasing use of pHEV. Nevertheless, such complex systems require advanced control strategies. The controllers of pHEVs are usually responsible for defining engine start and stop, torque requested from each mover, and gear shift at each instant.

In this chapter, a novel optimization method is presented. It is devised so it provides a cost-effective solution that runs in real-time with the other vehicle modules, and fits the purpose of integrating EMS to an autonomous driving feature.

The chapter leverages models developed in the previous chapters to assess the fuel consumption of the novel algorithm. Appropriate benchmark algorithms are also built as to compare the performance of the present method. Finally, insight on the

benefits and limitations are discussed.

5.2 Range Extended Battery Electric Vehicle

In this study the application of a range extender in the previously validated BEV is investigated. The BEVx topology and driveline model are detailed in Chapter 04.

5.2.1 Auxiliary Power Unit

To create the BEVx model, an APU is added to the BEV model. The APU is composed of an engine and a generator. In the proposed topology, the APU is mechanically decoupled from the wheels, so it is still the traction motor responsibility to propel the vehicle. That strategy is used by manufacturers to keep the classification of the vehicle in some locations as electric and maximize governmental credits. The parameters used in the APU model are listed in the Appendix C.

The following details the two components of the APU.

Internal Combustion Engine

The ICE used in this study is a 1.0 litre engine provided with VI-CarRealTime. Figure 5.1 shows the brake-specific fuel consumption (BSFC) map and the max torque-speed curve.

From the previous maps, it is possible to calculate the engine efficiency as a function of speed and torque requested from the engine. First, Eq. 5.1 shows the conversion from mean effective pressure to engine torque T_{ice}. Then, Eq. 5.2 shows how to compute efficiency η_{ice} from the BSFC map.

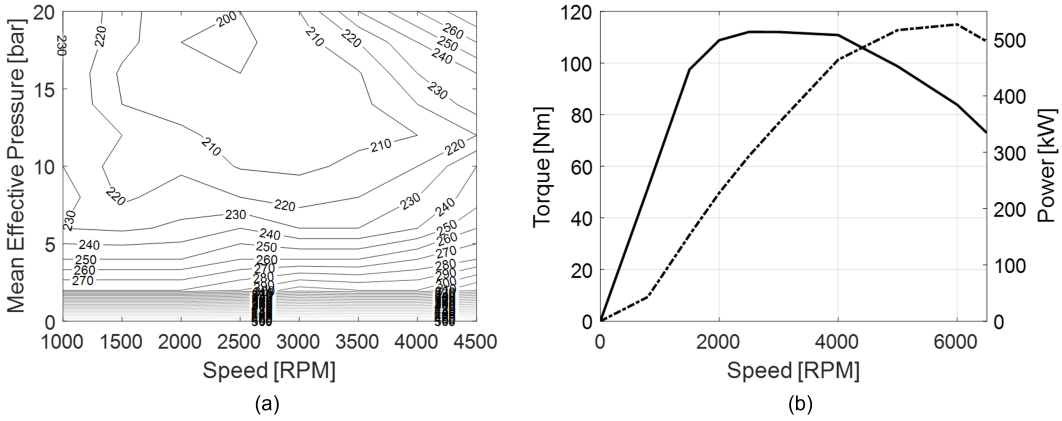

Figure 5.1: BSFC map in g/kWh as a function of the mean effective pressure and speed (a) and max torque/power curve (b) of the 1.0 L engine.

$$T_{ice} = \frac{N \cdot V \cdot P_{ME} \cdot 10^5}{2\pi \cdot S} \tag{5.1}$$

$$\eta_{ice} = 1/BSFC \cdot Q_{LHV} \tag{5.2}$$

Where T_{ice} is engine torque in N/m, W_{ice} is engine speed in rev/s, N is the number of cylinders in the engine, V is cylinder displacement in m^3, P_{ME} is the vector of the mean effective pressure values in the BSFC map, S is the number of revolutions per stroke, and Q_{LHV} is the fuel lower heat value in kWh/g. The BSFC values are in g/kWh.

The results are plotted on Fig. 5.2

Finally, 5.3 shows the computation of fuel rate $\dot{m}_f$ from the BSFC map.

$$\dot{m}_f = BSFC \cdot \frac{T_{ice} \cdot W_{ice}}{3600 \cdot 10^3} \tag{5.3}$$

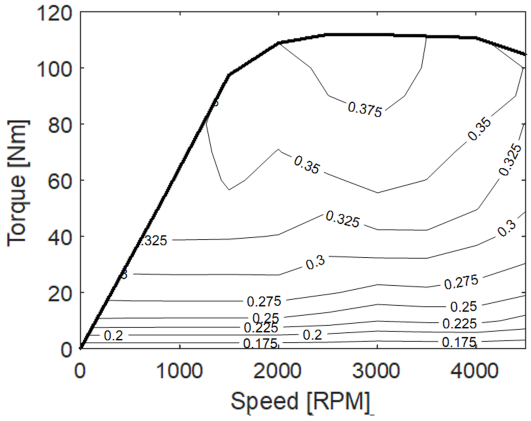

Figure 5.2: Efficiency map of the 1.0 L engine as a function of torque and speed.

Then, a search algorithm defines the maximum efficiency torque path for the engine speed vector. Figure 5.3 shows the results.

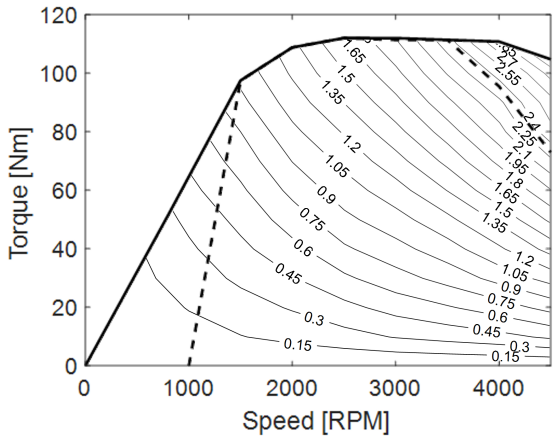

Figure 5.3: Fuel rate map in g/s within the max torque-speed curve (black solid line) and max efficient torque path (black dashed line).

The max efficient torque path is key for achieving fuel efficiency in the following algorithms.

Generator

The generator in the APU is responsible for converting fuel into electric energy. To do so, it is coupled to the engine through a transmission mechanism, as defined in the series hybrid driveline model.

Here, the Remy HVH-250-115-DOM motor is used as an example of generator. This type of motor is suitable for this application since it is scalable, available in housings, cartridges, or as stator/rotor assemblies. Figure 5.4 shows the efficiency map withing the continuous torque-speed curve at operational voltage.

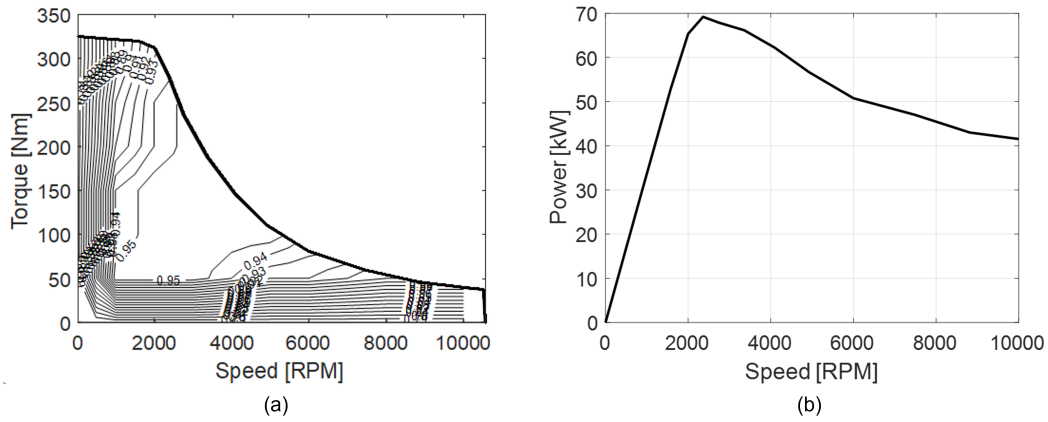

Figure 5.4: Generator efficiency map and continuous torque and power curves.

Centre of Gravity

Adding the APU to the BEV adds mass to sprung mass of the vehicle. That should be incorporated in the BEVx model as well as the update on the centre of gravity (CG). Assuming the APU will be packaged in the engine bay, the CG is dislocated toward the front of the vehicle. The new longitudinal position of the CG is 637 mm respective to the front axle as shown in Fig. 5.5.

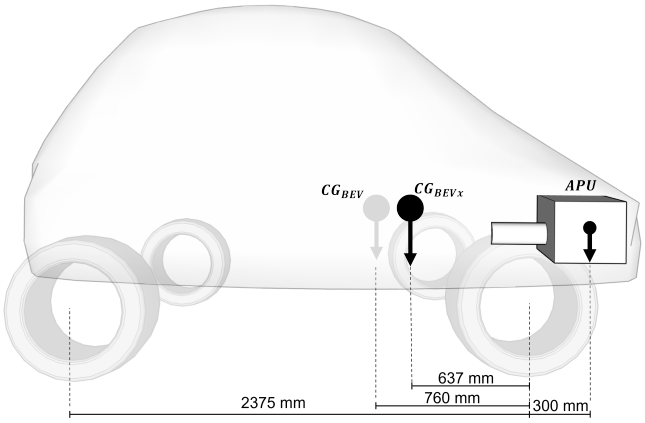

Figure 5.5: Centre of gravity update for the added mass of the APU.

The change in the longitudinal position of the CG is expected to have an influence on the performance of the vehicle under different conditions such as gradeability. Such impacts are evaluated in section 5.5.4. The vertical position of the CG (CG height) is considered to remain.

5.2.2 Functionality and Requirements

The following assumptions are included for the functionality of the APU:

- APU is mechanically decoupled from wheels
- When engine is off, it can only start to its idle speed (1000 RPM)
- No torque is provided for speeds below and equal to the idle speed
- Generator and engine are coupled with a constant ratio

As mentioned, engine speed is a great candidate for control variable. That is because in a BEVx configuration, the ICE is mechanically decoupled from the wheels.

That allows for running the engine on its most efficient torque path. In addition, generator is driven by engine, therefore it's torque is also a function of engine speed. As a consequence, the control problem becomes when to turn the engine on for charging, and which speed to drive it.

In addition, for a vehicle to be considered a BEVx and leverage full BEV credits it needs to comply with the following operation specifications. That should guide the design of the APU's functionality.

1. Super ultra low emission vehicle and zero evaporative emissions compliant on the battery system
2. Engine operation must not occur while SOC is above lower limit
3. Electric range must be equal to or greater than 80 miles
4. The APU range must not be greater than the electric provided range

Since the BEVx is built based on an homologated BEV with enourmous electric capability, it is assumed that requirement #01 is fulfilled.

To accommodate variations in the battery control without breaching the previously defined SOC safety limit, maximize electric range, and be compatible with benchmark vehicles, the level of SOC at which the charge sustaining operation starts is set to 6.5 %. Once the target SOC is set, the EMS should only start the engine for SOC levels below that target. That functionality settles requirement #02.

For requirements #03 and #04, the electric range in charge depleting mode must be verified and the range in charge sustaining operation must be bounded accordingly. That means defining the final size of the battery and the fuel tank, respectively. The

importance of designing an EMS is to provide a charge sustaining operation that minimizes the use of fuel, thus maximizing the MPG in that mode. Next section introduces the novel EMS developed in this research that should be an appropriate candidate algorithm to perform the energy management.

5.3 Regen-based Equivalent Consumption Minimization Strategy

Considering a pHEV, the requirements for the controller usually are: to request torque from the movers so the torque demanded is provided, to achieve fuel efficiency by splitting the torque between different energy sources, and to track battery's SOC so the vehicle sustain a minimum predefined level of energy by the end of the mission. The last requirement is commonly referred to as charge sustaining requirement.

This section presents a novel EMS built to leverage electrification capabilities such as regenerative braking and a model of the vehicle dynamics. The regen-based equivalent consumption minimization strategy (R-ECMS) introduces a new formulation of the energy consumption and adds a new parameter to its cost function, adding a new dimension to the problem but also new functionalities to the algorithm. Next section explains the theory of the R-ECMS in detail and next sections explore an application for that method.

5.3.1 Theory

Recalling a generic ECMS algorithm, the power split between movers is defined at each time-step by minimizing a cost function that computes the equivalent fuel consumption as presented in Eq. 5.12. The algorithm uses discretization of control inputs, therefore its output is not continuous.

$$\dot{m}_{eq}(U) = \dot{m}_f(U) + \dot{m}_b(U) \tag{5.4}$$

Where $\dot{m}_f$ is the fuel cost from the engine and $\dot{m}_b$ is the battery equivalent fuel cost, both associated with the control matrix U. Battery equivalent fuel cost is calculated as in Eq. 5.5.

$$\dot{m}_b = \frac{s}{Q_{LHV}} \cdot P_{batt}(U) \cdot p(SOC) \tag{5.5}$$

Where s is the equivalence factor, Q_{LHV} is the fuel's lower heat value, P_{batt} is the instantaneous battery power as a function of the control action, and p is a correction term as a function of SOC.

The equivalence factor converts electric energy into fuel mass. Often, two different values can be applied whether the vehicle is in charge or discharge operation - $s_{ch/dis}$, respectively. The correction term p is implemented so it penalizes the use of battery if SOC is under a threshold and stimulates the use of battery for SOC above a stipulated value.

Equation 5.5 shows that all electric power used is converted into fuel consumption. That implies that all energy coming out of the battery will be replenished through the engine. That disregards the fact that when the vehicle brakes, regenerative braking

contribute to charging the battery.

Therefore, if the regen is factored in, the accuracy of the actual fuel cost is enhanced. Besides, it would alleviate some of the equivalent cost of electric usage. That rationale motivated the design and naming of the R-ECMS.

The R-ECMS is designed as an on-line optimization algorithm that uses an estimation of the upcoming deceleration to foresee how much regenerative braking the powertrain system will provide when the vehicle brakes to a stop. The regenerative braking expectation is included in the formulation through the addition of a new parameter that associates driver style at the throttle to action on braking pedal. The power expected through braking is used to foresee what would be the final SOC if the driver decided to finish the mission at any given time. To calculate that expected final SOC, at every time-step, the controller computes the SOC next values for each candidate control action and then adds the SOC variation respective to the power calculated from the predicted regenerative braking. The difference between the expected final SOC and the desired final SOC is used to compute the electric cost and respective equivalent fuel mass since it represents a charge deviation that the engine would eventually have to overcome. At every time step, the control action chosen is the one that shows the lower equivalent fuel cost associated, thus the lower expected SOC deviation from target.

The following steps show how the implementation of the R-ECMS algorithm is performed in real-time.

5.3.2 Control Matrix

The functionality of the algorithm is based on how it selects control inputs for the powertrain components. Candidate control inputs are discretized according to each component characteristics and a calculation of respective discretized states are computed using the previously defined models.

The discretization of the control variables is done iteratively, using the control action from the previous time-step. Variables that can be used as control actions include gear engaged, engine speed and torque, and generator speed and torque. The range w and resolution d of the control variables are user-defined and should match the characteristics of the component. This time-step-based discretization avoids unfeasible "jumps", e.g. gear shift from first to fifth gear. In addition, it makes the code run faster since it reduces the size of the control matrix it needs to sweep.

Figure 5.6 illustrates the discretization of the control variables in real-time. In the example, engine torque is the control variable, u_{11} to u_{18}, where the first index denotes the index of the control input (1 = engine torque) and the second denotes the number of discretized candidates (1 to 8) based on the previously defined window w_1 and resolution d_1. Each control input is then combined to other control inputs from other components (2 and 3 in the example) to form the candidate control matrix U. In the figure, m denotes the final number of combinations.

5.3.3 State Variable Matrix

A calculation of the state variables is done using the candidate control matrix, the vehicle kinematics of the chosen powertrain topology, and the previous value of the state variables, if applicable. Among others, the SOC is a state variable of much

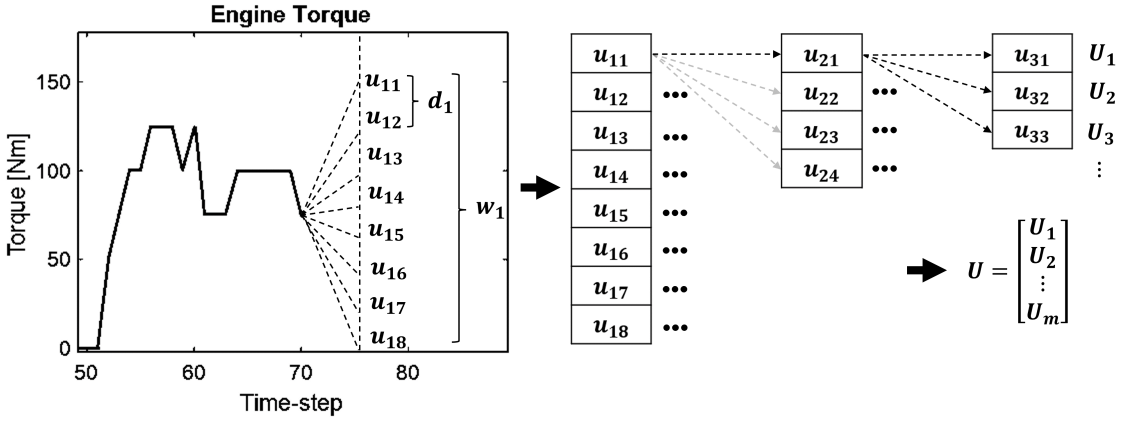

Figure 5.6: Example of candidate control actions being combined into the control matrix.

interest since the requirement to constraint its final/minimum value. The SOC values found in this step, given the control actions, are called SOC_{Next} and represent the candidate next possible values each associated with a candidate control action. Figure 5.7 exemplifies that step of the algorithm. In the figure, the impact of the control actions over the states is symbolically represented by the '+' sign. The resultant X matrix is the state variable matrix and it is the same size as U.

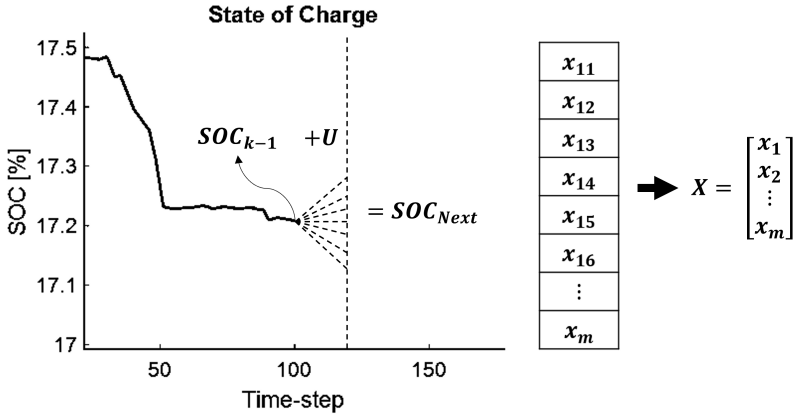

Figure 5.7: State variable matrix given the candidate control actions.

5.3.4 Cost Function

When a electrified vehicle brakes, the braking force is provided by the motor plus any friction brake needed to achieve desired level of deceleration. That means that if the deceleration is known, it is possible to compute how much regen a braking event will produce.

Therefore, a longitudinal vehicle dynamics model attached to a simple battery model can translate expected braking power into expected SOC regen (ΔSOC).

At this point, the algorithm has a matrix with candidate control actions for the current time-step U. Also, a matrix showing the respective candidate state variable values X. Assuming the deceleration value to be known, the algorithm uses the longitudinal vehicle dynamics model attached to the driveline model both from Chapter 04 to calculate the braking force and the respective power. That braking power is used to compute an SOC variation respective to the expected braking profile ΔSOC_{Regen} using a simple battery model. Adding this value to the state variable matrix, the result is an expected final SOC if the vehicle initiated a braking manoeuvrer to a stop in the next time-step. That calculation is performed for every candidate control action. Figure 5.7 shows a schematic of that process. Equations 5.6 and 5.7 show the mentioned calculations.

$$X_k = SOC_{Next} = SOC_{k-1} + f(U_k) \tag{5.6}$$

$$SOC_{FinalPredict} = SOC_{Next} + \Delta SOC_{Regen} \tag{5.7}$$

The deviation between the target SOC (user-defined) and the expected final SOC

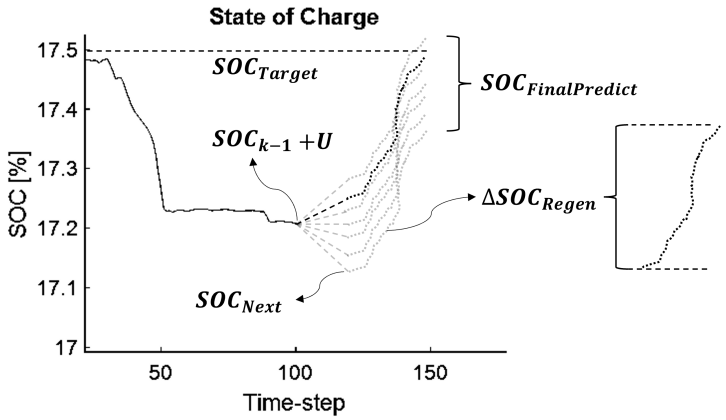

Figure 5.8: Illustration of the computation of the delta SOC regen to define final SOC predict.

previously computed, in terms of power, is the residual power P_{Res} that the engine will need to provide to compensate for any undesired variations. This calculation is showed in Eq. 5.8.

$$P_{Res} = (SOC_{Target} - SOC_{FinalPredict}) \cdot \frac{Q_{batt \cdot V}}{dt} \tag{5.8}$$

Where Q_{batt} is the battery capacity in ampere $\cdot$ second , V is the terminal voltage in volts and dt is the discretized time in seconds.

Analyzing Eq. 5.8 one can conclude:

- If $SOC_{Target} > SOC_{FinalPredict}$, $P_{Res} > 0$, meaning a lack of SOC is expected, needs to charge
- If $SOC_{Target} < SOC_{FinalPredict}$, $P_{Res} < 0$, meaning a surplus of SOC is expected, no need to charge

Therefore the correction term p needed in the original ECMS can be removed, since charge depleting is covered by situation two.

The battery equivalent cost $\dot{m}_b$ is updated given the new perspective on battery cost. The new equivalent fuel cost equation is showed in Eq. 5.9. The equivalence factor s is renamed to r.

$$\dot{m}_{eq}(U) = \dot{m}_f(U) + \dot{m}_b(U) = \dot{m}_f(U) + \frac{r}{Q_{LHV}} \cdot P_{Res}(U, \vec{d}) \tag{5.9}$$

At each time-step, the controller chooses the policy u by minimizing the cost funtion $J(U)$ as formalized by Eq. 5.10. The cost-function $J(U)$ is the equivalent fuel consumption $\dot{m}_{eq}(U)$. The residual power P_{Res} is a function of the candidate control actions as well as the deceleration $\vec{d}$ that defines the braking power in the longitudinal vehicle dynamics model.

$$u = \arg\min_{u} J(U) \tag{5.10}$$

Deceleration Expectation

The R-ECMS method was devised so it fits best an autonomous application powered by journey mapping. Nevertheless, the algorithm should be able to manage non-autonomous driving modes. To assume that the deceleration profile is known is reasonable for autonomous driving operation, but not for human-driven modes. Since the design and the homologation of the system requires it to be tested in human-driven modes, this parameter should be somehow incorporated in the optimization.

The strategy to incorporate that third parameter leverages driver style studies. Many researchers have contributed to the study of driver classification and styles. Methods used for classifying driver style include RB Sarker and Haque (2020), FL Fernandez and Ito (2016), Gaussian mixture model (GMM) Miyajima *et al.* (2007),

Fourier Transforms Güzel and GöL (2021), and Hidden Markov Models (HMM) Tran *et al.* (2012) and Deng *et al.* (2017). In addition, there is an increasing use of ML methods for the same purpose as thoroughly reviewed in Martinez *et al.* (2017) and in Alkinani *et al.* (2020).

From the results of previous works, it is reasonable to assume that the style in which drivers act on the throttle reflects the way they act on the brake pedal. That rationale is used in the R-ECMS to build the d_{ex} parameter. It is assumed that, when braking, driver will provide a deceleration proportional to the acceleration when the vehicle drove-off for the last time. That relationship is showed in Eq. 5.11. That proportionality is defined by the unknown parameter d_{ex}, and it is called the deceleration expectation. The deceleration expectation is the third parameter in the optimization,

$$\vec{d} = d_{ex} \cdot \vec{a} \tag{5.11}$$

Where $\vec{a}$ is the drive-off acceleration reset at every stop, and $\vec{d}$ is the deceleration at braking. The d_{ex} value is unknown though, and might vary between different drivers and driver styles. Therefore, it should be integrated in the optimization together with the charge and discharge regen-equivalence factors.

Furthermore, assuming that every surrounding driving condition contributes to driver decision making, having a parameter that translates driver input in the cost function contributes to making the algorithm flexible in regards to driving conditions. That is verified in further sections when the flexibility of the R-ECMS method to different cycles is evaluated.

The R-ECMS algorithm can be implemented to any type of HEV to which the

charge sustaining requirement applies. Minor changes respective to the control variables is in order to fit different applications. In a PHEV for instance, the control variables can be engine and secondary motor torques. Gear engaged can also be added as a control variable. In a SHEV, engine torque or speed can be selected as control variable. In this work, the application of the R-ECMS algorithm as the EMS for a BEVx is studied.

5.3.5 Parameter Optimization

The R-ECMS algorithm is applied to the previously discussed BEVx topology. Since for the BEVx the engine runs independently of the wheel speed and the max efficient torque as a function of speed was extracted, the only control input needed is engine speed. Window is set to 1000 RPM and resolution of 500 RPM. As for state variable, SOC is selected.

The optimization aim to minimize fuel (associated with engine events) assuring charge sustaining behaviour, i.e. the SOC by the end of the cycle should match the initial SOC. The algorithm is optimized using two standard driving cycles, the UDDS and the HWFET. The backward simulation approach is used. The powertrain kinematic equations are defined in Chapter 4 - Electrified Driveline Models, the range extended driveline model.

As explained in the theory section, the R-ECMS contains three parameters: the regen-equivalence factor that is subdivided in charge r_{chg} and discharge r_{dis} equivalence factors, and the deceleration expectation d_{ex}. The first two parameters translate battery cost into fuel cost for charging and discharging situations, respectively. They follow the same rationale of the ECMS's equivalence factors s_{chg} and s_{dis}. The third

parameter is the deceleration expectation and it gives the algorithm a perspective of the deceleration profile, thus a perceptive of the regenerative power once the vehicle brakes to a complete halt.

Genetic Algorithm is used for optimizing the parameters under two drive cycles, the UDDS and the HWFET. Since the objective of the optimization is to find the parameters that provide the minimum fuel cost for a still charge sustaining operation, the optimization is set-up with a multi-objective cost function. Fuel consumption is objective 01 and final SOC deviation is objective 02.

The optimizer works as follows. At each iteration, the driveline model runs with parameters suggested by GA, the simple battery model provides the profile and end value of SOC and the engine model provides the fuel consumption. The next generation of parameters in the GA is chosen based on the fuel and final SOC results of the previous generation. The multi-objective GA tries to find parameters that will minimize each of the two.

Figure 5.9 shows the results for an optimization using population size of 200 individuals over 15 generations.

It is possible to see that the optimization results in a Pareto front graph, where both objectives concur. In other words, for a near-zero SOC deviation the fuel consumption is maximized while for a zero fuel consumption result the SOC deviation is maximum. That makes sense since fuel and electric energy are the only two sources of power in the BEVx.

The requirement though, is that the system should provide a charge sustaining operation, meaning final and initial SOC should be the same within a tolerance. Defining this tolerance to be 0.01 %, the results of the optimization are filtered and

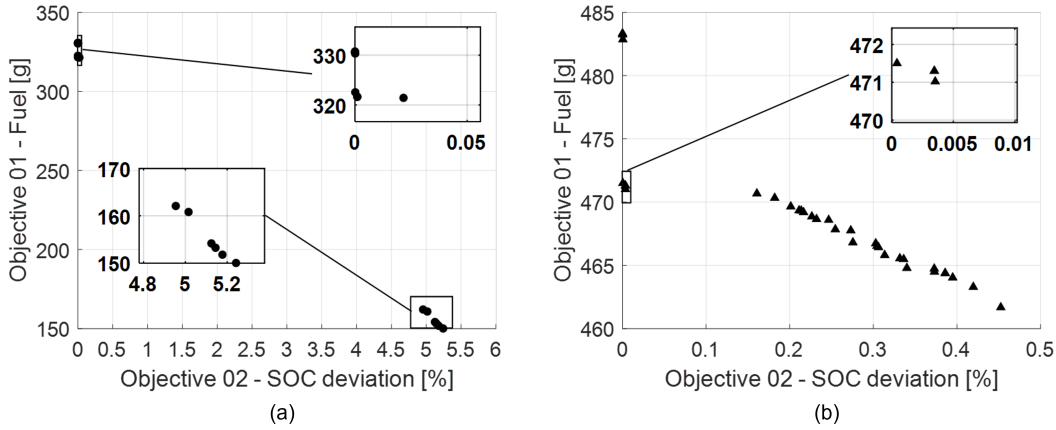

Figure 5.9: Multi-objective R-ECMS optimization for the UDDS cycle (a) and HWFET cycle (b).

plotted again. Figure 5.10 shows the remaining results. On the left the updated Pareto front graph and on the right the respective parameter values

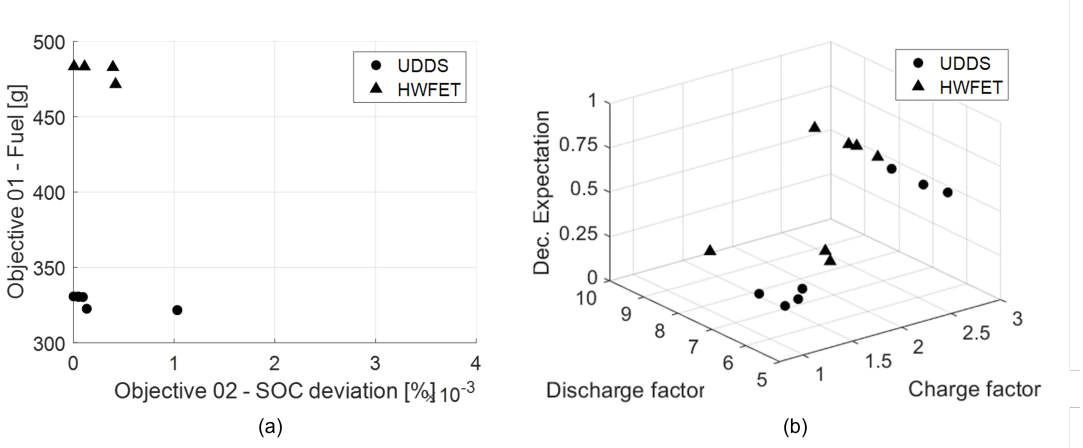

Figure 5.10: Optimization results filtered for the defined tolerance of SOC deviation (a) and respective optimized parameters (b).

Using a cycle-specif set of parameters is not practical in real life and as for emission homologation, it could be ruled as illegal practise. Therefore, the final step of the optimization is to run the cycles again with a single set of parameters. That set of

parameters is selected based on a statistic analysis made with the results that meet the SOC deviation criteria. Figure 5.11 shows a box-plot for each parameter. The boxplot shows the statistic distribution of the parameters returned by each optimization. Table 5.1 show the results for the statistic analysis that creates the box-plot.

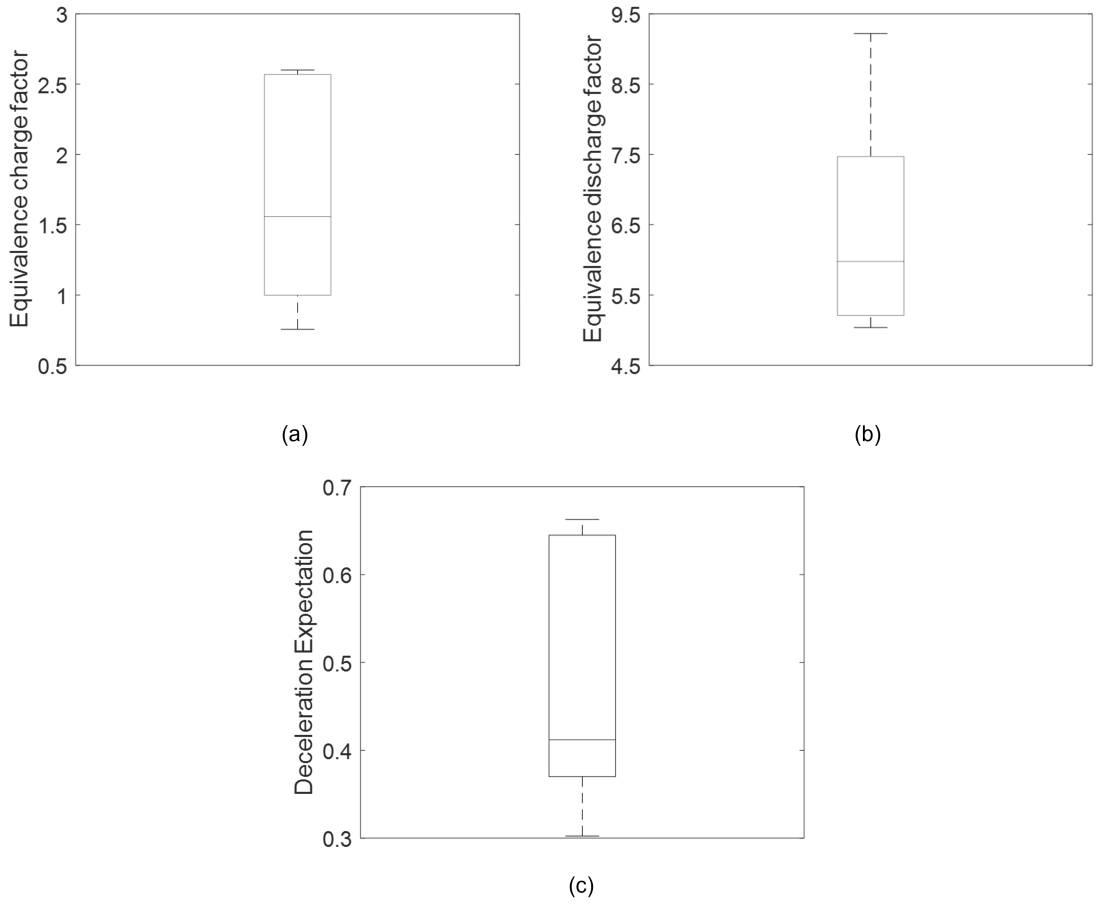

Figure 5.11: Statistic distribution of the results after optimizing the regen-equivalence charge (a) discharge (b) factors, and the deceleration expectation (c).

The median values in the table are the selected set of parameters for the following analysis.

Table 5.1: Statistics of the R-ECMS optimized parameters that meet the charge sustaining criteria

Statistics	Eq. discharge factor	Eq.charge factor	Deceleration expectation
Number of values	15	15	15
Median	5.9779	1.5577	0.4118
75th percentile	7.4693	2.5688	0.6448
25th percentile	5.2090	0.9987	0.3698
Upper adjacent	9.2200	2.6008	0.6626
Lower adjacent	5.0376	0.7560	0.3023

The resulting SOC profiles for the UDDS and HWFET using the median parameters are plotted in Fig. 5.12. Table 5.2 details the results of fuel consumption and SOC deviation for those parameters in both cycles.

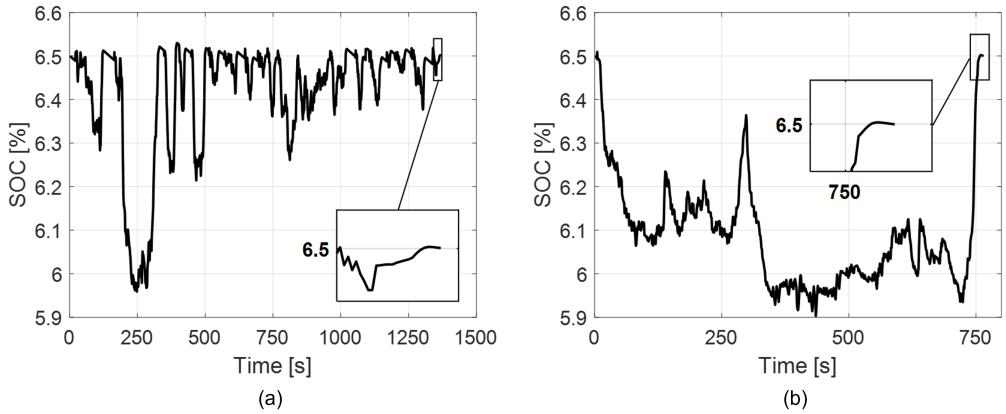

Figure 5.12: R-ECMS results of SOC for charge sustaining operation on the UDDS cycle (a) and on the HWFET cycle (b).

The most relevant observation is that the set of parameters selected from the statistic analysis is able to deliver a charge sustaining operation for both cycles. It is also interesting to note how the fuel increase is similar in both cases. The fuel increase is calculated using as reference the performance of the algorithm with the parameters that delivered the most efficient solution individually per cycle.

Table 5.2: Fuel consumption and final SOC deviation for the selected set of parameters

Drive Cycle	Final SOC deviation	Fuel consumption	Fuel increase from best result
UDDS	0.0003 %	332.04 g	+2.85 %
HWFET	0.0002 %	483.33 g	+2.44 %

5.3.6 Benchmark Algorithms

Energy management algorithms are reviewed in Chapter 3. Here are the details of each method used as benchmark. The benchmark algorithms use the same system modelling approach and the same driveline kinematics used for the R-ECMS algorithm. All methods are optimized for two standard driving cycles, the UDDS and the HWFET. The same SOC operation window defined for the charge sustaining mode of the R-ECMS is used in all benchmark algorithms.

Equivalent Consumption Minimization Strategy

Since the R-ECMS algorithm is built upon the ECMS, it is appropriate to compare it with its peer. The ECMS built here is identical the R-ECMS in every regard but for the cost function. As detailed in Chapter 3, the cost function of ECMS is the sum of the fuel cost and the equivalent fuel cost of battery usage as retrieved in Eq. 5.12.

$$\dot{m}_{eq}(t) = \dot{m}_f(t) + \dot{m}_{batt}(t) = \dot{m}_f(t) + \frac{s_{chg/dis}}{Q_{LHV}} \cdot P_{Batt}(t) \cdot p(x) \tag{5.12}$$

The conversion of battery to fuel cost is provided by the s factor, that needs to be optimized for specific driving cycles. Differentiation between charge and discharge modes is also enabled. Therefore, the design and optimization of the ECMS algorithm will produce two parameters, s_{chg} and s_{dis} for each drive cycle.

The optimization of the ECMS equivalent factors is performed with GA in the

same format and size as it was performed for the R-ECMS algorithm. Figure 5.13 shows the Pareto front for the multi-objective optimization and Tab. 5.3 shows the statistic distribution of the parameters that provide the charge sustaining operation with the requirement of 0.01 % SOC deviation.

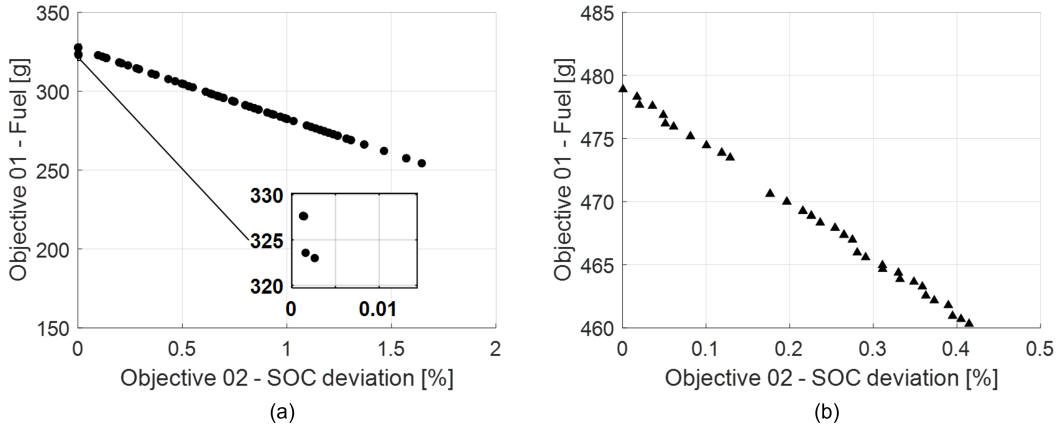

Figure 5.13: Multi-objective ECMS optimization for the UDDS cycle (a) and HWFET cycle (b).

Table 5.3: Statistics of the ECMS optimized parameters that meet the charge sustaining criteria

Statistics	Eq. discharge factor	Eq.charge factor
Number of values	14	14
Median	5.7046	0.9368
75th percentile	6.2741	1.3748
25th percentile	5.1278	0.6567
Upper adjacent	6.4675	1.5681
Lower adjacent	5.0115	0.35162

The final set of parameters are set as the median values in the statistical distribution. Figure 5.14 depicts the resulting SOC profile of the ECMS algorithm for the selected parameters and Tab. 5.4 details the final results of both objectives, final SOC deviation and fuel consumption.

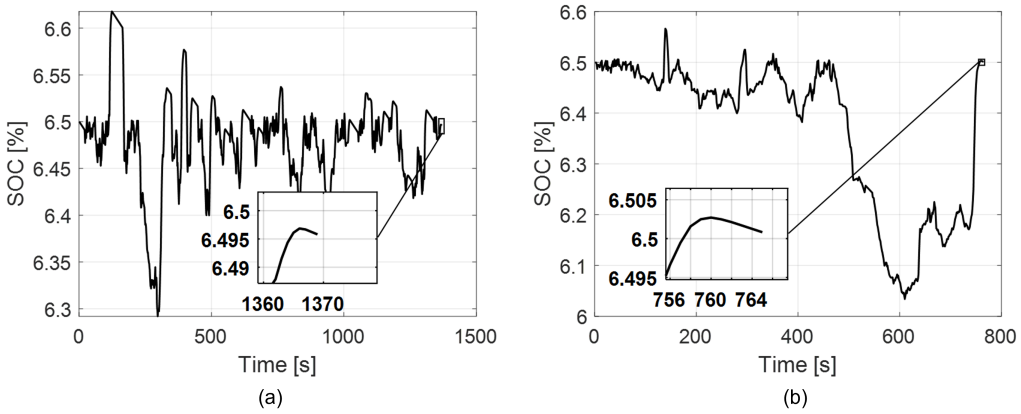

Figure 5.14: ECMS results of SOC for charge sustaining operation on the UDDS cycle (a) and on the HWFET cycle (b).

Table 5.4: R-ECMS fuel consumption and final SOC deviation for the selected set of parameters

Drive Cycle	Final SOC deviation	Fuel consumption	Fuel increase from best result
UDDS	0.0042 %	327.08 g	-0.17 %
HWFET	0.0008 %	478.88 g	+0.025 %

It is possible to see that this methodology for parameter selection seems to affect the ECMS less when compared to the R-ECMS. Also, fuel consumption at this point is lower with the ECMS. Both methods provide equivalent charge sustaining operation for the current conditions and drive cycles. One issue with the ECMS is the fact that it charges battery above the charge sustaining level (6.5 %). That is verified for both cycles. Retrieving requirement # 02 of BEVx, the engine operation must not occur while SOC is above the predefined SOC lower limit.

Dynamic Programming

The DP is created as to provide a global optimal solution for comparison. The algorithm leverages the dpm function provided in Sundstrom and Guzzella (2009) with

appropriate modifications to accommodate the investigated BEVx topology. For state variables, SOC and engine speed are selected. For control variables, engine speed variation (shift) per time-step. The algorithm is structured so the driveline capabilities are compatible with the previous algorithms. Table 5.5 details the configuration of the DP for the investigated topology.

Table 5.5: Dynamic programming algorithm configuration.

	Series-Hybrid
Time-step	1.0 s
State variables	SOC, Engine Speed
State variables: number of grid points	SOC: 2600
	Engine Speed: 10
State variables: range	SOC: [5.0 - 6.5%]
	Engine Speed: [0 - 4500 RPM]
State variables: final state constraint	SOC: [6.49 6.51%
	Engine Speed: 0 RPM
Control variables	Engine speed shift
Control variables: number of grid points	3 (decrease, remain, increase)
Control variables: range	[-500:0:500] RPM

The DP optimization does not output parameters to the controller, instead it provides the optimal control actions per time-step to achieve optimal control. As reviewed in Chapter 3, it runs backwards so it assures the final state constraint.

At every time-step, DP will assess the fuel cost associated with the state change caused by every single candidate control. It then runs forwards choosing the control policies that provide the overall lowest fuel cost from start to end of the mission. The DP is therefore, the best benchmark to assess the global optimal fuel cost of a powertrain over a driving cycle.

The results of DP justify its global optimization performance. DP uses the entire SOC window provided (from 6.5 % to 5.0 %) SOC. In addition, it choses the most efficient engine speed whenever a charge situation is triggered. That contributes for

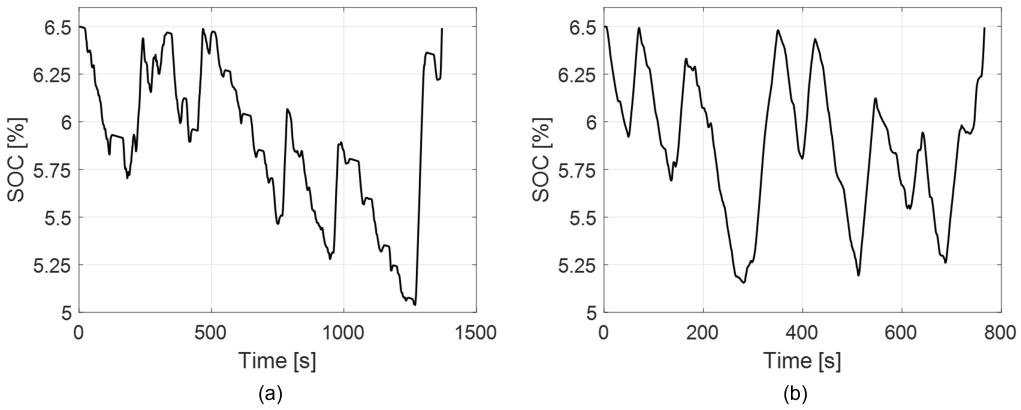

Figure 5.15: DP results of SOC for charge sustaining operation on the UDDS cycle (a) and on the HWFET cycle (b).

Table 5.6: ECMS fuel consumption and final SOC deviation for the selected set of parameters

Drive Cycle	Final SOC deviation	Fuel consumption
UDDS	0.003 %	266.58 g
HWFET	0.0008 %	391.02 g

DP not charging every moment.

5.4 Real-time Assessment

Once the algorithms are optimized, the next step is to assess their performance in real-time using the driving simulator. This human-driven approach increases the realism of the assessments. Besides emulating the real testing with higher fidelity (when compared to off-line simulation) the human-driven tests allow for adding the driver perception and feeling to the design, in which has been termed, driver-in-the-loop. As a consequence the approach is considered a blending between experiment and simulation giving engineers a better perspective of what their control systems

can achieve once deployed in the vehicle.

The tests are conducted as if the actual vehicle was being tested to improve realism. Estimation of the road loads is performed, followed by a consumption assessment with human-driven drive cycles. Then, drivability issues caused by engine events and impacts of incorporating engine operation restrictions are investigated. For the consumption assessment, and drivability study the R-ECMS and its benchmark algorithms are compared. Finally, a performance study is conducted to evaluate the effects of the mass added to the vehicle.

5.4.1 Performance Check

The first assessment is to evaluate the performance deterioration due to adding mass to the vehicle. The variation of the mass distribution changes the weight on the driving wheels, thus the ability to propel under various conditions is also changed. This section leverages the proving ground derailed in Chapter 2, to evaluate what is the expected performance change for the addition of the APU to the BEV. The benchmark for the following analysis is the original BEV model.

Acceleration

The ability of the vehicle to accelerate when requested is important to verify. Here, an acceleration manoeuvre is performed from zero to max speed with wot. The criteria adopted is detailed in Tab. 5.7.

Table 5.7: Acceleration comparison between BEV and BEVx models.

Model	0-100 kph	60-100 kph	80-120 kph
BEV	8.25 s	4.00 s	5.58 s
BEVx	8.85 s	4.29 s	5.96 s
Deterioration	6.78 %	6.76 %	6.37 %

Tip-in

Another performance scenario that must be included is the tip-in manoeuvrer. That simulates a instantaneous torque request from a cruising speed. Driver stabilizes the vehicle at 60.0 kph and then applies wot to reach max speed. That type of manoeuvrer simulates driving events such as merging to highway and vehicle overtaking. Table 5.8 sumarizes the results for the tip-manoeuvre.

Table 5.8: Tip-in comparison between BEV and BEVx models.

Model	Peak acceleration	60-100 kph
BEV	3.99 m/s^2	3.92 s
BEVx	3.77 m/s^2	4.28 s
Deterioration	5.51 %	8.41 %

Launch-ability

The ability to overcome the inertia and propel from halt is termed launch-ability. Vehicle must respond to driver pedal input and drive-off with acceleration proportional to driver intend.

Two launch manoeuvres are performed. First, driver accelerates with pedal position at 25.0 % then 50.0 %. That simulates a launch in urban environments where vehicle often comes to a stop and go situations due to traffic control.

Table 5.9: Launch comparison between BEV and BEVx models.

	Pedal 25 %		Pedal 50 %	
Model	Peak acceleration	0-50 kph	Peak acceleration	0-50 kph
BEV	1.00 m/s^2	14.16 s	1.98 m/s^2	7.48 s
BEVx	0.94 m/s^2	15.39 s	1.72 m/s^2	8.23 s
Deterioration	6.00 %	7.99 %	13.13 %	9.11 %

Gradeability

One performance variable of great importance is greadeability. It consists in the ability of the vehicle to overcome slopes. It is key that the BEVx complies with the current gradeability performance of the BEV for the sake of user experience cross-model and safety. Three test cases are conducted for each vehicle, 10 %, 15 %, and 20 % grades. The vehicle climbs from halt and driver inputs wot. The performance parameter evaluated is the acceleration at which the vehicle climbs each slope.

Table 5.10: Gradeability comparison of BEV and BEVx models for different grades.

Model	10 % Grade	15 % Grade	20 % Grade
BEV	3.02 m/s^2	2.57 m/s^2	2.10 m/s^2
BEVx	2.75 m/s^2	2.29 m/s^2	1.82 m/s^2
Deterioration	8.94 %	10.89 %	13.33 %

That concludes the performance check for the addition of the APU to a BEV. Detailed discussion is provided in section 5.6.5.

5.4.2 Estimation of Road-load Coefficients

Prior to conduct the consumption assessments, it is necessary to extract the road load coefficients through a coastdown procedure.

The estimation of road loads using coastdown is defined in SAE (1996). The procedure consists of letting the vehicle coast from high to low speed, while recording

time and velocity. Off-line least square estimation of the drag and rolling resistance coefficients is then performed. Other estimation methods developed include recursive least squares (RLS) Rhode and Gauterin (2013); Zhang *et al.* (2015), Kalman filters and ANN Andriaminahy *et al.* (2019). These works rely exclusively on physical experiments for function validation, resulting in a large cost and limiting the performance of the estimator to the driving conditions that it was tested. Driving conditions highly affect the loads during a mission Bruck *et al.* (2019a). By analyzing the previous works and given the characteristics of the road loads, one can conclude that the driving conditions such as wind speed, surface friction, grade, and driver behavior are the most significant in the calculation of the road-load coefficients. Therefore, in order to design and validate a road-load estimator, it is imperative to test it under various driving conditions.

Assuming no drivetrain losses, for a vehicle coasting freely (powertrain disengaged), the propelling force at the wheels F_x is zero. Retrieving Eq. 4.79 from the longitudinal model and 4.97 it is possible to deduce that the vehicle then decelerate due to the resistant forces only: drag F_{drag}, rolling resistance F_{roll}, and grade F_{grade}. Equation 4.79 can be simplified to a non-physics model detailed in Eq. eq:abc, where the grade component is assumed to be zero.

$$F_{road} = A + B \cdot \dot{x} + C \cdot \dot{x}^2 \tag{5.13}$$

Kalman Filter and other state observers are usually applied for such nonlinear systems. However, such method requires observable systems. Due to the interdependence of the parameters to the calculation of the deceleration force in the model, the system is not observable.

Recursive Least Square

Adaptive filter algorithms such as the least mean squares (LMS) and RLS are considered. The former is a stochastic estimation that reduces the mean square error between current estimate and measurement, while the latter is a deterministic algorithm that minimizes a weighted cost function recursively Uncini (2015). Since the RLS converges faster, and is numerically stable, it is ideal for real-time applications.

In the RLS method, a correlation matrix is computed every time-step using a forgetting factor which means that as time increases, recent data becomes more relevant to the estimation Uncini (2015). To apply the RLS, a linear regression model is built as shown in Eq. 5.14. In this work, the three inputs are present in the CAN bus: velocity, acceleration, and slope.

$$\hat{y}_k = \Theta_k^T \phi_k \tag{5.14}$$

Where $\hat{y}$ is the estimated output at time-step k. The matrices, Θ and ϕ are the parameter vector and the regressor, respectively, both calculated as follows:

$$\Theta_k^T = \begin{bmatrix} A \\ B \\ C \end{bmatrix}_k \tag{5.15}$$

$$\phi_k = \begin{bmatrix} 1 & \dot{x} & \dot{x}^2 \end{bmatrix}_k \tag{5.16}$$

The measured output, y is calculated as shown in Eq. 5.17, using the measurements of acceleration a and slope α, the user-entered mass of the vehicle m and gravity g.

$$y_k = m\dot{x}_k - mg\sin(\alpha_k) \tag{5.17}$$

Figure 5.16 shows the estimation algorithm. At every sampled time-step, the system receives the input signals and the current model is used to produce an estimate of the deceleration force acting on the vehicle (Eq. 5.14). That estimate is compared to the force computed directly from the acceleration and slope measurements (Eq. 5.17) and the error e is calculated.

The gain G is computed using the correlation matrix P, the forgetting factor λ and the regressor ϕ. It is then used with the error to update the parameter vector Θ. The correlation matrix P is also updated every time-step. The initial values of p_{11}, p_{22}, and p_{33} come from manual calibration. Initial values of A, B, and C are defined assuming the expected amplitude of each parameter. The term γ is computed as shown in Fig. 5.16. The forgetting factor λ used is equals to 1. That makes our estimator a growing memory RLS, where past and present errors have the same weight on the estimation. That value was also chosen after manual calibration. The initial parameters of the RLS algorithm are depicted in Tab. 5.11.

Table 5.11: RLS calibrated parameters

Parameter	Value	Parameter	Value
γ	1	Initial A	10
p_{11}	0.01	Initial B	0.1
p_{22}	0.1	Initial C	0.01
p_{33}	0.1		

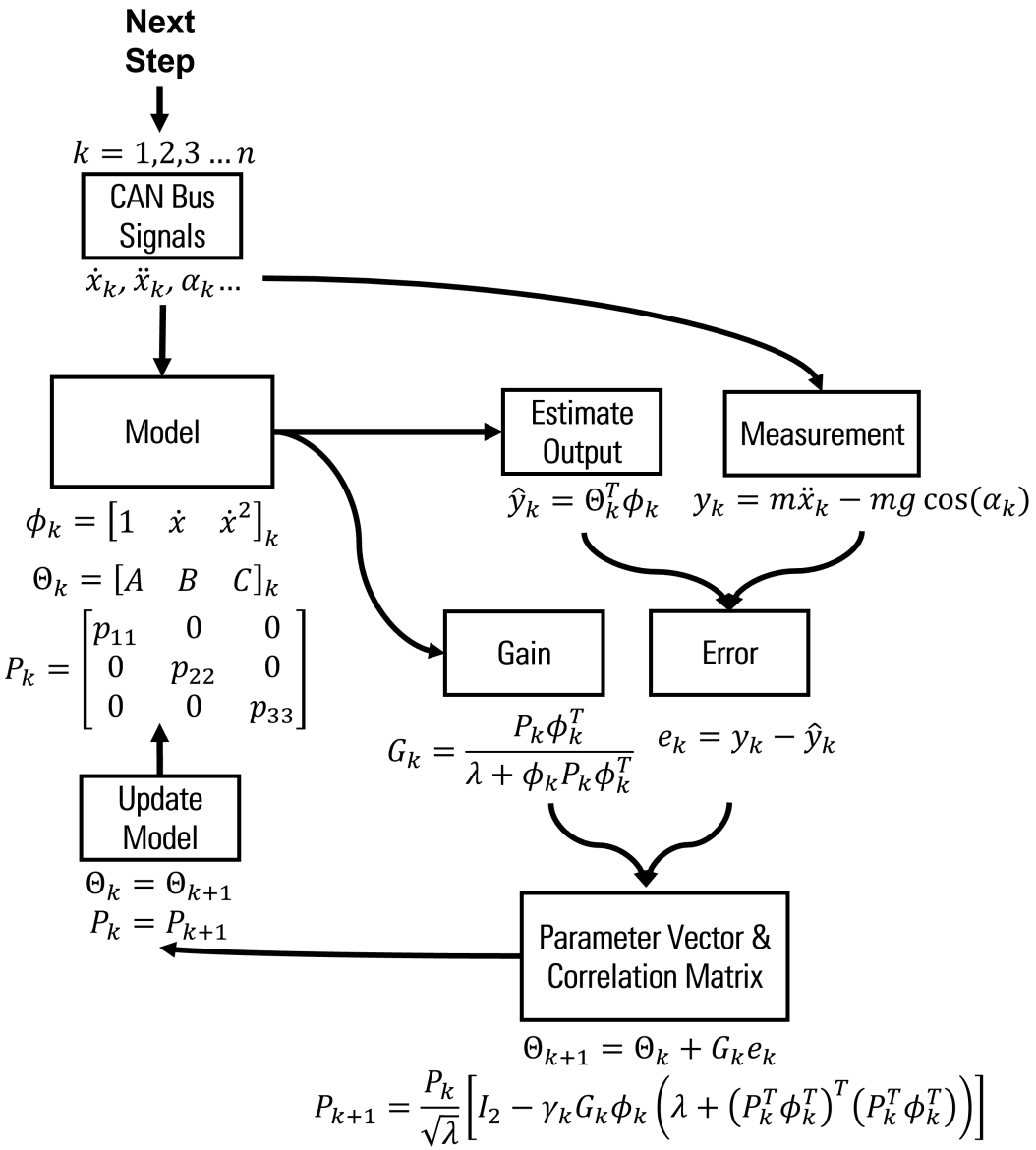

Figure 5.16: RLS algorithm structure applied to road load coefficients estimation.

Coastdown

The standard presented in (SAE, 1996) is used for the validation of the algorithm. The procedure consists in accelerating the vehicle to a velocity greater than 108Km/h, then shifting the transmission to neutral (when present), allowing the vehicle to coast freely from at least 100km/h to 40km/h (the initial 8km/h surplus avoids the shifting to impact the estimation). The standard instructs the driver to avoid acting on the steering wheel, brakes and to not engage gears during the coasting. In the norm, the estimation of the parameters is based on ten independent runs that are conducted to mitigate the impact of surrounding driving conditions.

The BEV model created in Chapter 02 is used to validate the performance of the RLS estimation as demonstrated in Tab. 5.12 before applying it to the BEVx model. That is decided since the road-load coefficients of such model were experimentaly provided.

Table 5.12: Estimated road load parameters for each of the ten runs - BEV

Runs 01-05	01	02	03	04	05
A	23.2952	23.1647	23.1916	23.1663	23.1997
B	0.3945	0.3996	0.3984	0.3998	0.3977
C	0.01242	0.01236	0.01236	0.01235	0.01237
Runs 06-10 / Runs	06	07	08	09	10
A	23.4138	23.4138	23.2298	23.2938	23.1692
B	0.3883	0.3998	0.3937	0.4014	0.3955
C	0.01247	0.01232	0.01241	0.01230	0.01238

Table 5.13 compares the averaged result of the ten runs with the reported values of the A, B, and C coefficients. The accuracy in the estimation is overall above 97 %. That motivates using this method for estimating the road load coefficients of the proposed BEVx topology, which has a mass increase compared to the BEV.

The same test is conducted for the BEVx model created from the BEV model.

Table 5.13: Averaged road load parameters - BEV

Coefficients	Estimated Average	ANL Measured	Accuracy
A	23.2416	23.3637	99.47 %
B	0.3868	0.3946	97.99 %
C	0.01237	0.01245	99.35 %

The results are depicted in Tab. 5.14.

Table 5.14: Estimated road load parameters for each of the ten runs - BEVx

Estimated Coefficients / Runs	01	02	03	04	05
A	25.3914	25.4506	25.4059	25.5373	25.3897
B	0.4418	0.4387	0.4410	0.4351	0.4407
C	0.01352	0.01355	0.01352	0.01359	0.01354
Estimated Coefficients / Runs	06	07	08	09	10
A	25.3679	25.3906	25.3725	25.3652	25.4423
B	0.4423	0.4403	0.4416	0.4417	0.4380
C	0.01351	0.01353	0.01353	0.01352	0.01356

The averaged results are depicted in Tab. 5.15. They are uploaded to the dynamometer model in Simulink that is used for the following consumption tests.

Table 5.15: Averaged road load parameters - BEVx

Coefficients	Estimated Average
A	25.4113
B	0.4401
C	0.01353

5.4.3 Consumption Assessment

Hybrid electric vehicles are subjected to a two-stage procedure for consumption homologation. First, the charge depleting test, where the vehicle behaves as a BEV and engine remains off. Second, the charge sustaining test, where engine is switched on

to prevent vehicle from running out of battery power. The consumption assessment procedures are reviewed in Chapter 3.

As reviewed, consumption assessment is commonly performed in-lab, using dynamometers. Here, the driving simulator in the MARCdrive lab provides the testbed for the analysis. In the emulation of a consumption test, the driver is required to follow a predetermined speed schedule. The driving cycles are loaded in a real-time HMI and a real driver performs them in the straight road environment detailed in Chapter 2, section 2.5.1.

The drive cycles are performed according to SAE Recommended Practice (2012). The tolerances respected are specified in the EPA dynamometer driving schedules procedure, Chapter I - Part 86. It establishes a upper and a lower limit of 2 mph within one second at any given time during the test. Speed variations greater than tolerances are allowed during braking spikes are accepted provided they do not last more than 2 seconds. Figure 5.17 shows examples of the resulting velocity profile for two cycles, the UDDS and the HWFET. Nevertheless, US06 and SC03 are also conducted since they are part of the 5-Cycle procedure.

Each drive cycle is performed on-line once. The models of the powertrain components run on-line with the test and signals such as vehicle velocity, power, and torque request are recorded. The cycles and measured data are then stitched together and looped off-line according to the type of test that is required (charge depleting or charge sustaining assessment).

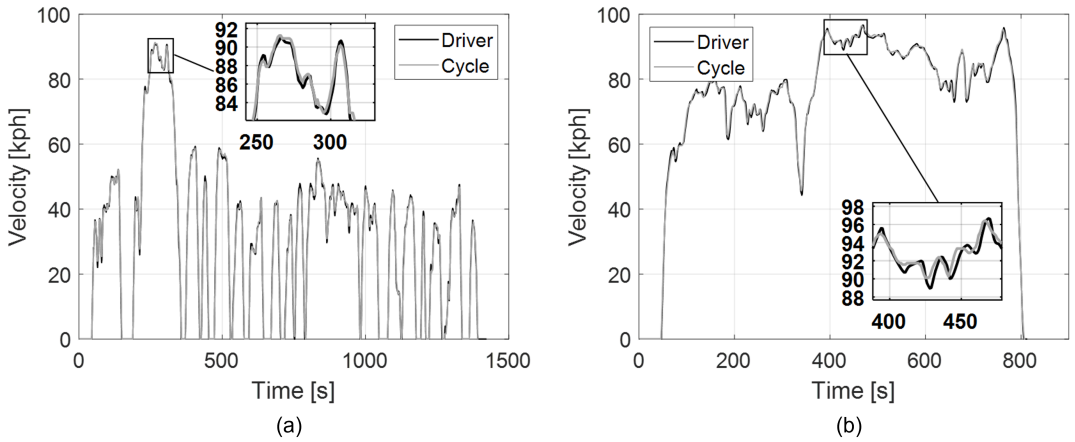

Figure 5.17: Velocity profile of two drive cycles conducted in the simulator, UDDS (a) and HWFET (b).

Charge Depleting: single cycle test

In charge depleting mode, the vehicle behaves as a BEV. Therefore, the 2-Cycle procedure is used in the same fashion it was used in Chapter 2 to validate the baseline BEV. For the BEVx, the charge depleting range is calculated from max SOC to charge sustaining SOC level (6.5 %) when engine starts to operate.

The R-ECMS algorithm penalizes electric usage based on the difference between current SOC to target SOC (6.5 %) as demonstrated in Eq. 5.8. Therefore, it is expected to provide an automated charge depleting operation whenever the SOC is greater than the charge sustaining level. As for the ECMS, once optimized for a cycle it will provide a charge sustaining level regardless of the initial SOC. Therefore, a correction factor must be added to penalize engine start during charge depleting operation. That is implemented in the benchmark algorithm.

Since all algorithms perform the charge depleting test without engine operation (as required), the energy consumption result is the same for all. Table 5.16 shows a

the energy economy results of the BEVx compared to the baseline BEV validated in Chapter 2.

Table 5.16: BEV and BEVx consumption results

	MPGe Adjusted (UDDS / HWFET / Combined)	Miles Adjusted
BEVx	111.9 / 102.9 / 107.9	72.8
BEV Model	120.7 / 110.3 / 116.1	79.7
Difference	-7.3 % / -6.7 % / -7.0 %	-8.6 %

The results show that the additional mass of the APU caused an average reduction of MPGe of approximately 7.0 %. More importantly, it has reduced the adjusted mile range in 8.6 %.

Requirement #03 of BEVx states "electric range must be equal or greater than 80 miles" Although regulation does not specify if the minimum electric range requirement refers to adjusted or unadjusted value, the battery capacity is revised to meet that requirement in the worst case scenario. That leads to a new battery capacity of 66 Ah. Since the original battery pack weights 215 kg, the new capacity is expected to increase the mass of the vehicle in approximately 21.5 kg. After the edit the cycles is re-run and the results are depicted in Tab. 5.17.

Table 5.17: BEV and BEVx consumption results after battery update to 66 Ah.

Charge depleting	MPGe Adjusted (UDDS / HWFET / Combined)	Miles Adjusted
BEVx Model	112.1 / 103.0 / 108.0	80.2
BEV Model	120.7 / 110.3 / 116.1	79.7
Difference	-7.1 % / -6.6 % / -6.9 %	+0.62 %

After the proposed modification the MPGe difference is marginally changed while the range is increased to an acceptable level (above 80 mi). The next step is to assess the BEVx model in the 5-Cycle test to define its fuel tank size and overall economy.

Charge Sustaining: 5-Cycle Test

As reviewed in Chapter 3, the fuel economy of pHEVs can be assessed using the the 5-Cycle test procedure. The cycles are conducted in the following order and conditions detailed in Tab. 5.18.

Table 5.18: Drive cycles performed in the simulator for the 5-Cycle test procedure

Cycle	Driving Conditions	Auxiliary load
UDDS	Low-speed urban driving	A/C off (300 W)
HWFET	Medium-speed highway driving	A/C off (300 W)
US06	Low and high-speed aggressive driving	A/C off (300 W)
SC03	Low-speed urban driving	A/C on (1500 W)
UDDS	Low-speed urban driving	A/C off (300 W)

Figure 5.18 shows the SOC profile for the charge sustaining test of the R-ECMS (a) and the ECMS (b) algorithms. Both algorithms provide a solution which a single charge sustaining cycle is needed to conclude the test.

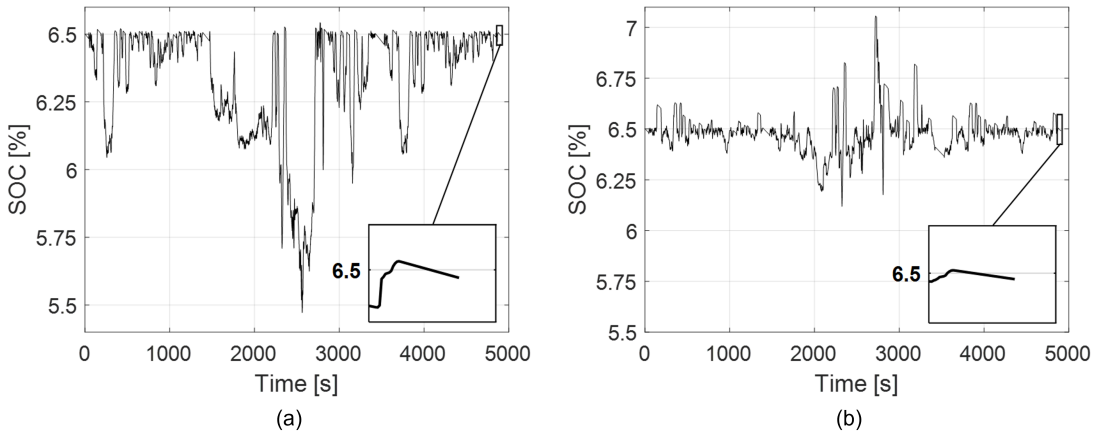

Figure 5.18: Charge sustaining SOC profiles produced by the R-ECMS (a) and the ECMS (b) for the 5-Cycle procedure.

The fuel economy values are presented in Tab. 5.19. Although not feasible in real-time, DP results are provided for comparison.

Table 5.19: Charge sustaining test consumption results

Charge sustaining	MPG	Fuel mass	Fuel volume	Compared to DP
R-ECMS	55.98	1735.9 g	3.60 L	83.5 %
ECMS	56.81	1710.4 g	3.45 L	84.7 %
DP	67.2	1449.54 g	2.07 L	-

Requirement #04 states "the APU range must not be greater than the electric provided range". Using the results of the 5-Cycle test it is possible to estimate the size of the fuel tank to comply with such requirement. For the present results and model simplifications, a fuel tank of 5.5 L (1.45 Gallons) should provide a range of 80 miles on charge sustaining mode, which complies with the regulation.

5.4.4 Drivability Calibration

The previous analysis provided a comparison of the fuel consumption that each algorithm achieved so the BEVx operates in charge sustaining mode. It assesses the algorithms under standard drive cycles and realistic scenarios. Nevertheless, the current results are a mathematical solution. It is important to verify their feasibility given components constrains, and most importantly, drivability.

In the context of the BEVx, one important aspect of drivability is the mode shift. More specifically, engine start/stop events. Several studies are presented in literature to study engine start/stop dynamics. In Miro-Padovani *et al.* (2015), it is demonstrated that the time for the engine to start and reach stability at its idle speed varies from 0.2 s to 1.4 s depending on the starter components and method. In Jing *et al.* (2021) the range is from 0.1 s to 1.2 s considering different prefil torques. In the present work the engine is assumed to need 1.0 s to start and reach its idle speed of 1000 rpm.

Figure 5.19 shows the engine speed profiles provided by the real-time algorithms for the vehicle operating under the express way experiment. The R-ECMS provides a solution with 110 engine events, 70.9.5 % of which are engine off immediately followed by engine on. The ECMS provides 94 events, 59.5 % of which are engine off immediately followed by engine on.

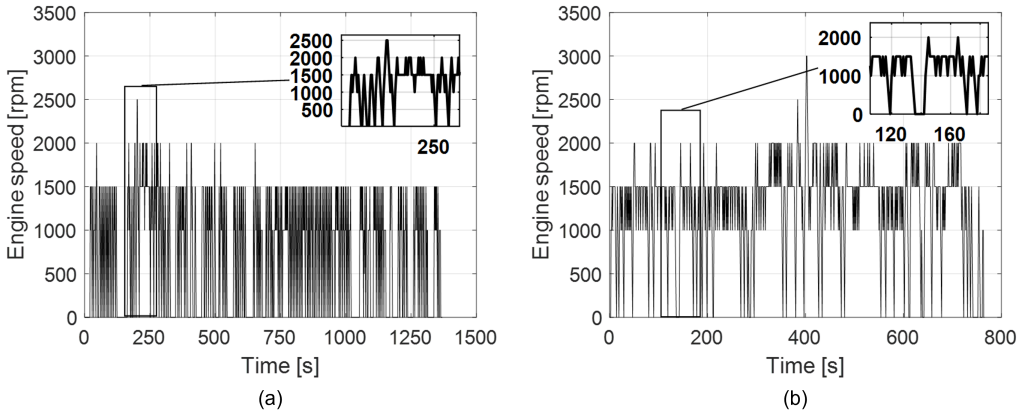

Figure 5.19: Engine speed profile provided by the R-ECMS in the UDDS (a) and in the HWFET (b) cycles

Such eventful operation not only contributes to bad drivability but is unpractical. One way of controlling the number of short engine events is to constrain the engine's mean dwell time (MDT). That means enforcing engine off for a specified period of time so driver is not disturbed with frequent and short start/stop events.

In this step, a sensitivity analysis is performed with the objective to define a MDT that is appropriate in the light of drivability requirements but at the same time interfere the least in the charge sustaining achievement and fuel consumption previously optimized.

Table 5.20 shows the results of final SOC deviation for MDTs varying from 0 to 60s in iterations of 10 s.

Table 5.20: Impact of mean dwell time control to charge sustaining ability

	R-ECMS		ECMS	
Mean dwell time	UDDS	HWFET	UDDS	HWFET
0.0 s	0.0005 %	0.0003 %	0.0038 %	0.0007 %
10.0 s	0.0022 %	0.0022 %	0.6098 %	0.8465 %
20.0 s	0.0543 %	0.0309 %	1.3259 %	2.2709 %
30.0 s	0.0213 %	0.0018 %	2.7379 %	2.5342 %
40.0 s	0.0316 %	0.1187 %	3.7698 %	3.5232 %
50.0 s	0.0027 %	0.1778 %	4.3985 %	3.7762 %
60.0 s	0.0261 %	0.0364 %	5.3254 %	4.7225 %

An MDT of 10.0 s is chosen for the following analysis since this is the value that impacts the least the charge sustaining ability of both real-time algorithms.

5.4.5 Real-world scenarios

The driving simulator also enables the emulation of real-world driving. R-ECMS and ECMS are compared in the neighbourhood and express way scenarios. Both algorithm are loaded with the parameters from optimization and MDT of 10.0 s. Initial SOC is 6.5 % and in neither cases the journey is known by the algorithms.

Neighbourhood

In the neighbourhood environment the driver follows a predefined path detailed in Tab. 5.21 in a very short trip around a residential area. The driver acts natural, emulating a real driving situation. Figure 5.20 shows the velocity profile extracted from the experiment and a sample picture of the ego vehicle inserted in the neighbourhood environment. The compliance with traffic control and speed limits reflects the driver style and behaviour, not being a hard constraint of the experiment.

The SOC profiles for the real-time algorithms are plotted in Fig. 5.21. It is

Table 5.21: Navigation in the neighbourhood experiment.

Reference	Directions	Intersection
At stop sign	Turn left	1
At stop sign	Turn right	2
At traffic light	Turn left	3
At stop sign	Turn right	4
At stop sign	Turn right	5
At intersection	Turn right	6
At traffic light	Turn left	7
At intersection	Keep straight	8
At stop sign	Turn right	9
At the end of the road	Park	-

possible to see that the R-ECMS algorithm returns the desired charge sustaining operation by the end of the cycle wheres the ECMS returns a much lower SOC level.

The neighbourhood area provides the right setting for comparing both algorithms. Note that the R-ECMS returns an SOC profile where at every stop, the SOC is boosted back to the initial value of 6.5 %. That occurs because the algorithm is optimized to return to 6.5% by the end of the mission but does not known when it is since it has no information about the journey in a manual driving scenario. Therefore, every stop is treated as a potential end of mission.

Given its low speed stop and go characteristics, the neighbourhood environment returns a lower MPG compared to the values assessed in the stardard drive cycles. Also, the presence of other vehicles and pedestrians, and the necessity to respect traffic control contribute for the rapid transients in the velocity profile. That analysis also supports the idea detailed in Chapter 3, which states that real-driving (subjected to diverse driving conditions) contributes to lower fuel economy when compared to drive cycle assessment.

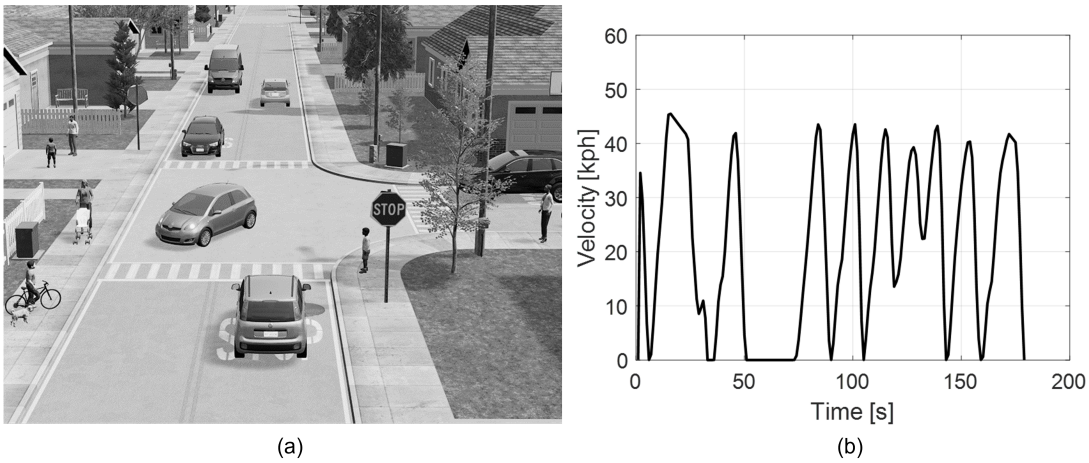

Figure 5.20: Snapshot of the ego vehicle in the neighbourhood environment (a) and the respective speed profile (b).

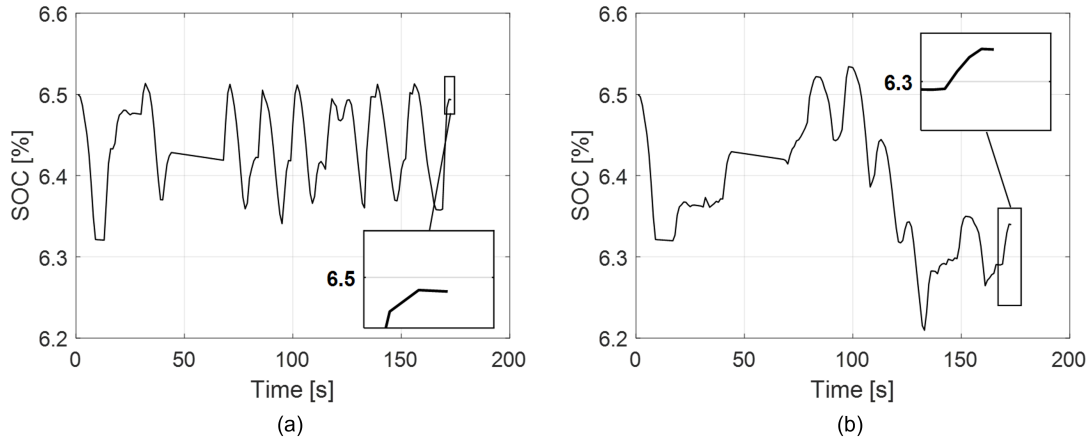

Figure 5.21: SOC profiles produced by the R-ECMS (a) and the ECMS (b) for the real-time assessment in the neighbourhood area.

Express way

In the express way experiment the driver follows the path to a highway environment and completes a circuit in the map described in Chapter 2.

Table 5.22 details the path taken. Figure 5.22 shows the velocity profile extracted from the experiment and a sample picture of the ego vehicle inserted in the express way environment. The driver style, behaviour and compliance are the same as in the previous experiment.

Table 5.22: Navigation in the express way experiment.

Reference	Directions
At express way entry	Entry to the right
At the acceleration lane	Increase velocity to be compatible with traffic
At the merging lane	Merge with incoming traffic
At express way	Follow circuit changing lanes when necessary
At exit	Exit to the right
At deceleration lane	Decrease velocity to be compatible with traffic
At intersection	Merge with incoming traffic
At the end of the road	Park

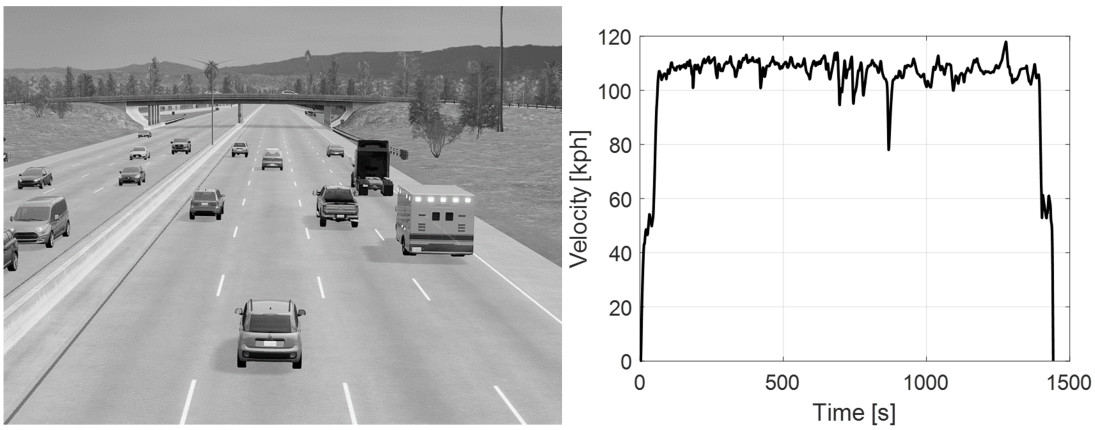

Figure 5.22: Snapshot of the ego vehicle in the express way environment (a) and the respective speed profile (b).

Figure 5.23 depicts the SOC profile of both algorithms. The R-ECMS deals well with the cycle and outputs a charge sustaining operation. The ECMS does not deliver the same operation and allows a breach of the minimum value of 5.0 %.

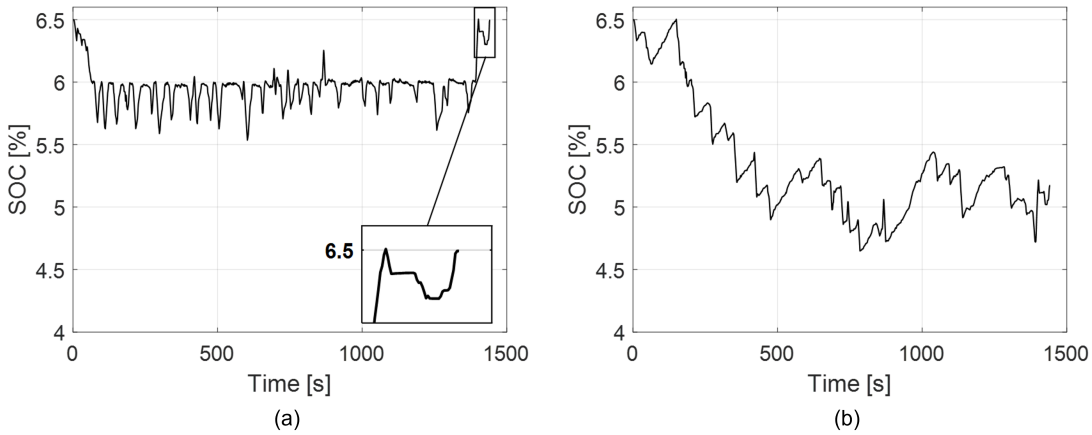

Figure 5.23: SOC profiles produced by the R-ECMS (a) and the ECMS (b) for the real-time assessment in the express way.

In terms of fuel, the R-ECMS consumed 47.20 g and 1564.30 g for the neighbourhood and express way scenarios, respectively. That rivals with the corrected ECMS results of 45.11 g and 1517.80 g in the same cycles.

Although the corrected consumption of the ECMS is lower than the R-ECMS results, its inability to provide a consistent charge sustaining solution at each stop and end of mission and the lack of flexibility toward drivability controls are considered major disadvantages that makes its applicability unfeasible.

5.5 Discussions

This section discusses the previous results and provides useful considerations regarding adding an APU to a BEV model.

5.5.1 Performance Considerations

The driving simulator provided a test bed for evaluating the performance impacts of adding the APU to the BEV in the making of the BEVx. Overall, the addition mass was found to decrease performance, as expected.

The results indicate that gradeability should be the greatest concern since its average deterioration is the highest among the performance manoeuvrer, 11.05 %.

For non-wot manoeuvres such as launch-ability, it is possible to improve the verified performance by recalibrating the pedal map to a more aggressive response. Nonetheless, for wot manoeuvrer such as acceleration, tip-in, and gradeability no control method would compensate that deterioration.

5.5.2 Charge Sustaining Compliance

The first requirement for the EMS is that it provides a charge sustaining operation. It was demonstrated that both real-time algorithms comply with such criteria for the drive cycles they were optimized. In addition they also provide the desired operation under the human-driven 5-Cycle procedure.

Interesting to note, R-ECMS and ECMS return very similar equivalent parameters. Table 5.23 compares the equivalence factors achived through parameter optimization and statistic distribution.

Table 5.23: Equivalence factors for the R-ECMS and ECMS algorithms.

Method	Eq. charge factor	Eq. Discharge factor
R-ECMS	1.5577	5.9779
ECMS	0.9368	5.7040

We must be careful comparing the parameters since they act differently in each

algorithm. In the ECMS the equivalence factors directly convert electric energy in fuel mass while in the R-ECMS they convert the residual power after the expected regeneration is accounted for. Because the the R-ECMS accounts for future credit of regen energy, it is expected to penalize more charging events. That is verified in the results. As for discharge, both algorithms present very similar values. That is justified by the fact that in the BEVx all propelling energy comes from the battery through the traction motor.

For experiments with drive cycles different that the ones used in the optimization, the R-ECMS algorithm has demonstrated more consistency, respecting the final SOC deviation constraint in all cases. The ECMS on the other hand has shown a conservative control output, providing excessive charging events and finishing the cycles with surplus of SOC.

5.5.3 Fuel Efficiency and Range

Once the charge sustaining compliance is checked and both algorithms are constrained to the same SOC deviation requirement, it is possible to compare their expected fuel consumption under the 5-Cycle procedure.

As expected, DP provides the most efficient fuel path. That makes DP the benchmark for fuel consumption. Without considering drivability constrains, the ECMS algorithm has shown a insignificant better match to DP results when compared to the R-ECMS, 84.7 % against 83.7 %.

That result is appropriate to evaluate the ability of the algorithm to pursue efficiency, but it is not applicable in real life since no drivability requirements are added. Most important than providing a fuel efficient solution, the algorithm should be robust

enough to hold that performance once other controls are added to improve realistic powertrain behaviour.

For the sake of investigating the impact of the addition of the MDT to the controller, and compiling the final label results for the BEVx, the 2-Cycle and 5-Cycle procedures are performed for the R-ECMS in its final configuration. Table 5.24 shows the expected label results for the BEVx with the R-ECMS EMS in electric (charge depleting) and hybrid (charge sustaining) modes, respectivly.

Table 5.24: Final label results of the BEVx model managed by the R-ECMS EMS.

	MPGe (Electric)	MPG (Gasoline)	Miles on Electricity	Total Range
BEVx Model	108.0	55.50	80.2 mi	160 mi

5.5.4 Algorithm Robustness

Another test case associated with robustness is to verify the algorithms performance for drive cycles they were not optimized for. Here the US06 drive cycle is used to evaluate that ability of the R-ECMS in contrast to the ECMS approach. The SOC profile is depicted in Fig. 5.24.

Even without being optimized for the US06, the R-ECMS algorithm outputs a charge sustaining operation with final SOC deviation of 0.005 %. The ECMS on the other hand ends up charging the battery creating an SOC deviation of 6.69 %. That indicates that for real-life situations, where the velocity profile is unknown and varies depending on driving conditions, the R-ECMS will output a much more consistent operation than the R-ECMS. That gives drivers predictability and heps with lowering range anxiety.

In fact, that is verified in both real-world emulation experiments that the ECMS

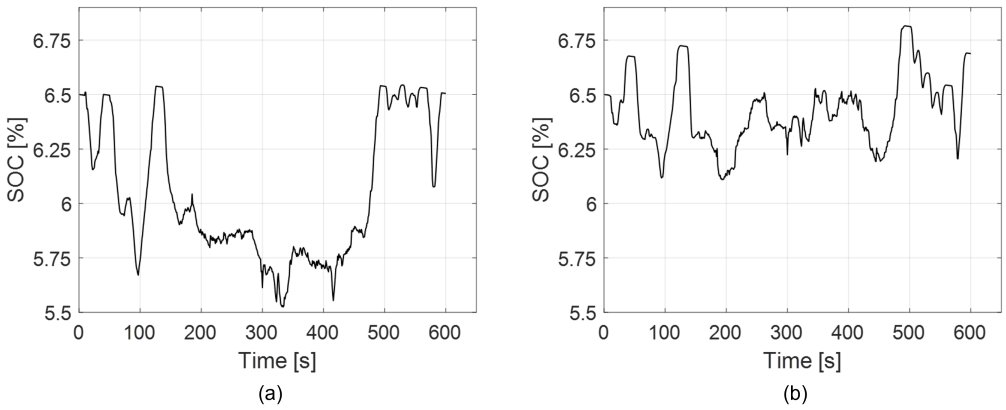

Figure 5.24: SOC profile for the R-ECMS (a) and ECMS (b) on the US06 cycle.

algorithm outputs a surplus of SOC while the R-ECMS algorithms fulfils its charge sustaining purpose

5.5.5 Modes of Operation

Another important feature to discuss is how the transition between charge depleting to charge sustaining operation is handled by the algorithm. To evaluate that ability of the R-ECMS algorithm, the single cycle test is performed iteratively from max SOC until it reaches the charge sustain operation. No additional control rule is created, the purpose is to evaluate the algorithms ability to transition automatically.

In the figure, the small zoom box shows the moment the SOC enters the charge sustaining mode in the R-ECMS algorithm, reaching the target SOC by the end of that cycle. The R-ECMS method provides a natural automated transition from charge depleting to charge sustaining mode. That is justified by its cost function (Eq. 5.8 that uses as a target reference the charge sustaining SOC level. Therefore, whenever SOC is greater than that target, the algorithm computes a surplus of SOC

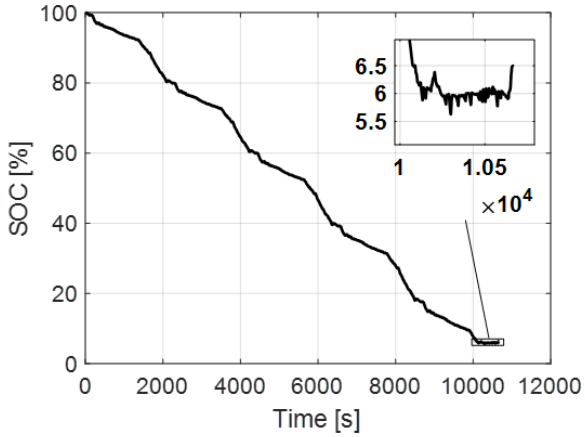

Figure 5.25: SOC profile for the R-ECMS algorithm under the single cycle test procedure for evaluation of the transition between charge depleting to charge sustaining operation.

and the cost of electric energy goes negative.

That configures an advantage of the R-ECMS over the ECMS method since the formeris known to require additional control rules and/or penalties to keep engine from turning on during charge depleting operation. Although of simple implementation, if not done correctly such corrections might cause delay in engine start that might contribute to excessive drops of SOC during mode transition.

Another two investigated modes of operation are known as ”hold” and ”charge” modes. Although not permitted in North-American BEVx, in Europe such vehicles can have a ”hold” function that allows drivers to select a level of SOC they want the vehicle to hold. Such function is key for maintaining vehicle performance during hill climbing and other high-power conditions. The charge mode, on the other hand, is a function that allows drivers to select a desired SOC level that the vehicle should achieve with charging.

Both functionalities are evaluated without creating additional control rules. The

hold mode is tested for different target SOCs with a fixed initial SOC of 100 %. The charge mode is tested for different target SOCs with a fixed initial SOC of 10 %. The single cycle test is used iteratively for testing both cases. Figure 5.26 shows sample examples of the hold mode and charge mode tests performed. For both functions, once target SOC is reached it does not go below 1.0 % of that value. Also, by the end of the cycle SOC variation to target respects the 0.01 % criteria defined in the parameter optimization.

Such functionalities are available with the R-ECMS algorithm again because of its SOC target-oriented cost function. Depending on what target soc is set the algorithm will pursue that target over the drive cycle. The same functions are not available with the ECMS.

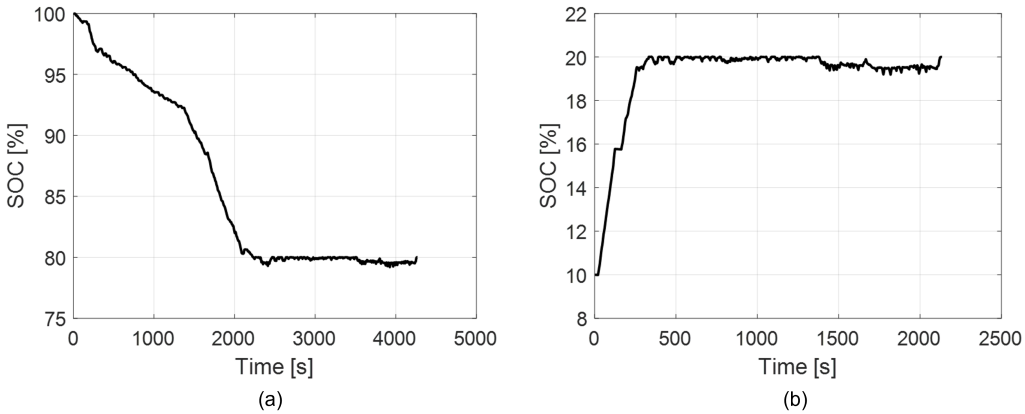

Figure 5.26: Examples of hold mode activated for 80.0 % SOC and charge mode activated for 20.0 %.

5.5.6 Applicability

Once drivability controls are added, in this study in the form of imposed MDT, the algorithm should be able to absorb that new condition and provide a fuel efficient

charge sustaining operation regardless.

The R-ECMS algorithm is able to absorb such change with minor impact to the final SOC as demonstrated in section 5.5.3.

It is possible to see that the ECMS algorithm is much more sensitive to the drivability control when compared to the R-ECMS algorithm (Tab. 5.20). In fact, it looses completely its ability of provide a charge sustaining operation when MDT is added. When MDT is greater than 20s, even the lower boundary of 5.0 % SOC is breached. In contrast, the R-ECMS adapts accordingly and provides a final SOC deviation lower than 0.1 % in almost every case evaluated.

That indicates that a drivability control added post optimization (which is a very usual practise in industry) will have a great impact to the ECMS algorithm, whereas the R-ECMS is more prone to accommodate such changes.

Furthermore, analyzing Figures 5.21 it is possible to see that the R-ECMS matches final SOC to initial SOC for every short trip inside the mission. That means every time the vehicle stops it reaches the charge sustaining level. Although that contributes to lower fuel economy in the overall cycle, that is a desirable behaviour from the perspective of real-time applicability. That is because in the real world the end of the mission is unknown, therefore every stop might be the last. Even in the express way experiment the R-ECMS provided a similar behaviour. In that case it reached the charge sustaining SOC level after exiting the road, even without stopping. Then after the following power demand it depletes battery but returns to the desired value when vehicle brakes to a halt.

5.6 Summary

The results have demonstrated that once optimized the R-ECMS strategy is effective in providing a charge sustaining operation for the cycles in which it was optimized (UDDS and HWFET) and for those which it was not (US06, SC03, and 5-Cycle procedure). It also accommodates the addition of controls that aim to improve drivability. The algorithm also provided an automated transition from charge depleting to charge sustaining operation. Moreover, it makes available a hold and a charge mode without the addition of any control rules.

As for theoretical fuel efficiency. The algorithm was compared to a global optimization method (DP) and the method that originated it (ECMS). The R-ECMS method has demonstrated competitive fuel consumption with slightly lower performance to the ECMS.

Therefore, the R-ECMS algorithm is a great candidate strategy for performing the energy management of HEVs. It is robust, flexible, allows different functionalities and does not sacrifice fuel economy to achieve that. Important to note that the R-ECMS is built aiming an autonomous application, where the deceleration profile is known or easily predicted. The results in the present chapter considered an estimated deceleration based on a factor that translates acceleration style into deceleration style. Such factor has been useful for human-driven applications, capturing the drive cycle essence and embedded driving conditions.

Chapter 6

Integrated Autonomous Driving and Energy Management

6.1 Introduction

Besides energy efficiency, another demand has been pushing automotive developers to the edge of technology, autonomous driving. The act of driving itself, although pleasant for enthusiasts, can be very dull and tiresome for the vast majority of the day-to-day situations that it is required. Furthermore, driving skill is very particular to each person even post training, therefore the safety level human drivers provide also vary. Several autonomous systems and features aim to mitigate those problems, adding comfort and safety in our life.

Systems such as adaptive cruise control (ACC), anti-lock brake system (ABS), automatic emergence braking (AEB), electronic stability control (ESC), automatic

parking, collision avoidance system (CAS), forward collision warning (FCW), hill descendant control (HDC), hill start assist (HSA), lane keeping system (LKS), lane departure warning (LDW), and tire pressure monitoring (TPM) are examples of ADAS. They require different levels of perceptual sensors and control actions over the vehicle to achieve each of their goals, separately these systems contribute to specific improvement of the previously mentioned. Together however, they are a key step toward full automation.

To better understand how they contribute to full automation it is necessary to list the different levels. As defined by SAE Reccomended Practice (2014) and illustrated in Fig. 6.1, there are six levels of automation, from no automation (level 0) to full automation (level 5). Up to level 2, it is the driver's responsibility to monitor the driving environment, level one being the one with driver assistance features able either to steer, brake or accelerate the vehicle but not all at the same time and not for long periods, some feature examples are ACC, LKS, and AEB systems. Level 2 represents partial automation, where both actions of steering and braking/propelling can be performed at the same time, within specific conditions. The combination of ACC and Lane Centering systems is a good example of level 2 automation. To be classified as level 3 to 5 the automated driving system should be able to take over the driver's responsibility to monitor the environment. Level 3 is called conditional automation, where the system performs the driving task but the fall-back system is still the human driver, that should be ready to take over when requested. Level 4 represents high automation, in this level, the system does not rely on the human fall-back response as much as before but it is still limited in regard to the driving modes which means it does not perform all driving tasks. In level 5 (full automation)

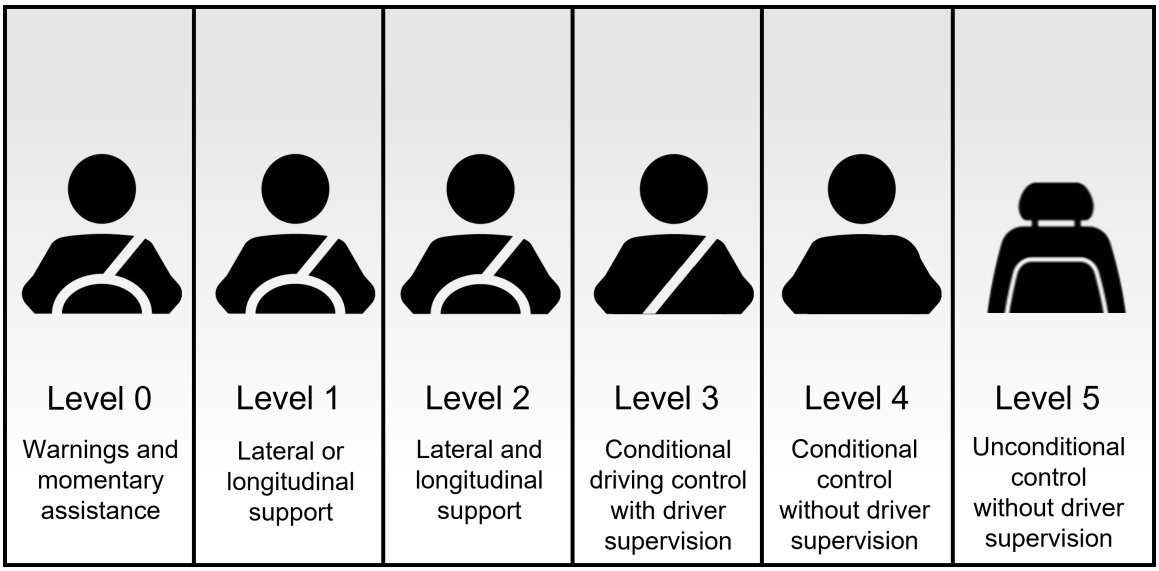

Figure 6.1: Autonomous levels according to SAE J3016, 2018.

the system is responsible for the whole driving task, from departure to arrival, it also does not rely on human to any level, it monitors the environment and has control over all the vehicle controls.

By analyzing the different levels of autonomy, one can conclude that integrating such functions to other vehicle systems is a requirement. Regarding functions that account for longitudinal control, that integration is even an opportunity to improve energy consumption.

This chapter presents an autonomous feature that performs longitudinal control in a mapped highway environment. The longitudinal control could be integrated to a level 2 system although elements of level 3 are also present. The feature leverages journey mapping to identify vehicle's location in the environment and output appropriate propelling and braking actions.

Such feature functions as a study case for the previously developed R-ECMS where its capability of output a cost-effective fuel solution is maximized by the presence of

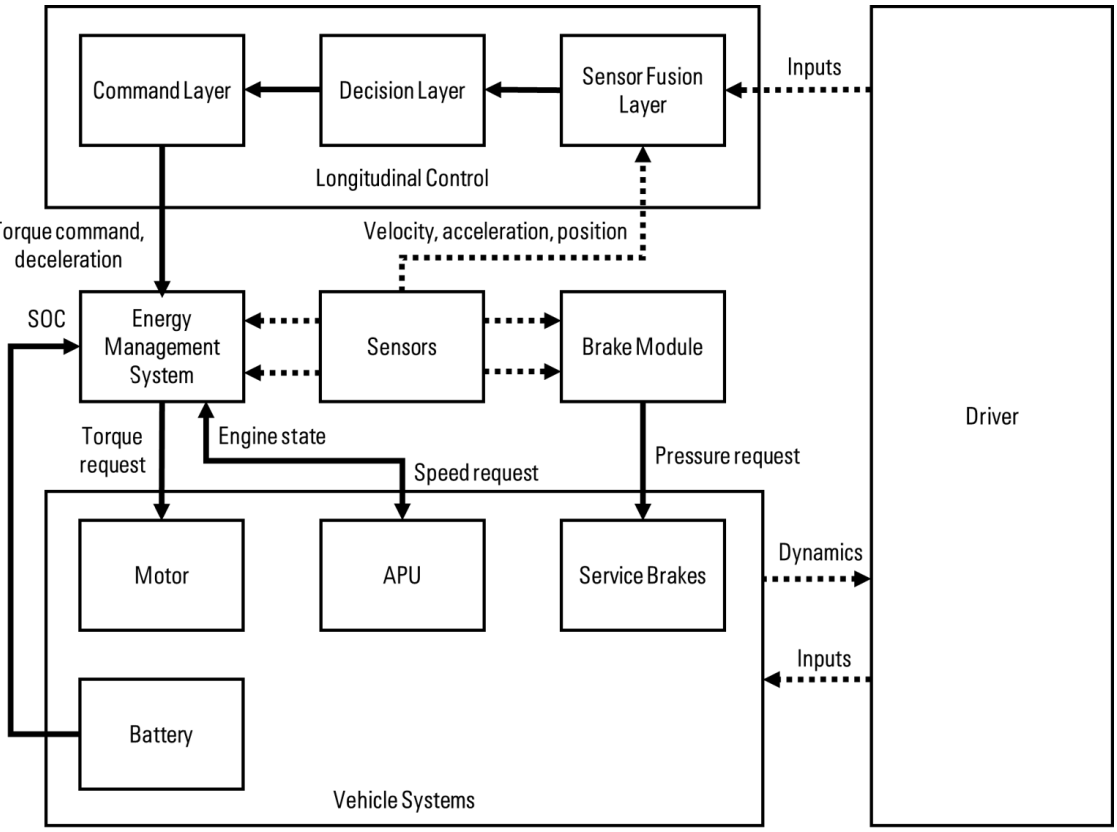

Figure 6.2: Control structure for the logitudinal control of the ADS integrated with EMS.

an autonomous driving systems. Figure 6.2 shows a diagram of control structure connecting the longitudinal controller to the EMS.

6.2 System Design

This section outline the designed functionalities, characteristics, and responsibilities within the longitudinal controller.

6.2.1 Functionality

The autonomous feature is available to driver upon entry into the mapped road if the vehicle's velocity is above 60 kph. The system then increases vehicle speed on the acceleration lane until reaching target speed. From the journey mapping requirement, target speed is set to 110 kph (express way speed limit), but could be user defined.

After activation, the longitudinal control behaves similarly to a cruise control. Once stabilization is reached, system will provide sufficient torque as to maintain target speed, balancing the road-loads. Driver maintains control of the direction of the vehicle and brakes as needed due to traffic. During braking events the propelling command is suspended returning once brake pedal position is back to rest.

System iteratively tracks vehicle position and upon exit, brakes the vehicle from cruising speed to releasing speed. From the journey mapping requirement, target speed is set to 60 kph, but could be user defined.

6.2.2 Control Layers

Sensor Fusion

Vehicle signals such as wheel speed, longitudinal acceleration, brake, and throttle pedal positions and vehicle location through GPS are sent to the sensor fusion that is responsible for detecting in which segment of the road the vehicle currently is. Such information is provided thanks to the mapping of the environment.

Longitudinal Controller

Once position and conditions are known the controller defines which action to take, i.e. whether to activate or not, and how much to accelerate the vehicle. The controller uses road speed limit as target speed. Then it defines the acceleration request to the command layer. The magnitude and profile of the acceleration request is a tunable parameter that is devised using drivability constrains and road geometry later detailed.

For exit manoeuvres, the command layer is responsible for defining the deceleration profile, just the same as it is responsible for the acceleration profile in entry manoeuvrer. That deceleration information is shared with the R-ECMS for maximizing the fuel economy on the cycle. In the decision process and quantification of the torque command it is important to account for road conditions, vehicle dynamics, and passenger feeling so the system outputs a safe and comfortable driving experience.

Command Layer

The command layer is activated by the controller and it computes the torque command to the ECU based on the acceleration request. To do so it assesses a longitudinal vehicle dynamics model that contains information about the vehicle's estimated road-load coefficients, mass, efficiencies and inertias.

6.2.3 Integration with Energy Management

In this section the signal exchange between longitudinal controller and energy management is outlined. As detailed earlier, the testing scenario is a blending between

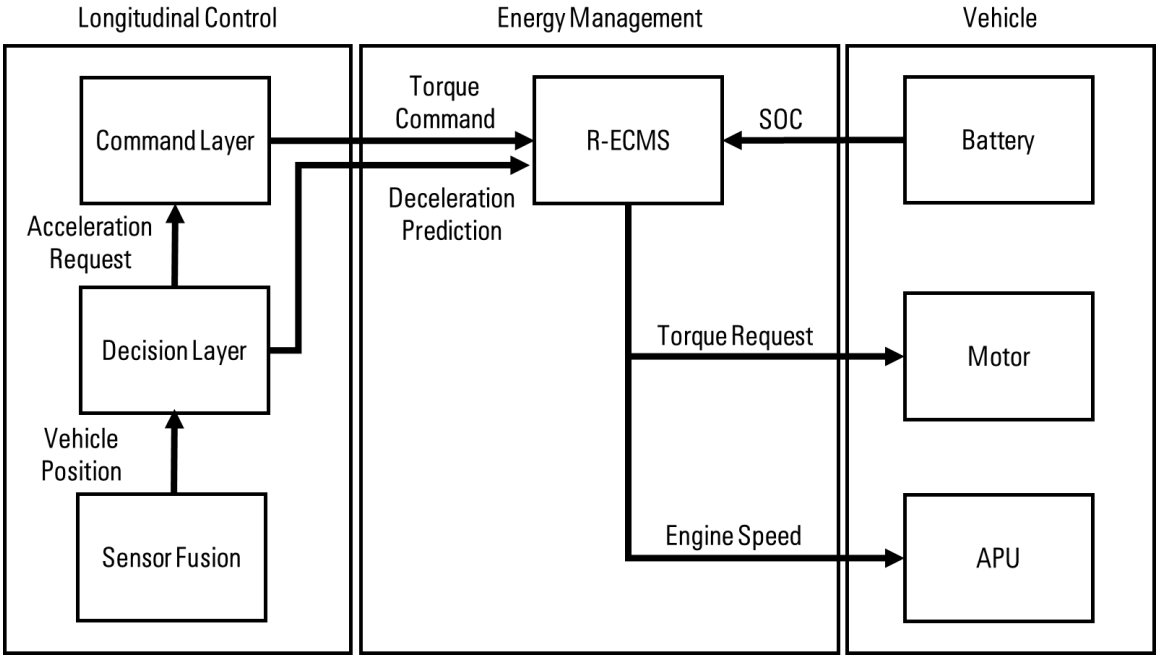

Figure 6.3: Signal exchange between longitudinal control and energy management systems.

manual and autonomous driving. Therefore, the EMS should be prepared for functioning regardless of the condition.

The R-ECMS method is chosen as the EMS given its benefits highlighted in Chapter 5. The core function of the R-ECMS depends on the expectation of the deceleration. That value is used in a vehicle dynamics model to compute a expectation of regeneration. Previously, that deceleration expectation was optimized as a parameter of the algorithm. Considering the autonomous scenario outlined in this chapter, where journey mapping provides the locations of each segment of the express way, that deceleration expectation can be substituted by an actual deceleration prediction that the longitudinal controller plans for the end of the trip. Figure 6.3 details the signal exchange and functionality of both functions in sync.

The R-ECMS algorithm is chosen as the most appropriate EMS for the present

application. The deceleration profile, key information for the R-ECMS algorithm to function is received from the longitudinal controller. For manual driving situations the deceleration expectation optimized in the previous chapter is used. The EMS receives the command torque and is responsible for sending torque and speed requests to motor and APU, respectively.

The feature is created in Simulink and loaded in the BEVx model on the driving simulator using the same method described in Chapter 2. Following, the real-time assessment of the systems performance.

6.3 System Constrains

To develop the autonomous feature, the functionalities should be bounded by calibrated thresholds and limits. Such system constrains become requirements in the development of the function.

6.3.1 Journey Mapping

To set the boundaries and targets of the autonomous feature, journey mapping is chosen. Here, the express way environment is used to illustrate the functionality of the systems. The environment is mapped according to its path. Longitudinal and lateral positions are depicted in Fig. 6.4. The map is composed of highway and peripheral roads that access it. The highway is a closed circuit with straights, light turns, and two rounded curves on its edges. Due to low variation in the vertical axis the road is considered to be flat. The complete journey is 41.5 km long.

The road speed limit is defined as 110 kph as to emulate several Canadian roads

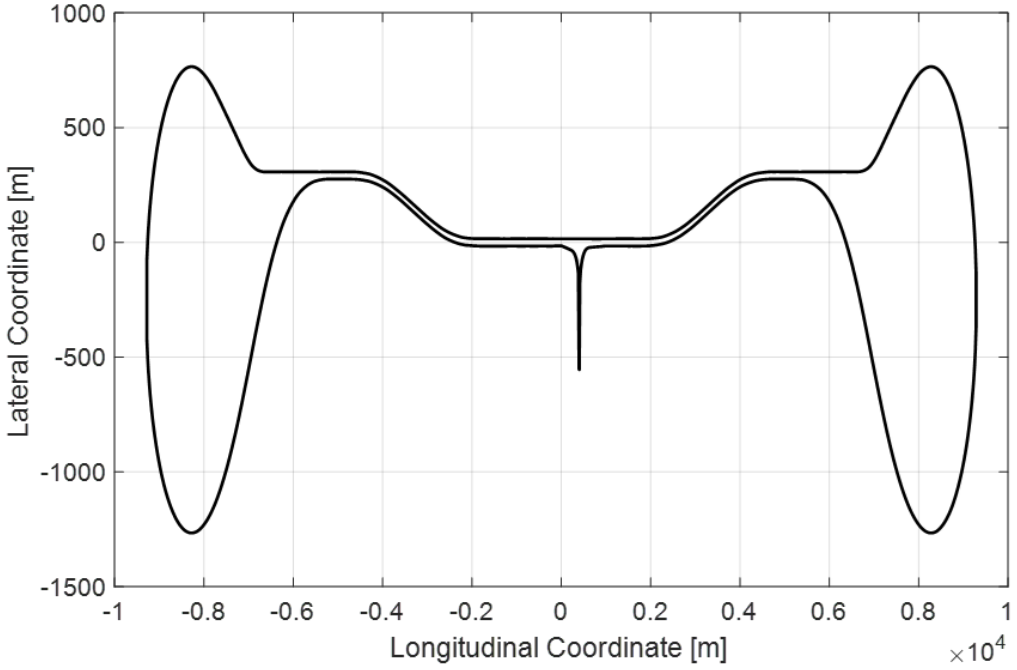

Figure 6.4: Longitudinal and lateral coordinates of the express way environment .

such as segments of Highway 401, 402, 404, and 417. Nevertheless, if real-time communication between highway and vehicle is available, a real-time speed limit can be informed from road to longitudinal control. That practise is specially useful when an accident is detected or when high traffic causes average speed to decrease abruptly. That sets the first boundary for the system: vehicle must not drive with velocity above speed limit.

Once the environment is mapped, it is possible to analyze its most relevant segments for the autonomous longitudinal controller.

Acceleration Lane

The acceleration lane is the lane at which the vehicles enters the road and merges with incoming traffic. For the current example, it is considered to start at the end of the turn that follows the express way entry. It composed of a single lane and is 300 m long in length. That sets the acceleration distance boundary for the longitudinal controller since the vehicle is required to merge with compatible velocity.

Middle Section

The middle section is everything on the road besides the acceleration lanes and exit lanes. In the present road the middle section has four driving lanes, an emergency lane on the far left and a shoulder on the far right. Driver and computer-driven vehicles can only drive on the driving lanes. The middle section composes the most part of the driving task.

Exit Lane

The exit lane is the lane at which the vehicles decelerate and exit the road, merging with incoming traffic in the peripheral roads. The journey mapping returns the characteristics of the current exit lane. It is composed of a single lane and is 150 m long. That sets the deceleration boundary for the longitudinal controller since vehicle is required to merge the peripheral roads with compatible velocity. Furthermore, before exiting the lane shows a sharp turn (to right). Therefore the deceleration event must be completed before reaching such turn.

Peripheral Roads

Peripheral roads are every other road that is connected to the express way. That include side perpendicular roads and bridge over the highway. Speed limit on the peripheral roads is 50 kph. In the proposed path, the length driven on the peripheral road before express way entry is 300m The autonomous driving feature does not activate at the peripheral roads.

Summary of the requirements

In summary, the journey mapping defined the following requirements

- On acceleration lane, function should drive vehicle from current to target speed within 300 m.
- On middle section, function should balance torque request and road loads as to maintain target speed.
- On exit lane, function should decelerate vehicle from target speed to 60 kph within 150 m.
- On peripheral roads, function should not activate.

6.3.2 Vehicle Dynamics

Once the environment boundaries are set, it is necessary to bound the behaviour of the system with respect to driver perception. The objective is to provide a system that delivers intuitive dynamics with smooth transitions from manual to autonomous operation.

The vehicle is required to perform the acceleration, cruising, and deceleration events maintaining an appropriate level of safety and comfort. Such criteria is defined by analyzing vehicle dynamic behaviour.

This section performs different tests as to define the vehicle ability to meet the road requirements and the impact of each control on driver's feeling. It evaluates the two key events related to driver perception of comfort: the acceleration event, and the deceleration event. Tests are conducted on the driving simulator in the straight road environment.

Acceleration Calibration

The acceleration event happens in the acceleration lane and consists of increasing vehicle's longitudinal velocity to the target velocity. A minimum velocity threshold of 60 kph is defined for function activation. That means system will not activate below that value. The metrics used for evaluating the acceleration event are distance travelled from 60 kph to 110 kph and jerk measurements. In addition, subjective feedback from the driver is included in the results. The former is chosen as to assure system compliance with road constrains, the latter is chosen as a measure of driver comfort Huang and Wang (2004). Tests are conducted on the driving simulator in the straight road environment.

Since the decision layer communicates acceleration request to the command layer, the effects of different acceleration requests are assessed. First, five step inputs are analyzed with ranges from 0.1 g to 0.5 g. The figure shows that besides provoking jerk at activation (in), the system provokes jerk upon reaching the target velocity and releasing (out). The results for the step input of 0.3 g is depicted in Fig. 6.5. Table

6.1 shows the results for all tested step requests.

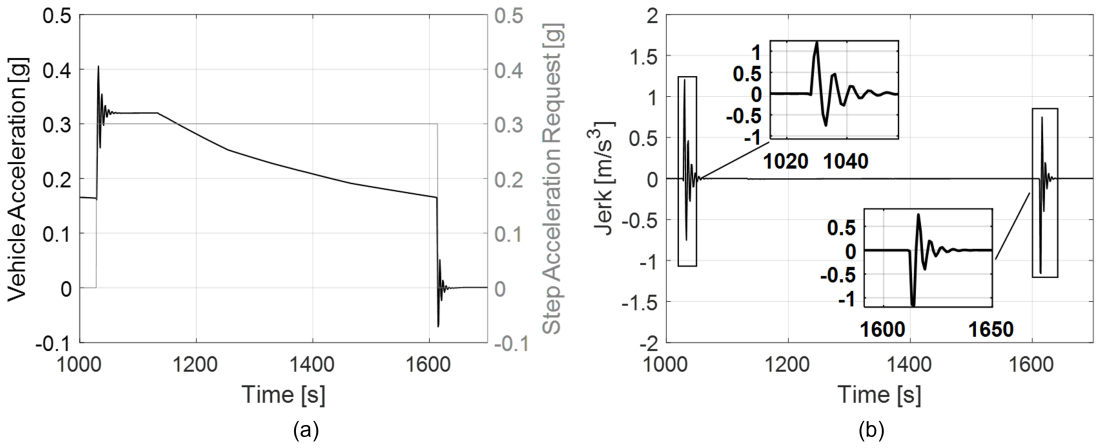

Figure 6.5: Vehicle response for step input of 0.3 g - acceleration request.

Table 6.1: Results for the step acceleration request experiment.

Input	Max sustained acc.	Max jerk (in)	Distance	Driver feedback
0.1 g	0.1075 g	0.414 m/s^3	306.5 m	Lack of performance
0.2 g	0.2141 g	0.510 m/s^3	163.0 m	Smooth and progressive
0.3 g	0.3195 g	1.205 m/s^3	142.6 m	Lack of progressiveness
0.4 g	0.3521 g	1.524 m/s^3	141.3 m	Lack of progressiveness
0.5 g	0.3522 g	1.616 m/s^3	141.0 m	Lack of progressiveness

It is possible to see from the figure and results that every tested input besides the 0.1 meet the distance requirement of 300 m. Nevertheless, for acceleration requests higher than 0.2 g the vehicle response is saturated by its ability to propel (driveline torque limitations). Therefore, vehicle cannot output a constant steady acceleration throughout the entire acceleration time for values higher than 0.2 g. That lack of progressiveness is perceived by the driver during the tests. As for jerk values, the greater the magnitude of the input the greater the jerk at function activation.

Given the non-linear behaviour of the vehicle for a step input, it is advised to modulate acceleration request, creating a ramp that blends with driver action. That

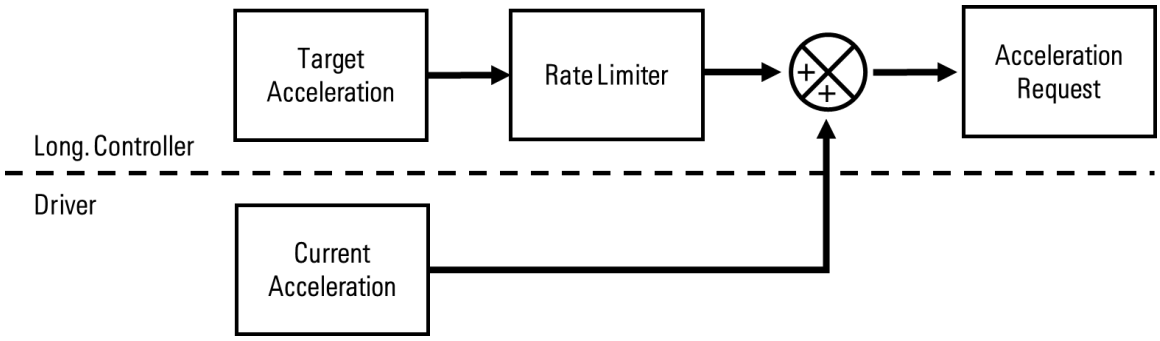

Figure 6.6: Blending strategy using rate limiter and driver's current acceleration.

should reduce the jerk and provide a more intuitive dynamic behaviour.

To that end, a rate limiter is applied. That tool creates a ramp based on the target acceleration by limiting the first derivative of its value passing through. To provide a smooth transient between driver and controller, the current acceleration is added to the output of the rate limiter as depicted in the diagram of Fig. 6.6. Important to note that the use of a rate limiter without the addition of the current acceleration may cause loss of performance jeopardizing drivability.

The max output changes (gradient) is manually calibrated. Five values from 0.02 to 0.1 are tested. The increments of each value is 0.02. From the previous analysis, 0.3 g is chosen as target acceleration.

The results for the gradient of 0.04 is depicted in Fig. 6.7. Table 6.2 shows the results for all tested step requests.

Table 6.2: Results for the ramp acceleration request experiment.

Rate	Max sustained acc.	Max jerk (in)	Distance	Driver feedback
0.02	0.1058 g	0.531 m/s^3	375.4 m	Lack of performance
0.04	0.1662 g	0.011 m/s^3	226.0 m	Transition unnoticed
0.06	0.2641 g	1.088 m/s^3	149.3 m	Good balance, kick
0.08	0.2946 g	1.272 m/s^3	143.5 m	Lack of progressiveness
0.1	0.3223 g	1.662 m/s^3	141.4 m	Lack of progressiveness

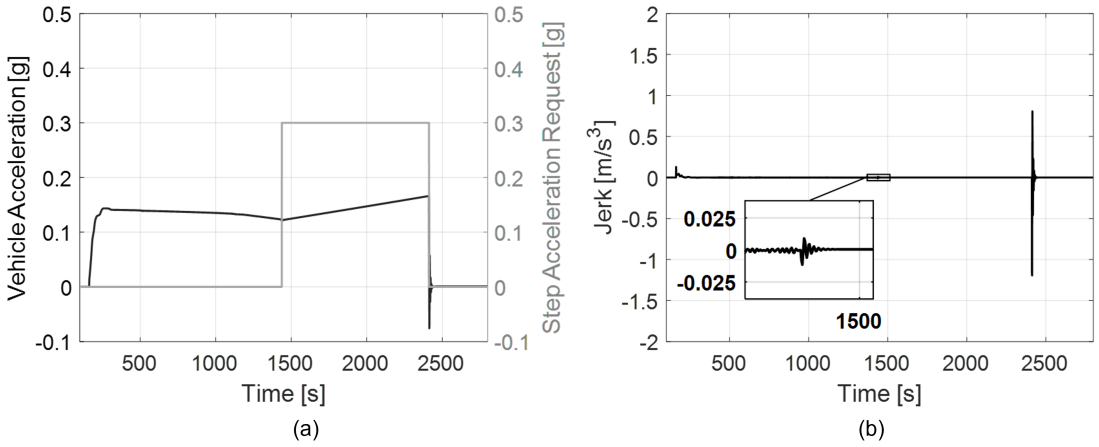

Figure 6.7: Vehicle response for ramp input with rate limiter of 0.04 - acceleration request.

It is possible to see from the Fig. 6.7 and jerk results in Tab. 6.2 how the blending strategy promotes a smoother transition. For the current tests, the rate of 0.04 is observed as the less impactful to longitudinal comfort. Plus it meets the road requirements of distance travelled from 60 kph to 110 kph.

Deceleration Calibration

It is also important to calibrate the longitudinal controller for the deceleration event. The deceleration event happens in the exit lane and consists of decreasing vehicle's longitudinal velocity to the exit velocity. In this case, that means from 110 kph to 60 kph.

Similar methodology to the calibration of the acceleration is applied. First, a analysis of a step input deceleration request, then the application of the rate limiter to improve comfort. Distance travelled, jerk, and driver feedback are also used as metrics. The results for the step inputs can be seen in Tab. 6.3

Following, the analysis for the application of the rate limiter on Tab. 6.4. The tool

Table 6.3: Results for the step deceleration request experiment.

Input	Max sustained decel.	Max jerk (in)	Distance	Driver feedback
0.1 g	0.1033 g	0.825 m/s^3	319.9 m	Lack of performance
0.2 g	0.2062 g	1.463 m/s^3	160.6 m	Lack of performance
0.3 g	0.3096 g	1.205 m/s^3	121.2 m	Good balance, kick
0.4 g	0.3862 g	1.524 m/s^3	116.6 m	Aggressive, tire screech
0.5 g	0.3862 g	1.616 m/s^3	115.6 m	Aggressive, tire screech

is applied in the same fashion as in the acceleration calibration, same slews are tested. To analyze the SOC recuperation, the power output from the braking manoeuvrer is fed to a battery model.

Table 6.4: Results for the ramp deceleration request experiment.

Rate	Max sustained decel.	Max jerk (in)	Distance	Driver feedback
0.02	0.084 g	0.292 m/s^3	571.5 m	Lack of performance
0.04	0.125 g	0.512 m/s^3	357.3 m	Transition unnoticed
0.06	0.160 g	0.771 m/s^3	272.5 m	Good balance
0.08	0.194 g	1.055 m/s^3	215.4 m	Good balance, kick
0.1	0.223 g	1.241 m/s^3	183.8 m	Best performance

The results show that adding progressiveness to the deceleration profile increases considerably the distance travelled. No candidate rate was able to return a final braking distance compatible with the required by the road. Therefore, the less aggressive yet compliant solution from the step input is chosen, step deceleration request of 0.3 g.

6.4 Real-time Assessment

6.4.1 Dynamic Performance

The evaluation of the system performance on the road an experiment is performed without traffic with vehicle driving on the far right lane throughout the entire path. Table 6.5 shows the results for the experiment in terms of distances travelled, acceleration, peak jerk, and driver feedback.

Table 6.5: Performance of the system in the express way without traffic.

Event	Peak acc.	Peak jerk	Distance	Driver feedback
Acceleration	0.1325 g	0.057 m/s^3	324.2 m	Good transition, progressive
Cruising	0.0275 g	0.028 m/s^3	39760 m	Smooth and comfortable
Deceleration	0.3150 g	2.379 m/s^3	147.9 m	Aggressive, improve comfort

In addition, Fig. 6.8 shows the velocity profile of the test, the acceleration and jerk.

The results show that once applied to the mapped environment, the dynamic response of the vehicle varies. Acceleration event is progressive and comfortable.

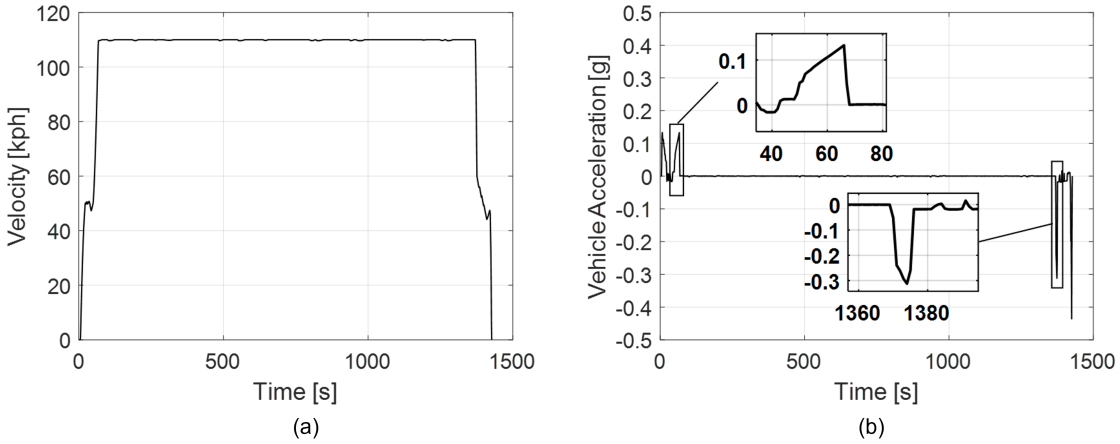

Figure 6.8: Evaluation of system performance in a non-traffic scenario.

Transition between driver and system acceleration is almost unnoticed Although vehicle does not reach target velocity before entering the road, entry velocity of 107.9 kph is considered adequate. Cruising behaviour is smooth and comfortable, single jerk events are noted but imperceptible to driver. The deceleration event is the most invasive manoeuvrer but such behaviour is necessary to achieve path requirements.

6.4.2 Energy Consumption

For the energy assessment the same methods applied in Chapter 5 are used. The consumption is evaluated for a scenario with swarming traffic.

Since the objective is to evaluate the charge sustaining ability and consumption of the R-ECMS algorithm in such scenario, it is assumed that mission starts with SOC at charge sustaining level of 6.5 %. The previously optimized R-ECMS plus MDT criteria is used. It is important to highlight that the autonomous feature provides future information of the braking profile (thus expected regenerative braking power) at the exit of the road. Information about destination, route, traffic, and weather are not included.

Figure 6.9 shows the velocity profile and the resulting SOC profile for the experiment. Table 6.6 summarizes the energy consumption results.

Table 6.6: Autonomous driving energy consumption test with traffic.

MPG	Final SOC deviation	Fuel Consumption
45.97	0.001 %	1484.3 g

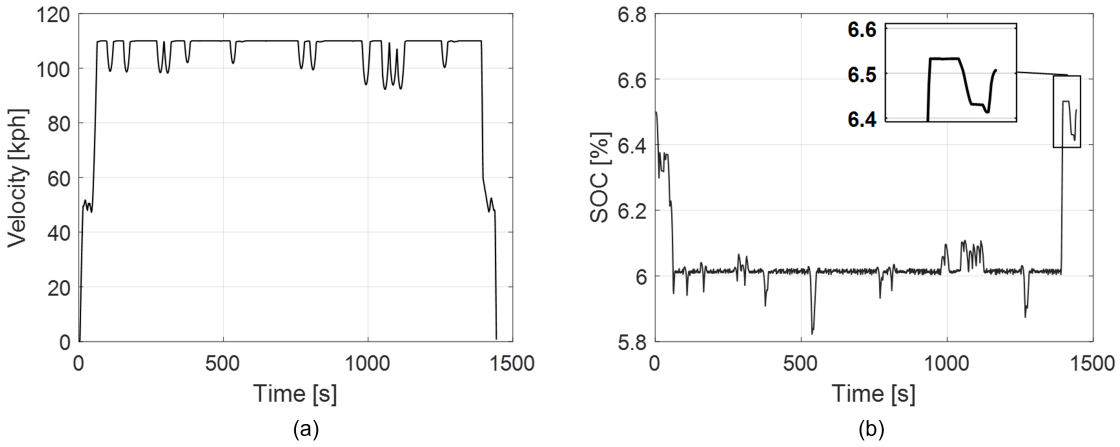

Figure 6.9: Velocity profile resulted from the longitudinal control (left) and SOC profile resulted from the EMS (right) in the autonomous driving scenario.

6.5 Discussions

From the real-time assessments it is possible to conclude that the longitudinal controller built based on journey mapping and vehicle dynamic considerations delivers an adequate overall performance.

Drivability is successfully calibrated for the acceleration event. Acceleration targets are selected based on vehicle response and driver feedback. The integration of a rate limiter and driver's current acceleration contributes to a smooth human-machine transition and a comfortable ride. Cruising is also comfortable and effective. Vehicle behaves with smooth and intuitive operation. The results suggest that a more aggressive/responsive acceleration controller might be preferred since the performance in this event has shown tight tolerance with target distance. As for the deceleration control, the tight road requirement is met with aggressive deceleration.

Regarding energy management, the R-ECMS delivers an effective charge sustaining operation. The final energy economy result shows a slight deviation from the

expected label results computed in Chapter 5. That is justified by the presence of driving conditions such as traffic and road inclination.

6.6 Summary

This chapter devised an integrated an automated longitudinal control and energy management. The autonomous feature is outlined and its layers and functionalities are defined. Its requirements are set based on journey mapping and its calibration accounts for vehicle dynamics and driver perception.

Driving simulation is used to be able to generate a realistic environment to calibrate and test the function. In addition, it allows for adding the driver feedback to the design.

The EMS devised in Chapter 5 has shown robustness to the new mission. The deceleration expectation is here replaced with the deceleration prediction from the longitudinal control which enhances the algorithm capability to provide a charge sustaining operation.

The overall dynamic performance of the system is acceptable. The longitudinal controller just meets the path requirements with tolerances.

Further research should investigate different methods for controlling vehicle drivability as well as vehicle to road connectivity.

Chapter 7

Conclusions and Future Work

7.1 Conclusions

This research investigated new methods and assessment tools for the development of electrified powertrains. Energy management is reviewed thoroughly and classified. The current status of consumption assessment methods is also analyzed. Vehicle models of various levels were created. The importance of driving conditions is highlighted and techniques to include them in the EMS are listed with highlight to the journey mapping.

A novel algorithm is proposed originated from the well researched ECMS, the R-ECMS. In this novel approach, driving style and conditions are added to the cost calculation indirectly through the deceleration expectation parameter. The algorithm is applied to a BEVx model for investigation of its applicability. Besides being competitive in terms of fuel efficiency, matching DP's cost in 84.7 %, when compared to its peer it is more robust against drivability calibration, more flexible to diverse drive cycles and conditions, and enables different modes of operation. That solves many

issues associated with ECMS that have been keeping it from being implemented generally. Finally, the algorithm is assessed in an autonomous driving context, integrated to a longitudinal control feature. Functionality is defined based on journey mapping and vehicle dynamics requirements.

Regarding assessment, this thesis presented a comprehensive survey on driving simulation technology, depicting it as an alternative to bridge the gap between simulation and testing. The simulator is used to create a real-time baseline vehicle and then to analyze impacts caused by its modification to a different topology. Using driving simulation allowed testing consumption, performance and drivability. In addition, it allowed including driver feeling, actions, and expectations in the design of the new functions. Furthermore, it allowed the creation of environments such as real-life scenarios and proving grounds.

The baseline BEV model built on the simulator demonstrated high accuracy to the experimental data, for consumption (94.4 %), range (97.2 %) and performance (88.75-93.26 %). Once updated to BEVx, the simulator responds to the changes as expected and shows the expected performance deterioration. That is also relevant in drivability analysis, where the modification of control gains can be perceived both by driver while executing the mission and model in the form of jerk and acceleration peaks.

Besides being a great tool for accelerate design, driving simulation also contributes to lowering the emissions associated with vehicle development. In a world scenario where every piece of emission contributes to environment deterioration, the experiments presented in this research amounted countless miles but not a single drop of gasoline was consumed.

7.2 Future Work

Future work is proposed based on three streams of work presented in this thesis: driving simulation, energy management, and autonomous driving system.

Regarding driving simulation, the present co-simulation structure that connects vehicle model to a powertrain template enables the testing of numerous powertrain configurations and control methods in real-time. It also allows for the verification of the behaviour of a powertrain in realistic environment and when connected to other vehicle systems. Therefore, it is expected that such structure is used in future research as a testing platform that allows driver-in-the-loop assessment of the newest technology developed at the McMaster Automotive Resource Centre. That will enable new designs to include driver perception, drivability and performance calibration in early stages of development.

Furthermore, the co-simulation template allows for diversification of component models. Therefore, leveraging the other labs and equipment to build more accurate models that then have their controls calibrated using the simulator. One example is to extract pedal maps and modes of operation of current vehicles using the chassis dynamometer and digital twining such vehicles in the simulator with that information. Similarly, powertrain dynamometer and battery cycler can be use to feed accurate models into the simulator and to receive realistic testing loads from the simulator. In that way, it is possible to have driver and hardware-in-the-loop assessment and a blended design that leverages virtual and experimental tools which shows a great potential for research and industry application.

With respect to the inclusion of the driver to the design, a potential future work is a detailed evaluation of the impact of different driver styles and actions to fuel

consumption accounting for diverse demographics, environments, and scenarios.

The present work has not investigated noise vibrational and harshness (NVH) impact to driver comfort. Given the simulator's ability to create and reproduce accurate noise models, that poses another great future research topic, especially considering the increasing demand of that type of analysis for electrified vehicles.

Regarding EMS, especially the R-ECMS algorithm developed in this thesis. The present work defines the R-ECMS and shows its improvements compared to the algorithm it is originated from, the ECMS. For future application, the R-ECMS algorithm should be exposed and compared to different benchmark algorithms, including NN and RB approaches. In addition, more diverse scenarios should be created including grade and weather variations.

Further investigation on different optimization techniques and methods for computing the regen-equivalence factors and the deceleration expectation also shows great potential. Finding more accurate ways of predicting the deceleration effort is expected to enhance the fuel efficiency provided by the R-ECMS algorithm and it is therefore recommended. In that area, the application of ML algorithms that classify and quantify driver aggressiveness is indicated as potential improvement and worths investigation.

Regarding the autonomous driving system, a longitudinal controller is presented as to support the integration with the R-ECMS algorihtm in a simple configuration. Although sufficient for the current scope, the initiative provided insights of relevant future work in that area.

In the conception of the autonomous feature, a hazard analysis is highly recommended, the system-theoretic process analysis (STPA) being a good candidate for

the task as it assists in defining control rules that will prevent undesired behaviour. Within that same spectrum, system performance in light of functional safety could also be explored in future works using the simulator as testbed. That should be done leveraging the planar model to assure lateral stability of the controls in realistic scenarios.

The planar model can also be used to integrate a lateral control to the current longitudinal control in the making of a higher level autonomous system. In addition, the means in which road and vehicle communicate should be further explored and reproduced using the simulator.

Finally, the relationship between autonomous driving and driver/passenger perception can also be further explored using the simulator, in a driver-centred analysis. Potential studies include but are not limited to human-machine transition (and vice versa), perception of comfort and safety, interactiveness, and user experience with the display and controls.

7.3 Publications

7.3.1 Journals

L. Bruck, A. Emadi, and K. P. Divakarla, "A review of the relevance of driving condition mapping and vehicle simulation for energy management system design," *International Journal of Powertrains*, vol. 8, no. 3, pp. 224–251, 2019.

L. Bruck, B. Haycock, and A. Emadi, "A review of driving simulation technology and applications," *IEEE Open Journal of Vehicular Technology*, vol. 2, pp. 1–16, 2021.

L. Bruck, A. Emadi, “Integrated energy management strategy and autonomous driving system: a driving simulation study,” (In progress)

7.3.2 Conferences

M. Haussmann, D. Barroso, C. Vidal, **L. Bruck** and A. Emadi, "A Novel Multi-Mode Adaptive Energy Consumption Minimization Strategy for P1-P2 Hybrid Electric Vehicle Architectures," *2019 IEEE Transportation Electrification Conference and Expo (ITEC)*, 2019, pp. 1-6.

L. Bruck, S. Veldhuis and A. Emadi, "Selection Method of a Driving Simulator Motion System," *2019 IEEE Transportation Electrification Conference and Expo (ITEC)*, 2019, pp. 1-6.

L. Bruck, S. Amirfarhangi Bonab, A. Lempert, A. Biswas et al., "An Iterative Histogram-Based Optimization of Calibration Tables in a Powertrain Controller," *SAE Technical Paper* 2020-01-0266, 2020.

L. Bruck, A. Lempert, S. Amirfarhangi Bonab, J. Lempert, et al., "A Dynamic Programming Algorithm for HEV Powertrains Using Battery Power as State Variable," *SAE Technical Paper* 2020-01-0271, 2020.

L. Bruck, and A. Emadi, “A Methodology for Modelling of Driveline Dynamics in Electrified Vehicles”. *SAE Technical Paper* 2021-01-0711, 2021.

L. Bruck, S. Rahimifard, S. Habibi, and A. Emadi, “Leveraging Driving Simulation for Designing an Estimator of Road-Load Coefficients” *Proceedings of the Driving Simulation Conference 2021 Europe VR*, Driving Simulation Association, Munich, Germany, 2021, pp. 117-122

L. Bruck, and A. Emadi. "A New Regen-based Energy Management Strategy

for Online Control of Hybrid Powertrains" *2021 IEEE Transportation Electrification Conference & Expo (ITEC)*, 2021, pp. 762-766.

E. Louback, F. Machado, **L. Bruck**, P. J. Kollmeyer, and A. Emadi, "Real-time performance and driveability analysis of a clutchless multi-speed gearbox for battery electric vehicle applications" *2022 IEEE Transportation Electrification Conference and Expo (ITEC)*, 2022, pp. 1041-1046.

M. Naguib, **L. Bruck**, and A. Emadi, "Neural network-based online energy management for multi-mode power split hybrid vehicles" *2022 IEEE Transportation Electrification Conference and Expo (ITEC)*, 2022, pp. 237-242.

Appendix A

Vehicle Model Parameters

Table A.1: Body parameters

Parameter	Value
Wheelbase	2.375 m
Sprung mass	1300 kg
Center of gravity height	0.54 m
Center of gravity distance to front wheels	0.760 m
Body inertias (I_{xx}, I_{yy}, I_{zz})	407.37 m^2, 1050.65 m^2, 965.68 m^2
Road-load coefficients	
f_0	0.0074
f_s	0.00027
C_d	0.320

Table A.2: Suspensions parameters

Parameter (front/rear)	Value
Track width	1.41 m / 1.39 m
Spring pre-load	3150 N / 2100 N
Compression ratio	1.045 / 1.215

Table A.3: Wheels and tires parameters

Parameter (front/rear)	Value
Dimensions	195 / 55 R15
Unloaded assembly diameter	0.594 m
Wheel center height	0.291 m / 0.291 m
Rim radius	0.190 m
Rim width	0.1524 m
Tire vertical stiffnes	187.2 N/mm
Tire Width	0.195 m

Table A.4: Steering parameters

Parameter	Value
Inertia	0.1 m^2
Damping	30.0 $Nmms^d eg$
Rack travel	1 (mm): 0.1454 (deg)

Table A.5: Brake parameters

Parameter (front/rear)	Value
Effective piston radius	105.9 mm / 100.61 mm
Piston area	2290.2 mm^2 / 907.9 mm^2
Material adherence	0.420 / 0.396

Table A.6: Battery parameters

Parameter	Value	Unit
Nominal cell voltage	3.7	[V]
Nominal system voltage	355.2	[V]
Rated pack capacity	52	[Ah]
Rated pack energy	18.4	[kWh]
Pack weight	215	[kg]

Table A.7: Powertrain parameters

Parameter	Value	Unit
Final drive ratio	3.87:1	[-]
Final Drive Inertia	0.2	[kg/m^2]
Wheel Inertia	0.6	[kg/m^2]
Motor Inertia	0.2	[kg/m^2]
Driveline efficiency	1.0	[-]

Appendix B

Electrified Driveline Models

The Electric Driveline Model

Step 01: Diagram

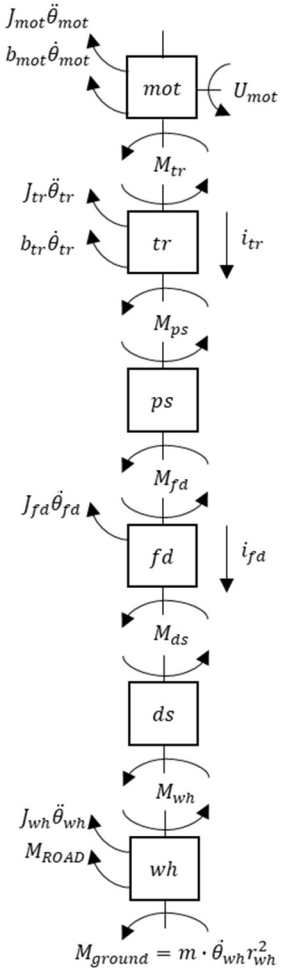

Step 02: Block Connections

$$mot \rightarrow tr: \begin{cases} M_{tr} = M_{mot_{out}} = U_{mot} - J_{mot}\ddot{\theta}_{mot} - b_{mot}\dot{\theta}_{mot} \\ \dot{\theta}_{tr} = \dot{\theta}_{mot}/i_{tr} \end{cases}$$

$$tr \rightarrow ps: \begin{cases} M_{ps} = M_{tr_{out}} = M_{tr}i_{tr} - J_{tr}\ddot{\theta}_{tr} - b_{tr}\dot{\theta}_{tr} = U_{mot}i_{tr} - J_{mot}\ddot{\theta}_{mot}i_{tr} \\ M_{ps} = U_{mot}i_{tr} - J_{mot}\ddot{\theta}_{mot}i_{tr} - b_{mot}\dot{\theta}_{mot}i_{tr} - J_{tr}\ddot{\theta}_{tr} - b_{tr}\dot{\theta}_{tr} \\ \dot{\theta}_{ps} = \dot{\theta}_{tr}/1 = \dot{\theta}_{mot}/i_{tr} \end{cases}$$

$$ps \rightarrow fd: \begin{cases} M_{fd} = M_{ps_{out}} = M_{tr}i_{tr} - J_{tr}\ddot{\theta}_{tr} - b_{tr}\dot{\theta}_{tr} \\ M_{fd} = U_{mot}i_{tr} - J_{mot}\ddot{\theta}_{mot}i_{tr} - b_{mot}\dot{\theta}_{mot}i_{tr} - J_{tr}\ddot{\theta}_{tr} - b_{tr}\dot{\theta}_{tr} \\ \dot{\theta}_{fd} = \dot{\theta}_{ps}/i_f = \dot{\theta}_{gm}/i_{tr}\, i_{fd} \end{cases}$$

$$fd \rightarrow ds: \begin{cases} M_{ds} = M_{fd_{out}} = M_{fd}i_{fd} - J_{fd}\ddot{\theta}_{fd} \\ M_{ds} = U_{mot}i_{tr}i_{fd} - J_{mot}\ddot{\theta}_{mot}i_{tr}i_{fd} - b_{mot}\dot{\theta}_{mot}i_{tr}i_{fd} - J_{tr}\ddot{\theta}_{tr}i_{fd} - b_{tr}\dot{\theta}_{tr}i_{fd} \\ \qquad -J_{fd}\ddot{\theta}_{fd} \\ \dot{\theta}_{ds} = \dot{\theta}_{fd}/1 = \dot{\theta}_{gm}/i_{tr}\, i_{fd} \end{cases}$$

$$ds \rightarrow wh: \begin{cases} M_{wh} = M_{ds_{out}} \\ M_{wh} = U_{mot}i_{tr}i_{fd} - J_{mot}\ddot{\theta}_{mot}i_{tr}i_{fd} - b_{mot}\dot{\theta}_{mot}i_{tr}i_{fd} - J_{tr}\ddot{\theta}_{tr}i_{fd} - b_{tr}\dot{\theta}_{tr}i_{fd} \\ \qquad -J_{fd}\ddot{\theta}_{fd} \\ \dot{\theta}_{wh} = \dot{\theta}_{ds} = \dot{\theta}_{gm}/i_{tr}\, i_{fd} \end{cases}$$

$$wh \rightarrow ground: \begin{cases} M_{wh} = (J_{wh} + mr_{wh}^2)\ddot{\theta}_{wh} + F_{ROAD}r_{wh} \\ V_{veh} = \dot{\theta}_{wh}r_{wh} \end{cases}$$

Step 03: States and inputs

According to first rule: $x = [\dot{\theta}_w]$

Given the propelling systems: $U = [U_{mot}]$

Step 04: States dynamics

Using both equations for M_{wh} from Step 02:

$$(J_{wh} + mr_w^2)\ddot{\theta}_{wh} + F_{ROAD}r_{wh} = U_{mot}i_{tr}i_{fd} - J_{mot}\ddot{\theta}_{mot}i_{tr}i_{fd} - b_{mot}\dot{\theta}_{mot}i_{tr}i_{fd} - J_{tr}\ddot{\theta}_{tr}i_{fd} - b_{tr}\dot{\theta}_{tr}i_{fd} - J_{fd}\ddot{\theta}_{fd}$$

Using speed equations to put it in terms of θ_{wh}:

$$(J_{wh} + mr_w^2)\ddot{\theta}_{wh} + F_{ROAD}r_{wh} = U_{mot}i_{tr}i_{fd} - J_{mot}\ddot{\theta}_{wh}i_{tr}^2i_{fd}^2 - b_{mot}\dot{\theta}_{wh}i_{tr}^2i_{fd}^2 - J_{tr}\ddot{\theta}_{wh}i_{fd}^2 - b_{tr}\dot{\theta}_{wh}i_{fd}^2 - J_{fd}\ddot{\theta}_{wh}$$

Isolating for $\ddot{\theta}_{wh}$:

$$\ddot{\theta}_{wh} = \frac{\dot{\theta}_{wh}\left(-b_{mot}i_{tr}^2i_{fd}^2 - b_{tr}i_{fd}^2\right)}{J_{BEV}} + \frac{U_{mot}i_{tr}i_{fd}}{J_{BEV}} - \frac{r_{wh}}{J_{BEV}}F_{ROAD}$$

Where $J_{BEV} = J_{wh} + mr_{wh}^2 + J_{mot}i_{tr}^2i_{fd}^2 + J_{tr}i_{fd}^2 + J_{fd}$

Step 05: State-space

$$\dot{x} = Ax + Bu + Hl$$

$$[\ddot{\theta}_{wh}] = [-a_{BEV}/J_{BEV}\,][\dot{\theta}_{wh}] + [(i_{tr}\, i_{fd})/J_{BEV}\,]u + [-r_{wh}/J_{BEV}\,]l$$

Where $a_{BEV} = b_{mot}i_{tr}^2i_{fd}^2 + b_{tr}i_f^2$, $u = U_{mot}$, and $l = F_{ROAD}$

The Range Extended Driveline Model

Step 01: Diagram

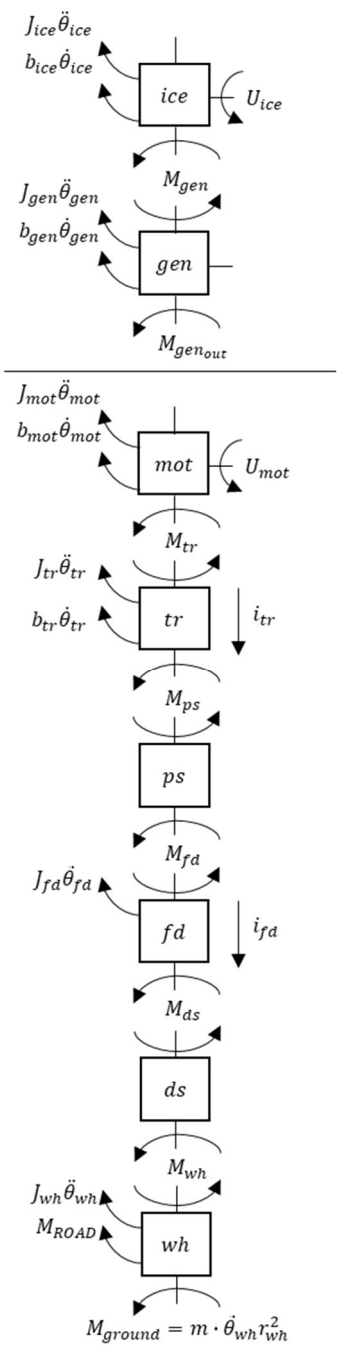

Step 02: Block Connections

$$mot \rightarrow tr: \begin{cases} M_{tr} = M_{mot_{out}} = U_{mot} - J_{mot}\ddot{\theta}_{mot} - b_{mot}\dot{\theta}_{mot} \\ \dot{\theta}_{tr} = \dot{\theta}_{mot}/i_{tr} \end{cases}$$

$$tr \rightarrow ps: \begin{cases} M_{ps} = M_{tr_{out}} = M_{tr}i_{tr} - J_{tr}\ddot{\theta}_{tr} - b_{tr}\dot{\theta}_{tr} = U_{mot}i_{tr} - J_{mot}\ddot{\theta}_{mot}i_{tr} \\ M_{ps} = U_{mot}i_{tr} - J_{mot}\ddot{\theta}_{mot}i_{tr} - b_{mot}\dot{\theta}_{mot}i_{tr} - J_{tr}\ddot{\theta}_{tr} - b_{tr}\dot{\theta}_{tr} \\ \dot{\theta}_{ps} = \dot{\theta}_{tr}/1 = \dot{\theta}_{mot}/i_{tr} \end{cases}$$

$$ps \rightarrow fd: \begin{cases} M_{fd} = M_{ps_{out}} = M_{tr}i_{tr} - J_{tr}\ddot{\theta}_{tr} - b_{tr}\dot{\theta}_{tr} \\ M_{fd} = U_{mot}i_{tr} - J_{mot}\ddot{\theta}_{mot}i_{tr} - b_{mot}\dot{\theta}_{mot}i_{tr} - J_{tr}\ddot{\theta}_{tr} - b_{tr}\dot{\theta}_{tr} \\ \dot{\theta}_{fd} = \dot{\theta}_{ps}/i_f = \dot{\theta}_{gm}/i_{tr}\, i_{fd} \end{cases}$$

$$fd \rightarrow ds: \begin{cases} M_{ds} = M_{fd_{out}} = M_{fd}i_{fd} - J_{fd}\ddot{\theta}_{fd} \\ M_{ds} = U_{mot}i_{tr}i_{fd} - J_{mot}\ddot{\theta}_{mot}i_{tr}i_{fd} - b_{mot}\dot{\theta}_{mot}i_{tr}i_{fd} - J_{tr}\ddot{\theta}_{tr}i_{fd} - b_{tr}\dot{\theta}_{tr}i_{fd} \\ \qquad -J_{fd}\ddot{\theta}_{fd} \\ \dot{\theta}_{ds} = \dot{\theta}_{fd}/1 = \dot{\theta}_{gm}/i_{tr}\, i_{fd} \end{cases}$$

$$ds \rightarrow wh: \begin{cases} M_{wh} = M_{ds_{out}} \\ M_{wh} = U_{mot}i_{tr}i_{fd} - J_{mot}\ddot{\theta}_{mot}i_{tr}i_{fd} - b_{mot}\dot{\theta}_{mot}i_{tr}i_{fd} - J_{tr}\ddot{\theta}_{tr}i_{fd} - b_{tr}\dot{\theta}_{tr}i_{fd} \\ \qquad -J_{fd}\ddot{\theta}_{fd} \\ \dot{\theta}_{wh} = \dot{\theta}_{ds} = \dot{\theta}_{gm}/i_{tr}\, i_{fd} \end{cases}$$

$$wh \rightarrow ground: \begin{cases} M_{wh} = (J_{wh} + mr_{wh}^2)\ddot{\theta}_{wh} + F_{ROAD}r_{wh} \\ V_{veh} = \dot{\theta}_{wh}r_{wh} \end{cases}$$

Step 03: States and inputs

According to first rule: $x = [\dot{\theta}_w]$

Given the propelling systems: $U = [U_{mot}]$

Step 04: States dynamics

Using both equations for M_{wh} from Step 02:

$$(J_{wh} + mr_w^2)\ddot{\theta}_{wh} + F_{ROAD}r_{wh} = U_{mot}i_{tr}i_{fd} - J_{mot}\ddot{\theta}_{mot}i_{tr}i_{fd} - b_{mot}\dot{\theta}_{mot}i_{tr}i_{fd} - J_{tr}\ddot{\theta}_{tr}i_{fd} - b_{tr}\dot{\theta}_{tr}i_{fd} - J_{fd}\ddot{\theta}_{fd}$$

Using speed equations to put it in terms of θ_{wh}:

$$(J_{wh} + mr_w^2)\ddot{\theta}_{wh} + F_{ROAD}r_{wh} = U_{mot}i_{tr}i_{fd} - J_{mot}\ddot{\theta}_{wh}i_{tr}^2i_{fd}^2 - b_{mot}\dot{\theta}_{wh}i_{tr}^2i_{fd}^2 - J_{tr}\ddot{\theta}_{wh}i_{fd}^2 - b_{tr}\dot{\theta}_{wh}i_{fd}^2 - J_{fd}\ddot{\theta}_{wh}$$

Isolating for $\ddot{\theta}_{wh}$:

$$\ddot{\theta}_{wh} = \frac{\dot{\theta}_{wh}(-b_{mot}i_{tr}^2i_{fd}^2 - b_{tr}i_{fd}^2)}{J_{BEVx}} + \frac{U_{mot}i_{tr}i_{fd}}{J_{BEVx}} - \frac{r_{wh}}{J_{BEVx}}F_{ROAD}$$

Where $J_{BEVx} = J_{wh} + mr_{wh}^2 + J_{mot}i_{tr}^2i_{fd}^2 + J_{tr}i_{fd}^2 + J_{fd}$

Step 05: State-space

$$\dot{x} = Ax + Bu + Hl$$

$$[\ddot{\theta}_{wh}] = [-a_{BEVx}/J_{BEVx}\,][\dot{\theta}_{wh}] + [(i_{tr}\; i_{fd})/J_{BEVx}\,]u + [-r_{wh}/J_{BEVx}\,]l$$

Where $a_{BEVx} = b_{mot}i_{tr}^2i_{fd}^2 + b_{tr}i_f^2$, $u = U_{mot}$, and $l = F_{ROAD}$

The Comprehensive Hybrid Driveline Model (1/2)

Step 01: Diagram

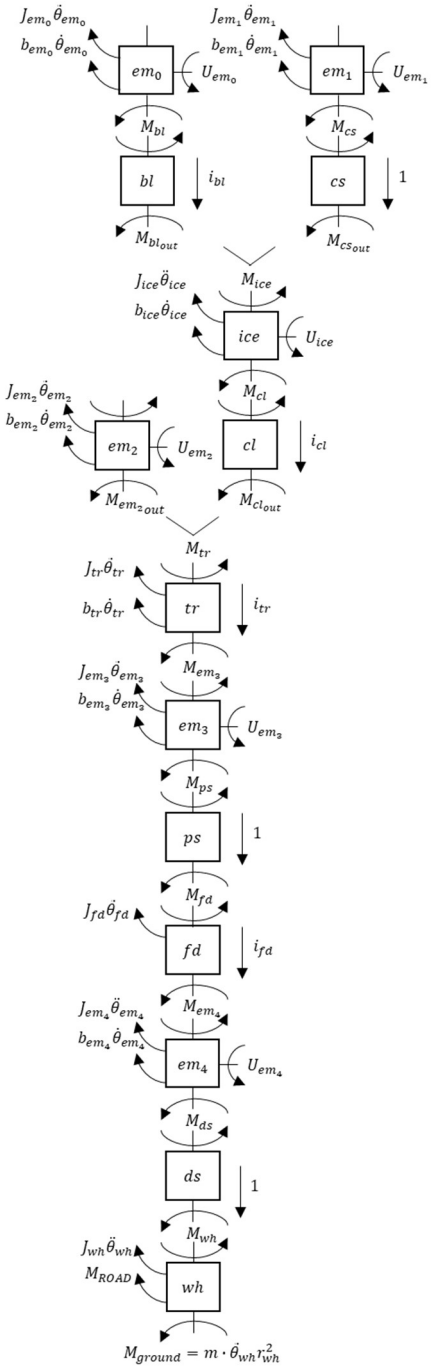

Step 02: Block Connections

$em_0 \rightarrow bl$:
$$\begin{cases} M_{bl} = M_{em_{0_{out}}} = U_{em_0} - J_{em_0}\ddot{\theta}_{em_0} - b_{em_0}\dot{\theta}_{em_0} \\ \dot{\theta}_{bl} = \dot{\theta}_{em_0}/i_{bl} \end{cases}$$

$em_1 \rightarrow cs$:
$$\begin{cases} M_{cs} = M_{em_{1_{out}}} = U_{em_1} - J_{em_1}\ddot{\theta}_{em_1} - b_{em_1}\dot{\theta}_{em_1} \\ \dot{\theta}_{cs} = \dot{\theta}_{em_1} \end{cases}$$

$bl + cs \rightarrow ice$:
$$\begin{cases} M_{ice} = M_{bl_{out}} + M_{cs_{out}} = M_{bl} i_{bl} + M_{cs} \\ M_{ice} = U_{em_0} i_{bl} - J_{em_0}\ddot{\theta}_{em_0} i_{bl} - b_{em_0}\dot{\theta}_{em_0} i_{bl} + U_{em_1} - J_{em_1}\ddot{\theta}_{em_1} \\ \qquad -b_{em_1}\dot{\theta}_{em_1} \\ \dot{\theta}_{ice} = \dot{\theta}_{bl} = \dot{\theta}_{em_0}/i_{bl}, \quad \dot{\theta}_{ice} = \dot{\theta}_{cs} = \dot{\theta}_{em_1} \end{cases}$$

$ice \rightarrow cl$:
$$\begin{cases} M_{cl} = M_{ice_{out}} = M_{ice} + U_{ice} - J_{ice}\ddot{\theta}_{ice} - b_{ice}\dot{\theta}_{ice} \\ M_{cl} = U_{em_0} i_{bl} - J_{em_0}\ddot{\theta}_{em_0} i_{bl} - b_{em_0}\dot{\theta}_{em_0} i_{bl} + U_{em_1} - J_{em_1}\ddot{\theta}_{em_1} - b_{em_1}\dot{\theta}_{em_1} \\ \qquad +U_{ice} - J_{ice}\ddot{\theta}_{ice} - b_{ice}\dot{\theta}_{ice} \\ \dot{\theta}_{cl} = \dot{\theta}_{ice} = \dot{\theta}_{em_0}/i_{bl} = \dot{\theta}_{em_1} \end{cases}$$

$cl + em_2 \rightarrow tr$:
$$\begin{cases} M_{tr} = M_{cl_{out}} + M_{em_{2_{out}}} = M_{cl} i_{cl} + U_{em_2} - J_{em_2}\ddot{\theta}_{em_2} - b_{em_2}\dot{\theta}_{em_2} \\ M_{tr} = U_{em_0} i_{bl} i_{cl} - J_{em_0}\ddot{\theta}_{em_0} i_{bl} i_{cl} - b_{em_0}\dot{\theta}_{em_0} i_{bl} i_{cl} + U_{em_1} i_{cl} - J_{em_1}\ddot{\theta}_{em_1} i_{cl} \\ \qquad -b_{em_1}\dot{\theta}_{em_1} i_{cl} + U_{ice} i_{cl} - J_{ice}\ddot{\theta}_{ice} i_{cl} + U_{em_2} - J_{em_2}\ddot{\theta}_{em_2} - b_{em_2}\dot{\theta}_{em_2} \\ \dot{\theta}_{tr} = \dot{\theta}_{cl}/i_{tr} = \dot{\theta}_{ice}/i_{tr} = \dot{\theta}_{em_0}/i_{bl} i_{tr} = \dot{\theta}_{em_1}/i_{tr}, \quad \dot{\theta}_{tr} = \dot{\theta}_{em_2}/i_{tr} \end{cases}$$

$tr \rightarrow em_3$:
$$\begin{cases} M_{em_3} = M_{tr_{out}} = M_{tr} i_{tr} - J_{tr}\ddot{\theta}_{tr} - b_{tr}\dot{\theta}_{tr} \\ M_{em_3} = U_{em_0} i_{bl} i_{cl} i_{tr} - J_{em_0}\ddot{\theta}_{em_0} i_{bl} i_{cl} i_{tr} - b_{em_0}\dot{\theta}_{em_0} i_{bl} i_{cl} i_{tr} + U_{em_1} i_{cl} i_{tr} \\ \qquad -J_{em_1}\ddot{\theta}_{em_1} i_{cl} i_{tr} - b_{em_1}\dot{\theta}_{em_1} i_{cl} i_{tr} + U_{ice} i_{cl} i_{tr} - J_{ice}\ddot{\theta}_{ice} i_{cl} i_{tr} \\ \qquad -b_{ice}\dot{\theta}_{ice} i_{cl} i_{tr} + U_{em_2} i_{tr} - J_{em_2}\ddot{\theta}_{em_2} i_{tr} - b_{em_2}\dot{\theta}_{em_2} i_{tr} - J_{tr}\ddot{\theta}_{tr} \\ \qquad -b_{tr}\dot{\theta}_{tr} \\ \dot{\theta}_{em_3} = \dot{\theta}_{tr} = \dot{\theta}_{ice}/i_{tr} = \dot{\theta}_{em_0}/i_{bl} i_{tr} = \dot{\theta}_{em_1}/i_{tr} = \dot{\theta}_{em_2}/i_{tr} \end{cases}$$

$em_3 \rightarrow ps$:
$$\begin{cases} M_{ps} = M_{em_{3_{out}}} = M_{em_3} + U_{em_3} - J_{em_3}\ddot{\theta}_{em_3} - b_{em_3}\dot{\theta}_{em_3} \\ M_{ps} = U_{em_0} i_{bl} i_{cl} i_{tr} - J_{em_0}\ddot{\theta}_{em_0} i_{bl} i_{cl} i_{tr} - b_{em_0}\dot{\theta}_{em_0} i_{bl} i_{cl} i_{tr} + U_{em_1} i_{cl} i_{tr} \\ \qquad -J_{em_1}\ddot{\theta}_{em_1} i_{cl} i_{tr} - b_{em_1}\dot{\theta}_{em_1} i_{cl} i_{tr} + U_{ice} i_{cl} i_{tr} - J_{ice}\ddot{\theta}_{ice} i_{cl} i_{tr} \\ \qquad -b_{ice}\dot{\theta}_{ice} i_{cl} i_{tr} + U_{em_2} i_{tr} - J_{em_2}\ddot{\theta}_{em_2} i_{tr} - b_{em_2}\dot{\theta}_{em_2} i_{tr} - J_{tr}\ddot{\theta}_{tr} \\ \qquad -b_{tr}\dot{\theta}_{tr} + U_{em_3} - J_{em_3}\ddot{\theta}_{em_3} - b_{em_3}\dot{\theta}_{em_3} \\ \dot{\theta}_{ps} = \dot{\theta}_{em_3} = \dot{\theta}_{tr} = \dot{\theta}_{ice}/i_{tr} = \dot{\theta}_{em_0}/i_{bl} i_{tr} = \dot{\theta}_{em_1}/i_{tr} = \dot{\theta}_{em_2}/i_{tr} \end{cases}$$

$ps \rightarrow fd$:
$$\begin{cases} M_{fd} = M_{ps_{out}} = M_{ps} \\ \dot{\theta}_{fd} = \dot{\theta}_{ps}/i_{fd} = \dot{\theta}_{em_3}/i_{fd} = \dot{\theta}_{tr}/i_{fd} = \dot{\theta}_{ice}/i_{cl} i_{tr} i_{fd} = \dot{\theta}_{em_0}/i_{bl} i_{cl} i_{tr} i_{fd} \\ \dot{\theta}_{fd} = \dot{\theta}_{em_1}/i_{tr} i_{fd} = \dot{\theta}_{em_2}/i_{tr} i_{fd} \end{cases}$$

$fd \rightarrow em_4$:
$$\begin{cases} M_{em_4} = M_{fd_{out}} = M_{fd} i_{fd} - J_{fd}\ddot{\theta}_{fd} \\ M_{em_4} = U_{em_0} i_{bl} i_{cl} i_{tr} i_{fd} - J_{em_0}\ddot{\theta}_{em_0} i_{bl} i_{cl} i_{tr} i_{fd} - b_{em_0}\dot{\theta}_{em_0} i_{bl} i_{cl} i_{tr} i_{fd} \\ \qquad +U_{em_1} i_{cl} i_{tr} i_{fd} - J_{em_1}\ddot{\theta}_{em_1} i_{cl} i_{tr} i_{fd} - b_{em_1}\dot{\theta}_{em_1} i_{cl} i_{tr} i_{fd} \\ \qquad +U_{ice} i_{cl} i_{tr} i_{fd} - J_{ice}\ddot{\theta}_{ice} i_{cl} i_{tr} i_{fd} - b_{ice}\dot{\theta}_{ice} i_{cl} i_{tr} i_{fd} + U_{em_2} i_{tr} i_{fd} \\ \qquad -J_{em_2}\ddot{\theta}_{em_2} i_{tr} i_{fd} - b_{em_2}\dot{\theta}_{em_2} i_{tr} i_{fd} - J_{tr}\ddot{\theta}_{tr} i_{fd} - b_{tr}\dot{\theta}_{tr} i_{fd} \\ \qquad +U_{em_3} i_{fd} - J_{em_3}\ddot{\theta}_{em_3} i_{fd} - J_{fd}\ddot{\theta}_{fd} \\ \dot{\theta}_{em_4} = \dot{\theta}_{fd} = \dot{\theta}_{em_3}/i_{fd} = \dot{\theta}_{tr}/i_{fd} = \dot{\theta}_{ice}/i_{tr} i_{fd} = \dot{\theta}_{em_0}/i_{bl} i_{tr} i_{fd} \\ \dot{\theta}_{em_4} = \dot{\theta}_{em_1}/i_{tr} i_{fd} = \dot{\theta}_{em_2}/i_{tr} i_{fd} \end{cases}$$

Continue next page

The Comprehensive Hybrid Driveline Model (2/2)

$$em_4 \rightarrow ds: \begin{cases} M_{ds} = M_{em_{4_{out}}} = M_{em_4} + U_{em_4} - J_{em_4}\ddot{\theta}_{em_4} - b_{em_4}\dot{\theta}_{em_4} \\ M_{ds} = U_{em_0} i_{bl} i_{cl} i_{tr} i_{fd} - J_{em_0}\ddot{\theta}_{em_0} i_{bl} i_{cl} i_{tr} i_{fd} - b_{em_0}\dot{\theta}_{em_0} i_{bl} i_{cl} i_{tr} i_{fd} + U_{em_1} i_{cl} i_{tr} i_{fd} - J_{em_1}\ddot{\theta}_{em_1} i_{cl} i_{tr} i_{fd} - b_{em_1}\dot{\theta}_{em_1} i_{cl} i_{tr} i_{fd} \\ \quad + U_{ice} i_{cl} i_{tr} i_{fd} - J_{ice}\ddot{\theta}_{ice} i_{cl} i_{tr} i_{fd} - b_{ice}\dot{\theta}_{ice} i_{cl} i_{tr} i_{fd} + U_{em_2} i_{tr} i_{fd} - J_{em_2}\ddot{\theta}_{em_2} i_{tr} i_{fd} - b_{em_2}\dot{\theta}_{em_2} i_{tr} i_{fd} - J_{tr}\ddot{\theta}_{tr} i_{fd} \\ \quad - b_{tr}\dot{\theta}_{tr} i_{fd} + U_{em_3} i_{fd} - J_{em_3}\ddot{\theta}_{em_3} i_{fd} - b_{em_3}\dot{\theta}_{em_3} i_{fd} - J_{fd}\ddot{\theta}_{fd} + U_{em_4} - J_{em_4}\ddot{\theta}_{em_4} - b_{em_4}\dot{\theta}_{em_4} \\ \ddot{\theta}_{ds} = \dot{\theta}_{em_4} = \dot{\theta}_{fd} = \dot{\theta}_{em_3}/i_{fd} = \dot{\theta}_{tr}/i_{fd} = \dot{\theta}_{ice}/i_{tr} i_{fd} = \dot{\theta}_{em_0}/i_{bl} i_{tr} i_{fd} = \dot{\theta}_{ice}/i_{tr} i_{fd} = \dot{\theta}_{em_1}/i_{tr} i_{fd} = \dot{\theta}_{em_2}/i_{tr} i_{fd} \end{cases}$$

$$ds \rightarrow wh: \begin{cases} M_{wh} = M_{ds_{out}} = M_{ds} \\ M_{wh} = U_{em_0} i_{bl} i_{cl} i_{tr} i_{fd} - J_{em_0}\ddot{\theta}_{em_0} i_{bl} i_{cl} i_{tr} i_{fd} - b_{em_0}\dot{\theta}_{em_0} i_{bl} i_{cl} i_{tr} i_{fd} + U_{em_1} i_{cl} i_{tr} i_{fd} - J_{em_1}\ddot{\theta}_{em_1} i_{cl} i_{tr} i_{fd} \\ \quad - b_{em_1}\dot{\theta}_{em_1} i_{cl} i_{tr} i_{fd} + U_{ice} i_{cl} i_{tr} i_{fd} - J_{ice}\ddot{\theta}_{ice} i_{cl} i_{tr} i_{fd} - b_{ice}\dot{\theta}_{ice} i_{cl} i_{tr} i_{fd} + U_{em_2} i_{tr} i_{fd} - J_{em_2}\ddot{\theta}_{em_2} i_{tr} i_{fd} \\ \quad - J_{em_4}\ddot{\theta}_{em_4} - b_{em_4}\dot{\theta}_{em_4} - b_{em_2}\dot{\theta}_{em_2} i_{tr} i_{fd} - J_{tr}\ddot{\theta}_{tr} i_{fd} - b_{tr}\dot{\theta}_{tr} i_{fd} + U_{em_3} i_{fd} - J_{em_3}\ddot{\theta}_{em_3} i_{fd} - b_{em_3}\dot{\theta}_{em_3} i_{fd} \\ \quad - J_{fd}\ddot{\theta}_{fd} + U_{em_4} \\ \dot{\theta}_{wh} = \dot{\theta}_{ds} = \dot{\theta}_{em_4} = \dot{\theta}_{fd} = \dot{\theta}_{em_3}/i_{fd} = \dot{\theta}_{tr}/i_{fd} = \dot{\theta}_{ice}/i_{tr} i_{fd} = \dot{\theta}_{em_0}/i_{bl} i_{tr} i_{fd} = \dot{\theta}_{em_1}/i_{tr} i_{fd} = \dot{\theta}_{em_2}/i_{tr} i_{fd} \end{cases}$$

$$wh \rightarrow ground: \begin{cases} M_{wh} = (J_{wh} + m r_{wh}^2)\ddot{\theta}_{wh} + F_{ROAD} r_{wh} \\ V_{veh} = \dot{\theta}_{wh} r_{wh} \end{cases}$$

Step 03: States and inputs

According to first rule: $x = [\dot{\theta}_w]$

Given the propelling systems: $U = [U_{ice} \quad U_{em_0} \quad U_{em_1} \quad U_{em_2} \quad U_{em_3} \quad U_{em_4}]^T$

Step 04: States dynamics

Using both equations for M_{wh} from Step 02:

$$\begin{aligned} (J_{wh} + m r_w^2)\ddot{\theta}_{wh} + F_{ROAD} r_{wh} &= U_{em_0} i_{bl} i_{cl} i_{tr} i_{fd} - J_{em_0}\ddot{\theta}_{em_0} i_{bl} i_{cl} i_{tr} i_{fd} - b_{em_0}\dot{\theta}_{em_0} i_{bl} i_{cl} i_{tr} i_{fd} + U_{em_1} i_{cl} i_{tr} i_{fd} - J_{em_1}\ddot{\theta}_{em_1} i_{cl} i_{tr} i_{fd} - b_{em_1}\dot{\theta}_{em_1} i_{cl} i_{tr} i_{fd} \\ &+ U_{ice} i_{cl} i_{tr} i_{fd} - J_{ice}\ddot{\theta}_{ice} i_{cl} i_{tr} i_{fd} - b_{ice}\dot{\theta}_{ice} i_{cl} i_{tr} i_{fd} + U_{em_2} i_{tr} i_{fd} - J_{em_2}\ddot{\theta}_{em_2} i_{tr} i_{fd} - b_{em_2}\dot{\theta}_{em_2} i_{tr} i_{fd} - J_{tr}\ddot{\theta}_{tr} i_{fd} \\ &- b_{tr}\dot{\theta}_{tr} i_{fd} + U_{em_3} i_{fd} - J_{em_3}\ddot{\theta}_{em_3} i_{fd} - b_{em_3}\dot{\theta}_{em_3} i_{fd} - J_{fd}\ddot{\theta}_{fd} + U_{em_4} - J_{em_4}\ddot{\theta}_{em_4} - b_{em_4}\dot{\theta}_{em_4} \end{aligned}$$

Using speed equations to put it in terms of θ_{wh}:

$$\begin{aligned} (J_{wh} + m r_w^2)\ddot{\theta}_{wh} + F_{ROAD} r_{wh} &= U_{em_0} i_{bl} i_{cl} i_{tr} i_{fd} - J_{em_0}\ddot{\theta}_{wh} i_{bl}^2 i_{cl}^2 i_{tr}^2 i_{fd}^2 - b_{em_0}\dot{\theta}_{wh} i_{bl}^2 i_{cl}^2 i_{tr}^2 i_{fd}^2 + U_{em_1} i_{cl} i_{tr} i_{fd} - J_{em_1}\ddot{\theta}_{wh} i_{cl}^2 i_{tr}^2 i_{fd}^2 - b_{em_1}\dot{\theta}_{wh} i_{cl}^2 i_{tr}^2 i_{fd}^2 \\ &+ U_{ice} i_{cl} i_{tr} i_{fd} - J_{ice}\ddot{\theta}_{wh} i_{cl}^2 i_{tr}^2 i_{fd}^2 - b_{ice}\dot{\theta}_{wh} i_{cl}^2 i_{tr}^2 i_{fd}^2 + U_{em_2} i_{tr} i_{fd} - J_{em_2}\ddot{\theta}_{wh} i_{tr}^2 i_{fd}^2 - b_{em_2}\dot{\theta}_{wh} i_{tr}^2 i_{fd}^2 - J_{tr}\ddot{\theta}_{wh} i_{fd}^2 \\ &- b_{tr}\dot{\theta}_{wh} i_{fd}^2 + U_{em_3} i_{fd} - J_{em_3}\ddot{\theta}_{wh} i_{fd}^2 - b_{em_3}\dot{\theta}_{wh} i_{fd}^2 - J_{fd}\ddot{\theta}_{wh} + U_{em_4} - J_{em_4}\ddot{\theta}_{wh} - b_{em_4}\dot{\theta}_{wh} \end{aligned}$$

Isolating for $\ddot{\theta}_{wh}$:

$$\begin{aligned} \ddot{\theta}_{wh} = &\frac{\dot{\theta}_{wh}\left(-b_{em_0} i_{bl}^2 i_{cl} i_{tr}^2 i_{fd}^2 - b_{em_1} i_{cl} i_{tr}^2 i_{fd}^2 - b_{ice} i_{cl} i_{tr}^2 i_{fd}^2 - b_{em_2} i_{tr}^2 i_{fd}^2 - b_{tr} i_{fd}^2 - b_{em_4}\right)}{J_{HEV}} \\ &+ \frac{1}{J_{HEV}}\left[i_{cl}\left(U_{em_0} i_{bl} i_{tr} i_{fd} + U_{em_1} i_{tr} i_{fd} + U_{ice} i_{tr} i_{fd}\right) + U_{em_2} i_{tr} i_{fd} + U_{em_3} i_{fd} + U_{em_4}\right] - \frac{r_{wh}}{J_{HEV}} F_{ROAD} \end{aligned}$$

Where $J_{HEV} = J_{wh} + m r_{wh}^2 + J_{em_0} i_{bl}^2 i_{cl} i_{tr}^2 i_{fd}^2 + J_{em_1} i_{cl} i_{tr}^2 i_{fd}^2 + J_{ice} i_{cl} i_{tr}^2 i_{fd}^2 + J_{em_2} i_{tr}^2 i_{fd}^2 + J_{tr} i_{fd}^2 + J_{em_3} i_{fd}^2 + J_{em_4} + J_{fd}$

Step 05: State-space

$$\dot{x} = Ax + Bu + Hl$$

$$[\ddot{\theta}_{wh}] = [-a_P/J_{HEV}\,][\dot{\theta}_{wh}] + [1/J_{HEV}\,]u + [-r_{wh}/J_{HEV}\,]l$$

Where $a_{HEV} = b_{em_0} i_{bl}^2 i_{cl} i_{tr}^2 i_{fd}^2 + b_{em_1} i_{cl} i_{tr}^2 i_{fd}^2 + b_{ice} i_{cl} i_{tr}^2 i_{fd}^2 + b_{em_2} i_{tr}^2 i_{fd}^2 + b_{tr} i_{fd}^2 + b_{em_4}$,
$u = i_{cl}\left(U_{em_0} i_{bl} i_{tr} i_{fd} + U_{em_1} i_{tr} i_{fd} + U_{ice} i_{tr} i_{fd}\right) + U_{em_2} i_{tr} i_{fd} + U_{em_3} i_{fd} + U_{em_4}$, and $l = F_{ROAD}$

The Split Hybrid Driveline Model

Step 01: Diagram

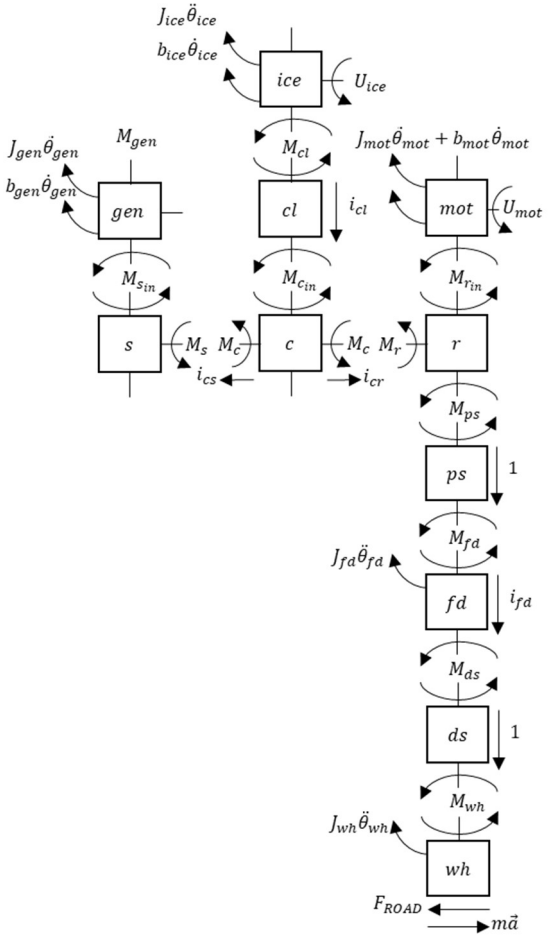

Step 02: Block Connections

$ice \rightarrow cl$:
$$\begin{cases} M_{cl} = M_{ice_{out}} = U_{ice} - J_{ice}\ddot{\theta}_{ice} - b_{ice}\dot{\theta}_{ice} \\ \dot{\theta}_{cl} = \dot{\theta}_{ice} \end{cases}$$

$gen \rightarrow sun$:
$$\begin{cases} M_{s_{in}} = M_{gen_{out}} = M_{gen} - J_{gen}\ddot{\theta}_{gen} - b_{gen}\dot{\theta}_{gen} \\ \dot{\theta}_s = (\dot{\theta}_c - i_{cr}\dot{\theta}_r)/i_{cs} = \dot{\theta}_{gen} = (\dot{\theta}_{ice} - i_{cr}\dot{\theta}_{mot})/i_{cs} \end{cases}$$

$cl \rightarrow carrier$:
$$\begin{cases} M_c = M_{cl_{out}} = M_{c_{in}} - M_{c_{out}} = M_{cl}i_{cl} \\ M_c = M_{c_{in}} - 0 = U_{ice}i_{cl} - J_{ice}\ddot{\theta}_{ice}i_{cl} - b_{ice}\dot{\theta}_{ice}i_{cl} \\ \dot{\theta}_c = \dot{\theta}_{cl} = \dot{\theta}_{ice} \end{cases}$$

$mot \rightarrow ring$:
$$\begin{cases} M_{r_{in}} = M_{mot_{out}} = U_{mot} - J_{mot}\ddot{\theta}_{mot} - b_{mot}\dot{\theta}_{mot} \\ \dot{\theta}_r = \dot{\theta}_{mot} \end{cases}$$

$carrier \rightarrow ring$:
$$\begin{cases} M_r = M_{r_{in}} - M_{r_{out}} = -i_{cr}M_c \\ M_r = M_{mot_{out}} - M_{r_{out}} = -i_{cr}(U_{ice}i_{cl} - J_{ice}\ddot{\theta}_{ice}i_{cl} - b_{ice}\dot{\theta}_{ice}i_{cl}) \\ M_{r_{out}} = U_{mot} - J_{mot}\ddot{\theta}_{mot} - b_{mot}\dot{\theta}_{mot} + U_{ice}i_{cl}i_{cr} - J_{ice}\ddot{\theta}_{ice}i_{cl}i_{cr} \\ \qquad -b_{ice}\dot{\theta}_{ice}i_{cl}i_{cr} \\ \dot{\theta}_r = (\dot{\theta}_c - i_{cs}\dot{\theta}_s)/i_{cr} = \dot{\theta}_{mot} = (\dot{\theta}_{ice} - i_{cs}\dot{\theta}_{gen})/i_{cr} \end{cases}$$

$ring \rightarrow ps$:
$$\begin{cases} M_{ps} = M_{r_{out}} \\ M_{ps} = U_{mot} - J_{mot}\ddot{\theta}_{mot} - b_{mot}\dot{\theta}_{mot} + U_{ice}i_{cl}i_{cr} - J_{ice}\ddot{\theta}_{ice}i_{cl}i_{cr} \\ \qquad -b_{ice}\dot{\theta}_{ice}i_{cl}i_{cr} \\ \dot{\theta}_{ps} = \dot{\theta}_r = \dot{\theta}_{mot} = (\dot{\theta}_{ice} - i_{cs}\dot{\theta}_{gen})/i_{cr} \end{cases}$$

$ps \rightarrow fd$:
$$\begin{cases} M_{fd} = M_{ps_{out}} = M_{ps} \\ \dot{\theta}_{fd} = \dot{\theta}_{ps}/i_{fd} = \dot{\theta}_{mot}/i_{fd} = (\dot{\theta}_{ice} - i_{cs}\dot{\theta}_{gen})/i_{cr}i_{fd} \end{cases}$$

$fd \rightarrow ds$:
$$\begin{cases} M_{ds} = M_{fd_{out}} = M_{fd}i_{fd} - J_{fd}\ddot{\theta}_{fd} \\ M_{ds} = U_{mot}i_{fd} - J_{mot}\ddot{\theta}_{mot}i_{fd} - b_{mot}\dot{\theta}_{mot}i_{fd} + U_{ice}i_{cl}i_{cr}i_{fd} \\ \qquad -J_{ice}\ddot{\theta}_{ice}i_{cl}i_{cr}i_{fd} - b_{ice}\dot{\theta}_{ice}i_{cl}i_{cr}i_{fd} - J_{fd}\ddot{\theta}_{fd} \\ \dot{\theta}_{ds} = \dot{\theta}_{fd} = \dot{\theta}_{mot}/i_{fd} = (\dot{\theta}_{ice} - i_{cs}\dot{\theta}_{gen})/i_{cr}i_{fd} \end{cases}$$

$ds \rightarrow wh$:
$$\begin{cases} M_{wh} = M_{ds_{out}} = M_{ds} \\ M_{wh} = U_{mot}i_{fd} - J_{mot}\ddot{\theta}_{mot}i_{fd} - b_{mot}\dot{\theta}_{mot}i_{fd} + U_{ice}i_{cl}i_{cr}i_{fd} \\ \qquad -J_{ice}\ddot{\theta}_{ice}i_{cl}i_{cr}i_{fd} - b_{ice}\dot{\theta}_{ice}i_{cl}i_{cr}i_{fd} - J_{fd}\ddot{\theta}_{fd} \\ \dot{\theta}_{wh} = \dot{\theta}_{ds} = \dot{\theta}_{fd} = \dot{\theta}_{mot}/i_{fd} = (\dot{\theta}_{ice} - i_{cs}\dot{\theta}_{gen})/i_{cr}i_{fd} \end{cases}$$

$wh \rightarrow ground$:
$$\begin{cases} M_{wh} = (J_{wh} + mr_{wh}^2)\ddot{\theta}_{wh} + F_{ROAD}r_{wh} \\ V_{veh} = \dot{\theta}_{wh}r_{wh} \end{cases}$$

Step 03: States and inputs

According to first rule: $x = [\dot{\theta}_w]$

Given the propelling systems: $U = [U_{mot} \quad U_{ice}]$

Step 04: States dynamics

Using both equations for M_{wh} from Step 02:

$$(J_{wh} + mr_w^2)\ddot{\theta}_{wh} + F_{ROAD}r_w = U_{mot}i_{fd} - J_{mot}\ddot{\theta}_{mot}i_{fd} - b_{mot}\dot{\theta}_{mot}i_{fd} + U_{ice}i_{cl}i_{cr}i_{fd} - J_{ice}\ddot{\theta}_{ice}i_{cl}i_{cr}i_{fd} - b_{ice}\dot{\theta}_{ice}i_{cl}i_{cr}i_{fd} - J_{fd}\ddot{\theta}_{fd}$$

Using speed equations, and $\dot{\theta}_{ice} = \beta\dot{\theta}_{mot}$, to put it in terms of θ_{wh}:

$$(J_{wh} + mr_w^2)\ddot{\theta}_{wh} + F_{ROAD}r_{wh} = U_{mot}i_{fd} - J_{mot}\ddot{\theta}_{wh}i_{fd}^2 - b_{mot}\dot{\theta}_{wh}i_{fd}^2 + U_{ice}i_{cl}i_{cr}i_{fd} - J_{ice}\ddot{\theta}_{wh}i_{cl}i_{cr}i_{fd}^2\beta - b_{ice}\dot{\theta}_{wh}i_{cl}i_{cr}i_{fd}^2\beta - J_{fd}\ddot{\theta}_{wh}$$

Isolating for $\ddot{\theta}_{wh}$: $\ddot{\theta}_{wh} = \frac{\dot{\theta}_{wh}(-b_{mot}i_{fd}^2 - b_{ice}i_{cl}i_{cr}i_{fd}^2\beta)}{J_{SH}} + \frac{(U_{mot}i_{fd} + U_{ice}i_{cl}i_{cr}i_{fd})}{J_{SH}} - \frac{r}{J_{SH}}F_{ROAD}$

Where $J_{SH} = J_{wh} + mr_{wh}^2 + J_{mot}i_{fd}^2 + J_{ice}i_{cl}i_{cr}i_{fd}^2\beta + J_f$

Step 05: State-space

$$\dot{x} = Ax + Bu + Hl$$

$$[\ddot{\theta}_{wh}] = \left[-\frac{a_{SH}}{J_{SH}}\right][\dot{\theta}_{wh}] + \left[\frac{i_{fd}}{J_{SH}}\right]u + \left[-\frac{r_{wh}}{J_{SH}}\right]l$$

Where $a_{SH} = b_{mot}i_{fd}^2 + b_{ice}i_{cl}i_{cr}i_{fd}^2\beta$, $u = U_{mot} + U_{ice}i_{cl}i_{cr}$, and $l = F_{ROAD}$

Appendix C

Auxiliary Power Unit Parameters

Table C.8: Engine parameters

Engine size	1.0 L
Weight	90 kg
Peak efficiency	0.3876
Number of cylinders	4
Cylinder displacement	0.00025 m^3
Number of revolutions per stroke	2
Max torque	112 Nm @ 2500 RPM
Idle speed	1000 RPM
Max speed	4500 RPM
Fuel density	0.013 kWh/g

Table C.9: Generator parameters

Operating DC voltage range	350-700 V
Peak efficiency	0.95 70
Weight	50 kg
Peak current	300 Arms
Max continuous torque	325 Nm
Max continuous power	70 kW
Max speed	1100 RPM

References

Ahmed, R., El Sayed, M., Arasaratnam, I., Tjong, J., and Habibi, S. (2014a). Reduced-order electrochemical model parameters identification and soc estimation for healthy and aged li-ion batteries part i: Parameterization model development for healthy batteries. *IEEE journal of emerging and selected topics in power electronics*, **2**(3), 659–677.

Ahmed, R., El Sayed, M., Arasaratnam, I., Tjong, J., and Habibi, S. (2014b). Reduced-order electrochemical model parameters identification and state of charge estimation for healthy and aged li-ion batteries—part ii: Aged battery model and state of charge estimation. *IEEE Journal of Emerging and Selected Topics in Power Electronics*, **2**(3), 678–690.

Ahmed, R., Gazzarri, J., Onori, S., Habibi, S., Jackey, R., Rzemien, K., Tjong, J., and LeSage, J. (2015). Model-based parameter identification of healthy and aged li-ion batteries for electric vehicle applications. *SAE International Journal of Alternative Powertrains*, **4**(2), 233–247.

Ali, A., Elnaggarz, A., Reichardtz, D., and Abdennadher, S. (2016). Gamified virtual reality driving simulator for asserting driving behaviors. In *2016 1st International Conference on Game, Game Art, and Gamification (ICGGAG)*, pages 1–6. IEEE.

Alkinani, M. H., Khan, W. Z., and Arshad, Q. (2020). Detecting human driver inattentive and aggressive driving behavior using deep learning: Recent advances, requirements and open challenges. *IEEE Access*, **8**, 105008–105030.

Andriaminahy, F., Amamou, A., Kelouwani, S., Zioui, N., Ghobadpour, A., and Agbossou, K. (2019). Comparative study of vehicle aerodynamic and rolling resistance coefficients estimation methods. In *2019 IEEE Vehicle Power and Propulsion Conference (VPPC)*, pages 1–5. IEEE.

Arani, S. K., Niasar, A. H., and Zadeh, A. H. (2016). Energy management of dual-source propelled electric vehicle using fuzzy controller optimized via genetic algorithm. In *2016 7th Power Electronics and Drive Systems Technologies Conference (PEDSTC)*, pages 338–343. IEEE.

Asadi, H., Lim, C. P., Mohamed, S., Nahavandi, D., and Nahavandi, S. (2019). Increasing motion fidelity in driving simulators using a fuzzy-based washout filter. *IEEE Transactions on Intelligent Vehicles*, **4**(2), 298–308.

Asus, Z., Aglzim, E.-H., Chrenko, D., Daud, Z.-H. C., and Le Moyne, L. (2014). Dynamic modeling and driving cycle prediction for a racing series hybrid car. *IEEE Journal of Emerging and Selected Topics in Power Electronics*, **2**(3), 541–551.

Aulia, A. I., Hindersah, H., Rohman, A. S., and Hidayat, E. (2019). Design of mpc-based motion cueing for 4 dof simulator platform. In *2019 IEEE 9th International Conference on System Engineering and Technology (ICSET)*, pages 183–188. IEEE.

Balci, O. (2003). Verification, validation, and certification of modeling and simulation applications. In *Winter Simulation Conference*, volume 1, pages 150–158.

Barlow, T. J., Latham, S., McCrae, I., and Boulter, P. (2009). A reference book of driving cycles for use in the measurement of road vehicle emissions. *TRL Published Project Report*.

Barroso, D. G., Yang, Y., Machado, F. A., and Emadi, A. (2022). Electrified automotive propulsion systems: State-of-the-art review. *IEEE Transactions on Transportation Electrification*, **8**(2), 2898–2914.

Baumgartner, E., Ronellenfitsch, A., Reuss, H.-C., and Schramm, D. (2019). Using a dynamic driving simulator for perception-based powertrain development. *Transportation research part F: traffic psychology and behaviour*, **61**, 281–290.

Bender, F. A., Kaszynski, M., and Sawodny, O. (2013). Drive cycle prediction and energy management optimization for hybrid hydraulic vehicles. *IEEE Transactions on vehicular technology*, **62**(8), 3581–3592.

Benedito, E. and Dòria-Cerezo, A. (2018). Influence of cooperative-controlled driving in the traffic flow. In *2018 IEEE International Conference on Industrial Technology (ICIT)*, pages 1795–1800. IEEE.

Benloucif, M., Sentouh, C., Floris, J., Simon, P., and Popieul, J.-C. (2019). Online adaptation of the level of haptic authority in a lane keeping system considering the driver's state. *Transportation research part F: traffic psychology and behaviour*, **61**, 107–119.

Bianchi Piccinini, G., Lehtonen, E., Forcolin, F., Engström, J., Albers, D., Markkula, G., Lodin, J., and Sandin, J. (2019). How do drivers respond to silent automation

failures? driving simulator study and comparison of computational driver braking models. *Human factors*, page 0018720819875347.

Bilgin, B., Magne, P., Malysz, P., Yang, Y., Pantelic, V., Preindl, M., Korobkine, A., Jiang, W., Lawford, M., and Emadi, A. (2015). Making the case for electrified transportation. *IEEE Transactions on Transportation Electrification*, **1**(1), 4–17.

Biswas, A. and Emadi, A. (2019). Energy management systems for electrified powertrains: State-of-the-art review and future trends. *IEEE Transactions on Vehicular Technology*, **68**(7), 6453–6467.

Biswas, A., Anselma, P. G., and Emadi, A. (2019). Real-time optimal energy management of electrified powertrains with reinforcement learning. In *2019 IEEE Transportation Electrification Conference and Expo (ITEC)*, pages 1–6. IEEE.

Biswas, A., Anselma, P. G., Rathore, A., and Emadi, A. (2020). Comparison of three real-time implementable energy management strategies for multi-mode electrified powertrain. In *2020 IEEE Transportation Electrification Conference & Expo (ITEC)*, pages 514–519. IEEE.

Blana, E. (1996). A survey of driving research simulators around the world.

Blissing, B. and Bruzelius, F. (2018). Exploring the suitability of virtual reality for driving simulation. In *Driving Simulation Conference 2018*, pages 163–166.

Blommer, M., Curry, R., Swaminathan, R., Tijerina, L., Talamonti, W., and Kochhar, D. (2017). Driver brake vs. steer response to sudden forward collision scenario in manual and automated driving modes. *Transportation research part F: traffic psychology and behaviour*, **45**, 93–101.

Bruck, L., Emadi, A., and Divakarla, K. P. (2019a). A review of the relevance of driving condition mapping and vehicle simulation for energy management system design. *International Journal of Powertrains*, **8**(3), 224–251.

Bruck, L., Veldhuis, S., and Emadi, A. (2019b). Selection method of a driving simulator motion system. In *2019 IEEE Transportation Electrification Conference and Expo (ITEC)*, pages 1–6. IEEE.

Bruck, L., Bonab, S. A., Lempert, A., Biswas, A., Anselma, P. G., Roeleveld, J., Rane, O., Madireddy, K., Wasacz, B., Belingardi, G., *et al.* (2020). An iterative histogram-based optimization of calibration tables in a powertrain controller. Technical report, SAE Technical Paper.

Bruschetta, M., Maran, F., and Beghi, A. (2016). A nonlinear, mpc-based motion cueing algorithm for a high-performance, nine-dof dynamic simulator platform. *IEEE Transactions on Control Systems Technology*, **25**(2), 686–694.

Bruschetta, M., Maran, F., and Beghi, A. (2017a). A fast implementation of mpc-based motion cueing algorithms for mid-size road vehicle motion simulators. *Vehicle system dynamics*, **55**(6), 802–826.

Bruschetta, M., Cenedese, C., Beghi, A., and Maran, F. (2017b). A motion cueing algorithm with look-ahead and driver characterization: Application to vertical car dynamics. *IEEE Transactions on Human-Machine Systems*, **48**(1), 6–16.

Bruschetta, M., Chen, Y., Cunico, D., Mion, E., and Beghi, A. (2018). A nonlinear mpc based motion cueing strategy for a high performance driving simulator

with active seat. In *2018 IEEE 15th International Workshop on Advanced Motion Control (AMC)*, pages 23–28. IEEE.

Bruschetta, M., Cenedese, C., and Beghi, A. (2019). A real-time, mpc-based motion cueing algorithm with look-ahead and driver characterization. *Transportation research part F: traffic psychology and behaviour*, **61**, 38–52.

Bukal, A., Haycock, B., and Grant, P. R. (2019). An adaptive model predictive control based motion drive algorithm. In *AIAA Scitech 2019 Forum*, page 0423.

Chandak, G. A. and Bhole, A. (2017). A review on regenerative braking in electric vehicle. In *2017 Innovations in Power and Advanced Computing Technologies (i-PACT)*, pages 1–5. IEEE.

Chang, X., Li, H., Qin, L., Rong, J., Lu, Y., and Chen, X. (2019). Evaluation of cooperative systems on driver behavior in heavy fog condition based on a driving simulator. *Accident Analysis & Prevention*, **128**, 197–205.

Chen, S.-H. and Fu, L.-C. (2010). An optimal washout filter design for a motion platform with senseless and angular scaling maneuvers. In *Proceedings of the 2010 American Control Conference*, pages 4295–4300. IEEE.

Chen, Z., Li, L., Yan, B., Yang, C., Martínez, C. M., and Cao, D. (2016). Multimode energy management for plug-in hybrid electric buses based on driving cycles prediction. *IEEE Transactions on Intelligent Transportation Systems*, **17**(10), 2811–2821.

Chiew, Y., Jalil, M. A., and Hussein, M. (2008). Kinematic modeling of driving simulator motion platform. In *2008 IEEE Conference on Innovative Technologies in Intelligent Systems and Industrial Applications*, pages 30–34. IEEE.

Chrenko, D., Gan, S., Gutenkunst, C., Kriesten, R., and Le Moyne, L. (2015). Novel classification of control strategies for hybrid electric vehicles. In *2015 IEEE vehicle power and propulsion conference (VPPC)*, pages 1–6. IEEE.

Cohen-Lazry, G., Katzman, N., Borowsky, A., and Oron-Gilad, T. (2019). Directional tactile alerts for take-over requests in highly-automated driving. *Transportation research part F: traffic psychology and behaviour*, **65**, 217–226.

Colombet, F., Paillot, D., Mérienne, F., and Kemeny, A. (2011). Visual scale factor for speed perception. *Journal of Computing and Information Science in Engineering*, **11**(4).

Dagci, O. (2018). *Hybrid Electric Powertrain Design and Control with Planetary Gear Sets for Performance and Fuel Economy*. Ph.D. thesis.

Deng, C., Wu, C., Lyu, N., and Huang, Z. (2017). Driving style recognition method using braking characteristics based on hidden markov model. *PloS one*, **12**(8), e0182419.

Di Loreto, C., Chardonnet, J.-R., Mackenzie, J., Dutchke, J., Van den Berg, A., Forrest, M., Merienne, F., and Sandoz, B. (2019). Science Arts & Métiers (SAM) Real car versus driving simulator comparison of head dynamics in emergency braking events. In *Driving Simulation Conference & Exhibition*, pages 51–55, Strasbourg, France.

Divakarla, K. P., Nalakath, S., Drennan, M., Ahmed, R., Emadi, A., and Razavi, S. (2015). Battery characterization and state-of-charge prediction for different journey

conditions with the help of the" journey mapping" concept. In *IECON 2015-41st Annual Conference of the IEEE Industrial Electronics Society*, pages 003683–003688. IEEE.

Divakarla, K. P., Emadi, A., and Razavi, S. N. (2016). Journey mapping—a new approach for defining automotive drive cycles. *IEEE Transactions on Industry Applications*, **52**(6), 5121–5129.

Duan, J., Li, R., Hou, L., Wang, W., Li, G., Li, S. E., Cheng, B., and Gao, H. (2017). Driver braking behavior analysis to improve autonomous emergency braking systems in typical chinese vehicle-bicycle conflicts. *Accident Analysis & Prevention*, **108**, 74–82.

Egardt, B., Murgovski, N., Pourabdollah, M., and Mardh, L. J. (2014). Electromobility studies based on convex optimization: Design and control issues regarding vehicle electrification. *IEEE Control Systems Magazine*, **34**(2), 32–49.

Emadi, A. (2011). Transportation 2.0. *IEEE Power and Energy Magazine*, **9**(4), 18–29.

Emadi, A. (2014). *Advanced electric drive vehicles*. CRC Press, Boca Raton, FL.

Enache, B., Lefter, E., and Stoica, C. (2013). Comparative study for generic battery models used for electric vehicles. In *2013 8TH INTERNATIONAL SYMPOSIUM ON ADVANCED TOPICS IN ELECTRICAL ENGINEERING (ATEE)*, pages 1–6. IEEE.

Eriksson, L. and Nielsen, L. (2014). *Modeling and control of engines and drivelines*. John Wiley & Sons.

Fang, Z. and Kemeny, A. (2012). Motion cueing algorithms for a real-time automobile driving simulator. In *Driving Simulation Conference*, pages 159–174.

Fang, Z., Tsushima, M., Kitahara, E., Machida, N., Wautier, D., and Kemeny, A. (2017). Motion cueing algorithm for high performance driving simulator using yaw table. *IFAC-PapersOnLine*, **50**(1), 15965–15970.

Fatehi, A., Abe, K., and Lucas, C. (1998). Challenges on the design of the fuzzy logic controller by the genetic algorithms. In *2nd Int. workshop on intelligent systems of the 4th joint conf. on information systems*. Citeseer.

Favarò, F. M., Seewald, P., Scholtes, M., and Eurich, S. (2019). Quality of control takeover following disengagements in semi-automated vehicles. *Transportation research part F: traffic psychology and behaviour*, **64**, 196–212.

Fernandez, S. and Ito, T. (2016). Driver classification for intelligent transportation systems using fuzzy logic. In *2016 IEEE 19th International Conference on Intelligent Transportation Systems (ITSC)*, pages 1212–1216.

Filtness, A. J., Larue, G., Schramm, A., Fuller, J., Rakotonirainy, A., Han, C., and Cairney, P. (2017). Safety implications of co-locating road signs: A driving simulator investigation. *Transportation research part F: traffic psychology and behaviour*, **47**, 187–198.

Fisher, D. L., Rizzo, M., Caird, J., and Lee, J. D. (2011). *Handbook of driving simulation for engineering, medicine, and psychology*. CRC Press, Boca Raton, FL.

Gao, D. W., Mi, C., and Emadi, A. (2007). Modeling and simulation of electric and hybrid vehicles. *Proceedings of the IEEE*, **95**(4), 729–745.

Gao, M. and Du, J. (2016). Design method of energy management strategy for range-extended electric buses based on convex optimization. In *2016 11th International Forum on Strategic Technology (IFOST)*, pages 286–290. IEEE.

Geering, H. P. (2007). *Optimal control with engineering applications*. Springer.

Gillespie, T. D. (1992). *Fundamentals of vehicle dynamics*, volume 400. Society of automotive engineers Warrendale, PA, Warrendale, PA.

Gruening, J., Bernard, J., Clover, C., and Hoffmeister, K. (1998). Driving simulation. *SAE transactions*, pages 376–385.

Guiggiani, M. (2014). The science of vehicle dynamics. *Pisa, Italy: Springer Netherlands*, page 15.

Gurkaynak, Y., Khaligh, A., and Emadi, A. (2010). Neural adaptive control strategy for hybrid electric vehicles with parallel powertrain. In *2010 IEEE Vehicle Power and Propulsion Conference*, pages 1–6. IEEE.

Güzel, İ. and GöL, M. (2021). Driving pattern recognition algorithm using fast fourier transform. In *2021 29th Signal Processing and Communications Applications Conference (SIU)*, pages 1–4. IEEE.

Han, L., Jiao, X., and Zhang, Z. (2020). Recurrent neural network-based adaptive energy management control strategy of plug-in hybrid electric vehicles considering battery aging. *Energies*, **13**(1), 202.

Haußmann, M., Barroso, D., Vidal, C., Bruck, L., and Emadi, A. (2019). A novel multi-mode adaptive energy consumption minimization strategy for p1-p2 hybrid electric vehicle architectures. In *2019 IEEE Transportation Electrification Conference and Expo (ITEC)*, pages 1–6.

Haycock, B., Campos, J., Koenraad, N., Potter, M., and Advani, S. (2019). Creating headlight glare in a driving simulator. *Transportation research part F: traffic psychology and behaviour*, **61**, 93–106.

Heitbrink, D. A. and Cable, S. (2007). Design of a driving simulation sound engine. In *Driving Simulation Conference, North America 2007 (DSC-NA 2007) Ford Motor CompanyNational Highway Traffic Safety AdministrationUniversity of Iowa, Iowa CityTransportation Research Board.*

Herrera, V. I., Saez-de Ibarra, A., Milo, A., Gaztañaga, H., and Camblong, H. (2015). Optimal energy management of a hybrid electric bus with a battery-supercapacitor storage system using genetic algorithm. In *2015 international conference on electrical systems for aircraft, railway, ship propulsion and road vehicles (ESARS)*, pages 1–6. IEEE.

Hu, Y., Yang, L., Yan, B., Yan, T., and Ma, P. (2015). An online rolling optimal control strategy for commuter hybrid electric vehicles based on driving condition learning and prediction. *IEEE Transactions on Vehicular Technology*, **65**(6), 4312–4327.

Huang, Q. and Wang, H. (2004). Fundamental study of jerk: evaluation of shift quality and ride comfort. Technical report, SAE Technical Paper.

Imamura, T., Ogi, T., Lun, E. T. C., Zhang, Z., and Miyake, T. (2013). Trial study of traffic safety education for high school students using driving simulator. In *2013 IEEE International Conference on Systems, Man, and Cybernetics*, pages 4606–4611. IEEE.

Irwin, C., Iudakhina, E., Desbrow, B., and McCartney, D. (2017). Effects of acute alcohol consumption on measures of simulated driving: a systematic review and meta-analysis. *Accident Analysis & Prevention*, **102**, 248–266.

Jamali, H., Wang, Y., Yang, Y., Habibi, S., and Emadi, A. (2021). Rule-based energy management strategy for a power-split hybrid electric vehicle with lstm network prediction model. In *2021 IEEE Energy Conversion Congress and Exposition (ECCE)*, pages 1447–1453. IEEE.

Jamson, A., Hibberd, D. L., and Merat, N. (2013). The design of haptic gas pedal feedback to support eco-driving. In *Proceedings of the Seventh International Driving Symposium on Human Factors in Driver Assessment, Training, and Vehicle Design*, pages 264–270. University of Iowa.

Jamson, A. H. J. (2010). *Motion cueing in driving simulators for research applications*. Ph.D. thesis, University of Leeds, Leeds, UK.

Jazar, R. N. (2017). *Vehicle dynamics: theory and application*. Springer, Cham, Switzerland.

Jia, G., Pan, G., Gao, Q., and Zhang, Y. (2019). Research on position inverse solution of electric-driven stewart platform based on simulink. *The Journal of Engineering*, **2019**(13), 379–383.

Jiang, Q., Ossart, F., and Marchand, C. (2017). Comparative study of real-time hev energy management strategies. *IEEE Transactions on Vehicular Technology*, **66**(12), 10875–10888.

Jin, Y., Chanal, H., and Paccot, F. (2015). *Parallel Robots. Handboo of Manufacturing Engineering and Technology*. Springer, Dordrecht, Netherlands.

Jing, J., Zhao, F., Liu, Y., and Huang, W. (2021). Research on control of engine start and stop in p2. 5 hybrid system. In *2021 International Conference on Computer, Control and Robotics (ICCCR)*, pages 161–172. IEEE.

Jinhao, M., Ricco, M., Guangzhao, L., Swierczynski, M. J., Stroe, D.-I., Stroe, A.-I., and Teodorescu, R. (2017). An overview of online implementable soc estimation methods for lithium-ion batteries. In *2017 International Conference on Optimization of Electrical and Electronic Equipment (OPTIM) & 2017 Intl Aegean Conference on Electrical Machines and Power Electronics (ACEMP)*, pages 573–580. IEEE Press.

Jones, S., Huss, A., Kural, E., Massoner, A., Parrilla, A. F., Allouchery, L., and Gocer, I. (2016). V2x based traffic light assistant for increased efficiency of hybrid & electric vehicles. In *AmE 2016-Automotive meets Electronics; 7th GMM-Symposium*, pages 1–5. VDE.

Kang, M.-W. and Momtaz, S. U. (2018). Assessment of driver compliance on roadside safety signs with auditory warning sounds generated from pavement surface–a driving simulator study. *Journal of traffic and transportation engineering (English edition)*, **5**(1), 1–13.

Katliar, M., Olivari, M., Drop, F. M., Nooij, S., Diehl, M., and Bülthoff, H. H. (2019). Offline motion simulation framework: Optimizing motion simulator trajectories and parameters. *Transportation research part F: traffic psychology and behaviour*, **66**, 29–46.

Kemmerer Jr, R., Hulbert, S., and Donohue, R. (1975). Ucla driving simulation laboratory: With a 360 degree scene around a full size car. In *Simulators and Simulation II: Design, Applications and Techniques*, volume 59, pages 158–170. International Society for Optics and Photonics.

Keshavarz, B., Hettinger, L. J., Vena, D., and Campos, J. L. (2014). Combined effects of auditory and visual cues on the perception of vection. *Experimental brain research*, **232**(3), 827–836.

Keshavarz, B., Campos, J. L., DeLucia, P. R., and Oberfeld, D. (2017). Estimating the relative weights of visual and auditory tau versus heuristic-based cues for time-to-contact judgments in realistic, familiar scenes by older and younger adults. *Attention, Perception, & Psychophysics*, **79**(3), 929–944.

Kharrazi, S., Augusto, B., and Fröjd, N. (2020). Vehicle dynamics testing in motion based driving simulators. *Vehicle system dynamics*, **58**(1), 92–107.

Kiencke, U. and Nielsen, L. (2000). Automotive control systems: for engine, driveline, and vehicle.

Koglbauer, I., Holzinger, J., Eichberger, A., and Lex, C. (2018). Autonomous emergency braking systems adapted to snowy road conditions improve drivers' perceived safety and trust. *Traffic injury prevention*, **19**(3), 332–337.

Kok, D., Knowles, M., and Morris, A. (2012). Building a driving simulator as an electric vehicle hardware development tool. In *Driving Simulation Conference 2012*, pages 1–7, Paris, France.

Kumar, P. R. and Bandyopadhyay, B. (2012). Stabilization of stewart platform using higher order sliding mode control. In *2012 7th International Conference on Electrical and Computer Engineering*, pages 945–948. IEEE.

Kural, E. and Güvenç, B. A. (2015). Integrated adaptive cruise control for parallel hybrid vehicle energy management. *IFAC-PapersOnLine*, **48**(15), 313–319.

Lackner, J. R. and DiZio, P. (2005). Vestibular, proprioceptive, and haptic contributions to spatial orientation. *Annu. Rev. Psychol.*, **56**, 115–147.

Lamb, W. F., Wiedmann, T., Pongratz, J., Andrew, R., Crippa, M., Olivier, J. G., Wiedenhofer, D., Mattioli, G., Al Khourdajie, A., House, J., *et al.* (2021). A review of trends and drivers of greenhouse gas emissions by sector from 1990 to 2018. *Environmental research letters*.

Lamprecht, A., Steffen, D., Haecker, J., and Graichen, K. (2019). Optimal control based reference generation for model predictive motion cueing algorithms. In *2019 IEEE Conference on Control Technology and Applications (CCTA)*, pages 203–208. IEEE.

Large, D. R., Burnett, G., Crundall, E., Lawson, G., Skrypchuk, L., and Mouzakitis, A. (2019). Evaluating secondary input devices to support an automotive touchscreen hmi: A cross-cultural simulator study conducted in the uk and china. *Applied ergonomics*, **78**, 184–196.

Lee, C.-H. and Wu, C.-H. (2015). Collecting and mining big data for electric vehicle systems using battery modeling data. In *2015 12th International Conference on Information Technology-New Generations*, pages 626–631. IEEE.

Leudet, J., Christophe, F., Mikkonen, T., and Männistö, T. (2019). Ailivesim: An extensible virtual environment for training autonomous vehicles. In *2019 IEEE 43rd Annual Computer Software and Applications Conference (COMPSAC)*, volume 1, pages 479–488. IEEE.

Li, S. and Cheng, X. (2014). A comparative study on rc models of lithium-ion battery. In *2014 IEEE Conference and Expo Transportation Electrification Asia-Pacific (ITEC Asia-Pacific)*, pages 1–4. IEEE.

Liessner, R., Dietermann, A., Bäker, B., and Lüpkes, K. (2016). Derivation of real-world driving cycles corresponding to traffic situation and driving style on the basis of markov models and cluster analyses.

Lin, J. and Niemeier, D. A. (2003). Estimating regional air quality vehicle emission inventories: constructing robust driving cycles. *Transportation Science*, **37**(3), 330–346.

Liu, J. and Peng, H. (2008). Modeling and control of a power-split hybrid vehicle. *IEEE transactions on control systems technology*, **16**(6), 1242–1251.

Liu, W. (2017). *Hybrid electric vehicle system modeling and control*. John Wiley & Sons.

Lotz, A., Russwinkel, N., and Wohlfarth, E. (2019). Response times and gaze behavior of truck drivers in time critical conditional automated driving take-overs. *Transportation research part F: traffic psychology and behaviour*, **64**, 532–551.

Ma, J., Shah, A. S., Baysal, M., and Ilhan, H. (2017). On-line energy management strategy for hybrid electric vehicles based on ampc. In *2017 10th International Conference on Electrical and Electronics Engineering (ELECO)*, pages 185–189. IEEE.

Machado, F. A., Kollmeyer, P. J., Barroso, D. G., and Emadi, A. (2021). Multi-speed gearboxes for battery electric vehicles: Current status and future trends. *IEEE Open Journal of Vehicular Technology*, **2**, 419–435.

Markkula, G., Romano, R., Waldram, R., Giles, O., Mole, C., and Wilkie, R. (2019). Modelling visual-vestibular integration and behavioural adaptation in the driving simulator. *Transportation research part F: traffic psychology and behaviour*, **66**, 310–323.

Martinez, C. M., Heucke, M., Wang, F.-Y., Gao, B., and Cao, D. (2017). Driving style recognition for intelligent vehicle control and advanced driver assistance: A survey. *IEEE Transactions on Intelligent Transportation Systems*, **19**(3), 666–676.

Masson-Delmotte, V., Zhai, P., Pirani, A., Connors, S. L., Péan, C., Berger, S., Caud, N., Chen, Y., Goldfarb, L., Gomis, M., *et al.* (2021). Climate change 2021: the physical science basis. *Contribution of working group I to the sixth assessment report of the intergovernmental panel on climate change*, page 2.

Matowicki, M., Přibyl, O., and Bouchner, P. (2016). Pragmatic overview of surrounding traffic implementation into driving simulator. In *2016 ELEKTRO*, pages 423–428. IEEE.

Merenda, C., Suga, C., Gabbard, J., and Misu, T. (2019). Effects of vehicle simulation visual fidelity on assessing driver performance and behavior. In *2019 IEEE Intelligent Vehicles Symposium (IV)*, pages 1679–1686. IEEE.

Miles, G. and Vincent, D. (1934). The institute's tests for motor drivers. *The Human Factor*, **8**(7), 245–257.

Miro-Padovani, T., Colin, G., Ketfi-Chérif, A., and Chamaillard, Y. (2015). Implementation of an energy management strategy for hybrid electric vehicles including drivability constraints. *IEEE Transactions on Vehicular Technology*, **65**(8), 5918–5929.

Miunske, T., Holzapfel, C., Baumgartner, E., and Reuss, H.-C. (2019). A new approach for an adaptive linear quadratic regulated motion cueing algorithm for an 8 dof full motion driving simulator. In *2019 International Conference on Robotics and Automation (ICRA)*, pages 497–503. IEEE.

Miyajima, C., Nishiwaki, Y., Ozawa, K., Wakita, T., Itou, K., Takeda, K., and Itakura, F. (2007). Driver modeling based on driving behavior and its evaluation in driver identification. *Proceedings of the IEEE*, **95**(2), 427–437.

Mohajer, N., Abdi, H., Nelson, K., and Nahavandi, S. (2015). Vehicle motion simulators, a key step towards road vehicle dynamics improvement. *Vehicle System Dynamics*, **53**(8), 1204–1226.

Mohammadi, A., Asadi, H., Mohamed, S., Nelson, K., and Nahavandi, S. (2018). Multiobjective and interactive genetic algorithms for weight tuning of a model predictive control-based motion cueing algorithm. *IEEE transactions on cybernetics*, **49**(9), 3471–3481.

Morra, L., Lamberti, F., Pratticó, F. G., La Rosa, S., and Montuschi, P. (2019). Building trust in autonomous vehicles: Role of virtual reality driving simulators in hmi design. *IEEE Transactions on Vehicular Technology*, **68**(10), 9438–9450.

Mourant, R. R. and Yin, Z. (2010). A turning cabin simulator to reduce simulator sickness. In *The Engineering Reality of Virtual Reality 2010*, volume 7525, page 752503. International Society for Optics and Photonics.

Murphey, Y. L., Park, J., Chen, Z., Kuang, M. L., Masrur, M. A., and Phillips, A. M. (2012). Intelligent hybrid vehicle power control—part i: Machine learning of optimal vehicle power. *IEEE Transactions on Vehicular Technology*, **61**(8), 3519–3530.

Nehaoua, L., Mohellebi, H., Amouri, A., Arioui, H., Espie, S., and Kheddar, A. (2008). Design and control of a small-clearance driving simulator. *IEEE Transactions on Vehicular Technology*, **57**(2), 736–746.

Nise, N. S. (2020). *Control systems engineering*. John Wiley & Sons.

Ogitsu, T. and Mizoguchi, H. (2015). A study on driver training on advanced driver assistance systems by using a driving simulator. In *2015 International Conference on Connected Vehicles and Expo (ICCVE)*, pages 352–353. IEEE.

Ou, Y.-J., Wang, X.-L., Jiang, J.-F., Wei, H.-Y., Huang, C.-L., and Hsu, K.-S. (2018). Simulator training to drive the risk perception of the reliability and validity. In *2018 IEEE International Conference on Applied System Invention (ICASI)*, pages 374–377. IEEE.

Pacejka, H. (2005). *Tire and vehicle dynamics*. Elsevier.

Pakdamanian, E., Feng, L., and Kim, I. (2018). The effect of whole-body haptic feedback on driver's perception in negotiating a curve. In *Proceedings of the Human Factors and Ergonomics Society Annual Meeting*, volume 62, pages 19–23. SAGE Publications Sage CA: Los Angeles, CA.

Palcu, P. and Bauman, J. (2017). Whole-day driving prediction control strategy: Analysis on real-world drive cycles. *IEEE Transactions on Transportation Electrification*, **4**(1), 172–183.

Pampel, S. M., Jamson, S. L., Hibberd, D. L., and Barnard, Y. (2015). How i reduce fuel consumption: An experimental study on mental models of eco-driving. *Transportation Research Part C: Emerging Technologies*, **58**, 669–680.

Papelis, Y. E., Watson, G. S., and Brown, T. L. (2010). An empirical study of the effectiveness of electronic stability control system in reducing loss of vehicle control. *Accident Analysis & Prevention*, **42**(3), 929–934.

Petermeijer, S., Doubek, F., and de Winter, J. (2017). Driver response times to auditory, visual, and tactile take-over requests: A simulator study with 101 participants. In *2017 IEEE International Conference on Systems, Man, and Cybernetics (SMC)*, pages 1505–1510. IEEE.

Phuc, D. H., Rasincharoensak, P., and Nagai, M. (2018). Study on driver model for hybrid truck based on driving simulator experimental results. *IATSS research*, **42**(1), 18–23.

Pitz, J., Nguyen, M.-T., Baumann, G., and Reuss, H.-C. (2014). Combined motion of a hexapod with a xy table system for lateral movements. In *presented at Driving Simulation Conference*.

Plett, G. L. (2004). Extended kalman filtering for battery management systems of lipb-based hev battery packs: Part 1. background. *Journal of Power sources*, **134**(2), 252–261.

Pourabdollah, M., Egardt, B., Murgovski, N., and Grauers, A. (2017). Convex optimization methods for powertrain sizing of electrified vehicles by using different levels of modeling details. *IEEE Transactions on Vehicular Technology*, **67**(3), 1881–1893.

Ramkhalawansingh, R., Keshavarz, B., Haycock, B., Shahab, S., and Campos, J. L. (2016). Age differences in visual-auditory self-motion perception during a simulated driving task. *Frontiers in Psychology*, **7**, 595.

Reid, L. and Nahon, M. (1985). Flight simulation motion-base drive algorithms: part 1. developing and testing equations. *UTIAS Report, No. 296*.

Rengifo, C., Chardonnet, J.-R., Paillot, D., Mohellebi, H., and Kemeny, A. (2018). Solving the Constrained Problem in Model Predictive Control Based Motion Cueing Algorithm with a Neural Network Approach. In *Driving Simulation Conference 2018 Europe VR*, pages 63–69, Antibes, France.

Rhode, S. and Gauterin, F. (2013). Online estimation of vehicle driving resistance parameters with recursive least squares and recursive total least squares. In *2013 IEEE Intelligent Vehicles Symposium (IV)*, pages 269–276. IEEE.

Rodriguez, J., Freeman, P., Wagner, J., Bridges, W., Pidgeon, P., and Alexander, K. (2016). Automotive steering system preferences evaluated using a driving simulator. *International journal of automotive technology*, **17**(1), 71–81.

Romano, R., Markkula, G., Boer, E., Jamson, H., Bean, A., Tomlinson, A., Horrobin, A., and Sadraei, E. (2019). An objective assessment of the utility of a driving simulator for low mu testing. *Transportation research part F: traffic psychology and behaviour*, **65**, 34–45.

Rommerskirchen, C. P., Helmbrecht, M., and Bengler, K. J. (2014). The impact of an anticipatory eco-driver assistant system in different complex driving situations on the driver behavior. *IEEE Intelligent Transportation Systems Magazine*, **6**(2), 45–56.

Sadraei, E., Romano, R., Jamson, S., Markkula, G., and Jamson, H. (2018). Driving simulator motion base right sizing. In *DSC 2018 Europe*. Driving Simulation Association.

SAE, S. (1996). J1263-road load measurement and dynamometer simulation using coastdown techniques.

SAE Reccomended Practice, S. (2014). Definitions for terms related to on-road motor vehicle automated driving systems. *Society of Automotive Engineers (SAE): Troy, MI, USA*.

SAE Recommended Practice, S. (2008). Vehicle dynamics terminology. *Society of Automotive Engineers (SAE): Troy, MI, USA*.

SAE Recommended Practice, S. (2012). Battery electric vehicle energy consumption and range test procedure. *Society of Automotive Engineers (SAE): Troy, MI, USA*.

Sampathnarayanan, B., Onori, S., and Yurkovich, S. (2014). An optimal regulation strategy with disturbance rejection for energy management of hybrid electric vehicles. *Automatica*, **50**(1), 128–140.

Sangwan, V., Sharma, A., Kumar, R., and Rathore, A. (2016). Estimation of optimal li-ion battery parameters considering c-rate, soc and temperature. In *2016 7th India International Conference on Power Electronics (IICPE)*, pages 1–6. IEEE.

Sarker, S. and Haque, M. M. (2020). A data change rule based empirical framework for labeling unlabeled time series driving data. In *2020 2nd International Conference on Advanced Information and Communication Technology (ICAICT)*, pages 476–479.

Schmieder, H., Nagel, K., and Schoener, H.-P. (2017). Enhancing a driving simulator with a 3d-stereo projection system. In *Proceedings of the Driving Simulator Conference,(Stuttgart, Germany)*.

Schramm, D., Hiller, M., and Bardini, R. (2014). *Vehicle dynamics: Modeling and Simulation*. Springer, Berlin , Germany.

Sciarretta, A., Back, M., and Guzzella, L. (2004). Optimal control of parallel hybrid electric vehicles. *IEEE Transactions on control systems technology*, **12**(3), 352–363.

Serrao, L., Onori, S., and Rizzoni, G. (2011). A comparative analysis of energy management strategies for hybrid electric vehicles. *Journal of Dynamic Systems, Measurement, and Control*, **133**(3).

Sharples, S., Shalloe, S., Burnett, G., and Crundall, D. (2016). Journey decision making: the influence on drivers of dynamic information presented on variable message signs. *Cognition, Technology & Work*, **18**(2), 303–317.

Shida, Y., Okajima, H., Matsuno, D., and Matsunaga, N. (2016). Evaluation of steering model depending on gazing distance by using driving simulator. In *2016 16th International Conference on Control, Automation and Systems (ICCAS)*, pages 39–44. IEEE.

Slob, J. (2008). State-of-the-art driving simulators, a literature survey. Technical Report DCT 2008.107, Eindhoven University of Technology, Eindhoven, Netherlands.

Souffran, G., Miegeville, L., and Guerin, P. (2011). Simulation of real-world vehicle missions using a stochastic markov model for optimal design purposes. In *2011 IEEE Vehicle Power and Propulsion Conference*, pages 1–6. IEEE.

Souffran, G., Miègeville, L., and Guérin, P. (2012). Simulation of real-world vehicle missions using a stochastic markov model for optimal powertrain sizing. *IEEE transactions on vehicular technology*, **61**(8), 3454–3465.

Strauch, C., Mühl, K., Patro, K., Grabmaier, C., Reithinger, S., Baumann, M., and Huckauf, A. (2019). Real autonomous driving from a passenger's perspective: Two experimental investigations using gaze behaviour and trust ratings in field and

simulator. *Transportation research part F: traffic psychology and behaviour*, **66**, 15–28.

Suh, J., Yi, K., Jung, J., Lee, K., Chong, H., and Ko, B. (2016). Design and evaluation of a model predictive vehicle control algorithm for automated driving using a vehicle traffic simulator. *Control Engineering Practice*, **51**, 92–107.

Suikat, R. (2005). The new dynamic driving simulator at dlr. In *Driving Simulator Conference*, number 8, pages 374–381.

Sun, J., Ma, Z., Li, T., and Niu, D. (2015). Development and application of an integrated traffic simulation and multi-driving simulators. *Simulation Modelling Practice and Theory*, **59**, 1–17.

Sundstrom, O. and Guzzella, L. (2009). A generic dynamic programming matlab function. In *2009 IEEE control applications,(CCA) & intelligent control,(ISIC)*, pages 1625–1630. IEEE.

Tamir, T. S., Xiong, G., Tian, Y., and Xiong, G. (2019). Passivity based control of stewart platform for trajectory tracking. In *2019 14th IEEE Conference on Industrial Electronics and Applications (ICIEA)*, pages 988–993. IEEE.

Tao, Y., Xie, X., Zhao, H., Xu, W., and Chen, H. (2017). A regenerative braking system for electric vehicle with four in-wheel motors based on fuzzy control. In *2017 36th Chinese Control Conference (CCC)*, pages 4288–4293. IEEE.

Tran, C., Doshi, A., and Trivedi, M. M. (2012). Modeling and prediction of driver behavior by foot gesture analysis. *Computer Vision and Image Understanding*, **116**(3), 435–445.

Tran, D.-D., Vafaeipour, M., El Baghdadi, M., Barrero, R., Van Mierlo, J., and Hegazy, O. (2020). Thorough state-of-the-art analysis of electric and hybrid vehicle powertrains: Topologies and integrated energy management strategies. *Renewable and Sustainable Energy Reviews*, **119**, 109596.

Ulahannan, A., Cain, R., Thompson, S., Skrypchuk, L., Mouzakitis, A., Jennings, P., and Birrell, S. (2020). User expectations of partial driving automation capabilities and their effect on information design preferences in the vehicle. *Applied ergonomics*, **82**, 102969.

Uncini, A. (2015). *Fundamentals of adaptive signal processing*. Springer.

Urlings, J. H., Roelofs, E., Cuenen, A., Brijs, K., Brijs, T., and Jongen, E. M. (2019). Development of single-session driving simulator-based and computer-based training for at-risk older drivers. *Educational Gerontology*, **45**(4), 283–296.

Valera, J., Heriz, B., Lux, G., Caus, J., and Bader, B. (2013). Driving cycle and road grade on-board predictions for the optimal energy management in ev-phevs. In *2013 World Electric Vehicle Symposium and Exhibition (EVS27)*, pages 1–10. IEEE.

Valverde, H. H. (1973). A review of flight simulator transfer of training studies. *Human Factors*, **15**(6), 510–522.

van Leeuwen, P. M., Happee, R., and de Winter, J. C. (2015). Changes of driving performance and gaze behavior of novice drivers during a 30-min simulator-based training. *Procedia Manufacturing*, **3**, 3325–3332.

Vasiljevic, G. and Bogdan, S. (2016). Model predictive control based torque vectoring algorithm for electric car with independent drives. In *2016 24th Mediterranean Conference on Control and Automation (MED)*, pages 316–321. IEEE.

Vidal, C., Malysz, P., Kollmeyer, P., and Emadi, A. (2020). Machine learning applied to electrified vehicle battery state of charge and state of health estimation: State-of-the-art. *IEEE Access*, **8**, 52796–52814.

Wang, J. and Söffker, D. (2016). Improving driving efficiency for hybrid electric vehicle with suitable interface. In *2016 IEEE International Conference on Systems, Man, and Cybernetics (SMC)*, pages 000928–000933. IEEE.

Wang, X., Wang, X., Cai, B., and Liu, J. (2019). Combined alignment effects on deceleration and acceleration: a driving simulator study. *Transportation research part C: emerging technologies*, **104**, 172–183.

Wang, Z., Zheng, R., Kaizuka, T., Shimono, K., and Nakano, K. (2017). The effect of a haptic guidance steering system on fatigue-related driver behavior. *IEEE Transactions on Human-Machine Systems*, **47**(5), 741–748.

Weatherhog, S. and Sharma, R. (2013). Component-wise physics-based modelling of a lithium-ion battery for power equalization. In *2013 IEEE Power & Energy Society General Meeting*, pages 1–5. IEEE.

Wei, C., Romano, R., Merat, N., Wang, Y., Hu, C., Taghavifar, H., Hajiseyedjavadi, F., and Boer, E. R. (2019). Risk-based autonomous vehicle motion control with considering human driver's behaviour. *Transportation Research Part C: Emerging Technologies*, **107**, 1–14.

Widmaier, E. P., Raff, H., Strang, K. T., and Vander, A. J. (2008). *Vander's Human physiology: the mechanisms of body function.* McGraw-Hill Higher Education, Boston, MA.

Wierwille, W. W. and Fung, P. P. (1975). Comparison of computer-generated and simulated motion picture displays in a driving simulation. *Human Factors*, **17**(6), 577–590.

Wilkie, R. and Wann, J. (2003). Controlling steering and judging heading: retinal flow, visual direction, and extraretinal information. *Journal of Experimental Psychology: Human Perception and Performance*, **29**(2), 363.

Wilkinson, M., Brown, T., and Ahmad, O. (2012). The national advanced driving simulator (nads) description and capabilities in vision-related research. *OPTOMETRY-JOURNAL OF THE AMERICAN OPTOMETRIC ASSOCIATION*, **83**(6), 285–288.

Wu, Y., Zhao, X., Rong, J., and Zhang, Y. (2017). How eco-driving training course influences driver behavior and comprehensibility: a driving simulator study. *Cognition, Technology & Work*, **19**(4), 731–742.

Wu, Y., Kihara, K., Takeda, Y., Sato, T., Akamatsu, M., and Kitazaki, S. (2019). Effects of scheduled manual driving on drowsiness and response to take over request: A simulator study towards understanding drivers in automated driving. *Accident Analysis & Prevention*, **124**, 202–209.

Xiao, D., Fang, Y., Zhang, Y., and Guo, Z. (2017). Analysis of driving behavior at the bridge-tunnel transition section in reduced visibility situations. In *2017 4th*

International Conference on Transportation Information and Safety (ICTIS), pages 581–588. IEEE.

Yang, L., Li, X., Guan, W., Zhang, H. M., and Fan, L. (2018). Effect of traffic density on drivers' lane change and overtaking maneuvers in freeway situation—a driving simulator–based study. *Traffic Injury Prevention*, **19**(6), 594–600.

Yoon, J., Cho, W., Kang, J., Koo, B., and Yi, K. (2010). Design and evaluation of a unified chassis control system for rollover prevention and vehicle stability improvement on a virtual test track. *Control Engineering Practice*, **18**(6), 585–597.

Yosif, S. A. E., Abdelwahab, M. M., ALagab, M. A. E., and Muhammad, F. (2017). Design of bus tracking and fuel monitoring system. In *2017 International Conference on Communication, Control, Computing and Electronics Engineering (ICCCCEE)*, pages 1–5. IEEE.

Yun, S., Teshima, T., and Nishimura, H. (2019). Human–machine interface design and verification for an automated driving system using system model and driving simulator. *IEEE Consumer Electronics Magazine*, **8**(5), 92–98.

Zaal, P., Nieuwenhuizen, F., Mulder, M., and van Paassen, M. (2006). Perception of visual and motion cues during control of self-motion in optic flow environments. In *AIAA Modeling and Simulation Technologies Conference and Exhibit*, page 6627.

Zeng, J. G., Liu, J. Y., and Yu, Q. (2014). Design and development of 6dof hydraulic motion platform for vehicle driving simulator. In *Applied Mechanics and Materials*, volume 505, pages 315–318. Trans Tech Publ.

Zhang, C. and Zhang, L. (2013). Kinematics analysis and workspace investigation of a novel 2-dof parallel manipulator applied in vehicle driving simulator. *Robotics and Computer-Integrated Manufacturing*, **29**(4), 113–120.

Zhang, D., Ivanco, A., and Filipi, Z. (2015). Model-based estimation of vehicle aerodynamic drag and rolling resistance. *SAE International Journal of Commercial Vehicles*, **8**(2015-01-2776), 433–439.

Zhang, S., Luo, Y., Li, K., and Wang, J. (2017). Predictive energy management strategy for fully electric vehicles based on hybrid model predictive control. In *2017 American Control Conference (ACC)*, pages 3625–3630. IEEE.

Zhao, L., Gao, B., Wu, J., and Chen, H. (2017). Optimization of gear number for hybrid electric vehicles using dynamic programming. In *2017 Chinese Automation Congress (CAC)*, pages 6646–6650. IEEE.

Zöller, C., Müller, A., Eggert, L., Winner, H., and Abendroth, B. (2019). Applicability of head-mounted displays in driving simulation. In A. Kemeny, F. Colombet, F. Merienne, and S. Espié, editors, *Proceedings of the Driving Simulation Conference 2019 Europe VR*, pages 9–15, Strasbourg, France. Driving Simulation Association.